CARBON GEOLOGICAL STORAGE

– UNDERLYING PHENOMENA AND IMPLICATIONS –

A Thesis
Presented to
The Academic Faculty

by

D. Nicolas Espinoza

In Partial Fulfillment
of the Requirements for the Degree
Doctor of Philosophy in the
School of Civil and Environmental Engineering

Georgia Institute of Technology
December 2011

CARBON GEOLOGICAL STORAGE

– UNDERLYING PHENOMENA AND IMPLICATIONS –

Approved by:

Dr. J. Carlos Santamarina, Advisor
School of Civil and Environmental Engineering
Georgia Institute of Technology

Dr. Susan Burns
School of Civil and Environmental Engineering
Georgia Institute of Technology

Dr. David Frost
School of Civil and Environmental Engineering
Georgia Institute of Technology

Dr. Guillermo Goldsztein
School of Mathematics
Georgia Institute of Technology

Dr. Christian Huber
School of Earth & Atmospheric Sciences
Georgia Institute of Technology

Date Approved: July 18, 2011

A mis padres y hermanos.

ACKNOWLEDGEMENTS

I am thankful to my family for their love, guidance, and unconditional support during my studies in Jujuy, Córdoba, and Atlanta.

This dissertation could not have been written without the support of my advisor, Carlos. He is a great academician, an outstanding teacher, and exceptional human being. Thank you for trusting me and pushing me beyond the boundaries of knowledge. I also thank the thesis dissertation committee members for their contribution and feedback.

This work is the result of the collective intelligence at the Particulate Media Research Laboratory and Geosystems Group at Georgia Tech: Tae-Sup Yun, Hyunki Kim, Yoo-jong Lee, Changho Lee, Douglas Cortes, Hosung Shin, Veronica Rebata Landa, Jongwon Jung, Minsu Cha, Seunghee Kim, Jaewon Jang, Sheng Dai, Cesar Pastén, Kevin Olson, Tomás Carbini, and Ba Te. I thank them all for sharing their curiosity and thoughts with me. I am also grateful to Georgia Tech staff: Mike Anderson, James Martino, Mike Sorenson, Andy Udell and Carol Maddox.

I would like to acknowledge former mentors and colleagues who played critical roles during my academic formation: Victor Rinaldi, Juan Jose Claria, Franco Francisca and other professors at Universidad Nacional de Córdoba, Argentina.

Finally, I want to express my ever-lasting gratitude to my friends from all over the world I met in Atlanta. Far away home, they have been my family here, and provided the support and happiness needed through this quest.

Support for this research was provided by the United States Department of Energy. Additional funding was provided by the Goizueta Foundation.

TABLE OF CONTENTS

LIST OF TABLES

LIST OF FIGURES

Page

SUMMARY

This thesis explores fundamental concepts related to carbon geological storage, including the possibility of CO_2-CH_4 replacement in hydrate-bearing sediments. CO_2 and CH_4 have pressure-temperature dependent physical properties and interaction with water. These complex interactions in the pore space of natural formations call for specific experimental and analytical research methods to study ensuing chemo-hydro-mechanical couplings in geological systems. This research is based on experimental methods, and is complemented with numerical and analytical techniques to gain a fundamental understanding of the following phenomena:

Interfacial properties of water, mineral, CO_2 and CH_4 systems. Interfacial tension and contact angle are needed to define multiphase interactions and fluid flow in enhanced gas recovery operations and in CO_2 injection and storage in geological formations. Two sections document interfacial tension and contact angle measurement for CO_2-water-mineral and CH_4-water-mineral systems and their implications.

CO_2 sealing capacity of clayey cap rocks. The interaction between clay particles and CO_2, and the response of sediment layers to the presence of CO_2 affect the sealing efficiency of clayey cap rocks as CO_2 trapping structures at injection sites. This study includes a specially designed device to test over-consolidated clay plugs to determine CO_2 breakthrough and CO_2 permeability in highly compacted fine-grained sediments.

Coupled processes and anticipation of potential implications for CH_4-CO_2 replacement in hydrate-bearing sediments. The replacement of CH_4 by CO_2 in methane hydrate requires specific conditions and affects the behavior of the host formation.

Results include physical monitoring data gathered for pure CH_4 hydrate and for CH_4 hydrate-bearing sediments during and after CO_2 injection. These studies investigate the time and space scale of CH_4-CO_2 hydrate replacement and the hydro-mechanical implications.

Experimental and analytical results highlight the prevailing chemical, hydrological, and mechanical processes, their couplings, and emergent phenomena that are critical in defining the response of geological formations to long term CO_2 sequestration.

CHAPTER 1

INTRODUCTION

The dependency on fossil fuels faces resource limitations and sustainability concerns. This situation requires new strategies for greenhouse gas emission management, and the development of new energy sources. Both carbon geological storage and hydrate-bearing sediments have become important research themes because of their potential applications. Carbon geological storage presents new challenges to geotechnical engineering, such as the identification of target formations, injection engineering, assessment of trapping mechanisms, and final monitoring. Additional challenges arise in CO_2 enhanced hydrocarbon recovery processes, such as in CH_4-CO_2 hydrate replacement in sediments.

The main objective of this thesis is to gain a fundamental understanding of the chemo-hydro-mechanical processes and couplings involved in carbon geological storage and CH_4-CO_2 gas replacement in hydrate-bearing sediments. This research is based on experimental methods; complimentary numerical simulation and analytical solutions help identify couplings and implications relevant to the reservoir scale. The study is organized into 7 central chapters as follows:

Chapter 2 explores geotechnical concepts relevant to carbon dioxide geological storage. A review of the chemo-physical properties of water-CO_2-mineral systems, reservoir conditions, and the fundamentals of CO_2 geological storage is followed by the identification of various hydro-chemo-mechanical coupled processes that may lead to emergent phenomena and increase the probability of geotechnical hazards. An additional

section shows potential geophysical strategies to monitor the evolution of CO_2 storage projects. This chapter was developed in collaboration with Seunghee Kim.

Chapter 3 investigates the interfacial properties of CO_2-water-mineral systems with an emphasis on the determination of interfacial tension and contact angle at high pressure. Complementary tests are conducted to evaluate the diffusivity of water in CO_2. Finally, CO_2 injectability and storage in geological formations are assessed based on the previously presented findings.

Chapter 4 parallels Chapter 3 but centers on interfacial phenomena in CH_4-water-mineral systems at reservoir pressure-temperature conditions, including advancing and receding contact angle measurements on various substrates that may be encountered in natural systems. Additional analyses identify multiphase flow characteristics in the context of natural gas production, hydrate-bearing sediments, and coal bed methane.

Chapter 5 presents a summary of previous CH_4-CO_2 replacement studies, identifies and analyzes underlying processes, and presents new experimental results. Results are used to evaluate reaction rates, to explore the pressure-temperature region for optimal exchange, and to anticipate potential geomechanical implications for CH_4-CO_2 replacement in hydrate-bearing sediments. The reported investigation was performed in collaboration with Jonwong Jung.

Chapter 6 uses P-waves to monitor the evolution of CH_4 hydrate formation, CO_2 flooding, CH_4-CO_2 replacement, and final hydrate dissociation in sands. The purpose of this chapter is to characterize the mechanical behavior of CH_4 hydrate-bearing sediments during CH_4-CO_2 hydrate replacement.

Chapter 7 explores the micro-scale interactions between liquid and supercritical CO_2 and clay minerals in order to determine the potential role of electrical and capillary forces on the performance of the cap rock. This chapter begins with an assessment of electrical and capillary forces in clay-water-CO_2 systems and is followed by experimental evidence gathered in simple and well constrained experiments. Finally, geomechanical and hydrological implications for CO_2 storage sites that involve clayey cap rocks are anticipated.

Chapter 8 analyzes the transport of CO_2 through well-characterized single-mineral sediments saturated with water and brine, and consolidated to reservoir level effective stress. The study explores the hydrological and geomechanical implications of CO_2 breakthrough in cap rocks, including the potential for leaks.

Finally, salient observations from this thesis are summarized in Chapter 9.

CHAPTER 2

CO_2 GEOLOGICAL STORAGE - GEOTECHNICAL IMPLICATIONS

2.1 Introduction

Quality of life, in terms of education, infant mortality and life expectancy, correlates with energy consumption. Global energy consumption will increase dramatically in the next decades, and it will largely rely on fossil fuels because of the available reserves, their low cost, the investment in current infrastructure, and the still limited development of renewable energy. Currently, 90% of the total primary energy sources in the world are fossil fuels, and more than 85% in the USA [*DOE*, 2010b].

The use of fossil fuels is intimately linked to the emission of CO_2 into the atmosphere. The current concentration of CO_2 in the atmosphere is ~385ppm (parts per million), which is almost twice the concentration before the Industrial Revolution [200 ppm - *IPCC*, 2001]. Anthropogenic CO_2 global emissions add to ~7 GtC/year (see Figure 2.1). The USA releases 1.59 GtC/yr and China 1.78 GtC/yr – 2007 data [*CDIAC*, 2009]. Power plants account for ~40% of total CO_2 emissions. Once released into the atmosphere, CO_2 enters into the global carbon cycle and interacts with the ocean and terrestrial sinks as shown in Figure 2.2.

The estimated net annual increase of CO_2 concentration in the atmosphere is problematic since CO_2 is a greenhouse gas. The mean surface temperature has increased ~0.6±0.2°C since the industrial revolution, and atmospheric models forecast as much as a

~3°C increase by 2100 if anthropogenic CO_2 emissions continue current trends (Figure 2.3).

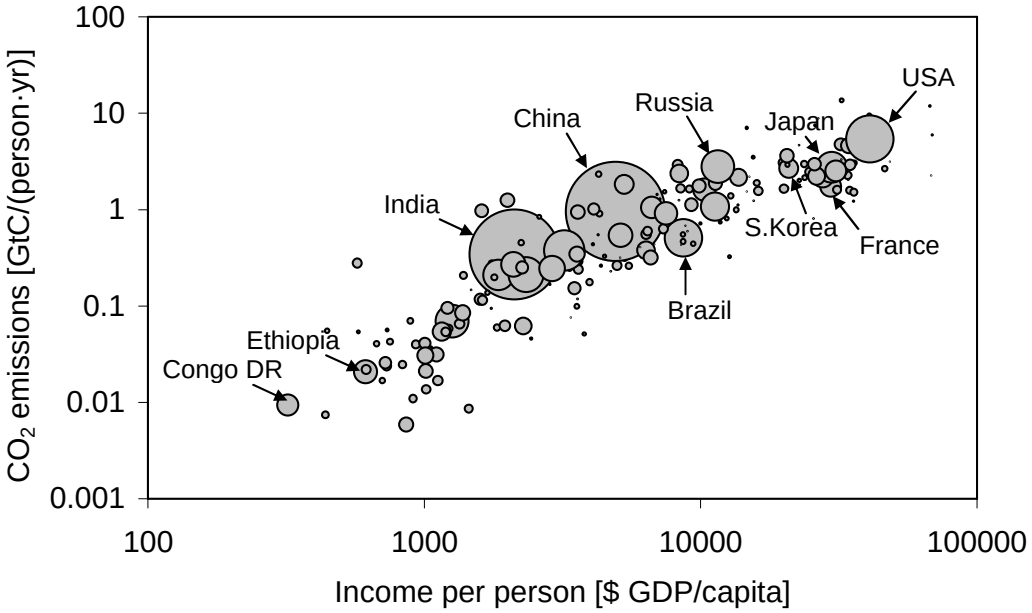

Figure 2.1. Annual CO_2 emissions per person as a function of Gross Domestic Product (adjusted for inflation) for different countries. Data from the Carbon Dioxide Information Analysis Center (www.cdiac.ornl.gov) and (www.gapminder.org).

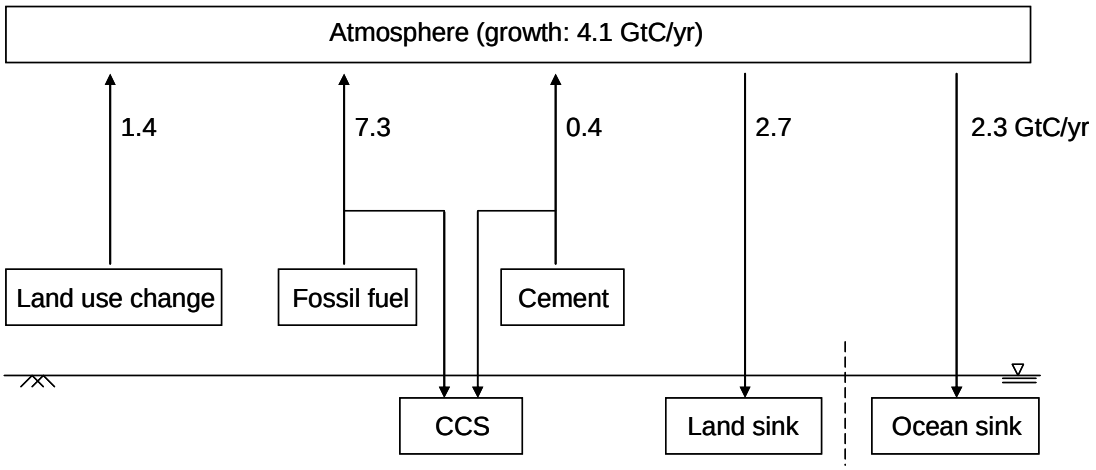

Figure 2.2. Anthropogenic perturbation of the carbon dioxide cycle – Values show the annual contribution [data from: *Global-Carbon-Project*, 2010].

The UN Framework Convention on climate change has suggested that the atmospheric concentration of CO_2 should not exceed 450 ppm to prevent a major impact on climate conditions. Several technologies have been proposed for mitigating the emission of CO_2 into the atmosphere (Table 2.1). Two clear options call for reducing the combustion of fossil fuels, and capturing the generated CO_2 followed by permanent sequestration.

Suggested minimum storage time for CO_2 geological storage ranges between 1,000 and 10,000 years. This requirement is less demanding than for nuclear waste in part due to the expectation that future technological developments might find other methods to mitigate global warming, and because of natural climate fluctuations such as the average glacial cycle period of 28,000 years [*Augustin et al.*, 2004]. Figure 2.4 shows a comparison of time scales for different processes related to human activities and geologic processes relevant to energy. The dramatic contrast between political, engineering, and geological time scales add difficulty to short-time decision making.

The purpose of this manuscript is to explore geotechnical concepts relevant to carbon dioxide geological storage. First, we review the chemo-physical properties of water-CO_2-mineral systems, reservoir conditions, and the fundamentals of CO_2 geological storage. Next, we explore various hydro-chemo-mechanical coupled processes that may lead to emergent phenomena and increase the probability of geotechnical hazards. Finally, we investigate potential geophysical strategies to monitor the evolution of CO_2 storage projects.

Table 2.1 . CO_2 emission mitigation technologies.

CO_2 emission mitigation technology	**Advantages**	**Difficulties**	**Capacity and certainty of execution**
DIRECT - capture, transport, and final sequestration of CO_2 generated from fossil fuel power plants,			
CO_2 geological storage coupled or not with fuel switching	- Existent injection technology for injection - Large capacity - May give additional revenue by enhanced hydrocarbon production	- Cost: it needs additional energy consumption ~20% for carbon capture and storage (1) - Monitoring, contamination, and liability	- Large capacity: 10^3~10^4 $GtCO_2$, mostly in saline aquifers (2)
Ocean storage	- Easy and relatively inexpensive. - No porous media involved	- Water acidification and effects on aquatic life (3) - Transportation to the site	- Very large capacity >> 10^3 $GtCO_2$ (volume of the ocean deeper than ~3000m)
Chemical carbonation	- Thermodynamically stable	- Expensive and labor intensive	- Very limited, for example: annual production of concrete is ~15Gt concrete
INDIRECT - produce CO_2-free energy, improve energy conservation and efficiency, or increase CO_2 natural uptake			
Alternative energy sources			
Renewables, Solar, Wind, Geothermal	- Do not generate CO_2	- Small contribution to the energy portfolio	- Currently provide 4% of the energy demand (4)
Nuclear fission	- Do not generate CO_2 - Available technology	- Nuclear waste - Non-commercial use of nuclear power technology	- Currently provide 6% of the energy demand (4)
Biofuels	- Consume bio-products in excess, e.g. sugar cane and corn	- Competes with food supply	- In Brazil ethanol accounts for less than 5% of the energy production (5)
Conservation and efficiency			
Change in people habits - e.g. promote mass transit	- No cost	- Changing habits require time and policy	- Depends on the country, some countries are already highly efficient.
More efficient end-use energy technologies and appliances - HVAC	- Under development by industries	- It needs a vigorous market-transforming policies (6)	- Efficient application could reduce carbon emissions from the building sector to levels equivalent to those 20 years ago.
CO2 surface uptake			
Terrestrial uptake	- Relatively inexpensive	- Difficult to increase natural sinks (trees, algae) - Uncertainties about the land use in the future (7)	- Currently at maximum - Uptake in about ~20% of total emissions.

(1) [*Dooley et al.*, 2006; *Heddle et al.*, 2003]; (2) [*IPCC*, 2005]; (3) [*Golomb*, 1993; *House et al.*, 2006]; (4) [*IEA*, 2009]; (5) [*World-Resources-Institute*, 2010a]; (6) [*Brown and Southworth*, 2008]; (7) [*Jaccard*, 2005].

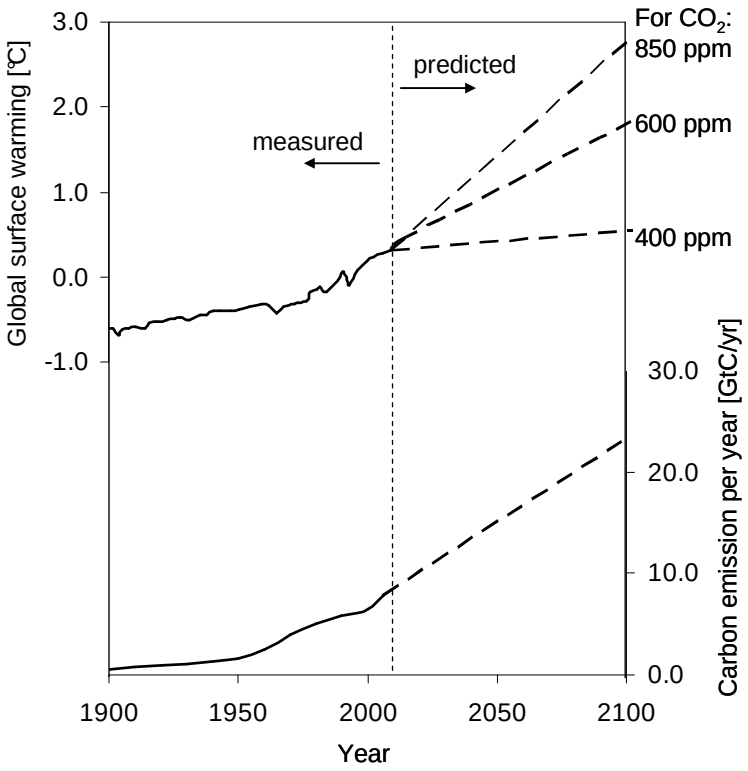

Figure 2.3. Past and extrapolated future CO_2 emissions [data from: *Pacala and Socolow*, 2004; *World-Resources-Institute*, 2010b] and global warming predictions for different CO_2 levels [data from: *Solomon*, 2007].

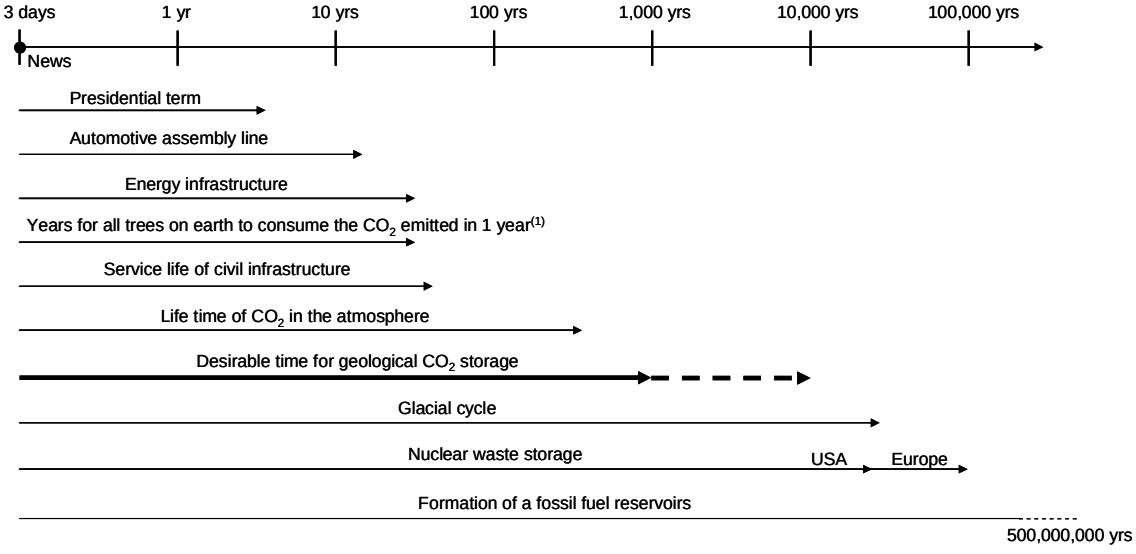

Figure 2.4. Time scales of relevant energy-related activities and processes [Note: (1) Estimation based on the capacity of forest to observe carbon in atmosphere, 0.17GtC/yr, from *IPCC*, 2001]

2.2 CO_2 geological storage and reservoir conditions

Volume Estimation. The injected CO_2 displaces the original fluids that fill the voids in geological formations. The volume of the geological formation V_{bulk} affected by the injection of a volume of CO_2 V_{CO2} is a function of the average porosity of the reservoir n,

$$V_{bulk} = \frac{1}{\psi}\frac{V_{CO2}}{n} \tag{2.1}$$

where the displacement efficiency coefficient is ψ~0.6 in media with spatially correlated random porosity and can be very low ψ<0.1 if fingered invasion takes place (note: buoyancy effects, closed hydraulic boundary conditions, and the use of multiple injection wellbores can lower efficiency by as much as ψ ~0.01 [*Ehlig-Economides and Economides*, 2010]). Let's assume a target sequestration of 4GtC/year (for a flat trend based on present data – Figure 2.2). The total amount of CO_2 to be sequestered in the next 50 years is 200 GtC or 730 $GtCO_2$. In a compressed state (ρ_{CO2}~0.7 tonnes/m^3), this mass would occupy a volume V_{CO2} = 1,050 km^3. The geological volume for storage would be V_{bulk}~27,500km^3 for a porosity n~0.2, and displacement efficiency ψ=0.5. A 100m thick reservoir would extend ~325km in each direction.

CO_2 Trapping. The trapping mechanisms to keep CO_2 within deep geological formations rely on physical as well as chemical processes [*Dooley et al.*, 2006; *IPCC*, 2005; *Jaccard*, 2005]. Physical trapping mechanisms include structural and stratigraphic trapping by cap rocks, hydrodynamic trapping by slow aquifer currents, and capillary trapping by interfacial forces. Chemical trapping mechanisms include dissolution of CO_2 in water, mineralization, CO_2 adsorption on coal and rich-organic shales, and CO_2 hydrate formation. Most trapping mechanisms and safe disposal conditions are found and

favored at depth. We note that there are natural accumulations of CO_2 in the Earth's upper crust where CO_2 has been contained for geological times such as the Ladbroke Grove and Katnook Gas Fields in southeastern Australia [*Watson et al.*, 2004].

Geological Formations. Stable sedimentary basins facilitate CO_2 storage, particularly when they are near emission points. These basins are found in most continents [*IPCC*, 2005]. The USA, Canada and Australia have extensive storage capacity [*Dooley et al.*, 2006].

Favorable storage sites must have a thick accumulation of permeable sediments to maximize storage capacity and injectivity, overlain by a highly impermeable seal or cap rock (generally shale and evaporites).

The increase in effective stress with depth *z* leads to low porosity fine grained sediment barriers. Pore size depends on porosity and specific surface. In high specific surface montmorillonitic shales, the mean poresize can be in the order of 10^{-8}m [*Armitage et al.*, 2010; *Hildenbrand et al.*, 2002]. High porefluid pressure at depth also lowers the mass density difference between water and CO_2, increases the solubility of CO_2 in water, and increases the adsorption of CO_2 in coal.

The geological system should be structurally simple. Candidate storage sites are assessed for reservoir size, depth and hydrogeology, geology and petrophysical characteristics of the reservoir and the seal cap rock, surface temperature and geothermal gradient, tectonic stability and faulting intensity, accessibility, infrastructure, and proximity to major CO_2 sources.

Figure 2.5 shows schematic diagrams of various formations for CO_2 geological storage. The principal targets for CO_2 injection are deep saline aquifers and depleted/semidepleted hydrocarbon reservoirs (which inherently include physical barriers and cap rocks). Injection into coal seams benefits from the co-production of CH_4. Similarly, hydrate-bearing sediments can also be used to sequester CO_2 while at the same time releasing CH_4 (a pilot test in the Alaska North Slope is planned for 2011, US DOE-NETL, project DE-NT0006553). Deep saline aquifers are most abundant and could store 110 to 2700 GtC [*Gale*, 2004].

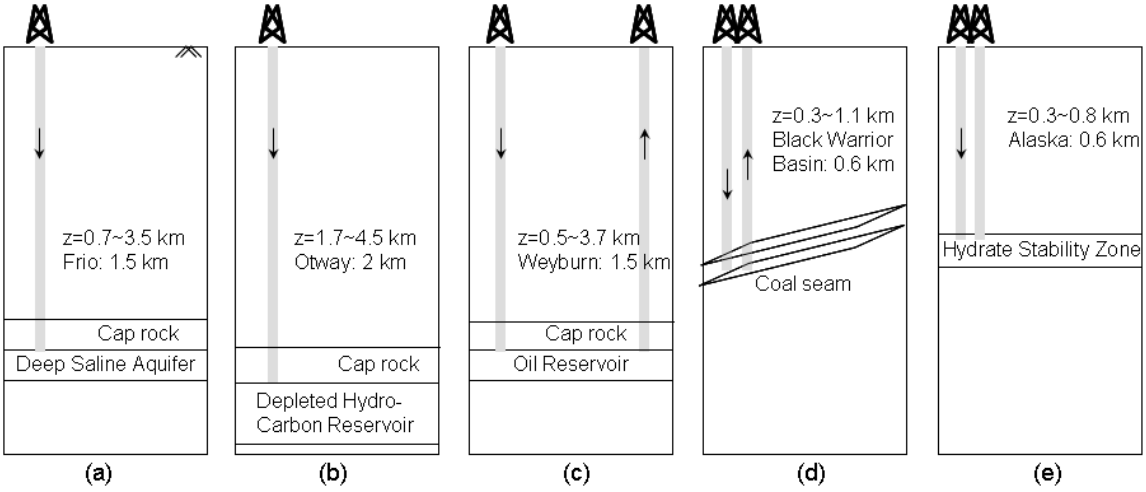

Figure 2.5. CO_2 storage alternatives. (a) Deep saline aquifers. (b) Depleted hydrocarbon reservoirs. (c) CO_2-enhanced oil recovery. (d) CO_2-enhanced gas recovery from coal bed methane. (e) CO_2-CH_4 replacement in hydrate bearing sediments. Depths shown for selected pilot projects.

Pilot Projects. There are more than 50 CO_2 injection projects reported worldwide [*DOE*, 2010a]. Figure 2.6 shows the mean pressure-temperature conditions at these storage sites. Most projects involve supercritical CO_2 and relatively small volumes.

Implementation. The injection of CO_2 underground can be implemented with technology developed for petroleum and gas production. In fact, acid gas injection is routinely done in Alberta, and CO_2-enhanced oil recovery is a common practice in oil

reservoirs around the world, and there are more than ~5000km of CO_2 pipelines in North America [*Dooley et al.*, 2006]. Still, the systematic geological storage of CO_2 will require improvements in risk assessment, adequate evaluation of regional capacity and reservoir integrity, matching emission sources with sinks, and enhanced monitoring technology [*Gale*, 2004]. In addition to these technical difficulties, economical, political, and legal obstacles have hindered the adoption of CSS technologies.

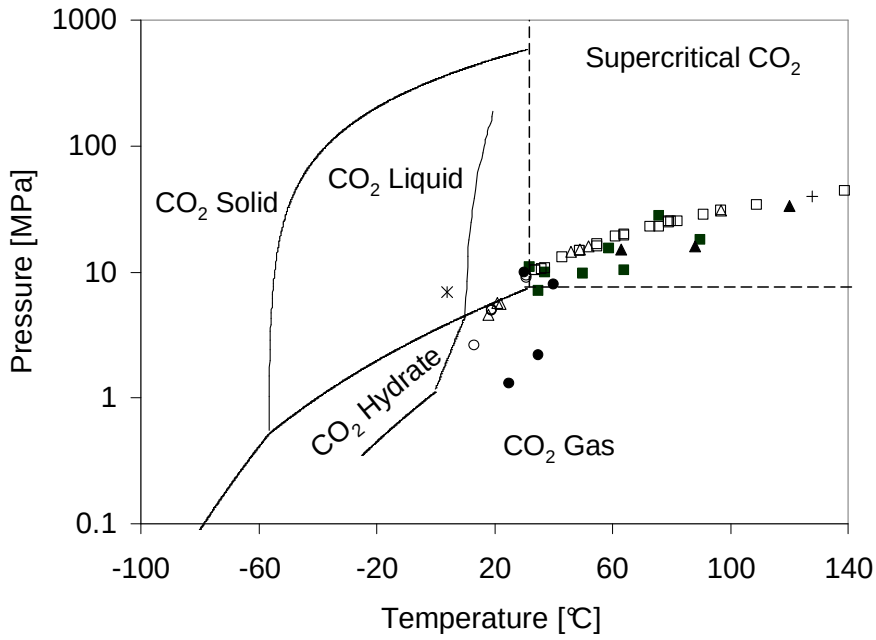

Saline aquifer: ■ P-T record □ Estimated value	CO_2-EOR: ▲ P-T record △ Estimated value	CO_2-ECBM: ● P-T record ○ Estimated value
EGR: +	CO_2-CH_4 replacement: ✳	

Figure 2.6. Pressure-temperature dependent CO_2 phases. Pilot CO_2 injection projects are superimposed on this plot. Unless reported in the original sources, the PT conditions are estimated as: $P = g\,\rho_w\,z$, $T = T_0\ (4°C) + 30°C/km \cdot z$. [CO2 hydrate phase boundary from *Sloan and Koh*, 2008; *Takenouchi and Kennedy*, 1965]

2.3 Underlying concepts and implications

2.3.1 Geochemical concepts

Properties of CO_2. The combustion of fossil fuels yields CO_2 among other byproducts. For example, burning methane produces

$$CH_4 + 2\ O_2 \rightarrow CO_2 + 2\ H_2O$$

The physical properties of CO_2 depend on pressure-temperature P-T conditions. The CO_2 phase diagram is shown in Figure 2.6. CO_2 is a gas at normal temperature and pressure, it turns into liquid at moderate pressures ~6.4MPa at 298K, and becomes supercritical when the temperature is higher than 304.1K and the pressure is greater than 7.38 MPa. The mass density ρ of CO_2 varies widely, in fact, CO_2 is heavier than seawater at pressures above ~28MPa at 277.15K (ρ_{CO2}=1035kg/m^3). Mass density can be approximated with a cubic equation of state [*Peng and Robinson*, 1976] or using more accurate but complex equations [*Span and Wagner*, 1996]. The mass densities of water and CO_2 are plotted in Figure 2.7 for typical P-T conditions present in onshore and offshore applications.

Other important P-T dependent properties of CO_2 include high bulk compressibility, typically an order of magnitude higher than that of water [*Span and Wagner*, 1996], and very low viscosity, typically 10 times lower than that of water as shown in Figure 2.7, [μCO2=10-4 Pa•s at 10MPa and 280K - *Fenghour et al.*, 1998].

Water-CO_2 interaction and properties. CO_2 dissolves in water to form aqueous carbon dioxide CO_2(aq). The solubility of CO_2 in water x_{CO2} [mol/L] can be estimated using Henry's law

$$x_{CO2} = k_H\, \varphi\, P_{CO2} \qquad (2.2)$$

where the Henry's coefficient is approximately $k_H \approx 10^{-1.46} = 0.0347$ and the fugacity coefficient $\varphi \leq 1$ can be estimated with an equation of state. Water at room temperature and at 0.1MPa contains $x_{CO2} \approx 0.03$-to-0.04 mol/L. That solubility increases by two orders of magnitude $x_{CO2} \approx 1$-to-2 mol/L as pressure and temperature increase to reservoir conditions, i.e., one to two moles of CO_2 per liter of brine (Figure 2.8).

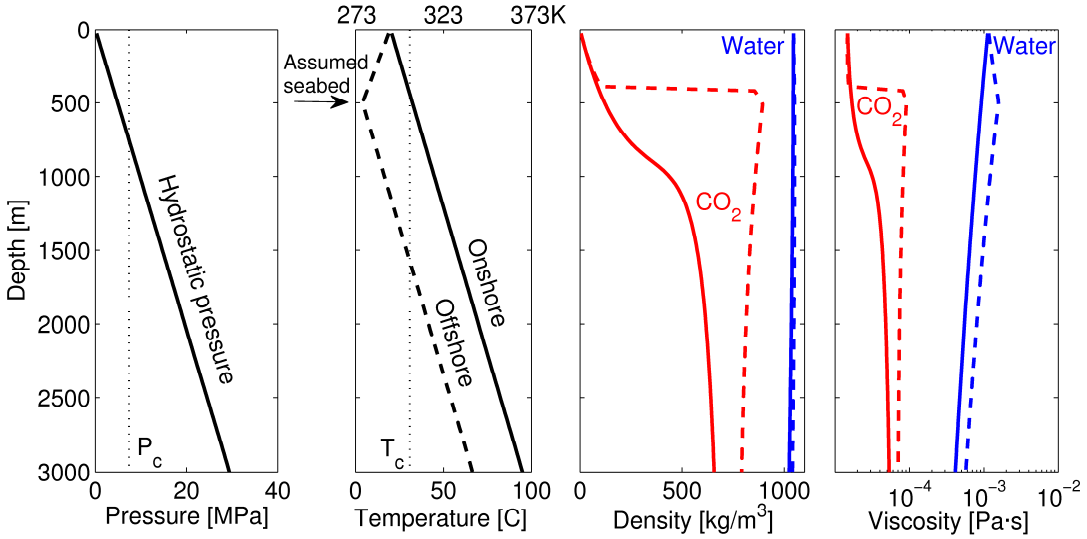

Figure 2.7. Density and viscosity of CO_2 and water as a function of depth, both on-shore and off-shore (for an assumed seabed at 500 m). P_c and T_c are the critical pressure and temperature for CO_2. Note: the density of liquid CO_2 exceeds the density of deep seawater when the seabed is deeper than 3000m.

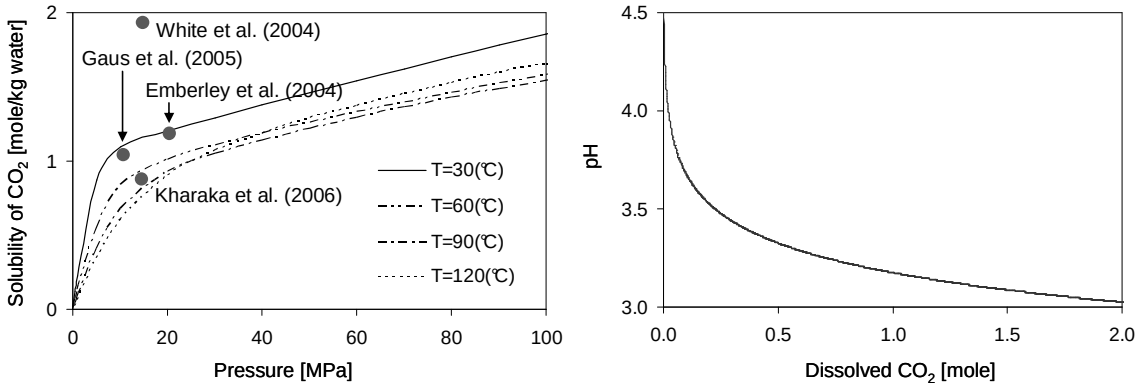

Figure 2.8. CO_2 solubility in water and pH. (a) CO_2 solubility in 1 m NaCl aqueous solution (Note: a salinity increase reduces CO_2 solubility). (b) pH as a function of dissolved CO_2 [Note: solubility data from *Duan and Sun*, 2003a].

Part of the aqueous carbon dioxide mixes with water to produce carbonic acid and ionizes stepwise, at 298K:

$CO_2(g) \rightleftharpoons CO_2(aq)$ $\log K_{eq} = 1.47$, Henry's law

$CO_2(aq) + H_2O(l) \rightleftharpoons H_2CO_3\,(aq)$ $\log K_{eq} = 2.81$,

$H_2CO_3^*\,(aq) \rightleftharpoons H^+ + HCO_3^-(aq)$ $\log K_{eq} = -6.35$,

$HCO_3^-(aq) \rightleftharpoons H^+ + CO_3^{2-}(aq)$ $\log K_{eq} = -10.33$

where $H_2CO_3^*(aq) = CO_2(aq) + H_2CO_3(aq)$. The final result of adding CO_2 to water is the production of ion carbonates, an increase in H^+, and a decrease in pH. At reservoir conditions, CO_2 dissolution in water yields a pH ≈3 (Figure 2.8).

Other relevant properties of the water-CO_2 system include (a) solubility of water in liquid and supercritical CO_2 [~0.05mol of water per kg of liquid CO2 at 10 MPa and 285K - *Spycher et al.*, 2003], (b) high diffusivity of water into liquid CO_2 [D≈2-to-20×10-8m2/s - at 7-25 MPa and 305±10K - *Espinoza and Santamarina,* 2010a], and (c) CO_2 hydrate formation at high pressure and low temperature [Figure 6 - *Sloan and Koh,* 2008].

Water-CO_2-mineral interaction. Table 2.2 summarizes representative chemical reactions, typical reaction rates and related comments. The equilibrium constant for dissolution reaction denotes the concentration of produced species relative to the concentration of reactant species at steady state conditions, i.e., a function of mineral solubility. The solubility of minerals in water depends on the pH. [*Stumm and Morgan,* 1996]. Furthermore, the reaction rate of minerals in CO_2-water depends on temperature, pressure (i.e., CO_2 solubility and pH), and the concentration of other species [*Algive et*

al., 2009; *Fredd and Fogler*, 1998; *Pokrovsky et al.*, 2005; *Renard et al.*, 2005]. Dissolution rates for calcite $CaCO_3$, anorthite $CaAl_2Si_2O_8$, and kaolinite $Al_2Si_2O_5(OH)_4$ are plotted as a function of pH in Figure 2.9. Silicates yield more dissolved cations (pH up to 8) than carbonates (pH up to 5) but the reaction rate is much slower [*Gunter et al.*, 2000]. Consider 1 mm spheres of calcite, anorthite, and kaolinite submerged into water acidified by 1 mole of dissolved CO_2 per liter (pH~3). Using dissolution rates in Figure 2.9 and assuming that the system is far from equilibrium, the time required to dissolve each sphere is 4 hours for calcite, 16 years for anorthite, and 226 years for kaolinite. It is also important to recognize the high reactivity of water dissolved in CO_2 with steel and minerals [*McGrail et al.*, 2009].

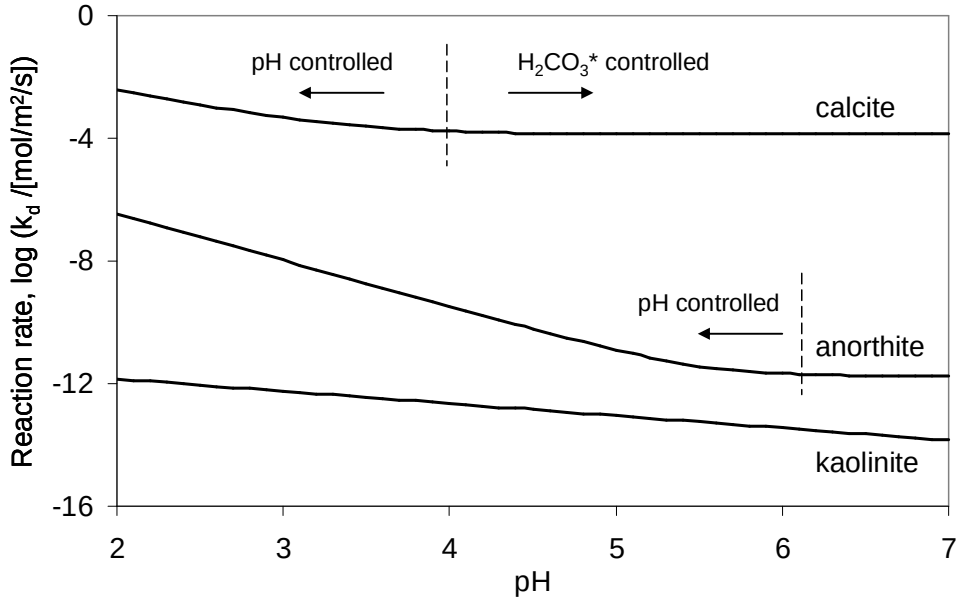

Figure 2.9. Reaction coefficient k_d for calcite $CaCO_3$, anorthite $CaAl_2Si_2O_8$, and kaolinite $Al_2Si_2O_5(OH)_4$ at a temperature of 40 °C and $[CO_{2(aq)}]$ = 1 mole. For calcite, $k_d = k_1[H^+] + k_2[H_2CO_3^*(aq)]$ where $k_1 = 0.745$, $k_2 = 8.6 \times 10^{-4}$ [mol/m^2/s] at 40 °C [*Algive et al.*, 2009; *Fredd and Fogler*, 1998; *Pokrovsky et al.*, 2005; *Renard et al.*, 2005]. For anorthite, $k_d = k_H[H+]^{1.5} + k_{H2O} + k_{OH}[OH^-]^{0.33}$ where $k_H = 6.883 \times 10^{-4}$, $k_{H2O} = 3.58 \times 10^{-12}$, and $k_{OH} = 4.51 \times 10^{-14}$ [mol/m^2/s] at 40 °C [*Li et al.*, 2006]. For kaolinite, $k_d = k_H[H+]^{0.4} + k_{OH}[OH^-]^{0.3}$ where $k_H = 2.79 \times 10^{-11}$ and $k_{OH} = 3.51 \times 10^{-16}$ [mol/m^2/s] at 40 °C [*Li et al.*, 2006].

Table 2.2. Mineral reactions with CO_2-acidified water.

Mineral	Typical reaction	Reaction rate	Notes
1) Silicates[a)]	$SiO_{2(s)} + 2H_2O \rightleftharpoons H_4SiO_4$ $\rightleftharpoons H^+ + H_3SiO_4^-$ $\rightleftharpoons H^+ + H_2SiO_4^{2-}$	1.26×10^{-14} mol·m^{-2}s^{-1} (White et al., 2005)	·Solubility of quartz does not change with concentration of dissolved CO_2
2) Aluminosilicates[b)]	Anorthite: $CaAl_2Si_2O_{8(s)} + 8H^+ \rightleftharpoons Ca^{2+} + 2Al^{3+} + 2H_4SiO_4$, $K_{eq} = 10^{21.7}$ Kaolinite: $Al_2Si_2O_5(OH)_4(s) + 6H^+ \rightleftharpoons 2Al^{3+} + 2H_4SiO_4 + H_2O$, $K_{eq} = 10^{3.8}$	Anorthite: 1.2×10^{-5} mol·m^{-2}s^{-1} Oligiocalse: 1.2×10^{-8} mol·m^{-2}s^{-1} Albite: 3.6×10^{-9} mol·m^{-2}s^{-1} Kaolinite: 10^{-14}-to-10^{-15} mol·m^{-2}s^{-1} (Gaus et al., 2005)	·Include feldspars, micas, and clays. ·Reaction rate is slow. ·Yields more dissolved cations than carbonate. ·Results in pH up to 8.
3) Carbonates[c)]	$CaCO_{3(s)} + H^+ \rightleftharpoons Ca^{2+} + HCO_3^-$, $K_{eq} = 10^{1.85}$ $CaCO_{3(s)} + CO_2 + H_2O \rightleftharpoons Ca^{2+} + 2HCO_3^-$, $K_{eq} = 10^{-4.5}$ $CaCO_{3(s)} + H_2O \rightleftharpoons Ca^{2+} + HCO_3^- + OH^-$, $K_{eq} = 10^{-8.48}$	Calcite: $1.6\text{-to-}3.2\times10^{-5}$ mol·m^{-2}s^{-1} (Brosse et al., 2005)	·Faster than aluminosilicates. ·Solubility depends on T, P, Salinity, ionic concentration, and pH. ·Dissolution rate is fast, but overall amount of reaction is small. ·Results in pH from 3 to 5

Sources: (a) [*Drever*, 1997]; (b) [*Li et al.*, 2006]; (c) [*Algive et al.*, 2009; *Fredd and Fogler*, 1998; *Renard et al.*, 2005; *Stumm and Morgan*, 1996]

CO_2 adsorption on organic surfaces. Coal and organic shales adsorb CO_2 [*DOE-NETL*, 2008; *Larsen*, 2004] Langmuir-type sorption isotherms are commonly used to characterize the adsorption at pressures <10MPa [*Ceglarska-Stefanska and Zarebska*, 2002b; *Mazumder et al.*, 2006]. For reference, about ~1.6 moles of CO_2 can be adsorbed per kg of coal at 3MPa and 298K (37 cm^3 of gas CO_2 at normal pressure and temperature per gram of coal). A higher fluid pressure promotes higher and faster uptake.

Summary. High fluid pressure and temperature bring CO_2 into liquid or supercritical phases and promote CO_2 solubility in water and adsorption onto organic

surfaces. In the presence of CO_2, water acidifies and more intense and faster mineral dissolution takes place. Liquid and supercritical CO_2 exhibit much lower viscosity than water.

2.3.2 Mixed fluid conditions

Pressure dependent T_s and θ. The water-CO_2 interfacial tension decreases from T_s~72 to 25 mN/m as the pressure increases from 0.1MPa to 6.4MPa at ~298K, eventually T_s reaches a plateau T_s =25±5 mN/m in supercritical state [*Espinoza and Santamarina*, 2010a; *Kvamme et al.*, 2007b]. Furthermore, the contact angle formed by the CO_2-water interface on mineral surfaces varies with fluid pressure in response to changes in CO_2-water interfacial tension: as the fluid pressure increases, the contact angle increases on non-wetting surfaces such as oil-wet amorphous silica and coal and slightly decreases in water-wet amorphous silica and calcite surfaces [*Chalbaud et al.*, 2009; *Chi et al.*, 1988; *Chiquet et al.*, 2007; *Dickson et al.*, 2006; *Espinoza and Santamarina*, 2010a].

Changes in interfacial tension T_s and contact angle θ (Section 2.3.1) will affect the capillary pressure, the evolution of flooding, the residual saturation, relative permeabilities, and capillary effects. In its simplest form, capillary pressure ΔP_c [Pa] is estimated from Laplace's equation,

$$\Delta P_c = P_{CO2} - P_w = \frac{2T_s}{r}\cos\theta \qquad (2.3)$$

Breakthrough pressure. The breakthrough pressure P^*_{thru} when CO_2 percolates through a porous medium depends on the mean pore size expressed in terms of specific surface S_s and void ratio $e = e_{1kPa} - C_c \log(p'/1kPa)$, the wettability of the minerals in the

presence of water and CO_2, and the standard deviation in pore size distribution. We can extend Laplace's capillary pressure equation to obtain the following expression for the breakthrough pressure [*Espinoza and Santamarina*, 2010a],

$$P^*_{thru} = \psi \frac{S_s \rho T_s \cos\theta}{e_{1\text{kPa}} - C_c \log \frac{p`}{1\text{kPa}}} \tag{2.4}$$

where *p'* is the in situ effective stress, and the factor ψ depends on clay fabric and grain size distribution; a value of $0.04<\psi<0.08$ applies to smectite clay barriers. The sealing capacity of cap rocks will depend on this breakthrough pressure; thereafter, the leak rate will be determined by the cap rock permeability to CO_2 [*Fleury et al.*, 2010; *Pusch et al.*, 2010].

Differences in mass density - Convection and self mixing. CO_2 is lighter than water or brine at reservoir P-T conditions (Figure 2.7). The Bond number *B* quantifies gravity-driven CO_2 migration as a function of the mass density difference ($\rho_w - \rho_{CO2}$) relative to capillary forces $T_s \cdot \cos\theta$ [*Pennell et al.*, 1996]:

$$B = \frac{(\rho_w - \rho_{CO_2}) g k k_{rCO2}}{T_s \cos\theta} \tag{2.5}$$

The mass density of the water with CO_2 in solution ρ_{sol} [kg/m^3] is slightly heavier than the formation water and can be estimated from the mass density of pure water ρ_w [kg/m^3] and the concentration of CO_2 in water x_{CO2} [mol/m^3] as

$$\rho_{sol} = \rho_w + m_{CO2} x_{CO2} - x_{CO2} \rho_w V_\varphi \tag{2.6}$$

where m_{CO2}[kg/mol] is the molecular weight of CO_2, and V_φ [m^3/mol] is the apparent molar volume of dissolved CO_2 as a function of temperature T[C], $V_\varphi = 37.51 \cdot 10^{-6} - 9.585 \cdot 10^{-8} T + 8.740 \cdot 10^{-10} T^2 - 5.044 \cdot 10^{-13} T^3$ [*Garcia*, 2001]. For example, there is an

increase in density $\Delta\rho$ ~ 10kg/m^3, for water saturated with CO_2 at 10MPa and 313K (x_{CO2} ~ 1230 mol/m^3). Dissolution-densification and gravity-driven flow will cause convective transport which will accelerate CO_2 mixing in the reservoir water [*Kneafsey and Pruess*, 2010; *Riaz et al.*, 2006].

Differences in viscosity: Fingering. Two dimensionless numbers control the pattern of fluid displacement: (1) the ratio of viscosities M between the invading fluid μ_{CO2} and the displaced fluid μ_w, and (2) the capillary number C which is the ratio between viscous and capillary forces,

$$M = \frac{\mu_{CO2}}{\mu_w} \tag{2.7}$$

$$C = \frac{q\mu_{CO2}}{T_s \cos\theta} \tag{2.8}$$

where q[m^3/s/m^2] is the injection rate, T_s[N/m] is the interfacial tension between water and CO_2, and θ is the contact angle formed by the water-CO_2 interface and the mineral surface. Stable displacement takes place when M>1 and C>1, viscous fingering when M<<1, and capillary fingering when C<<1 [*Lenormand et al.*, 1988]. Since the viscosity of CO_2 is at least one order of magnitude lower than that of water at reservoir P-T conditions (Figure 2.7), CO_2 may displace water from the pore space in the form of viscous fingers; in this case, the bulk volume of sediment V_{bulk} involved in storage will increase dramatically (Equation 2.1).

CO_2 lowers the viscosity of oil. CO_2 dissolves in crude oil (typically alkanes with less than 13 carbon atoms at reservoir conditions with P>10MPa and T>320K), lowers the viscosity of the crude oil, and favors oil recovery [*Blunt et al.*, 1993].

Summary. Interfacial tension and the capillary entry pressure for CO_2 into a water saturated seal cap rock decrease with pressure. The dissolution of CO_2 in water increases the density of water, promote gravity-driven flow and accelerate mixing. Pronounced differences in viscosities between in liquid or supercritical CO_2 and water tend to promote viscous fingering during CO_2 injection.

2.3.3 Chemo-hydro-mechanical coupling

Increased fluid pressure and fault reactivation. The increase in porefluid pressure during CO_2 injection can reactivate nearby faults if the state of effective stress approaches failure conditions [*Rutqvist and Tsang*, 2002; *Streit and Hillis*, 2004].

Capillary-driven deformation. The invasion of immiscible CO_2 in a water saturated reservoir gives rise to capillary forces and can cause significant volumetric deformation in fine-grained sediments [*Delage et al.*, 1996].

Fluid-driven fracture formation. Hydraulic fracture can take place in both cohesive-cemented and cohesionless-frictional sediments [*Bjerrum et al.*, 1972; *Jaworski et al.*, 1981; *Zhai and Sharma*, 2005]. Particle-scale mechanisms compatible with the effective-stress dependent strength of sediments take into consideration capillary forces induced by the tensile membrane between CO_2 and water, seepage drag forces, and skeletal forces to explain particle displacement and localization [*Shin and Santamarina*, 2010].

Effects of pH and permittivity on interparticle electrical forces - changes in clay fabric. Two fluid-mineral interactions anticipate changes in interparticle forces after CO_2 injection: (1) water acidification changes the mineral surface charge, and (2) the low

permittivity of CO_2 (κ'~2 to 3) compared to water (κ'=80) implies changes in van der Waal's attraction [*Israelachvili*, 1991; *Obriot et al.*, 1993; *Palomino and Santamarina*, 2005]. These fluid-mineral phenomena will alter the equilibrium between van der Waal's attraction and double layer repulsion forces at the clay particle scale, cause changes in clay fabric, and affect the seal capacity of cap rocks.

Reactive fluid transport - Wormholes. Acidified water dissolves minerals and enlarges pores along transport channels [*Emberley et al.*, 2004; *Gunter et al.*, 2000; *Kaszuba et al.*, 2005; *Watson et al.*, 2004]. The hydraulic conductivity may increase by a factor of 10-to-100 [*Verdon and Woods*, 2007], with even small changes in global porosity, as can be predicted using the Kozeny-Carman model. Two dimensionless numbers control the evolution of dissolution patterns: Damköhler number represents the ratio between advection and reaction times $Da= \kappa l/v$ (reaction rate κ[1/s], characteristic length l[m], velocity v[m/s]), while the Peclet number is the ratio between advection and diffusion time $Pe=vl/D$ (diffusion coefficient D[m^2/s]). The process is mass-transfer limited if a chemical reaction is very fast compared to mass-transfer kinetics $Da>>1$ (e.g., more likely in the dissolution of carbonates). Otherwise, the process is reaction-rate limited $Da<<1$ (e.g., more likely if the dissolution of aluminosilicates is involved). The dissolution pattern during reactive transport can be categorized as face/global dissolution ($Da>10^{-3}$, $Pe<10^{-3}$), dominant wormholes ($Da>10^{-3}$, $Pe>10^{-2}$), or uniform dissolution ($Da<10^{-3}$) [*Golfier et al.*, 2002]. A rapid mineral dissolution rate combines with the inherent sediment heterogeneity to facilitate a dominant wormholes tendency [*Fredd and Fogler*, 1998]. Wormhole formation would lead to marked CO_2 leakage.

Dissolution - Horizontal effective stress k_0 - Shear and tensile fractures. Complementary analytical, numerical (DEM and FEM), and experimental techniques show the effects of mineral dissolution and ensuing particle-level volume contraction on the evolution of the state of stress under constant overburden at zero-lateral strain boundary conditions during mineral dissolution. In particular, the stress ratio at zero lateral strain $k_0=\sigma'_h/\sigma'_v$ [*Jaky*, 1944; *Mayne and Kulhawy*, 1982] experiences a pronounced decrease during mineral dissolution, and it may reach the Rankine active failure condition k_a on the Coulomb failure plane [*Shin and Santamarina*, 2009]. Strain localization along shear planes may follow [*Shin et al.*, 2008]. Furthermore, mineral dissolution causes sediment compaction, and the cap rock may experience bending and tensile failure.

Coal swelling pressure. Coal swells, its fluid conductivity decreases, and the effective stress increases with the adsorption of CO_2 [*Mazumder et al.*, 2006; *Pekot and Reeves*, 2002; *Somerton et al.*, 1975]. Eventually, CO_2-CH_4 replacement in coal may become self-limiting because of coal swelling and reduced fracture porosity [*Ceglarska-Stefanska and Zarebska*, 2002a].

Summary. The trapping mechanisms of CO_2 in geological formations rely on physical, chemical, and mechanical processes identified above. Each has different time and spatial scales. We summarize potential implications on CO_2 storage in Table 2.3.

Table 2.3. Coupling and emergent phenomena

Coupling	Emergent phenomenon
Multiphase fluid phenomena	- Relative hydraulic conductivities - Differences in mass density and buoyancy - Differences in viscosity and viscous fingering - Fluid segregation - Pressure dependent interfacial tension and contact angle - Percolation and breakthrough pressure
Chemo-Hydro	- Reduction of oil viscosity by CO_2 - Increased porosity and pore size, reactive transport and wormhole formation - Spatial changes in hydraulic conductivity - Gravity-driven self mixing, CO_2 diffusion, pendular water, mineral precipitation. -Coal CO_2 adsorption: reduced fluid conductivity and swelling pressure -Hydrate formation and depressurization: fluid volume expansion, possible gas-driven fractures
Hydro-Mechanical	- Increased fluid pressure and lower σ' - Fault reactivation; hydraulic fracture of the cap rock - Capillarity-driven contraction, - Fluid-driven fracture formation
Chemo-Mechanical	- pH and permittivity effects on DLVO, changes in clay fabric - Pressure solution/precipitation - Mineral dissolution and sediment compaction, - Cap rock bending failure - Decrease in horizontal effective stress $k_{o,}$ shear fractures in contraction
Chemo-Hydro-Mechanical	- Combination of previous phenomena

2.4 Monitoring strategies and risk assessment

CO_2 leakage from storage sites back into the atmosphere decreases the efficiency of CO_2 storage, may pollute drinking water aquifers, and endanger living organisms. Faults and abandoned wells are preferential flow paths that add to the slow transport and diffusion through otherwise continuous strata [*Dooley et al.*, 2006; *Leuning et al.*, 2008]. Monitoring is required to assess the movement of CO_2 and to detect leaks. The design of a monitoring strategy must consider the large areal extent of CO_2 storage reservoirs (on the order of ~km^2) and account for spatial and temporal variability.

Potential monitoring methods, most of them already available for other applications, are summarized in Table 2.4. These monitoring methods take advantage of differences between physical properties (mass density, bulk stiffness, electrical resistivity and dielectric permittivity, and thermal characteristics), the detection of byproducts from chemical reactions, or coupled process effects such as subsidence or micro-seismicity. Tracers such as $\delta^{13}C$ and SF_6 may be included in the injected CO_2 to facilitate detection [*Leuning et al.*, 2008]. The most common subsurface geophysical methods for deep reservoir applications are based on elastic wave propagation and electrical resistivity [*Kiessling et al.*, 2010; *Nakatsuka et al.*, 2010]. The following analysis expresses their applicability to CO_2 geological storage. The bulk modulus B_{mix} of the sediment can be estimated from the Biot-Gassman equation,

$$B_{mix} = B_{sk} + \left(1 - \frac{B_{sk}}{B_g}\right)^2 \left[n \left(\frac{S_w}{B_w} + \frac{S_{CO2}}{B_{CO2}} \right) + \frac{1-n}{B_g} - \frac{B_{sk}}{B_g^2} \right]^{-1} \tag{2.9}$$

where subindices represent the skeleton *sk*, the mineral that makes the grains *g*, the water *w*, and the CO_2. The density of the mixture is $\rho_{mix} = (1-n)\rho_s + n(S_{CO2}\rho_{CO2} + S_w\rho_w)$. Then, the compressional V_P and shear V_S wave velocities are:

$$V_P = \sqrt{\left(\frac{B_{mix} + 4/3 \cdot G_{sk}}{\rho_{mix}} \right)} \tag{2.10}$$

$$V_S = \sqrt{\frac{G_{sk}}{\rho_{mix}}} \tag{2.11}$$

where G_{sk} is the shear modulus of the mineral skeleton.

The electrical conductivity of a geological formation depends on the concentration and mobility of hydrated ions in the pore fluid and the volume fraction of

fluid in the formation [*Santamarina et al.*, 2001a]. The injection of CO_2 displaces the electrolyte (conductivity σ_{fl}) and the formation conductivity can be estimated using the Archie's equation [*Mavko et al.*, 2009]:

$$\sigma_{form} = \sigma_{fl}\left[n(S_{perc} - S_{CO2})\right]^{\beta} \tag{2.12}$$

where $S_{CO2} \leq S_{perc}$, the maximum saturation of CO_2 at percolation. Figure 2.10 shows the variation of P-wave velocity V_P[m/s] and electrical conductivity σ_{form} as a function of the CO_2 saturation S_{CO2}. Because CO_2 is non conductive and has a much lower bulk modulus than water, both σ_{form} and V_P decrease as the relative saturation S_{CO2} increases. While forward predictions show a clear effect of CO_2 on V_p and σ_{form}, the inverse analysis is hindered by measurement errors and error propagation. Hence, the estimation of S_{CO2} from field measurements remains challenging.

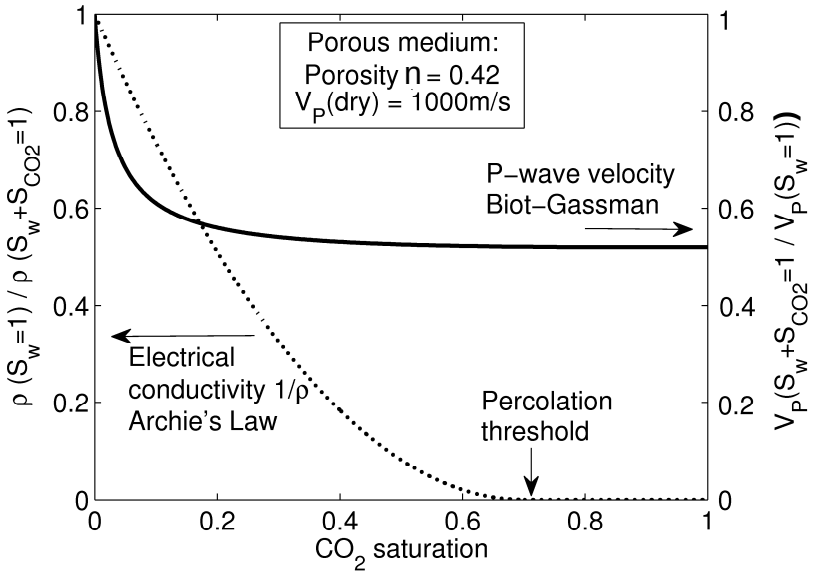

Figure 10. Reduction of P-wave velocity and electrical conductivity $\sigma_{form}=1/\rho_{form}$ with CO_2 saturation for a sediment with porosity n=0.42. Ratio of P-wave velocity computed with V_P(Brine) = 1540 m/s, $V_P(CO_2)$= 268 m/s (at T=40°C and P=10MPa), V_P(dry sediment)=1000m/s, and ν_{sk}=0.1. Electrical conductivity computed with an exponent β=2 for relative saturation and porosity, and a percolation threshold S_{perc}=0.7.

Table 2.4. CO_2 monitoring techniques

Method	Property measured	Principle, comments and issues
1. SUBSURFACE MONITORING		
Porewater geochemistry analysis [(1)]	CO_2, HCO_3^-, CO_3^{2-}, DIC*, major ions, pH, alkalinity, salinity, and isotopes.	CO_2 dissolves in water and changes water geochemistry
Seismic geophysical techniques [(2)]	P-wave velocity and amplitude	The bulk modulus of CO_2 is one order of magnitude lower than that of water
Electromagnetic geophysical techniques [(3)]	Resistivity and electromagnetic waves	High impedance mismatch of electric conductivity and dielectric permittivity between CO_2 and formation water.
Temperature signal [(4)]	Temperature	CO_2 causes non-isothermal events such as expansion induced cooling of CO_2 and thermal heat dissipation from CO_2 dissolution
Infrared monitoring [(5)]	Infrared absorption	CO_2 gas shows characteristic absorption spectrum for infrared waves.
2. NEAR SURFACE MONITORING		
Analysis of near-surface water [(6)]	Isotopic composition, tracers, bulk gas composition, and DIC	CO_2 dissolves in water. A meaningful analysis requires a thorough understanding of the geochemical cycle at the site.
Surface analysis of soil gas [(7)]	Composition of gas fluxes through the soil	CO_2 leaks would eventually percolate through the soil. Point measurements $<1m^2$ are accurate but they lack spatial resolution
Near surface analysis of air composition [(8)]	CO_2 concentration in the near surface by infrared gas analyzer, eddy correlation tower, and light detection and ranging measure	CO_2 from leaks readily mix with other atmospheric gases in the atmosphere. Local changes in turbulence and biological sources and sinks of CO_2 make the identification difficult.
3. ON-SURFACE MONITORING		
Time-lapse 3D reflection seismic imaging [(9)]	P-wave velocity and amplitude	Takes advantage of low bulk modulus of CO_2. It is routinely used the petroleum industry and can identify the plume subsurface movement.
Gravity [(10)]	Mass density	CO_2 is generally lighter than water
Ground displacements [(11)]	Subsidence and heave, vertical displacement	CO_2 injection alters pore pressure and effect on effective stress, and therefore strata compressibility
Surface analysis of carbon content in soil [(12)]	Carbon content by Inelastic Neutron Scattering INS	Increased CO_2 levels asphyxiate aerobic organisms.
Remote sensing of air composition [(7)]	CO_2 atmospheric concentration by hyperspectral remote sensing of vegetative stress and long open path infrared absorption	Applicable at larger scales

(1) [*Emberley et al.*, 2004; *Gunter et al.*, 2000; *Newell et al.*, 2008]; (2) laboratory studies [*Lei and Xue*, 2009; *Shi et al.*, 2007; *Xue et al.*, 2005] and pilot tests [*Bohnhoff et al.*, 2010; *Daley et al.*, 2007; *Daley et al.*, 2008; *Onishi et al.*, 2009]; (3) [*Gasperikova and Hoversten*, 2006; *Nakatsuka et al.*, 2010]; (4) [*Bielinski et al.*, 2008]; (5) [*Charpentier et al.*, 2009]; (6) [*Oldenburg et al.*, 2003]; (7) [*Leuning et al.*, 2008; *Oldenburg et al.*, 2003]; (8) [*Strazisar et al.*, 2009]; (9) [*Arts et al.*, 2004]; (10) [*Alnes et al.*, 2008]; (11) [*Alnes et al.*, 2008; *Kempka et al.*, 2008]; (12) [*Wielopolski and Mitra*, 2010].
Note: *DIC: Dissolved inorganic carbon.

2.5 Conclusions

• The volume of the geological formation that is affected by the injection of CO_2 depends on geometric boundaries, spatial variability, flow conditions and the emergence of viscous fingering.

• The physical properties of CO_2 such as density, viscosity, interfacial tension and bulk compressibility vary with pressure and temperature conditions, and must be properly modeled in numerical simulations of CO_2 geological storage.

• In particular, the CO_2-water interfacial tension decreases with fluid pressure. Lower interfacial tension reduces the capillary entry pressure for CO_2 into a water saturated seal cap rock.

• High CO_2 injection pressures can induce fluid driven fractures and trigger displacements along preexisting faults.

• The solubility of CO_2 in water is high at reservoir pressure conditions. The density of water increases with dissolved CO_2 and convective self-mixing takes place.

• Water acidification in the presence of CO_2 enhances mineral dissolution and alters the sediment fabric when clay minerals prevail. Silicates have a higher buffering capacity than calcite but the reaction rate is much slower.

• The evolution of dissolution and ensuing dissolution patterns depend on the interplay between the rates of advection, diffusion and dissolution. Dissolution may cause settlement, change in effective stress, and the formation of preferential channels for fluid flow, particularly in carbonates.

• The presence of CO_2 decreases the fluid bulk modulus, mass density, and electrical conductivity of the water-CO_2 two-fluid system. These changes support the application

of geophysical methods based on elastic and electromagnetic waves to monitor deep storage reservoirs. While forward predictions are manageable, inverse analysis is hindered by measurement difficulties and error propagation. Hence, the monitoring of CO_2 geological storage remains challenging.

CHAPTER 3

WATER-CO_2-MINERAL SYSTEMS: INTERFACIAL TENSION, CONTACT ANGLE AND DIFFUSION – IMPLICATIONS TO CO_2 GEOLOGICAL STORAGE

3.1 Introduction

Interfacial phenomena upscale through the sediment porous network to define multiphase flow characteristics. Thus, interfacial phenomena control enhanced oil and gas recovery [*Pope and Baviere,* 1991; *Rosen et al.*, 2005], methane production from hydrate bearing sediments [*Seo et al.*, 2002; *Sun et al.*, 2004; *Watanabe et al.*, 2005], and the ability to inject and store CO_2 in geological formations [*Chalbaud et al.*, 2009; *Chiquet et al.,* 2007; *Hildenbrand et al.,* 2004; *Plug and Bruining,* 2007; *Suekane et al.,* 2009]. Temperature and pressure vary considerably in these natural systems: from cold and relatively shallow permafrost and marine sediments (e.g., Alaska north slope: ~7MPa, 278K) to warm coal seams (e.g., Alabama Black Warrior Basin: ~7MPa, 296K), and deep hot rocks onshore (e.g., Weyburn oil field: ~14MPa, 323K). Therefore, CO_2 can form a gas, liquid, or supercritical phase in various applications or environments.

Interfacial tension arises at the molecular level as a result of van der Waals forces [*Butt et al.*, 2006; *Defay and Prigogine*, 1966]. Three interfacial tensions can be identified in a liquid *l*, fluid *f*, and solid substrate *s* system (Fig. 3.1). While fluid-liquid interfacial tension σ_{fl} is directly measurable, fluid-solid σ_{fs} and liquid-solid σ_{ls} interfacial tensions are assessed through indirect methods [*Butt et al.,* 2006]. Foreign substances on the solid surface or within the fluids can modify any of the three interfacial tensions. The

contact angle is influenced by other factors such as surface roughness, contact line fluctuations, vibrations, and viscous effects [see review by *Decker et al.*, 1999].

The interfacial tension σ_{fl} between CO_2 ("fluid" implies either gas or liquid) and liquid water is susceptible to changes in temperature and pressure. At ~298K, the interfacial tension decreases from ~72 to 25mN/m as pressure increases from 0.1MPa to 6.4MPa, and it reaches a constant value ~30mN/m after CO_2 liquefies [studies at 278-to-373K and up to 70MPa can be found in: *Chun and Wilkinson*, 1995; *Dickson et al.*, 2006; *Kvamme et al.*, 2007b; *Massoudi and King*, 1974b; *Sutjiadi-Sia et al.*, 2007]. Water salinity affects the interfacial tension between CO_2 and brine [*Chalbaud et al.*, 2009].

The interfacial tension σ_{fs} between the solid substrate and CO_2 decreases significantly with the increase in CO_2 pressure for different substrates [*Dickson et al.*, 2006; *Sutjiadi-Sia et al.*, 2008]. For an increase in pressure from P=0.1MPa to ~7MPa, the corresponding decrease in σ_{fs} is: 30-to-~0mN/m in glass hydrophobized with dichlorodimethydilane, 24-to-~0mN/m in teflon, and 80-to-17mN/m in glass.

On the other hand, the interfacial tension σ_{ls} between water and the solid substrate remains relatively stable with the increase in fluid pressure; for example, the water-teflon interfacial tension remains at σ_{ls}~25mN/m, for a pressure range between P=0.1MPa and ~7MPa [*Dickson et al.*, 2006]. Ionic species may interact with the solid substrate and alter σ_{ls}.

The Young-Dupre equation, relates the contact angle θ to the mutual interfacial tensions: $\cos\theta=(\sigma_{fs}-\sigma_{ls})/\sigma_{fl}$ (Fig. 3.1). It follows that changes in interfacial tensions σ_{fl}, σ_{fs}, and σ_{ls} with CO_2 pressure alter the contact angle in water-CO_2-substrate systems. For an increase in pressure from P=0.1MPa to ~8MPa, the increase in contact angle is: $\Delta\theta\approx45°$

on glass hydrophobized with dichlorodimethydilane, $\Delta\theta \approx 50°$ on teflon, $\Delta\theta \approx 15°$ on glass, $\Delta\theta \approx 25°$ on muscovite mica, and $\Delta\theta \approx 60°$ on coal [*Chi et al.*, 1988; *Chiquet et al.*, 2007; *Dickson et al.*, 2006; *Siemons et al.*, 2006; *Sutjiadi-Sia et al.*, 2007].

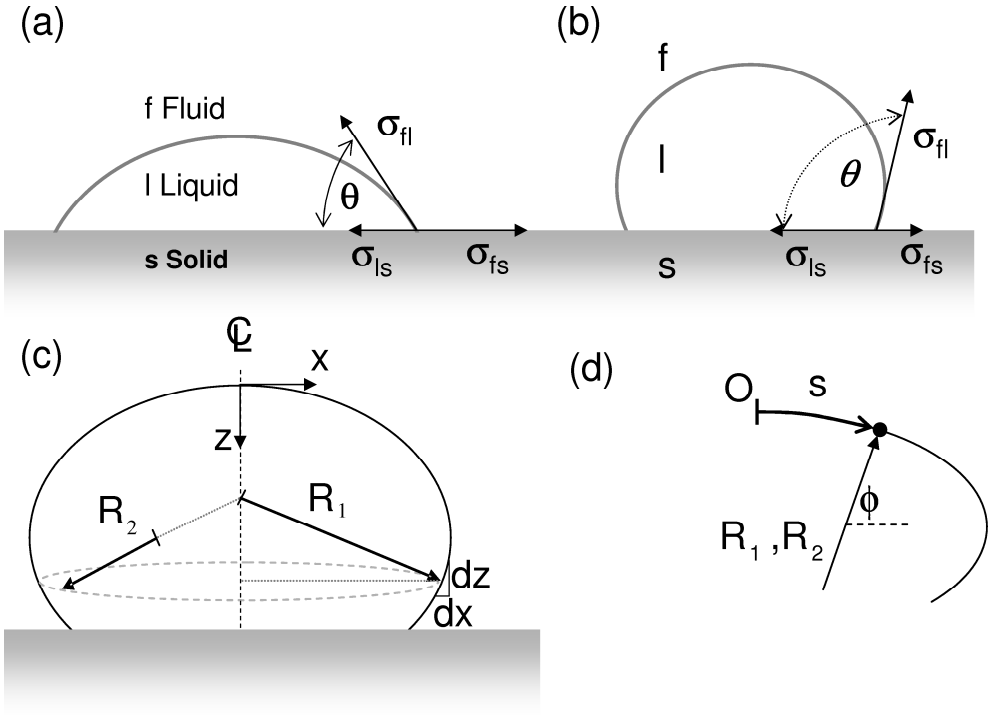

Figure 3.1. Contact angle: basic parameters in wettability. Components: surrounding fluid *f*, liquid droplet *l* and solid substrate *s*. (a) Partially wetting droplet. (b) Non-wetting droplet. Shape parameters in data reduction: (c) cartesian coordinates system (*x*,*z*) and (d) coordinates along arc length (*s*,ϕ).

The purpose of this manuscript is to extend the scope of previous studies summarized above to include other substrates and pore-fluid conditions that may be encountered in natural systems particularly in the context of CO_2 geological storage. We place emphasis on the simultaneous determination of interfacial tension and contact angle. We note that while there is extensive data on the solubility and diffusivity of CO_2 in water, there is very limited information on the diffusivity of water in CO_2; therefore we

include complementary tests to evaluate molecular diffusion. Finally, we use experimental results to assess CO_2 injectability and storage in geological formations.

3.2 Device and materials – Test procedure – Data reduction

Apparatus. We use the sessile droplet method to determine the evolution in interfacial tension σ_{fl} and contact angle. This test configuration allows us to explore the effect of relative density from gas CO_2 to liquid CO_2 conditions. Tests are conducted within a stainless steel high pressure cell, internal volume ~55cm^3, which has a sapphire window to allow for optical measurements (Fig. 3.2-a). The cell is instrumented with a pressure transducer (OMEGA PX303-GV) and a thermocouple (copper-constantan, Conax Buffalo) placed in the vicinity of the droplet. A fiber optic port provides internal illumination. Separate injection ports are available for CO_2 and water. The water droplet sits on the selected substrate at the center of the cell (Fig. 3.2-b).

Materials. Water droplets involve of either deionized water or brine prepared by mixing water with natural halite crystals at room temperature and atmospheric pressure. The tested substrates include: polytetrafluoroethylene PTFE film, calcite crystal, clean glass (amorphous silica) and glass coated with oil [surface pretreated with toluene and n-heptane and coated with oil of medium viscosity from Maracaibo Lake reservoirs - procedure in *Bryar and Knight*, 2003].

Test procedure. The chamber is first subjected to vacuum and gradually flushed with CO_2 (99.99% purity) to remove air. Then, we use using a precision syringe to place a small water droplet (between 10-to-30mm^3) on the horizontally resting substrate; such small droplets minimize gravitational effects and provide insight relevant to the scale of

pendular water at interparticle contacts within sediments. The system is pressurized with CO_2 in stages, from an initial pressure of 0.1MPa to a maximum pressure of 20MPa. Temperature remains within 297±1K at all times. We record the evolution of the droplet geometry using high-resolution time-lapse photography (3μm pixel size). Fig. 3.3 shows a typical sequence of images gathered during pressurization, and during water diffusion into liquid CO_2. These images capture characteristic trends observed in most tests.

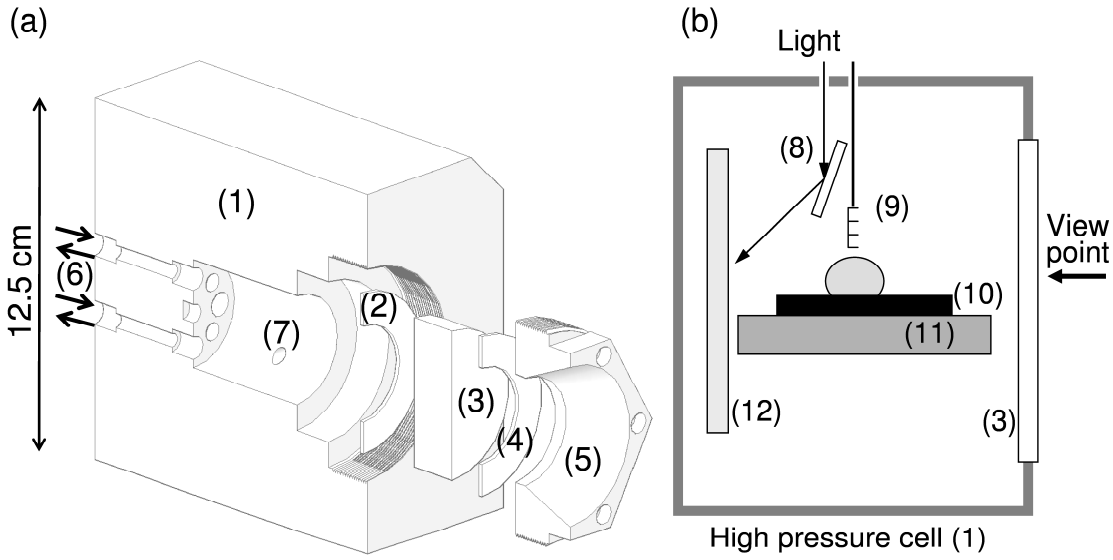

Figure 3.2. High pressure cell: (a) Vertical cross section and (b) chamber detail. Components: (1) Stainless steel body, (2) PTFE gasket, (3) Sapphire window, (4) Copper gasket, (5) Screwable window fastener, (6) Inlet-outlet fluid ports, (7) Ports for transducers and illumination. (8) Mirror (9) Length scale and thermocouple, (10) Substrate, (11) Stainless steel base, and (12) White light diffuser background.

We use images captured at stable temperature and pressure conditions to measure interfacial tension and contact angle, typically 8 min after each pressurization step. Although CO_2 diffuses quickly into the water at the interface, chemical equilibrium is not guaranteed and chemical reactions such as CO_2 speciation and calcite dissolution may

continue during the test. Note that the water droplet consistently advances or recedes during pressurization.

Data reduction – Interfacial tension and contact angle. Images are scaled and digitally processed to find the interface boundary using the Canny edge detection algorithm [*Canny*, 1986]. The CO_2-water interfacial tension σ_{fl}, curvature radii R_1 and R_2, and the pressure jump ΔP at any point on the interface are related by Laplace's equation [*Blokhuis*, 2004; *Rotenberg et al.*, 1983]:

$$\sigma_{fl}\left(\frac{1}{R_1}+\frac{1}{R_2}\right)=\Delta P \tag{3.1}$$

Gravity g and the difference in density $\Delta\rho$ between water or brine and CO_2 cause a pressure gradient $\Delta\rho gz$ along the droplet height. Let's consider cartesian coordinates (x,z) measured from the droplet apex (see Fig. 3.1-c), and a parametrized representation of the interface based on the curve length s (Fig. 3.1-d); then:

$$\frac{dx}{ds}=\cos\phi \quad \text{and} \quad \frac{dz}{ds}=\sin\phi \tag{3.2}$$

Since curvature radii are $1/R_1=d\phi/ds$ and $R_2=x/\sin(\phi)$, Equation 3.1 can be re-written as:

$$\sigma_{fl}\left(\frac{d\phi}{ds}+\frac{\sin\phi}{x}\right)=\frac{2\sigma_{fl}}{R_0}+\Delta\rho\, gz \tag{3.3}$$

where R_0 is the curvature at the droplet apex. The recorded droplet profile permits recovering local values of ϕ, s, z everywhere, and measuring R_0 at the apex. The difference in mass densities $\Delta\rho$ is computed from equations of state. For water density we use expressions in Perry and Green [1997] and McCutcheon et. al. [1993]; we do not correct for minor changes in water density associated with CO_2 dissolution. For CO_2, we

consider it as a pure phase and compute its density using expression in Duan and Sun [2003a].

The only remaining unknown in Equation 3.3 is the interfacial tension σ_{fl}. We choose to simultaneously fit a large number of points (x,z) to increase accuracy. We digitize the complete droplet profile (1000-to-6000 points) and fit the points with the lowest degree polynomial that properly justifies the data; typically a degree 3 to 5 suffices. Contact angle θ (tangent when coordinates correspond to the substrate position), droplet volume and surface area are calculated from the fitted polynomial assuming axisymmetry. Interfacial tension is obtained by minimizing the L^2 norm $E = \Sigma\varepsilon_i^2$ of individual errors in pressure ε_i at each point along the droplet profile, where ε_i is the difference between the pressure predicted with local curvatures $\sigma_{fl}(1/R_1+1/R_2)$ and the pressure as a function of depth z form the apex ($2\sigma_{fl}/R_0 + \Delta\rho gz$). All calculations are repeated for both left and right halves of the droplet. This data-intensive measurement method gives consistent results and the estimated error is $\Delta\sigma$ =±2.5mN/m for interfacial tension and $\Delta\theta$=±0.6° for contact angle.

Data reduction - Diffusion: Water diffuses into the surrounding CO_2 until the two phases equilibrate. The instantaneous droplet volume and surface area allow us to evaluate the rate of water diffusion into the surrounding CO_2 medium. The diffusion coefficient D is inverted from successive forward simulations of the diffusion equation in terms of the concentration c of water in liquid CO_2; in radial coordinates r and time t:

$$\frac{\partial c}{\partial t} = D\left(\frac{2}{r}\frac{\partial c}{\partial r} + \frac{\partial^2 c}{\partial r^2}\right) \tag{3.4}$$

We estimate the droplet volume and initial droplet equivalent radius R from the droplet shape. The injected liquid CO_2 is water free, therefore $c(r>R,t=0)=0$. Even though the water droplet decreases in size, we assume that water dissolved in the space previously occupied by the contracting droplet is negligible, and consequently the concentration c of water in liquid CO_2 at a distance equal to the droplet original radius is constant and equal to the solubility limit at that particular pressure and temperature $c(r=R,t)=C_0$. Because the water droplet is placed within a closed system size r_b, there is no flux through the boundaries and the spatial derivative is $\partial c/\partial r|_{r=rb}=0$ at the chamber walls. The reaction $H_2O + CO_2 \rightarrow H_2CO_3$ and further speciation are assumed to be much faster than the diffusion time.

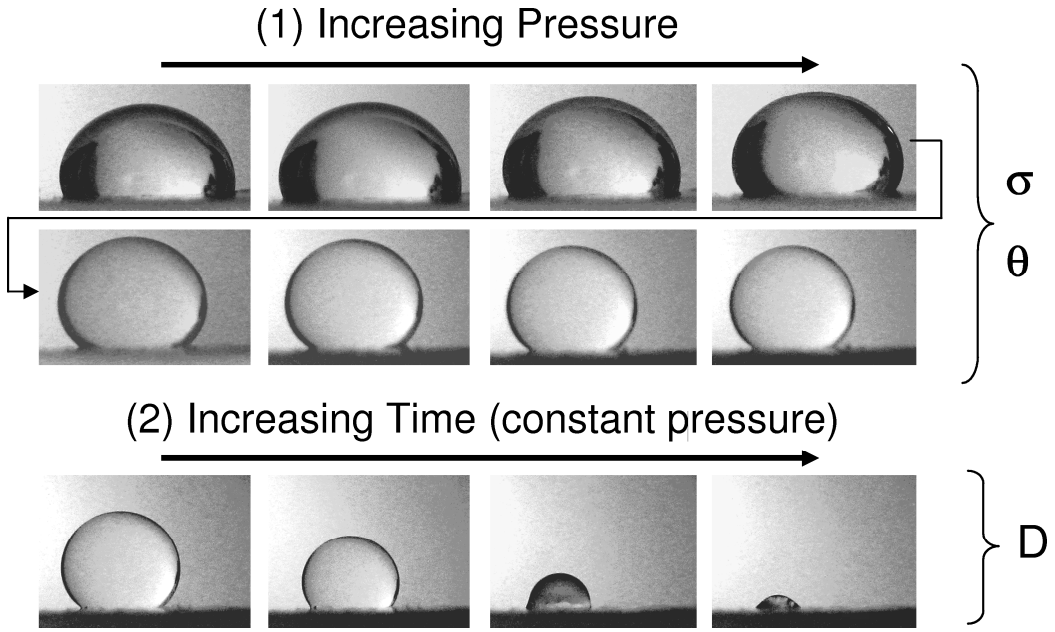

Figure 3.3. A water droplet on PTFE substrate surrounded by CO_2. (1) Changes in interfacial tension σ and contact angle θ as CO_2 pressure increases from 0.1 to 18.5 MPa. (2) size reduction as water diffuses into the surrounding liquid CO_2 (Duration ~400 min).

3.3 Results and analyses

Table 3.1 shows tests conditions explored in this study. Experiments are designed to achieve high measurement precision and to improve invertibility of unknown parameters. In particular, interfacial tension cannot be properly resolved when the contact angle is θ<80° and the droplet is flat, so emphasis is placed on non-wetting substrates when interfacial tension data are sought. The liquid CO_2 is pre-saturated with water to prevent water diffusion and to improve interfacial tension measurements in long duration tests. Experimental results and related analyses are presented next for the three parameters studied in this research: interfacial tension, contact angle and water diffusion in liquid CO_2.

Table 3.1. Scope of the experimental study. Numbers in the table indicate the number of independent tests conducted for each condition.

Gas	Droplet liquid	Substrate	σ_{gs}	θ	D
CO_2	H_2O	$CaCO_3$	NA	3	–
		PTFE	3	3	1
		Amorphous SiO_2	NA	1	–
		Oil-wet SiO_2	3	3	2
	Brine	$CaCO_3$	NA	1	–
		PTFE	2	2	1
		Amorphous SiO_2	NA	1	–

3.3.1 Interfacial tension

Fig. 3.4 shows the measured interfacial tension σ_{fl} between CO_2 and water as a function of pressure; data compiled from the literature are shown as well. Interfacial tension decreases as CO_2 pressure increases and it remains constant once the CO_2 vapor-liquid boundary is reached (~6.43MPa at 298K). Three sets of experiments are identified:

- Deionized water droplets (filled circles in Fig. 3.4): our results are in agreement with previous studies [*Chun and Wilkinson*, 1995; *Kvamme et al.*, 2007b; *Massoudi and King*, 1974b; *Sutjiadi-Sia et al.*, 2007]. The interfacial tension between CO_2 and water σ_{fl} starts at ~72mN/m at 0.1MPa and 295K and decreases linearly at a rate of ~7mN·m per MPa increase in CO_2 pressure until the liquid-vapor boundary is reached. Thereafter, the interfacial tension remains nearly constant at σ_{fl} ≈20-to-30mN/m [Note: *Kvamme et al.*, 2007b observed a smooth transition in the supercritical regime].
- Brine droplets (open diamonds in Fig. 3.4): The interfacial tension σ_{fl} between CO_2 and brine is higher than between CO_2 and deionized water, and it exhibits lower sensitivity to pressure. (Note: higher pressure sensitivity has been observed in the supercritical regime at significantly higher temperatures [*Chalbaud et al.*, 2009]).
- Water droplets with organic compounds that dissolved from the substrate (crosses in Fig. 3.4): The CO_2-water interfacial tension σ_{fl} is lower than for deionized water without organic contaminants, but rates of decrease with pressure are the same [in agreement with data in *Chun and Wilkinson*, 1995].
- Overall, values of CO_2-water interfacial tension can vary by ±10mN/m

depending on the dissolved compounds in water.

These results are the consequence of molecular interaction taking place within the liquid and between water and the surrounding CO_2.

Interactions within the liquid. Foreign species modify the local electrical field within the liquid. Variations in interfacial tension σ[mN/m] with solute concentration c[mol/L] are anticipated in terms of surface excess of solute Γ[mol·m^{-2}] [*Butt et al.*, 2006; *Pegram and Record*, 2007; *Tuckermann*, 2007],

$$\left.\frac{\partial\sigma}{\partial(\gamma c)}\right|_T = -\frac{RT}{\gamma c}\Gamma \qquad (3.5)$$

where γ [dimensionless] is the solute activity coefficient and T[K] is temperature. In agreement with this theory, ions are depleted at the interface $\Gamma<0$ in inorganic solutions, but there is enrichment of organic species $\Gamma>0$ at the interface when organic compounds are present. In the case of CO_2, there is high concentration of dissolved CO_2 near the interface, $\Gamma>0$, causing the observed drop in interfacial tension [*Chun and Wilkinson*, 1995; *Massoudi and King*, 1974a; *Sutjiadi-Sia et al.*, 2008]. Gibbs' isotherms $\Gamma=f(\gamma c)$ give insight into molecular mechanisms responsible for adsorption at the interface and differences among gases [*Massoudi and King*, 1974b]. Molecular dynamics simulations show the preferential alignment of water molecules near interface ions [*Bhatt et al.*, 2004] and of water and CO_2 molecules at the interface [*da Rocha et al.*, 2001; *Kuznetsova and Kvamme*, 2002; *Kvamme et al.*, 2007b].

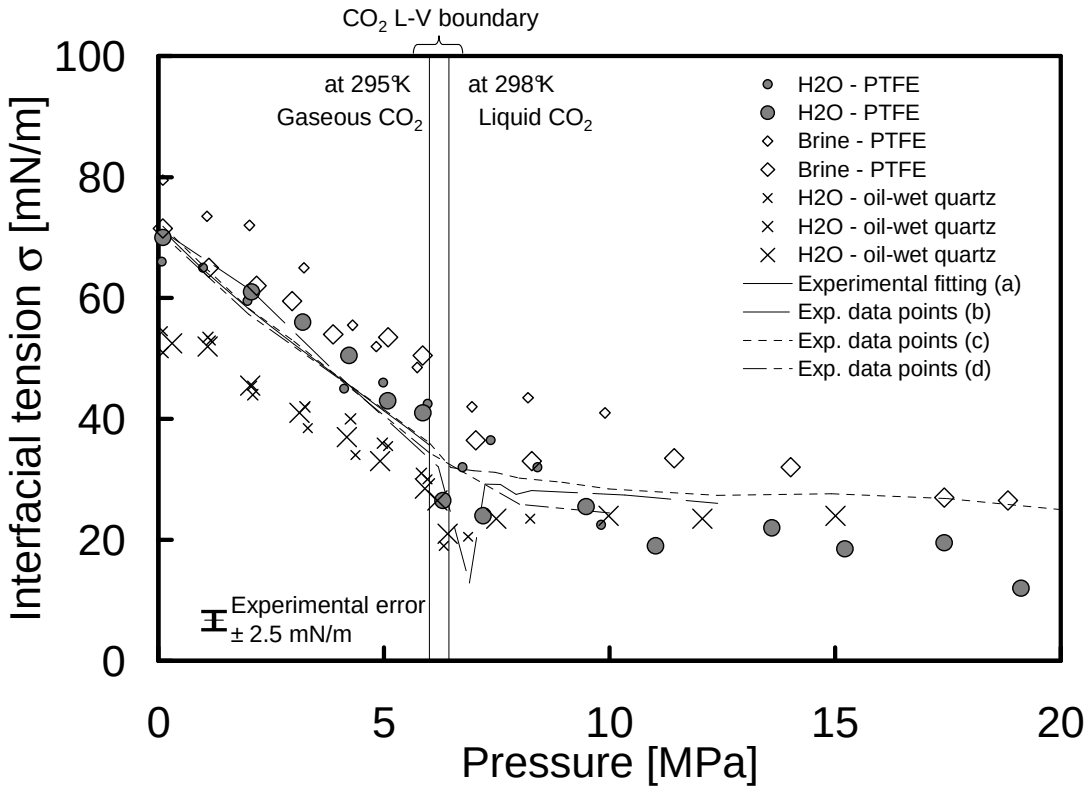

Figure 3.4. Interfacial tension between water and CO_2. Lines indicate values reported in the literature for deionized water at ~298K [b- *Chun and Wilkinson*, 1995; c- *Kvamme et al.*, 2007b; a- *Massoudi and King*, 1974a; d- *Sutjiadi-Sia et al.*, 2007]. Note: the salt concentration in brine is ~200g(NaCl)/kg(water).

Interaction with the surrounding fluid. The proximity to and the number of near-neighbor charges in the surrounding fluid depends on the difference between fluid densities. Hence, higher interaction and lower interfacial tension are expected with increasing CO_2 pressure and density as suggested by the Sugden-Macleod equation $\sigma = f(\Delta\rho)$ [*Chalbaud et al.*, 2009; *Chun and Wilkinson*, 1995]. Consequently, the interaction with the external fluid and the value of σ_{fl} remain relatively constant once the pressure exceeds the vapor-liquid boundary.

3.3.2 Contact angle

Fig. 3.5 shows the evolution of contact angle θ with pressure for all substrates. It can be observed that:

- The contact angle on non-wetting PTFE substrates increases from $\theta \approx$100-to-140º as pressure increases and remains almost constant after the pressure exceeds the liquid-vapor interface.
- The contact angle on oil-wet-silica increases slightly from $\theta \approx$85-to-90º when CO_2 pressure increases from 0.1MPa to the pressure at the liquid-vapor boundary ~6.43MPa at 298K; thus this substrate can turn from slightly hydrophilic to hydrophobic upon pressurization. At any given pressure, contact angles are similar for brine and deionized water.
- Contact angles on amorphous silica SiO_2 and calcite $CaCO_3$ substrates remain nearly constant with pressure. Dissolved NaCl in water increases the contact angle by ~20º for brine on SiO_2 and ~4° for brine on $CaCO_3$.
- Published results for glass, PTFE and coal substrates are similar to those obtained in this study [*Chi et al.*, 1988; *Dickson et al.*, 2006; *Sutjiadi-Sia et al.*, 2007].

Our results also show that contact angles between (1) liquid-CO_2 and water, and (2) liquid-CO_2 and all tested solid substrates ($CaCO_3$, oil-wet SiO_2 and PTFE) approach $\theta \approx 0$ in a vapor-CO_2 atmosphere.

Let's consider the Young-Dupre's equation in differential form to identify the influence that changes in each component exert on $\cos\theta$ upon small changes in gas pressure,

$$\frac{d(\cos\theta)}{dp} = -\frac{\sigma_{fs} - \sigma_{ls}}{\sigma_{fl}^{\,2}}\frac{\partial \sigma_{fl}}{\partial p} + \frac{1}{\sigma_{fl}}\frac{\partial \sigma_{fs}}{\partial p} - \frac{1}{\sigma_{fl}}\frac{\partial \sigma_{ls}}{\partial p} \tag{3.6}$$

This expression explains changes in contact angle reported in Fig. 3.5:

- On hydrophobic substrates (PTFE and oil-wet amorphous silica): a reduction in σ_{fl}=$\sigma_{CO2\text{-}H2O}$ combines with a decrease in σ_{fs}=$\sigma_{CO2\text{-}substrate}$ (reported in the literature) to cause an increase in contact angle with pressure.
- On hydrophilic amorphous silica and calcite: the addition of NaCl increases σ_{fl}=$\sigma_{CO2\text{-}H2O}$ and results in a higher contact angle. On the other hand, the decrease in σ_{fl}=$\sigma_{CO2\text{-}H2O}$ is partially compensated by a decrease in σ_{fs}=$\sigma_{CO2\text{-}substrate}$ (not observed explicitly), and the contact angle remains relatively unchanged.

The observed contact angle $\theta \approx 0°$ for liquid CO_2-substrate in vapor CO_2 atmosphere is in agreement with the reported $\sigma_{CO2(vapor)\text{-}CO2(liquid)} \approx 0$.

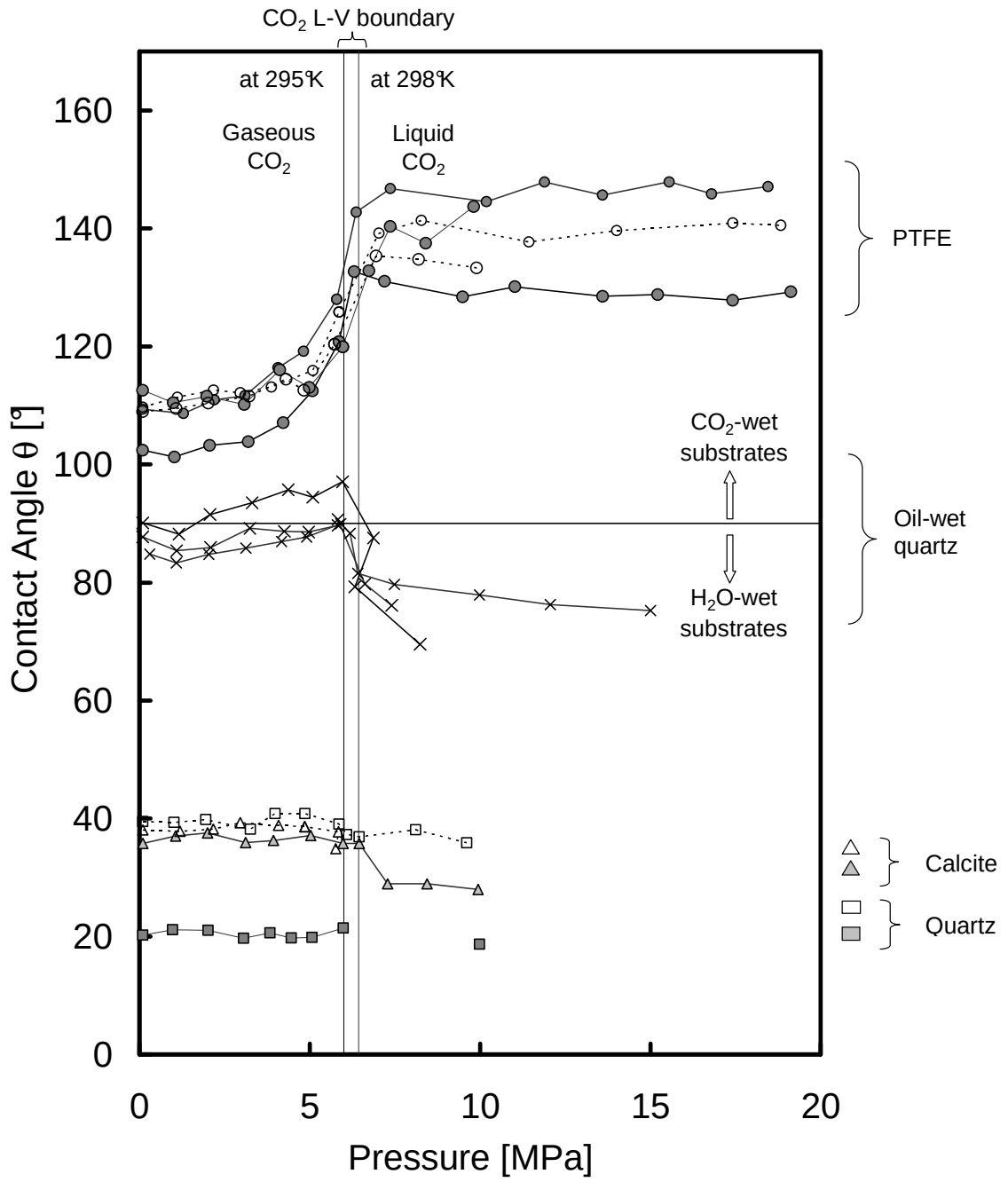

Figure 3.5. Contact angle evolution with pressure for a water droplet surrounded by CO_2 and resting on hydrophobic substrates (oil-wet amorphous silica and PTFE) and hydrophilic substrates (amorphous silica and calcite). Continuous line: deionized water; dashed lines: brine ~200g(NaCl)/kg(water).

3.3.3 Water diffusion in liquid CO_2

The decrease in droplet volume with time observed in Fig. 3.3 was measured for several conditions. We inverted for the diffusion coefficient D of water in liquid CO_2 using the procedure outlined earlier; results are summarized in Fig. 3.6. The water solubility in liquid CO_2 was assumed to vary from 1.05kg/m^3 at 10MPa to 2.1kg/m^3 at 25MPa [measurements at 298-to-303K - *Chrastil*, 1982; *Jackson et al.*, 1995; *Sabirzyanov et al.*, 2002; *Spycher et al.*, 2003; *Wiebe*, 1941]. Our measured values and previously reported data are plotted in Fig. 3.7:

- Previously published, NMR experiments D=1.5-to-2×10^{-8}m^2/s at 298K from 13-to-20MPa [*Xu et al.*, 2003], and molecular simulations D=16-to-2×10^{-8}m^2/s at 308.9K from 6.3-to-17.1MPa [*Danten et al.*, 2005].
- In our measurements, uncertainty in the solubility of water in CO_2 is responsible for an estimation error of $\varepsilon \approx \pm 4 \cdot 10^{-8}$m^2/s.
- Values range from D=1.2-to-1.8×10^{-7}m^2/s for water, to D=1.0×10^{-7}m^2/s for brine. The lower diffusion coefficient for brine reflects the attraction of water to ions in the aqueous solution. In fact, we observe salt precipitation as water molecules leave the droplet and migrate into the bulk liquid CO_2.
- The measured diffusion of water in liquid CO_2 is much faster than the diffusion of CO_2 in water D=2-to-5×10^{-9}m^2/s [*Thomas and Adams*, 1965b], ions in water D~10^{-9}m^2/s [*Sharma and Reddy*, 2001], and organic compounds in supercritical CO_2 D=2-to-1×10^{-8} m^2/s [Experiments at 313K - *Funazukuri et al.*, 1992; *Liong et al.*, 1992; *Sassiat et al.*, 1987].

- A decrease in D with pressure is apparent.

We corroborated our droplet-based results by means of a 1D configuration using a capillary tube to create a steady state diffusion condition (data also shown in Fig. 3.7). Values inverted from droplet tests are approximately twice higher from the 1D steady state experiment $D=6.0\times10^{-8}$ m^2/s (probably due to convective currents). Nevertheless, all our experiments confirm the very high diffusivity of water in liquid CO_2.

The high diffusivity of water in liquid CO_2 is attributed to the small size of water molecules in terms of equivalent molecular radius, and the low viscosity of liquid CO_2. Note: μ increases with pressure and decreases with temperature; values range from 2×10^{-5} Pa·s at 5MPa and 318K to 10^{-4} Pa·s at 30MPa and 298K [*Fenghour et al.*, 1998].

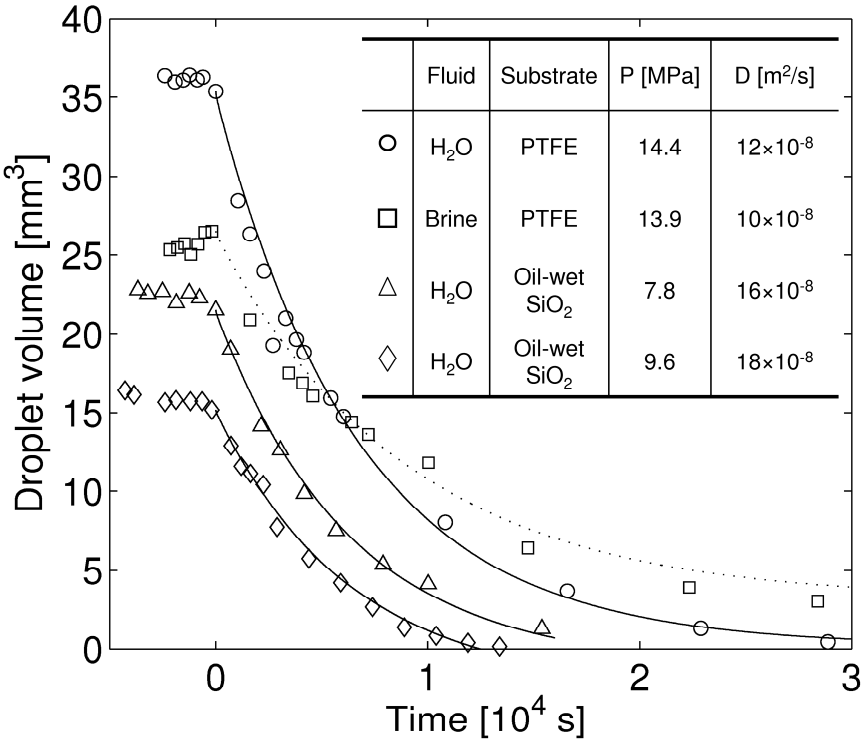

Figure 3.6. Water diffusion in liquid CO_2. Change in droplet volume with time. Lines represent the best fit using the diffusion model (Equation 3.5).

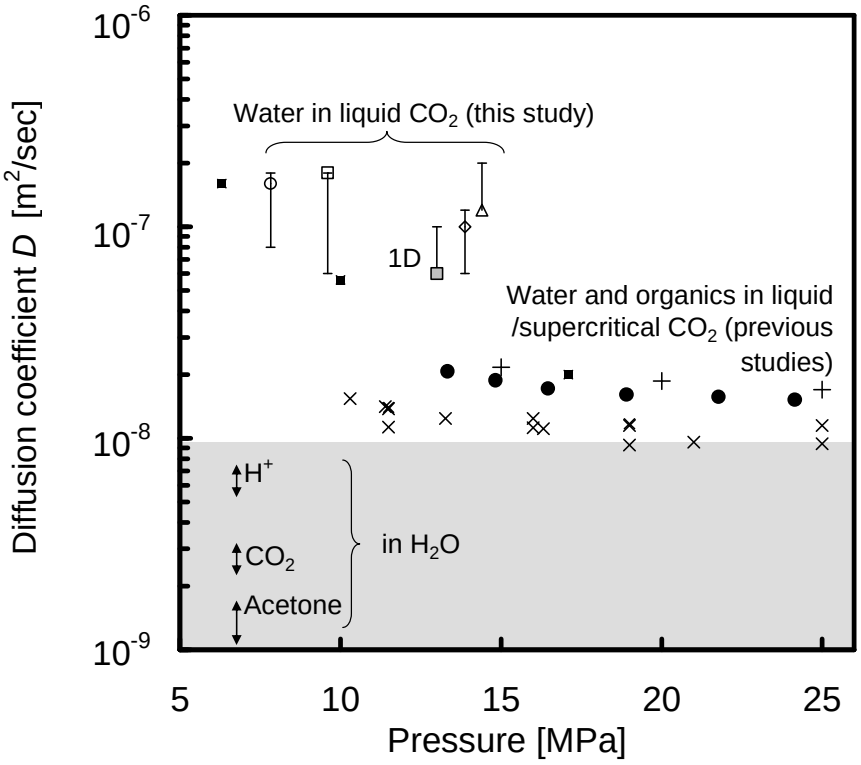

Figure 3.7. Water diffusion in liquid CO_2 at 297±1K (the shaded square represents the value measured in a 1D tube). Literature data for diffusion coefficients of 1) water in liquid and supercritical CO_2 "■"[298K, *Xu et al.*, 2003] and "●"[308.9 and 313.9K, *Danten et al.*, 2005], 2) CO_2 in supercritical CO_2 "+"[313.16K, *Suarez-Iglesias et al.*, 2008], and 3) organic compounds in supercritical CO_2 "×" include benzene and naphthalene [313K, *Funazukuri et al.*, 1992]; benzene, naphthalene and acetone [313K, *Sassiat et al.*, 1987] and ester C4:0 [313K, *Liong et al.*, 1992]. The water diffusion coefficients for species dissolved in water are relatively insensitive to pressure – shown as a shaded area [~298K, *Krynicki et al.*, 1978].

3.3.4 CO_2-H_2O-substrate chemical reactions

We witness mineral corrosion during these tests. Furthermore, we also observed the re-precipitation of calcite in the form of typical trigonal-rhombic crystals on the mineral surface after water evaporation or water diffusion out of the droplet. SEM images are shown in Fig. 3.8. Similar micron-size precipitated crystals are reported for calcite precipitation from calcium slurry [*Montes-Hernandez et al.*, 2007]. Note: bicarbonate

may precipitate as aragonite if temperature exceeds T>303K [*Cowan and Weintritt*, 1976].

The presence of CO_2 changes the chemistry of the water droplet. Carbon dioxide dissolves in water with a solubility that depends on pressure and temperature ('aq' stands for aqueous form),

$$CO_2(\text{g-or-l}) \leftrightarrow CO_2(\text{aq})$$

$$H_2O(\text{l}) + CO_2(\text{aq}) \leftrightarrow H_2CO_3(\text{aq}) \quad \text{carbonic acid}$$

Carbonic acid ionizes stepwise to produce bicarbonate and carbonate ions,

$$H_2CO_3(\text{aq}) \leftrightarrow H^+(\text{aq}) + HCO_3^-(\text{aq})$$

$$HCO_3^-(\text{aq}) \leftrightarrow H^+(\text{aq}) + CO_3^{2-}(\text{aq})$$

Table 3.2 shows the concentration of these species at different pressures obtained from thermodynamic equations. The increase in CO_2 pressure results in both higher solubility of CO_2 and higher concentration of aqueous species. Reactions occur in the order of seconds for carbon hydration $d[CO_2]/dt \sim 0.03s^{-1}[CO_2]$ (brackets mean concentration in mol/L) and it is even faster for stepwise ionization [*Stumm and Morgan*, 1996]. Therefore, the availability of species within the droplet is diffusion-limited in real systems size L where the characteristic diffusion time is of the order of L^2/D.

Calcite $CaCO_3$ experiences relatively fast reactions with water acidified by CO_2:

$$CaCO_3(\text{s}) + H_2O + CO_2(\text{g}) \leftrightarrow Ca^{2+} + 2 \cdot HCO_3^-$$

Dissolution rates are proportional to the pH difference with respect to the equilibrium condition and aqueous species are produced proportionally to the CO_2(g-or-l) pressure increase [*Drever*, 1997]. Conversely, a reduction in CO_2(g) pressure produces nucleation of CO_2 in gaseous form and the precipitation of calcite. $CaCO_3$(s) buffering and

dissolution causes a ~2 orders of magnitude increase in HCO_3^-, as compared with the non-reactive case. Both, chemical analyses of $CaCO_3$ dissolution and the estimated volume of precipitates in SEM images (thickness assumed ~0.3μm) provide similar mass estimates.

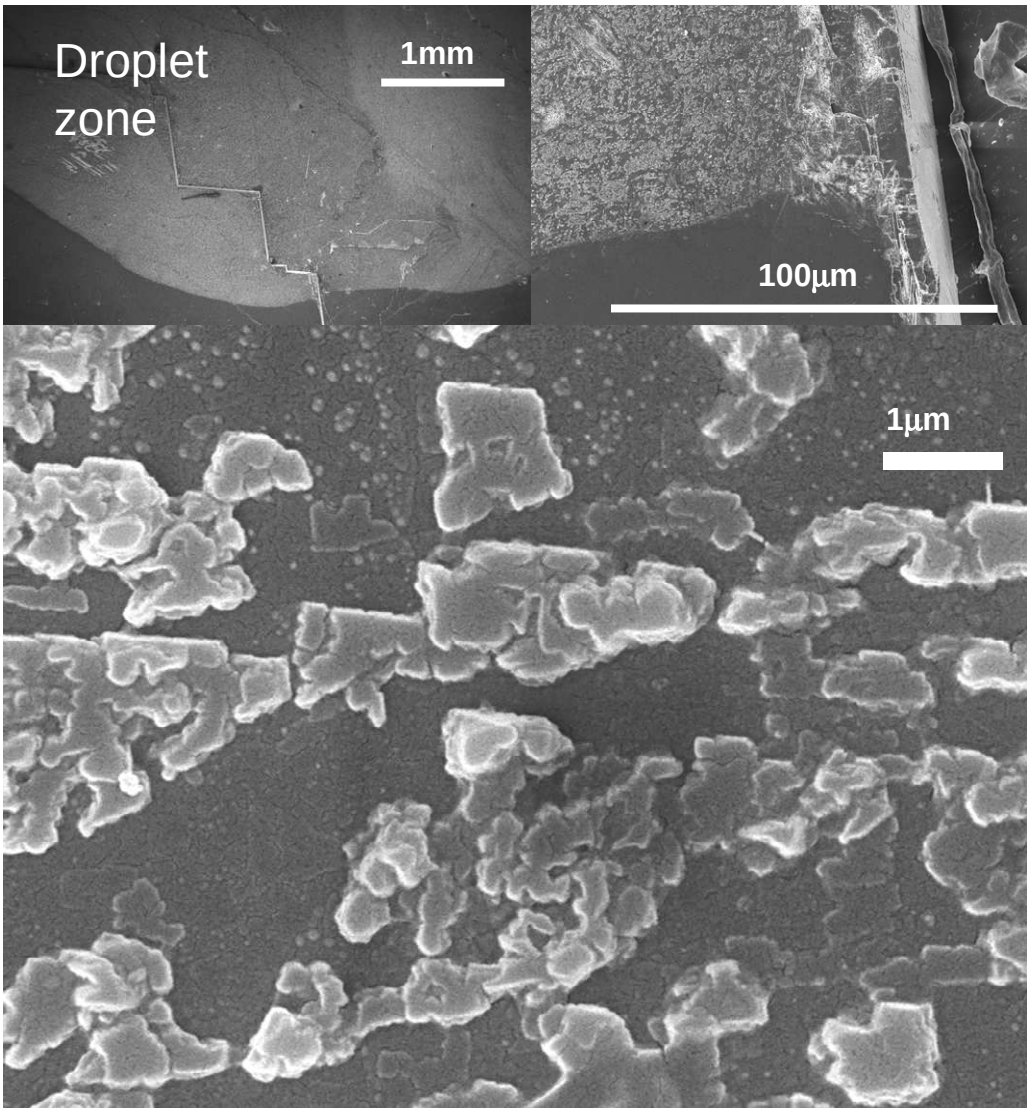

Figure 3.8. Precipitated calcite observed underneath the initial location of the water droplet after evaporation. Dissolution was caused by CO_2 acidification of water in the droplet.

Table 3.2. Carbon dioxide solubility and aqueous species concentration at equilibrium under CO_2 pressure with and without $CaCO_3$. Temperature=298K. CO_3^{-2} concentration is negligible. The SUPCRT92 thermodynamic database is used for high pressure calculations [*Johnson et al.*, 1992]. CO_2 solubility obtained from Duan and Sun [2003a].

CO_2 pressure [Mpa]	**Solubility of CO_2 in water at 298.15K** [mol/L]	**Equilibrium pH**	**Concentration** [mol/L]		
			$H_2CO_3^0$	**HCO_3^-**	**Ca^{2+}**
In the absence of $CaCO_3$					
$10^{-4.5}$	$\sim 10^{-5}$	5.65	10^{-5}	$10^{-5.5}$	
0.1	0.0325	3.92	0.027	1.21×10^{-4}	
6.4	1.376	3.09	1.14	8.14×10^{-4}	
10	1.421	3.07	1.18	8.14×10^{-4}	
20	1.559	3.05	1.29	8.83×10^{-4}	
In the presence of $CaCO_3$					
6.4	1.376*	4.85	1.14	0.047	0.023
10	1.421*	4.83	1.18	0.048	0.024
20	1.559*	4.79	1.29	0.054	0.027

(*) Assumption: CO_2 solubility in water is not significantly affected by Ca^{2+}.

3.4 Discussion: implications to CO_2 geological storage

Interfacial tension and contact angle define interparticle capillary forces, the capillary strengthening of the granular skeleton, and irreducible saturation or capillary trapping. In turn, pore-scale and grain-scale effects determine the thermo-hydro-chemo-mechanical coupled response of the geological formation. Injectability and seal performance are considered next in view of experimental results obtained in this study.

3.4.1 CO_2 injectability

The displacement of the saturating brine by liquid CO_2 depends on their viscosities μ_{CO2} and μ_{brine}, the pore flow velocity v, and capillary resistance at pore throats. Let's consider a pore as a cylindrical tube length L going from node i to node j. The equilibrium condition when liquid CO_2 displaces brine along the tube is given by:

$$p_i = p_j + 4\frac{\sigma\cos\theta}{d} + v\frac{32L}{d^2}\left(\frac{l_{CO2}\mu_{CO2} + l_{brine}\mu_{brine}}{L}\right) \qquad (3.7)$$

where the second term is Laplace's equation and the third term is Poiseuille's equation. Therefore, wettability (e.g., $\sigma\cos\theta>0$ if the host fluid is the wetting one) and viscous drag determine imbibition and the occupancy of pores by either the wetting or the non-wetting fluid. The balance between participating forces can be captured in two dimensionless ratios: between viscous components M, and between viscous and capillary forces C,

$$M = \frac{\mu_{CO_2}}{\mu_{brine}} \quad \text{and} \quad C = \frac{v\mu_{CO_2}}{\sigma\cos\theta} \qquad (3.8)$$

Values of viscosity $\mu_{brine}=(1\pm0.5)\times10^{-3}$ Pa·s at 323K and $\mu_{CO2}=$(2-to-8)$\times10^{-5}$ Pa·s at 318K and, from 5-to-30MPa [*Fenghour et al.*, 1998; *Netherton et al.*, 1977] readily show that that the viscosity number is low for liquid CO_2-brine systems $M=\mu_{CO2}/\mu_{brine}\sim10^{-2}$.

On the other hand, the *C* ratio varies with distance to injection wells and pressure-dependant σ and θ values.

Different invasion patterns develop as a function of *M* and *C* [*Lenormand et al.*, 1988; *Pennell et al.*, 1996]. We can anticipate the following situations developing during liquid CO_2 injection into the reservoir:

- *Near the injection well - high flow velocity* (high *C* - low *M*): Viscosity controls the invasion of CO_2 into the formation. Given the low viscosity number *M* for liquid CO_2-brine systems, liquid CO_2 will preferentially displace brine from the largest pores, but it will be prone to instability and viscous fingering may emerge [*Lenormand et al.*, 1988].
- *Far from the injection well: low flow velocity* ($v \rightarrow 0$, low *C*. Note: this condition applies as well at the interface against the seal layer during long-term quasi-static storage): capillary forces control CO_2 invasion into the porous medium. Brine is the wetting phase and remains in the smaller pores. Capillary fingering may develop.

Both viscous and capillary fingering patterns result in large irreducible saturation of the host fluid (brine). Oil-CO_2 phases behave differently to brine-CO_2 since part of the oil is miscible with CO_2 [*Blunt et al.*, 1993].

3.4.2 Sealing capacity of geological formations

The long-term storage of CO_2 is a quasi-static condition (v=0, C=0) controlled by capillary forces at pore throats. The following analysis is conducted to identify the governing parameters and their interrelation.

1. *Pore size distribution - Mean value*: Let's assume a log-normal distribution for pore-size normalized by 1nm x=log(d/nm) with mean μ_x=mean[log(d/nm)], standard deviation σ_x^2=variance[log(d/nm)] and probability density function:

$$P(x) = \frac{1}{\sigma_x \sqrt{2\pi}} \exp\left(-\frac{(x-\mu_x)^2}{2\sigma_x^2} \right) \tag{3.9}$$

The mean μ_x can be extracted from mercury intrusion porosimetry [*Juang and Holtz*, 1986] or estimated theoretically as a function of the void ratio e, the specific surface S_s and the mineral density ρ. For conglomerates made of edge-to-face and face-to-face aggregations of clay particles (geometric factor k between 6 and 12):

$$\mu_x = \log\left(\frac{k\, e}{S_s \rho} \frac{1}{\text{nm}} \right) \tag{3.10}$$

2. *Void ratio and compressibility*: The void ratio depends on the effective stress p' in agreement with Terzaghi's consolidation theory [*Burland*, 1990a; *Terzaghi et al.*, 1996],

$$e = e_{1\text{kPa}} - C_c \log \frac{p'}{1\text{kPa}} \tag{3.11}$$

where the void ratio $e_{1\text{kPa}}$ at p'=1kPa and the compressibility coefficient of the sediment C_c increase with increasing specific surface.

3. *Breakthrough pressure*: For a given pore structure, there is breakthrough pressure p^*_c determined by the pressure-dependent interfacial tension σ and contact angle θ:

$$p_c^* = \frac{4\sigma \cos\theta}{d^*} \tag{3.12}$$

where the critical pore size d^* is herein defined as the minimum pore size along a percolating path across the seal layer.

4. *Critical pore size*: The analysis of gas breakthrough experimental data in [*Hildenbrand et al.*, 2002; *Hildenbrand et al.*, 2004; *Horseman et al.*, 1999] indicates that $d^*/\text{nm} > 10^{\mu x}$, hence, the percolating path is made of pores all larger than the mean. The value of d^* can be related to the mean μ_x by a factor α of the standard deviation σ_x,

$$\log\left(\frac{d^*}{\text{nm}}\right) = \mu_x + \alpha\sigma_x \tag{3.13}$$

Data in [*Horseman et al.*, 1999] are analyzed using this formulation to estimate $\alpha\sigma_x$. We compute d^* from breakthrough [Equation 12, water-helium interfacial properties from *Hough et al.*, 1952] and μ_x from porosity [Equation 10, mineral density and specific surface from *Rosborg and Pan*, 2008]. We obtain $\alpha\sigma_x = \log(d^*/\text{nm}) - \mu_x$. Results shown in Fig. 3.9 indicate that $\alpha\sigma_x$ is relatively independent of effective stress, and it ranges between $\alpha\sigma_x = 0.7 \pm 0.15$ for this sediment (assumed geometric factor k=12). Therefore, $d^*/\text{nm} = 10^{\mu_x + (0.7 \pm 0.15)}$.

Finally, we can express the breakthrough pressure for an immiscible fluid as a function of effective stress p', sediment compressibility ($e_{1\text{kPa}}$, C_c), pore structure (S_s, $\alpha\sigma_x$) and pressure-dependent interfacial tension σ and contact angle θ:

$$p_c^* = \psi \frac{S_s \rho \sigma \cos\theta}{e_{1\text{kPa}} - C_c \log\dfrac{p'}{1\text{kPa}}} \quad (\text{where } 0.04 \le \psi \le 0.08) \tag{3.14}$$

where the factor $\psi = 4/(k10^{\alpha\sigma x})$ groups theoretical and experimental constants, and provides an order of magnitude estimation. Results in Fig. 3.4 and 3.5 combine to make

the wetting factor $\sigma\cos\theta$ a linearly decreasing function of pressure in either quartzitic and carbonate sediments, from $[\sigma\cos\theta]\approx$60mN/m at atmospheric pressure to $[\sigma\cos\theta]\approx$30mN/m on the L-V boundary. The wetting factor is very low for oil-wet sediments $[\sigma\cos\theta]<$5mN/m, and capillary forces vanish. Spontaneous imbibition takes place when $[\sigma\cos\theta]<$0mN/m. High values of breakthrough pressure are anticipated for clayey formations due to the high specific surface and small pore size; in this case, the presence of high conductivity mesoscale features will define the geological plumbing and restrict storage capacity.

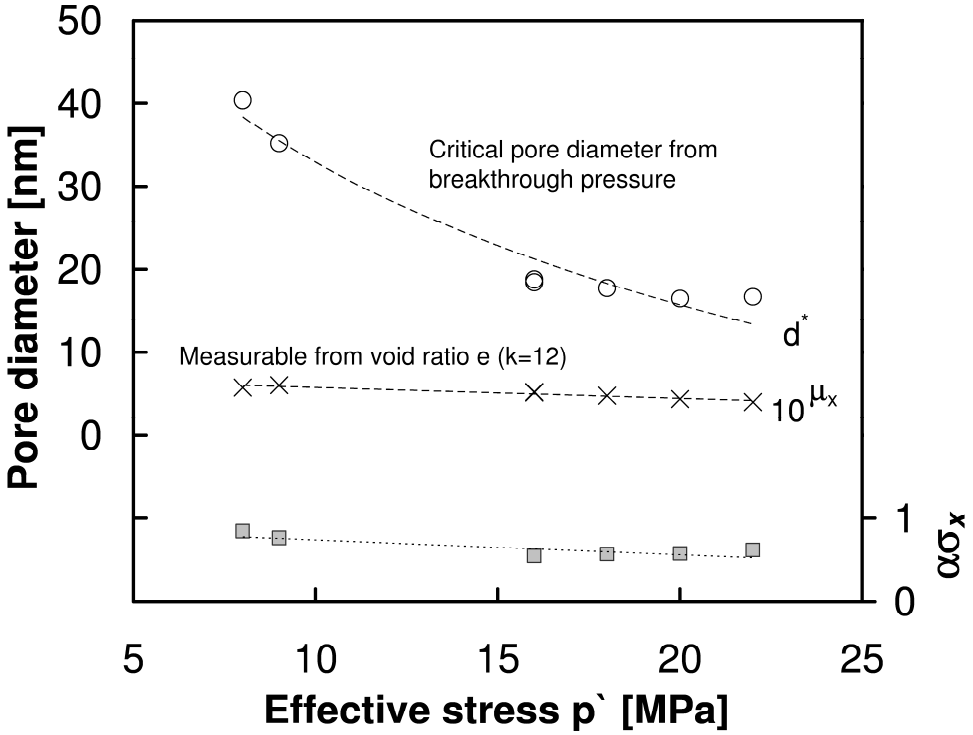

Figure 3.9. Critical pore diameter for gas breakthrough (Equation 3.12) and most prominent pore diameter as a function of effective stress in bentonite blocks [original data in *Horseman et al.*, 1999]. The secondary axis shows the factor $\alpha\sigma_x$ that quantifies the critical pore diameter d^* relative to the mean μ_x (Equation 3.13).

Other concerns regarding CO_2 injection in geologic formations include: change in surface charge of clays and associated double layer effects due to decreased pore fluid pH [*Palomino and Santamarina*, 2005] and mineral dissolution and ensuing changes in effective stress leading to strain localization [*Shin et al.*, 2008], and increase in permeability [*Phillips*, 1991].

3.5. Conclusions

Dissolved organic or inorganic species in water preferentially organize at the interface. Excess solute at the interface and the mass density of surrounding CO_2 determine interfacial tension. In particular, the interfacial tension between water and CO_2 decreases with pressure from ~65±14 mN/m at atmospheric pressure to ~25±7 mN/m beyond the CO_2 v-l boundary. The variability in each case reflects solute type and concentration.

Contact angle θ changes in agreement with Young's equation. On hydrophobic substrates, the increase in contact angle θ with pressure can be as high as 60°. Oil-wet mineral surfaces may turn from hydrophilic at low gas pressure to hydrophobic at high gas pressure. There is a small decrease in contact angle on hydrophilic silica and calcite substrates.

Water solubility in liquid CO_2 cannot be neglected when inter-particle pendular water is involved. The effective diffusivity of water in liquid CO_2 is high D=1.5±0.3×10^{-7} m^2/s (D~1.0×10^{-7} for brine) primarily due to the low viscosity of liquid CO_2. This value is two orders of magnitude greater than diffusion values frequently invoked for ionic species in water.

Pore water acidifies in the presence of CO_2 and can react with mineral substrates. Calcite dissolution, water diffusion out of droplets, and calcite reprecipitation can take place in short time scales (i.e., days) for pendular water between contacts.

Capillary pressure and viscous forces play an important role in determining CO_2 injectability and the sealing capacity of geological formations. Two end-member scenarios can be identified: high velocity viscosity-controlled flow (near injection wells), and quasi-static capillarity-controlled storage (far field and during long-term storage). Fingering and changes in imbibition patterns can develop.

The breakthrough pressure is a function of sediment characteristics (primarily specific surface), overburden effective stress, and fluid pressure dependent wetting conditions (interfacial tension and contact angle). The smallest pore size along a percolating path is larger than the mean pore diameter. It is anticipated that high conductivity mesoscale paths will control the sealing capacity of clayey rocks.

CHAPTER 4

WATER-CH4-MINERAL SYSTEMS: INTERFACIAL TENSION AND CONTACT ANGLE – IMPLICATIONS IN NATURAL GAS GEOLOGICAL SYSTEMS –

4.1 Introduction

The high demand for diminishing conventional oil and coal reserves promotes the exploration of other sources of fossil fuels. The USA currently satisfies 21% of its demand for natural gas from unconventional sources including gas shales and unmineable coal seams [*EIA*, 2011]. Japan seeks to produce commercially natural gas from offshore hydrate-bearing sediments at the Nankai Through [*Max*, 2000; *Nagakubo et al.*, 2011]. Furthermore, the production of natural gas from conventional and unconventional reservoirs can be enhanced by injecting carbon dioxide CO_2 [*Mathieson et al.*, 2010; *Vandeweijer et al.*, 2011]: CO_2 enhanced recovery facilitates methane displacement towards the production well, maintains the reservoir pressure to avoid subsidence and cap rock straining, and may contribute to carbon sequestration.

Gas reservoirs usually contain two or more fluid phases, including water, gas, oil, and CO_2. Interfacial phenomena between immiscible phases including minerals upscale through the sediment porous network to define multiphase flow characteristics. Thus, interfacial tension and contact angle determine gas recovery from both conventional and unconventional reservoirs [*Mazumder et al.*, 2008; *Moridis et al.*, 2009; *Seol and Kneafsey*, 2009; *Seto et al.*, 2009].

Interfacial tension arises at the molecular level as a result of van der Waals forces [*Butt et al.*, 2006; *Defay and Prigogine*, 1966]. Three interfacial tensions can be identified between a liquid *l* another fluid *f* and the solid substrate *s*. While the fluid-liquid interfacial tension σ_{fl} is directly measurable, fluid-solid σ_{fs} and liquid-solid σ_{ls} interfacial tensions are assessed through indirect methods [*Butt et al.*, 2006]. The Young-Dupre equation, relates the contact angle θ to the mutual interfacial tensions: $\cos\theta=(\sigma_{fs}-\sigma_{ls})/\sigma_{fl}$. The contact angle may also be influenced by other factors such as surface roughness, contact line fluctuations, vibrations, and viscous effects [*Decker et al.*, 1999].

The interfacial tension between CH_4 gas and liquid water is susceptible to changes in temperature and pressure. It decreases from ~72 to 51 mN/m as pressure increases from 0.1MPa to 40 MPa at 297K, and it decreases by ~10mN/m as temperature increases from 275K to 325K [experimental studies at 278-to-373K and up to 100MPa can be found in *Hough et al.*, 1951; *Jennings and Newman*, 1971; *Ren et al.*, 2000; *Sachs and Meyn*, 1995; *Sun et al.*, 2004; *Wiegand and Franck*, 1998]. Since the water-CO_2 interfacial tension is lower than the water-CH_4 interfacial tension, the interfacial tension of water with a CH_4-CO_2 gas mixture decreases as the molar fraction of CO_2 increases [*Ren et al.*, 2000]. The interfacial tension between different n-alkanes and methane gas ranges from ~0 to 30 mN/m as methane pressure increases from 0.1 to 15MPa; the associated change in contact angle on dolomite decreases from 134 to 113 [*Jaeger and Pietsch*, 2009].

The purpose of this manuscript is to study interfacial phenomena at reservoir conditions and to extend the scope of previous studies to include advancing and receding contact angle measurements on different substrates and several pore-fluids that may be

encountered in natural systems particularly in the context of natural gas production and enhanced fossil fuel recovery.

4.2 Device and materials – Test procedure – Data reduction

4.2.1 Apparatus, materials and test procedure

The sessile and pendant droplet methods are used to determine interfacial tension and contact angle in this study. The fluids are pressurized within a pressure chamber [devices and experimental details in Chapter 3]. Fluids include research purity CH_4, distilled water and 2M NaCl brine solution. The tested substrates are amorphous silica, calcite, coal (anthracite) and PTFE. Table 4.1 summarizes the pore fluid-substrate combinations and the range in pressure and temperature explored. Fluids are pressurized gradually with a gas booster and droplets are injected with a high pressure syringe.

4.2.2 Data reduction – Interfacial tension and contact angle

The CH_4-water interfacial tension is obtained by matching the solution of Laplace's equation in differential form and arc coordinates [s,φ] to the droplet contour in cartesian coordinates [x,z] inferred from thresholded images,

$$\frac{d\varphi}{ds} = \frac{2}{R_0} + \alpha\frac{\Delta\rho g z}{\sigma} - \frac{\sin\varphi}{x} \tag{4.1}$$

where $dx/ds=\cos\varphi$, $dz/ds=\sin\varphi$, R_0 is the radius of curvature at the apex, $\Delta\rho$ is the difference in mass density between the two fluid phases, g=9.81m/s^2, and α=1 for sessile droplets and α=-1 for pendant droplets. The density of CH_4 varies with pressure and temperature as predicted by the Peng-Robinson equation [*Peng and Robinson*, 1976]. The mass density of aqueous sodium chlorine solutions is computed taking into account

pressure, temperature and salinity [*Mavko et al.*, 2009; *Pitzer et al.*, 1984]. Finally, the contact angle measured during water injection and drawing is numerically determined from the digitally enhanced thresholded images.

Table 4.1 Experimental study. Numbers in parenthesis indicate the number of independent tests conducted for each condition.

Droplet	Substrate	σ	θ	T [K]	Maximum P [MPa]
Deionized Water	Amorphous SiO_2	-	(2)	270	19
	$CaCO_3$	-	(2)	278	17.9
	Coal	-	(2)	303	15
	PTFE	(2)	(2)	297	19.2
Brine 2M NaCl	Amorphous SiO_2	-	(2)	278-297	10.6
	$CaCO_3$	-	(2)	278-297	10.6
	Coal	-	(2)	303	10.6
	PTFE	-	(2)	303	10.6
	Hanging drop	(2)	-	297	19.5

4.3 Results and analyses

Table 4.1 shows tests conditions and pore fluid-substrate combinations explored in this study. Fig. 4.1 shows typical thresholded images. Experimental results and related analyses are presented next for the two parameters investigated in this study: interfacial tension and contact angle.

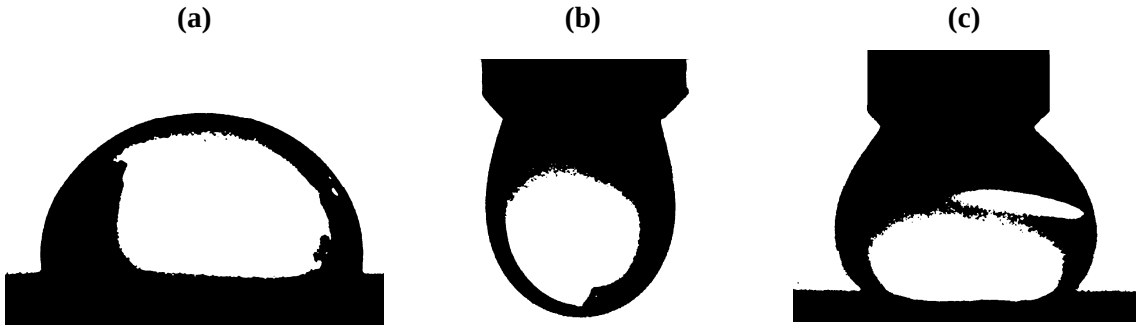

Figure 4.1 Test configurations used in this study. (a) Sessile drop on substrate (PTFE). (b) Pendant drop hanging from stainless steel needle. (c) Water droplet on substrate with volume control (coal). Thresholded images are shown.

4.3.1 Interfacial tension

Interfacial tension results for CH_4-water and CH_4-brine systems as a function of pressure summarized in Fig. 4.2 show that interfacial tension decreases as CH_4 pressure increases. There are two sets of experiments:

- Deionized water droplets (filled symbols in Fig. 4.2): results are consistently lower than the ones found in previous studies. The interfacial tension between CH_4 and water is ~65mN/m at 0.1MPa and decreases to 40mN/m at 19.2 MPa (experiments at 297K).
- Brine droplets (open symbols in Fig. 4.2): The interfacial tension between CH_4 and brine is slightly higher than for deionized water at 0.1MPa, and decreases with pressure at approximately the same rate.

For comparison, data compiled from the literature [*Ren et al.*, 2000; *Sachs and Meyn*, 1995; *Sun et al.*, 2004; *Wiegand and Franck*, 1998] are analyzed to extract an expression to estimate the value of interfacial tension between water and CH_4 as a function of pressure P and temperature T,

$$\sigma_{water-CH4} = a + b\frac{T}{\mathrm{K}} + \left(c + b\frac{T}{\mathrm{K}}\right)\exp\left(-d\frac{P}{\mathrm{MPa}}\right) \qquad (4.2)$$

where a=71.04mN/m, b=-0.0716mN/m, c=43.85mN/m, and d= =-0.0602. This equation is applicable to pressure-temperature conditions in the range from 0.1MPa to 200MPa and 298K to 373.15K, with an error less than 2mN/m. The trend is superimposed in Fig. 4.2.

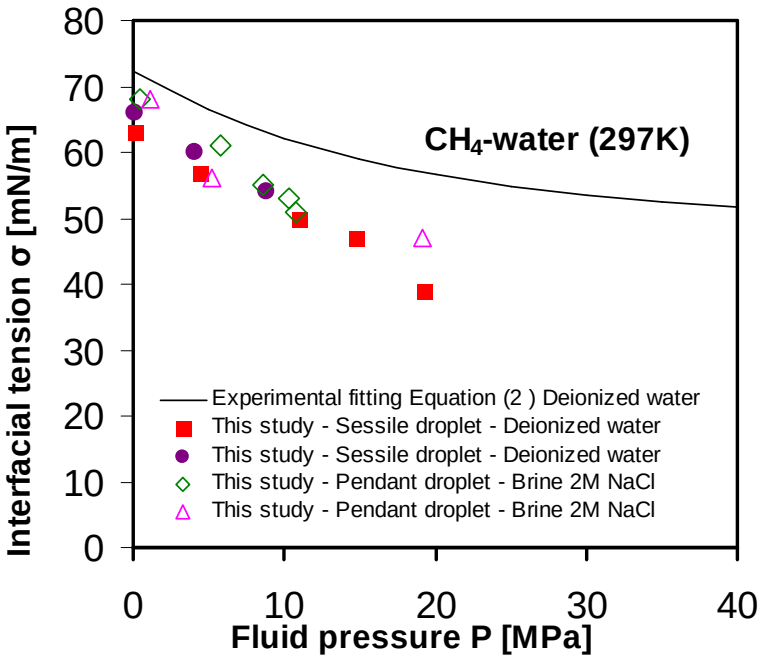

Figure 4.2 Interfacial tension between water and CH_4. Our experimental results (T=297K) are shown as empty symbols for deionized water and filled symbols for brine; the trends shown as continuous lines represent the curve fitting of previously published measurements (Eq. 4.2). The interfacial tension decreases upon pressure increase.

4.3.2 Contact angle

Single droplets. Fig. 4.3 shows the range of contact angles θ measured for water and brine droplets surrounded by CH_4 gas, from low to high pressure. It can be observed that

- Amorphous silica and calcite substrates are clearly hydrophilic, while coal and PTFE are hydrophobic.
- Contact angles of water droplets on amorphous silica SiO_2 and calcite $CaCO_3$ substrates remain nearly constant with pressure θ~60-to-70°. Contact angles on coal change moderately with pressure and remain between 110 and 130° (contact angle increase in coal is hindered by water penetration into the coal matrix upon pressurization). The contact angle on PTFE substrates increases from θ~100-to-110º as pressure increases from 0.1 to 20MPa
- The contact angles of brine on amorphous silica and on calcite are slightly smaller than the ones measured with deionized water. While lower contact angles are measured with brine droplets on coal in comparison to deionized water droplets, salts have the opposite effect on PTFE.
- Similar trends have been reported for CO_2-water systems upon pressurization on PTFE and coal [*Espinoza and Santamarina*, 2010a; *Siemons et al.*, 2006].

Advancing and receding contact angles. Fig. 4.4 shows the evolution of contact angle during water injection and drawing at a flow rate of ~1-2 mm^3/sec (See Fig. 4.1-c). Salient remarks follow:

- Amorphous silica remains hydrophilic during advance or recession. The contact angle varies between 40° and 60°.
- The contact angle varies from 40° to 140° on calcite, coal, and PTFE showing both hydrophilic and hydrophobic regimes.
- Calcite can be significantly hydrophobic during water invasion and the contact

angle can be as high as 110°.

- Coal is the most hydrophobic solid from the set of substrates studied here. The contact angle can be as high as 140° during water advance.
- PTFE is predominantly hydrophobic and shows a well defined hysteresis loop.

Repeated advance-recession loops showed trends consistent with those plotted in Fig. 4.4.

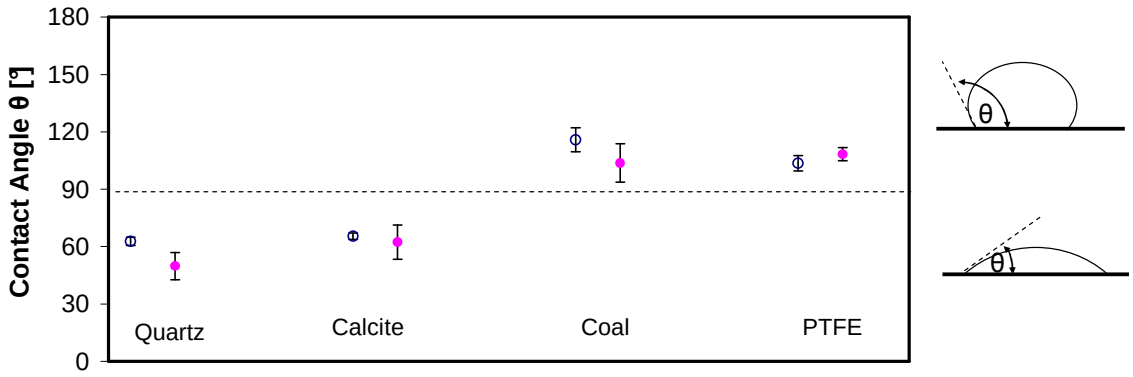

Figure 4.3 Contact angle for water (empty circles) and brine (filled circles - 2M NaCl) droplets on different substrates surrounded by CH_4 gas. The results show the average contact angle and standard deviation for pressures from 1 to up to 20 MPa (See specific experimental details in Table 4.1). Amorphous silica and calcite are clearly hydrophilic as opposed to coal and PTFE.

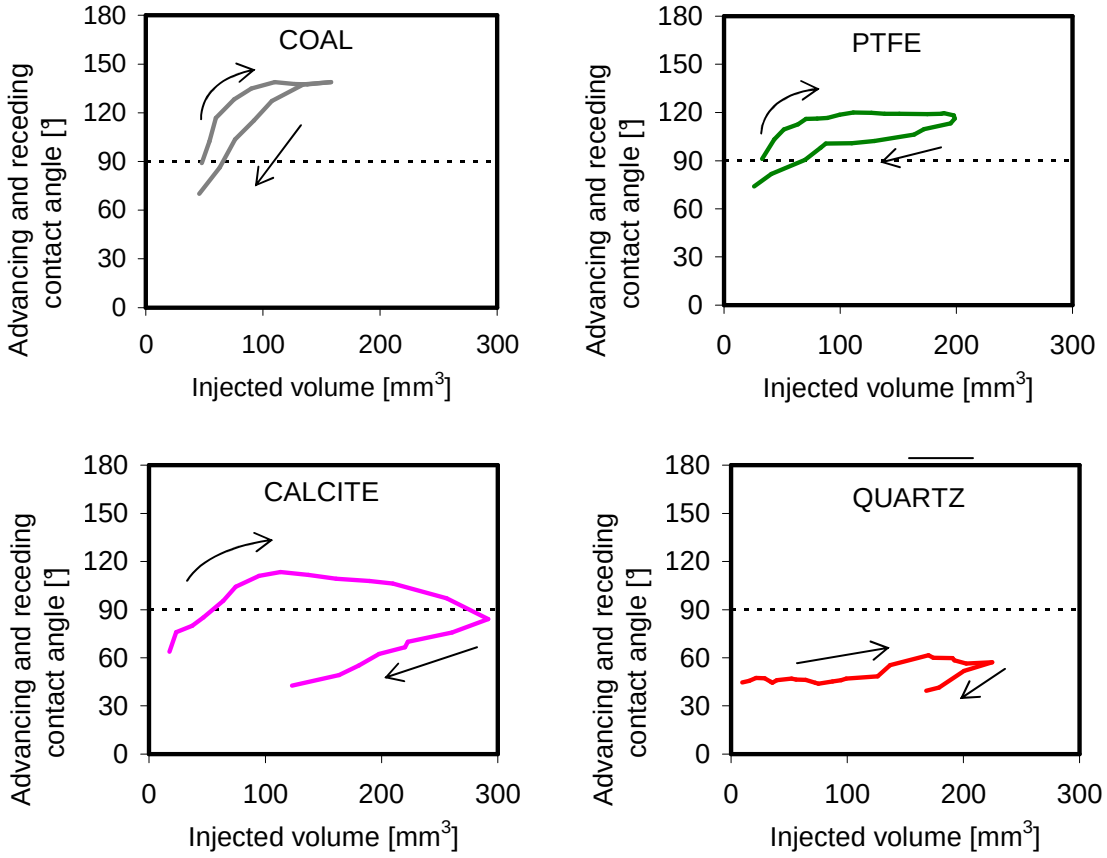

Figure 4.4 Advancing and receding contact angles for brine on different substrates in a CH_4 atmosphere at 10MPa. Hydrophobicity on coal, calcite and PTFE prevails during advance. Amorphous silica remains hydrophilic during advance and recession.

4.4 Discussion and implications in CH_4 geological systems

4.4.1 Changes in interfacial tension and contact angle

Changes in interfacial tension with pressure and temperature are the consequence of molecular phenomena and interactions taking place within water and the surrounding CH_4, such as, mass densities, gas solubility, and affinity of dissolved species to the gas-water interface [similar trends apply to systems involving water and other gases including CO2 - *Massoudi and King*, 1974b]. A thermodynamical model based on linear density

profiles of phases across the interface, Helmholtz free energy and chemical potential shows fair adequacy to model the interfacial properties of water and CH_4 [*Schmidt et al.*, 2007]. Fig. 4.5 shows the governing effect of differences in mass densities across the interface $\Delta\rho$ on interfacial tension and the secondary role of temperature T (normalized by the CH_4 critical temperature T_c=190.56K).

The variations in contact angle stem from changes in interfacial tensions between the participating species, including the substrate, and their effect on the equilibrium of the Young's contact angle equation. For example, an increase in contact angle in hydrophobic substrates is expected due to a decrease in the water-CH_4 interfacial tension as observed in PTFE and coal substrates [find an analogous case for CO_2 in Chapter 3]. Contact angle hysteresis is due heterogeneities in the surface, surface roughness, adsorption/desorption at the contact line and energy dissipation [*Butt et al.*, 2006]. Surface roughness and contaminant adsorption on surfaces (e.g., atomically smooth calcite cleaved surfaces) might have played a significant role on the measured contact angle hysteresis on the various substrates. [*Decker et al.*, 1999]. .

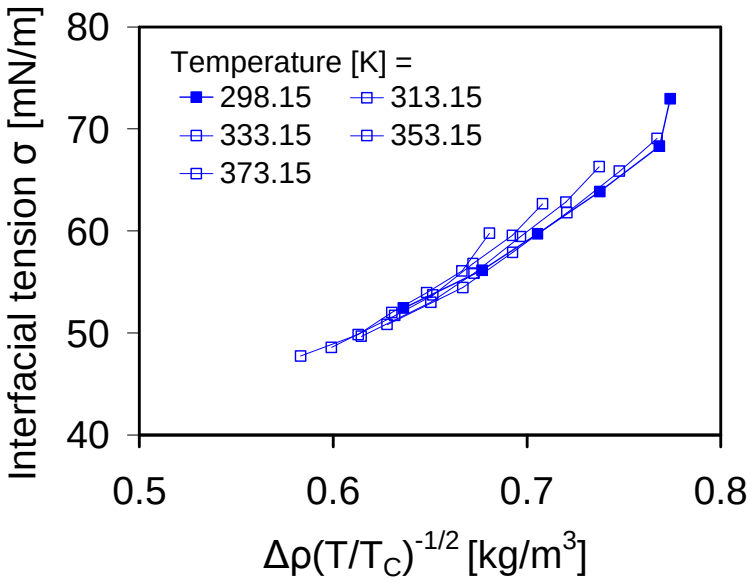

Figure 4.5 Water-CH_4 interfacial tension as a function of mass density difference and reduced temperature for several interfacial tension isotherms: T= 298.15K, 313.15K, 333.15K, 353.15K and 373.15K - data from [*Ren et al.*, 2000]. The difference in mass density correlates with interfacial tension.

4.4.2 Applications: reservoir CH_4 multiphase flow

Interfacial tension and contact angle define capillary forces and multiphase fluid flow characteristics, e.g. relative permeability and irreducible saturation. The recovery efficiency of CH_4 depends on the pore fluid viscosities μ, the fluid flow velocity v, and capillary resistance at pore throats. Let's consider a pore as a cylindrical tube diameter d and length L going from node i to node j. The equilibrium condition when the invading fluid displaces the host fluid a distance l along the tube is given by:

$$p_i = p_j + 4\frac{\sigma\cos\theta}{d} + v\frac{32L}{d^2}\left(\frac{l\mu_{invading} + (L-l)\mu_{diplaced}}{L}\right) \qquad (4.3)$$

where the second term is Laplace's equation and the third term is Poiseuille's equation; the contact angle is $\theta<90°$ when the invading fluid wets the surface, $p_{i,j}$ are the pressures at the tube nodes, μ is the fluid viscosity, and v the fluid average velocity (different

coefficients apply for the case of planar fractures). Therefore, wettability and viscous drag determine imbibition and the occupancy of pores by either the wetting or the non-wetting fluid. The balance between participating forces can be captured in two dimensionless ratios in terms of viscous resistance and capillarity,

$$M = \frac{\mu_{invading}}{\mu_{displaced}} \quad \text{and} \quad C = \frac{v\mu_{invading}}{\sigma \cos\theta} \tag{4.4}$$

The viscosity of brine is $\mu_{brine}=(1\pm0.5)\times10^{-3}$ Pa·s and the viscosity of CH_4 is $\mu_{CH4}=(2\pm0.5)\times10^{-5}$ Pa·s (T=323K, P=10-35MPa) [*NIST*.gov].

Two end-member cases can be identified in terms of the viscosity ratio *M*:

- *Large viscosity ratio M>>1*. This case corresponds to depressurization and consequent CH_4 displacement by brine (or oil) in natural gas reservoirs, $M = \mu_{brine}/\mu_{CH4}\sim50$. Capillarity may favor stable displacement if the solid is water-wet (imbibition, e.g., advancing contact angle on amorphous silica < 90°) or oppose fluid displacement (drainage, e.g., contact angles >90° in calcite). In either case, the displacement of a fluid by a more viscous one favors low residual saturation [*Lenormand et al.*, 1988]. Because water displaces CH_4 from the pores, low gas residual saturation is expected, i.e., high production efficiency.
- *Low viscosity ratio M<<1*. This is the case of CH_4 invasion into water-saturated fractures and pores during methane desorption from coal seams and during hydrate dissociation in hydrate-bearing sediments; $M=\mu_{CH4}/\mu_{brine}\sim1/50$. The invasion of a low viscosity fluid promotes bifurcation in the form of fingers. Amorphous silica, calcite and coal are gas-wet when CH_4 displaces water from the pore space (non-wetting fluid invasion). The value of *C* depends on the value of interfacial tension and velocity of desorption in the case of coal or

analogously, the rate of dissociation in the case of hydrates. Fig. 4.6 shows the case of a hydrate-reservoir and the variation of interfacial tension with pressure and temperature as expected during production. The fluid velocity *v* affects invasion patterns [*Lenormand et al.*, 1988]: viscous fingering is expected for rapid desorption while capillary fingering is expected at low depressurization. Both types imply high residual saturation of the host fluid (brine).

Changes in pore space occupancy patterns affect relative permeability. The relative permeability of invading CH_4 is expected to increase as water saturation decreases, interfacial tension decreases, and the medium becomes more water-wet [*Dullien*, 1979].

Note that there is still no evidence regarding interfacial properties between CO_2, CH_4 and mineral substrates. This information is relevant to coal bed methane enhanced recovery with CO_2 and CH_4-CO_2 hydrate replacement.

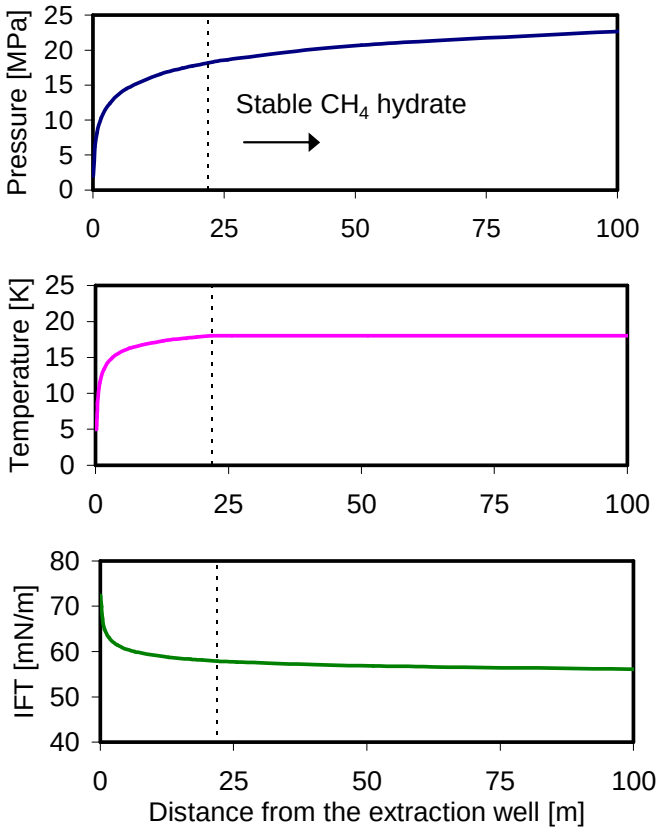

Figure 4.6 Water-CH_4 interfacial tension profile for a CH_4 hydrate-bearing reservoir depressurization (axisymmetry assumed). The formation temperature is assumed to be 18°C (291.15K) and the far field pressure ~20MPa; the pressure at the wellbore is 2MPa and the temperature 5C (278.15). Temperature follows the hydrate dissociation boundary. Interfacial tension increases as pressure and temperature decrease in the vicinity of the well.

4.5 Conclusions

A thorough characterization of CH_4-water-substrate interfacial properties facilitates the understanding of CH_4 recovery from geological formations.

The interfacial tension between water and methane depends on pressure, temperature and water salinity. Changes are moderate within reservoir conditions but become more pronounced when large depressurization is imposed. The magnitude of capillary effects will be mainly defined by the pore size.

Contact angle governs wettability. Variations of contact angle with pressure are not significant in CH_4-water-mineral systems. The contact angle is expected to be less than 90° (water-wet) in siliceous formations during both water advance or recession. Calcite and coal are gas-wet during water advance but may behave water-wet when water recedes, i.e. when gas invades the pore space.

Interfacial tension and contact angle stem from molecular interaction at interfaces. The change of water-CH_4 interfacial tension is due to CH_4 adsorption at the interface and correlates with the difference in mass density. Changes in contact angle are a result of variations in interfacial tension, surface heterogeneities and fluid adsorption/desorption.

The contact angle affects multiphase flow characteristics. Stable water invasion of gas-saturated reservoirs is anticipated in siliceous and carbonate formations during depressurization leaving behind low residual gas saturation. Conversely, non-wetting gas invasion into water-saturated formations will tend to form viscous or capillary fingers and leave considerable entrapped water behind in coal beds and hydrate-bearing sediments during CH_4-recovery.

CHAPTER 5

PROPERTIES AND PHENOMENA RELEVANT TO CH_4-CO_2 REPLACEMENT IN HYDRATE BEARING SEDIMENTS

5.1 Introduction

Global sustainability, in terms of energy needs and climate stress from greenhouse gases, requires new sources of energy and the management of CO_2 emissions. Methane hydrate is a potential energy source, with worldwide reserves on the order of 500-to-10,000 Gt of carbon [*Collett*, 2002; *Kvenvolden*, 1988; *Milkov*, 2004; *Ruppel and Pohlman*, 2008]. Methane can be recovered from hydrate bearing sediments by depressurization, heating or chemical injection. In particular, the injection of carbon dioxide, CO_2, into hydrate-bearing sediments can liberate methane, CH_4, and sequester CO_2 in hydrate form [*McGrail et al.*, 2007; *Ota et al.*, 2005a; *Stevens et al.*, 2008; *Svandal et al.*, 2006; *Zhou et al.*, 2008b].

The chemical potential difference between CH_4 and CO_2 hydrate indicates that CH_4-CO_2 gas replacement is thermodynamically favorable [*Seo and Lee*, 2001; *Svandal et al.*, 2006]. However, the extent of the reaction and its efficiency in real systems is determined by multiple factors and coexisting processes, such as (1) pressure and temperature-dependent solubilities and interfacial properties, (2) relative viscosity, permeability, and density between water and CO_2, (3) invasion patterns and specific surface of the hydrate phase, (4) fluid expansion after replacement, and (5) changes in effective stress. These phenomena couple to determine replacement efficiency and the geomechanical response of the sediment mass.

In this manuscript, we review previous CH_4-CO_2 replacement studies, identify and analyze underlying processes, present new experimental results, and anticipate potential implications.

5.2 Physical and thermodynamic properties

The process of replacing CH_4 with CO_2 in hydrate must be understood at both the molecular scale and the macroscale to anticipate conditions for efficient CH_4-CO_2 replacement and its consequences on thermal, mechanical and electrical properties. In this section, we summarize physical parameters in tabular form and highlight the most relevant observations in the text.

5.2.1 Structure: Geometry and length scales (Table 5.1-a)

Both CH_4 and CO_2 form structure I hydrate. This crystallographic structure is composed of 2 small cages for every 6 large cages, so the stoichiometric formula is $6X \cdot 2Y \cdot 46H_2O$, i.e., a maximum of 6 gas molecules X in large cages plus a maximum of 2 gas molecules Y in small cages, and 46 water molecules. The lattice repeats every ~12Å [*Sloan and Koh*, 2008]. Thus, gas molecules make up a significant molar fraction ~15% of the hydrate structure (compare to the gas solubility in liquid water ~0.1% molar fraction, section 5.2e).

The stoichiometric ratio (number of water molecules / number of gas molecules) often deviates from the theoretical value n=46/8=5.75 for structure I hydrate. In particular, the occupancy of CO_2 molecules in small cages increases with pressure and the stoichiometric ratio decreases from ~6.6 at 1.3MPa and 273.15K, to the theoretical

limit 5.75 at 4.5MPa and 283.15K [*Anderson*, 2003; *Klapproth et al.*, 2003]. The CH_4 molecule is slightly smaller than CO_2 and fits more easily in small cages, so the stoichiometric ratio for CH_4 hydrate is typically n=6 [*Circone et al.*, 2005]. As a result, the stoichiometric ratio of CH_4 hydrate is less sensitive to pressure than the stoichiometric ratio of CO_2 hydrate.

Fig. 5.1 shows hydrate forming molecules and related molecular structures; they are drawn using the corresponding van der Waals radii and are shown at the same scale. The size of the opening between water molecules that form the face of big cages is smaller than the size of both CO_2 and CH_4 molecules. This simple observation leads us to conclude that the hydrate cage must separate to release the CH_4 molecule before it can trap CO_2. The molecule of nitrogen N_2 is smaller than CO_2 and fits more easily in the small cages of sI hydrate; this explains the enhanced CH_4 replacement efficiency obtained when a mixture of CO_2 and N_2 is used in a water-limited CH_4 hydrate system of structure I, or of structure II if combined with C_2H_6 [*Park et al.*, 2006].

5.2.2 Thermal properties (Table 5.1-b)

In agreement with Le Châtelier's principle, hydrate formation is an exothermic reaction. In particular, the heat liberated during the formation of a mol of CO_2 hydrate varies between $H_{CO2\text{-}hyd}$=57.7 and 63.6 kJ/mol (Note: a mol of CO_2 hydrate is 44g + n 18g where n=5.75-to-6.6) [*Anderson*, 2003]. Conversely, hydrate dissociation is endothermic as heat is needed to disorganize the crystal structure. The heat adsorbed during the dissociation of a mol of CH_4 hydrate is $H_{CH4\text{-}hyd}$=52.7-to-55.4 kJ/mol where a mol of CH_4 hydrate is 16g + n 18g and n~5.75 [*Anderson*, 2004]. Therefore, CH_4-CO_2

replacement is exothermic. The path assumed here involves complete CH_4 hydrate dissociation before CO_2 hydrate formation. Molecular dynamic simulations for CH_4-CO_2 replacement in the first monolayer (interface between CH_4 hydrate and liquid CO_2) show only partial dissociation of the hydrate cage and lower enthalpy change for the complete replacement reaction [Bjorn Kvamme 2010, personal communication]. Experimental and numerical data are still needed to assess the evolution of the reaction when a large hydrate mass is involved, as in the pore space of sediments, where the characteristic length scale is much greater than the crystal nm-scale.

The thermal conductivity λ and diffusivity κ of liquid CO_2 are significantly lower than the corresponding values for either hydrates or water. In addition, water has the highest heat capacity *c* among all participating phases. This combination of thermal properties suggests reduced heat dissipation and increased local heating where liquid CO_2 displaces water and contacts CH_4 hydrate.

5.2.3 Mechanical properties (Table 5.1-c)

The viscosity of water is one-to-two orders of magnitude higher than the viscosity of liquid CO_2; this pronounced difference in viscosity will affect fluid invasion flow paths. Bulk densities are similar for hydrate and water, ordered as $\rho_{CH4hyd}<\rho_{H2O}<\rho_{CO2hyd}$. The density of liquid CO_2 may exceed that of water, $\rho_{CO2(l)}>\rho_{H2O}$ (e.g., at 273.15K for pressures above 25MPa); differences in fluid density contribute to buoyancy effects on fluid flow. Liquid CO_2 is heavier than water in deep sea locations, but remains lighter than water near the continental shelf.

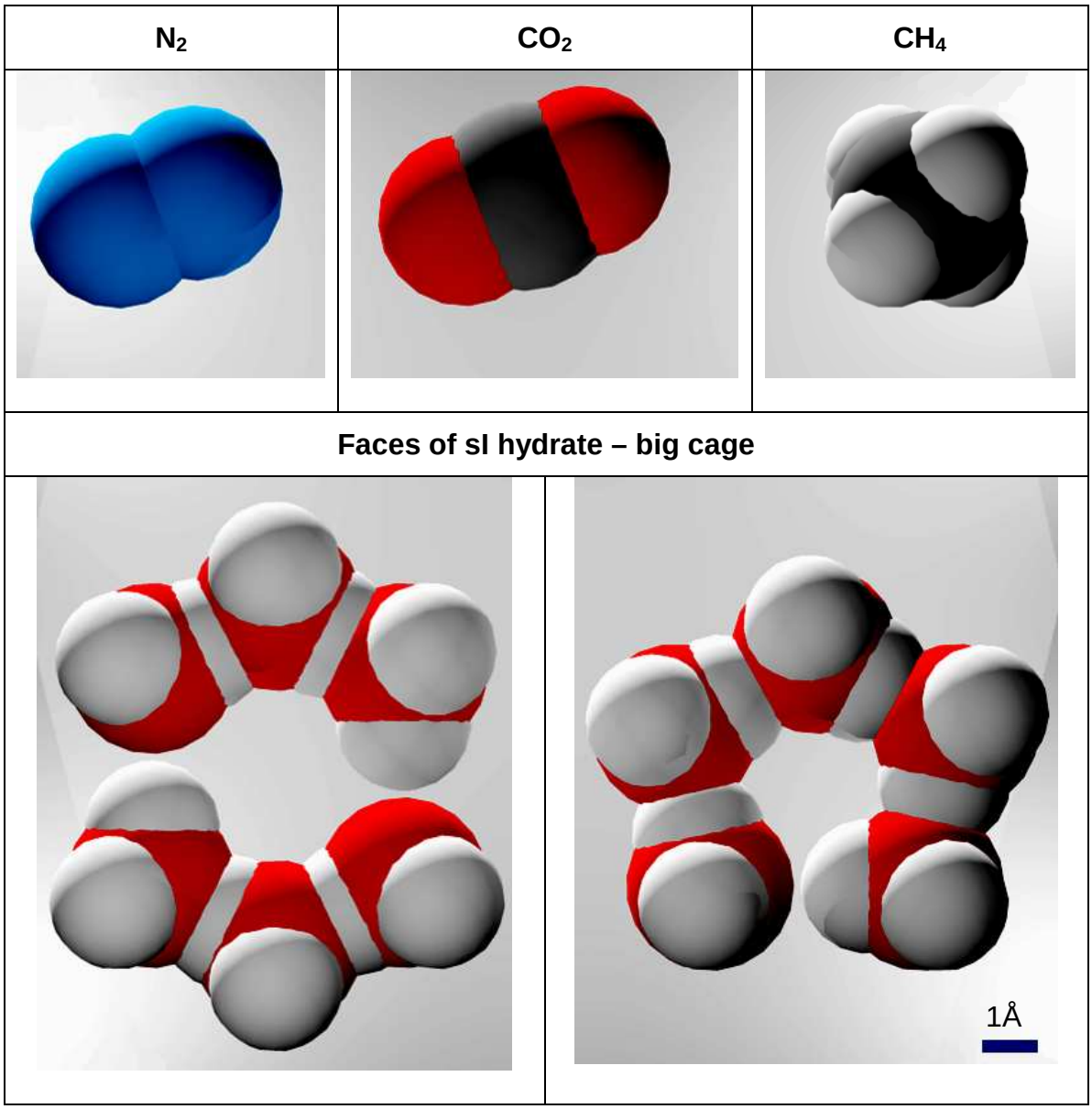

Figure 5.1. Hydrate forming molecules (N_2, CO_2 and CH_4) and two faces of the big cage in sI hydrate. All molecules are drawn using van der Waals radii to the same scale. Hexagonal and pentagonal faces are not regular polygons. Notice that the opening between water molecules is smaller than the size of N_2, CO_2 and CH_4 molecules.

The volume of water V_w increases when hydrate forms: V_{hyd}~1.234 V_w for CH_4 hydrate and V_{hyd}~1.279 V_w for CO_2 hydrate. Such a large volumetric change within the pore space causes volumetric strains in the sediment during hydrate formation and promotes skeletal instability and contraction during dissociation [*Lee et al.*, 2010]. The shear stiffness of CH_4 hydrate is $G \approx$ 3.5GPa (a similar value is expected for CO_2 hydrate). Bulk moduli for liquid H_2O and CO_2 are lower than that of solid hydrates, and the bulk modulus of liquid CO_2 is almost one order of magnitude lower than that of water. Correspondingly, the P-wave velocity is ~3 times slower in liquid CO_2 than in water. The addition of CO_2 in hydrate reservoirs could increase measured seismic wave velocities by forming additional hydrate, or it could lower the measured velocity by displacing pore water. The interpretation of seismic data gathered during CO_2 injection must account for changes in both hydrate saturation and pore-fluid composition.

5.2.4 Electrical properties (Table 5.1-d)

The permittivity of liquid water is determined by the orientational polarization of water molecules. The water dipole rotation is hindered in hydrates. In addition, CH_4 and CO_2 are non-polar molecules and do not contribute to orientational polarization. Hence, gas hydrates have much lower permittivity compared to liquid water [*Galashev et al.*, 2006]. The electrical conductivity of water increases almost linearly with ionic concentration at low salt concentration and it is much higher than the electrical conductivity of hydrates. The electrical conductivity of liquid CO_2 is even lower than the electrical conductivity of hydrate. As with seismic surveys, resistivity surveys must account for pore fluid changes as well as hydrate saturation changes. In contrast to

seismic results, in which added hydrate formation and CO_2 displacement of pure water have opposing effects on the measured velocity, the electrical properties are reduced both by added hydrate formation and pore water displacement. Tracking hydrate saturation and pore water chemistry is essential for correctly interpreting electrically-based monitoring techniques.

Table 5.1. Physical properties of CH_4 and CO_2 hydrate, pure CO_2 and water relevant to CH_4 replacement by CO_2 in hydrate bearing sediments.

Property	CH_4 hydrate(sI)	CO_2 hydrate (sI)	CO_2 liquid	H_2O liquid
a - Structure				
Stoichiometric ratio or hydration number, #H_2O mol/ #Gas mol	5.75 (100% cage occupancy) † [a] 5.81-6.10 [1.9-to-9.7MPa, 263-to-285K][å]	5.75 (100% cage occupancy) † [a] 6.57 [1.5MPa, 273K] [b]	Refer to Fig. 5.1	
Cage occupancy	~100% Large cage ~70% Small cage [10MPa, 273K] [b]	~100% Large cage ~50% Small cage [1.5MPa, 273K] [b]		
Cavity Size [Å]	7.9, 8.66 [a]	7.9, 8.66 [a]		
Guest Size [Å]	5.12 [a]	4.36 [a]		
Lattice constant *a* [Å]	11.95 [10MPa, 271.15K] [b]	12.07 [273.2K] [c]		
b - Thermal				
Heat capacity *c* [kJ·kg^{-1}·K^{-1}]	2.031 [263K] [d] 2.080 sI [a] 2.250 sI [e] 2.077 [270K] [f]	No data found	2.280 [280K,10MPa] (highly variable)[g]	4.218 [273K] 4.192 [283K] [d]
Thermal conductivity λ [W·m^{-1}·K^{-1}]	0.68 [273K] [d] 0.49 [263K] [a]	0.49 [263K] [a]	~0.13 [12.5MPa, 270K] [h]	0.56 [273K] 0.58 [283K] [d]
Thermal Diffusivity $\kappa = \lambda\rho^{-1}c_p^{-1}$ [m^{2}s^{-1}]	3.1×10^{-7} [i]	No data found	6.07×10^{-8} †	1.33×10^{-7} [273K] 1.38×10^{-7} [283K] [d]
Heat or Enthalpy of Dissociation and Formation ΔH_d [kJ/mol]	52.7-to-56.9 [273K] [d] ~53 [independent of P-T] [j]	63.6-to-57.7 (±1.8) [at quadruple points] [j]	Does not apply	(water to ice) ~6 [d]

Property	CH_4 hydrate(sI)	CO_2 hydrate (sI)	CO_2 liquid	H_2O liquid
c - Mechanical				
Viscosity μ [Pa·s]	Does not apply	Does not apply	(2-to-8)×10^{-5} [5-to-30MPa, 318K] [o]	~1.5×10^{-3} [293K] [p]
Density ρ [kg·m^{-3}]	929 [263K] [d] 940 [a] 910[273K] [d,q]	1110-to-1090 [r] [30MPa] 1054 [n]	~938-to-800 kg/m^3 [10MPa, 280-to-300K] (highly variable) [g]	999.9 [0.1MPa, 273K] 1003±1.5 [10MPa, 280-to-300K] 1030±2 [3.5% salinity; 10MPa, 280-to-300K] [s]
Water volume expansion upon hydrate formation V_{hyd}/V_w	1.234 † (n=6; ρ_{CH4hyd}=930kg/m^3; 100% occupancy)	1.279 † (n=6; ρ_{CO2hyd}=1100kg/m^3; 100% occupancy)	Does not apply	V_{ice}/V_w = 1.09
Coefficient of thermal expansion α [K^{-1}]	sI hydrate 7.7×10^{-5} [200K] [a] 2.64×10^{-4} [b]	sI hydrate 7.7×10^{-5} [200K] [a]	No data found	2±0.3×10^{-4} [50MPa, 273.15-to-283.15K] [w]
Bulk Modulus [GPa]	7.2 [277K] [f] ~9 [273K] [b] 8.73 [273K] [v]	No data found	0.338-to-0.124 GPa [10MPa, 280-to-300K] †	2.1-to-2.3 GPa [10MPa , 280-to-300K] †
Shear Modulus [GPa]	3.2 [277K] [f] 3.54 [273K] [v]	No data found	0	0
Poisson ratio	0.32 [273K] [v]	No data found	~0.5	~0.5
V_P [m/s]	3775 [273K] [v]	No data found	~600-to-400 m/s [10MPa, 280-to-300K] [g]	1450-to-1518 [10MPa, 280-to-300K] [x]
V_S [m/s]	1954 [273K] [v]	No data found	0	0
d - Electrical				
Electrical conductivity [S/m]	0.01 [y]	No data found	<10^{-2} at less than 3000K [z]	depends on ionic concentration Sea-water: ~5
Dielectric permittivity (freq. < 1GHz)	~2.5 [273K] [y]	No data found	1.0 to 1.5 from 1 to 20MPa, 308K [æ]	79-to-80 [œ]

† computed value; a-[*Sloan and Koh*, 2008]; å-[*Circone et al.*, 2005]; b-[*Klapproth et al.*, 2003]; c-[*Uchida et al.*, 1999]; d-[*Waite et al.*, 2009]; e-[*Makogon*, 1997]; f-[*Handa*, 1986] [*Yoon et al.*, 2003]; g-[*Span and Wagner*, 1996]; h- [*Vesovic et al.*, 1990]; i-[*Waite et al.*, 2007]; j-[*Anderson*, 2003; 2004]; k-[*Davies et al.*, 2008]; L-[*Mori and Mochizuki*, 2000]; m- as in [*Mochizuki and Mori*, 2006]; n-[*Uchida et al.*, 1999]; o-[*Thomas and Adams*, 1965a]; p-[*Fenghour et al.*, 1998; *Netherton et al.*, 1977]; q-[*Kiefte et al.*, 1985]; r-[*Aya et al.*, 1997]; s- [*Millero and Poisson*, 1981]; v-[*Helgerud et al.*, 2009]; w-[*Bradshaw and Schleicher*, 1970]; x-[*Belogol'skii et al.*, 2002]; y-[*Galashev et al.*, 2006]; z-[*Tanaka et al.*, 2008], æ-[*Goldfarb et al.*, 1999; *Obriot et al.*, 1993], and œ-[*Israelachvili*, 1991].

5.2.5 Chemical properties: phase boundaries, solubilities and diffusivities (Tables 5.2, 5.3 and 5.4)

Hydrate stability and gas solubility in water are pressure and temperature dependent.

1) Phase boundaries: We develop regression equations for CO_2 and CH_4 hydrate phase boundaries, and for the liquid-vapor, L-V, boundary for CO_2 by fitting values predicted using experimentally validated thermodynamic models by Duan and Sun [2003b; 2005] (Table 5.2). Hydrate grown from a mixed CH_4-CO_2 gas atmosphere exhibits an intermediate phase boundary, between the boundary for pure CH_4 and CO_2 hydrates, where the relative position scales with the mixture ratio [*Adisasmito et al.*, 1991; *Seo and Lee*, 2001]. The liquid-vapor, L-V, boundary shown in Fig. 5.2 corresponds to pure CO_2. Even small amounts of CH_4 in CO_2 cause the gas mixture L-V boundary to shift towards higher pressures, e.g. CO_2 with 10% CH_4 condenses at a pressure ~2MPa higher than the pressure needed for pure CO_2 [*Donelly and Katz*, 1954]. It can be observed from Fig. 5.2 that: CH_4 hydrate stability requires higher pressures than CO_2 hydrate for temperatures $T \leq 283.67$K. These boundaries partition the P-T space into four regions: CH_4 hydrate may be surrounded by liquid CO_2 (Zone A) or by gaseous CO_2 (Zone B) if $T < 277.1$K; CO_2 hydrate can coexist with either liquid CO_2 (zone C) or with gaseous CO_2 (zone D).

2) Solubility in liquid phases: Table 5.3-a shows a summary of solubility values for all participating species in different media; the simultaneous presence of CH_4 and CO_2 in water alters the solubilities shown for simple binary systems [*Qin et al.*, 2008]. The solubility of CH_4 and CO_2 in water affects gas transport, hydrate formation and hydrate dissolution in water that is not fully saturated with gas. The solubility of CO_2 in water is about 10 times greater than that of CH_4; both solubilities increase as pressure increases

and temperature decreases. The presence of hydrate in water inverts these trends. The amount of dissolved water in liquid CO_2 is not negligible, and can be as high as 0.003-to-0.006 mol/mol, that is ~1kg of water per m^3 of liquid CO_2 at T=285-to-293K and P=10-to-20MPa [*Spycher et al.*, 2003]. Hence, liquid CO_2 can remove water, effectively "drying" the sediment.

Table 5.2. Phase boundaries for pure CH_4 and CO_2 hydrates, and liquid-vapor boundary for pure CO_2, calculated by fitting values predicted using the experimentally validated formulation in Duan and Sun [2003b; 2005].

CH_4 hydrate stability boundary	***CO_2 hydrate stability boundary***
Ice-hydrate-CH_4 gas $P^* = 17.126T^* - 14.584$ if 263<T≤ 273.15K	Ice-hydrate-CO_2 gas $P^* = 8.082\ T^* - 7.020$ if 263<T≤ 272.15K
Liquid water-hydrate-CH_4 gas $T^* = 0.0396\ \mathrm{e}^{\left(-6.46\times10^{-4}P^*\right)}\left[24.348 + \mathrm{Ln}\left(P^*\right)\right]$ if 273.15<T<290K	Liquid water-hydrate-CO_2 gas $T^* = 0.0358\ \mathrm{e}^{\left(-0.00285P^*\right)}\left[27.829 + \mathrm{Ln}\left(P^*\right)\right]$ if 272.15<T≤ 283.17K
	Liquid water-hydrate-CO_2 liquid $P^* = 3.34\times10^{-4}\ \left(T^*\right)^{264.4}$ if 283.17<T<290K
CO_2 Liquid-vapor phase boundary	
$P^* = 3.45\ \left(T^*\right)^{7.00}$ if 263K<T≤ $T_{critical}$=304.1K (Note: boundary shifts to higher pressures in CH_4/CO_2 gas mixtures)[a]	

Definitions: P*=P/1MPa; T*=T/273.15K.
Note: (a) [*Donelly and Katz*, 1954].

Similarly, CH_4 is highly soluble in liquid CO_2; for example, a molar mixture of 12% CH_4 and 88% CO_2 remains liquid above a line defined between [6.6MPa, 273.1K] and [7.2MPa, 278.1K], as can be estimated from the bubble point line [*Donelly and Katz*,

1954]. This observation explains experimental results at 8.7MPa and 277.1K where no CH_4 bubbles were observed during CH_4-CO_2 replacement [~2/40 moles of CH4/moles of CO2] [*Dunk et al.*, 2006] as the liquid CO_2 was able to contain CH_4 molecules in solution preventing the formation of a separate phase. Finally, we observe that, the mixture CH_4-CO_2 has remarkably different bubble-point and dew-point lines as function of the molar ratio between CH_4 and CO_2[see: *Austegard et al.*, 2006; *Donelly and Katz*, 1954; *Mraw et al.*, 1978]. As a result, gaseous CO_2 and CH_4 will coexist in equilibrium with liquid CO_2 and CH_4 in a fairly large pressure interval.

3) Water vapor concentration in gaseous phase (Table 5.3-b): Water evaporates into gaseous atmospheres. For example, 0.016 kg of H_2O can be found per cubic meter of CO_2 gas at 3MPa-273K (0.011 mol H_2O / kg of CO_2) [*Spycher et al.*, 2003], and 0.005 kg of H_2O can be found per cubic meter of CH_4 gas at 3MPa-273K (0.012 mol H_2O / kg of CH_4) [*Folas et al.*, 2007]. We have consistently observed in separate experimental systems that water vapor in either CO_2 or CH_4 atmospheres can crystallize on hydrate surfaces promoting hydrate growth in relatively short time scale (days).

4) Mutual diffusivities (Table 5.4): Diffusion controls most long-term phenomena, including hydrate formation and CH_4-CO_2 replacement [*Davies et al.*, 2008; *Svandal et al.*, 2006]. The diffusivities of CO_2 and CH_4 in water are about the same, however, the diffusivity of H_2O in liquid CO_2 is up to two orders of magnitude higher [*Espinoza and Santamarina*, 2010b]. High water diffusivity and solubility in liquid CO_2 make liquid and supercritical CO_2 an effective water-drying fluid agent.

Table 5.3. Mutual solubilities in binary mixtures. (a) Liquid medium. (b) Gaseous medium.

Rich phase medium		Solute	**Concentration** [mol/kg]		
			3MPa, 273K	6.6MPa, 274K	10MPa, 285K
(a) Liquid	H_2O (without hydrate)	CH_4	0.11*	0.12*	0.13*
		CO_2	1.39* [~0.025 mol/mol]	1.66* [~0.030 mol/mol]	1.72
	H_2O (with hydrate)	CH_4	0.060	0.063	0.116
		CO_2	0.89 [0.016 mol/mol]	0.83 [0.015 mol/mol]	Outside HSZ
	CO_2	H_2O	Does not apply (Gas CO_2)	0.050 † [2.2×10^{-3} mol/mol]	0.056 [2.5×10^{-3} mol/mol]
		CH_4	Does not apply (Gas CO_2)	Bubble point for 12% molar CH_4/CO_2 mixture	Supercritical mixture
(b) Gas	CH_4	H_2O	0.016 [~2.5×10^{-4} mol/mol]	0.008 [1.34×10^{-4} mol/mol]	0.012 [2.0×10^{-4} mol/mol]
	CO_2	H_2O	0.011 [~5×10^{-4} mol/mol]	Does not apply (Liquid CO_2)	Does not apply (Liquid CO_2)
	CO_2	CH_4	Gas mixture	Does not apply (Liquid CO_2)	Does not apply (Liquid CO_2)

Sources: [*Donelly and Katz*, 1954; *Duan and Sun*, 2003b; *Folas et al.*, 2007; *Hashemi et al.*, 2006; *Spycher et al.*, 2003; *Sun and Duan*, 2007].
Notes: *These values are extrapolations of solubility without hydrate to lower temperatures. †Value for 285K.

The diffusivity of CO_2, CH_4 or H_2O molecules through the solid hydrate mass is much slower than through liquids (Note: preferential diffusive transport is expected along crystal imperfections and along the adsorbed water layer between hydrate and minerals). Therefore, CO_2 or CH_4 transport through solid hydrate will be much slower than through water. If the CH_4-CO_2 replacement is limited by diffusive transport, laboratory experiments and field implementations must seek to increase the surface contact area.

Table 5.4. Mutual diffusivities in binary water-CO_2 and water-CH_4 systems.

Rich phase medium		Diffusing substance	Diffusivity [m^2/s]	Pressure [MPa]	Temperature [K]	Method	Reference
Liquid	H_2O	CO_2	1.37×10^{-9} -to- 1.64×10^{-9}	0.1	291.5-to-298	Experimental	[*Thomas and Adams*, 1965a]
		CH_4	0.85×10^{-9} -to- 1.49×10^{-9}	0.1	277-to-293	Experimental	[*Witherspoon*, 1969]
	CO_2	H_2O	6×10^{-8} -to- 18×10^{-8}	7-15	298	Experimental	[*Espinoza and Santamarina*, 2010b]
Solid	H_2O (I)	CO_2	0.9×10^{-10}	No data	270	Molecular Dynamics	[*Ikeda-Fukazawa et al.*, 2004]
		CH_4	1.0×10^{-10}	No Data	270		
	CH_4 (H)	CH_4	3.4×10^{-13} -to- 7.6×10^{-13}	3-15	263-to-268	Experimental	[*Davies et al.*, 2008]
	CO_2 (H)	CO_2	1.0×10^{-12}	No Data	273	Molecular dynamics	[*Demurov et al.*, 2002]
		H_2O	1.0×10^{-23}	No data	200		

Note: (I) ice and (H) hydrate.

5.3 Previous studies – Rates of reaction

Previous CH_4-CO_2 replacement studies documented in the literature are summarized in Table 5.5 and P-T conditions are plotted on Fig. 5.2. As noted in Table 5.5, we describe the time dependent replacement of CH_4 by CO_2 using the replacement ratio in the hydrate: $CO_2/(CH_4+CO_2)=A(1-e^{-t/\alpha})$, with *A* being the maximum replacement ratio at long times, *t*. We obtain both *A* and the characteristic time, α, by fitting the published reaction-time data. The following preliminary observations can be made from these studies: (1) hydrate replacement rates increase near the CH_4 hydrate phase boundary (data in [*Ota et al.*, 2005a], also mentioned in [*McGrail et al.*, 2007]), (2) the reaction rate increases with increasing CO_2 gas pressure, eventually becoming constant

when CO_2 liquefies [data in *Ota et al.*, 2007]. We can also anticipate that high specific surface CH_4 hydrate experiences relatively fast replacement rates (refer to Kim et al. [1987]). There is some supportive evidence in the listed studies, but they are not conclusive due to lack of experimental details.

5.4 New pore scale experimental studies

Multiple coexisting processes take place during CH_4-CO_2 replacement, including heat release, dissolution of participating species into different phases, volume change and mass transport. The following two experimental studies document these pore-scale processes. Fig. 5.3 shows the experimental devices and P-T trajectories. Both experiments are monitored using time-lapse photography. We use digital image processing to estimate length and volume information (resolution: 1pixel~10μm), and we infer mass changes from measured volumes and the known density of the phases.

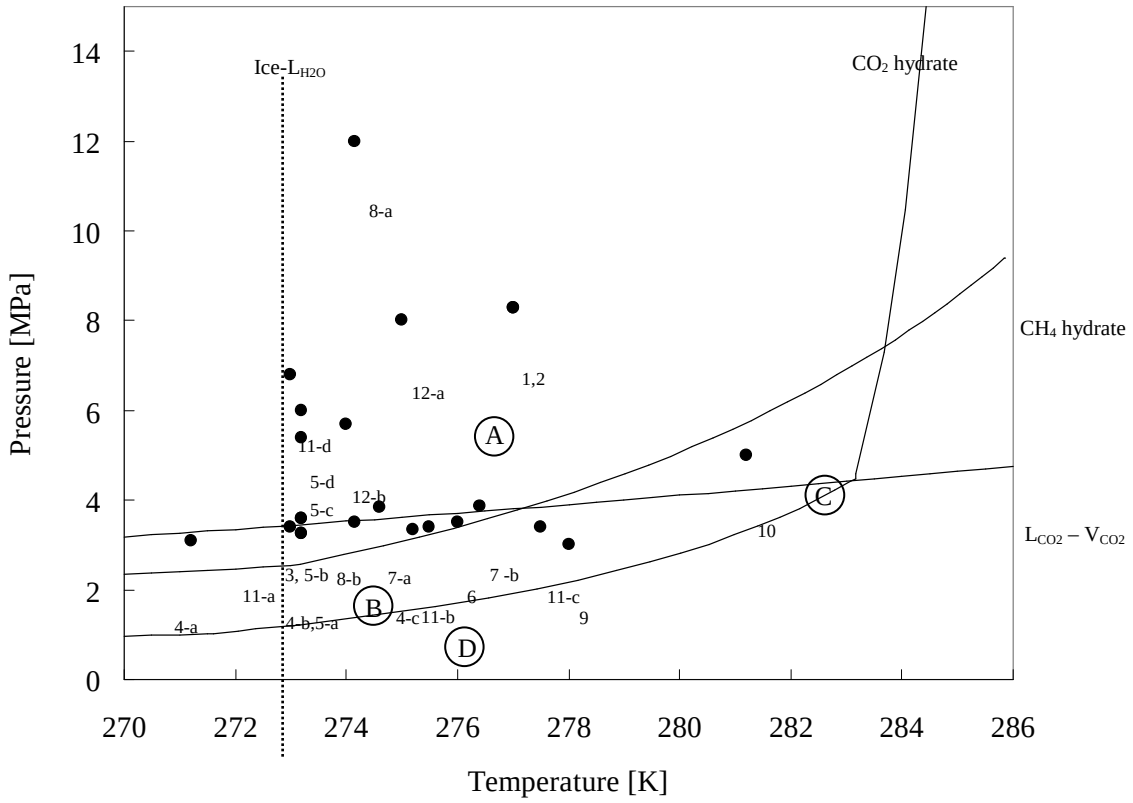

Figure 5.2. Dissociation phase boundaries for CO_2 and CH_4 hydrates, liquid-vapor phase boundary for pure CO_2, and liquid water-ice boundary. Data points show fluid pressure and temperature conditions for CH_4-CO_2 replacement studies reported in the literature (numbers correspond to references listed in Table 5.5). Notice that CO_2 and CH_4 hydrate phase boundaries cross at ~7.5MPa and 283.7K. Furthermore, the CO_2 liquid-vapor boundary intersects the two dissociation lines creating four different zones inside the CO_2 hydrate stability field, above the liquid water-ice boundary.

Table 5.5. Previous CH_4-CO_2 replacement studies. Note: cases are plotted in Fig. 5.2 using the same Test # listed here.

Test #	P [MPa]	T [K]	CH_4 hydrate formation method	Medium	Duration [hour]	Replacement ratio* [A]	Characteristic time* α [hour]	Monitoring	Reference
1	8.3	277	-	Sandstone	300	0.64	128	MRI	[*Husebo et al.*, 2008]
2	8.3	277		Sandstone	350	-	-	MRI	[*Stevens et al.*, 2008]
3	3.6	273.2	Stirring	No sediment	300	0.34	85	Raman spectroscopy	[*Ota et al.*, 2005b]
4-a	3.10	271.2	Stirring	No sediment	150	0.16	48	Raman spectroscopy	[*Ota et al.*, 2005a]
4-b	3.26	273.2			150	0.16	42		
4-c	3.34	275.2			150	0.21	39		
5-a	3.26	273.2	Stirring	No sediment	300	0.26	98	Raman spectroscopy	[*Ota et al.*, 2007]
5-b	3.6	273.2			300	0.34	94		
5-c	5.4	273.2			300	0.17	94 (1)		
5-d	6.0	273.2			300	0.31	94 (1)		
6	3.5	276	Powder ice: 100 μm	No sediment	12	0.92	1.0	Raman spectroscopy	[*Komai et al.*, 2000]
7-a	3.85	274.6	Stirring	No sediment	800	0.55	222	Water and gas produced	[*Hirohama et al.*, 1996]
7-b	3.88	276.4			800	0.64	329		
8-a	12.0	274.15	Powder ice: 5-50 μm	No sediment	30	0.92	4.2	NMR	[*Park et al.*, 2006]
8-b	3.5	274.15			30	0.85	5.2	NMR	
9	3.0	278	Powder ice: 100-250 μm	No sediment	150	1.00	22	Raman spectroscopy	[*Yoon et al.*, 2004]
10	5.0	281.2	-	Quartz sand	100	0.19	33 (L-CO_2)	Gas produced	[*Zhou et al.*, 2008a] (2)
						0.27	31 (90% emulsion)		
						0.26	29 (70% emulsion)		
						0.24	26 (30% emulsion)		
11-a	3.4	273	Stirring	No sediment	11	No data	No data	Raman spectroscopy	[*McGrail et al.*, 2007]
11-b	3.4	275.5			11				
11-c	3.4	277.5			11				
11-d	6.8	300-273	-	Sand	1.7				
12-a	8.0	275.0	-	No sediment	-	No data	No data	Time-lapse photography	This study
12-b	5.7	274.0			-	No data	No data		

*Note: replacement ratio=$A(1\text{-}e^{-\alpha t})$, A= final replacement ratio, α= replacement rate. (1) Limited data available. (2) Ill-defined test

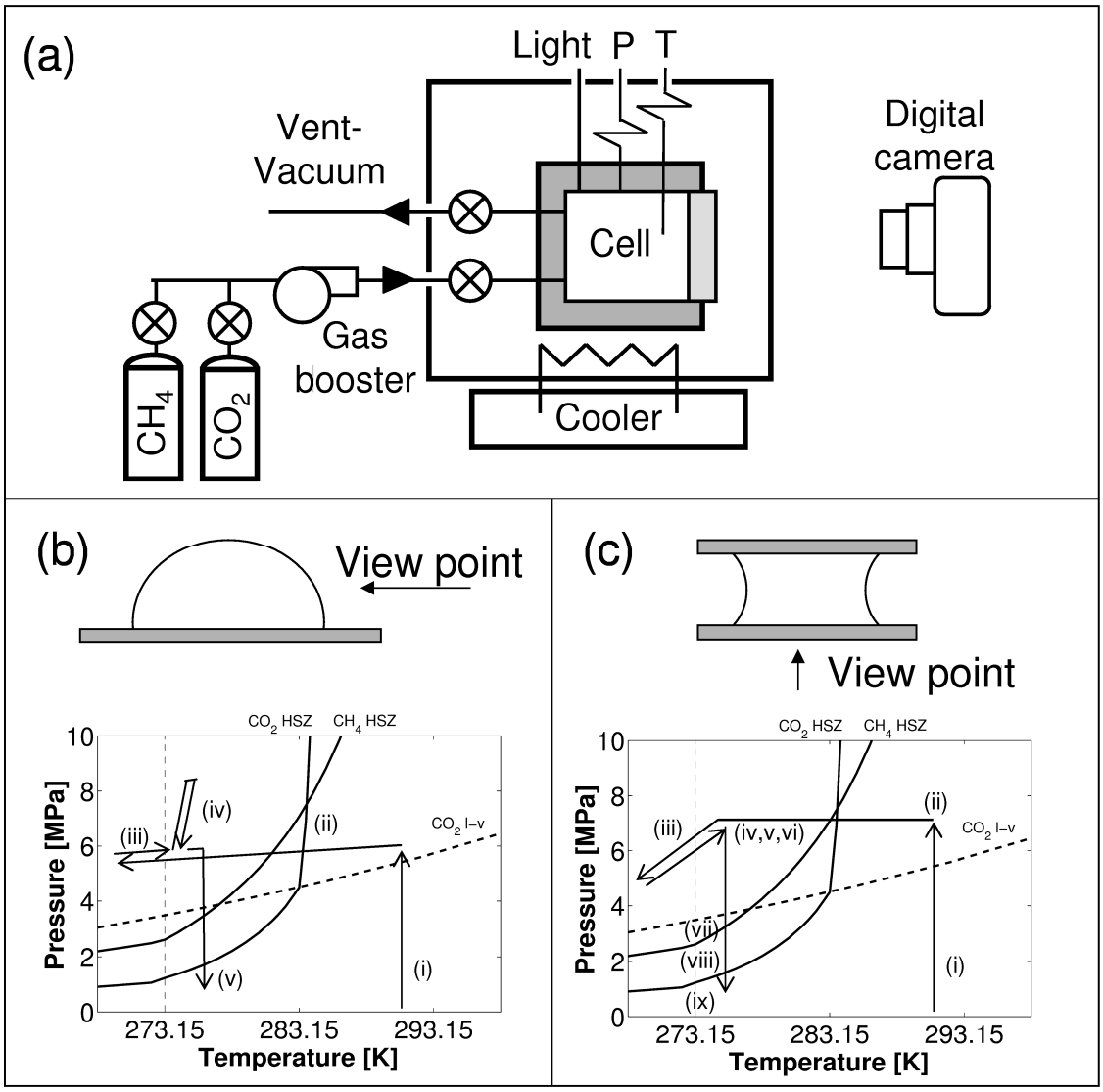

Figure 5.3. Experimental studies. (a) Pressure cell and devices. (b) Droplet experiments: i- CH_4 pressurization, ii- cooling, iii- CH_4 hydrate formation, iv- liquid CO_2 injection, v- CH_4-CO_2 hydrate dissociation. (c) Meniscus experiments: i- CH_4 pressurization, ii- cooling and ice formation, iii- ice formation, iv- ice melting, v- CH_4 hydrate formation, vi- injection of liquid CO_2, vii- liquid CO_2 to gas, viii- exit CH_4 hydrate stability field, and ix- exit CO_2 hydrate stability field. Both experiments are conducted using de-ionized water and research purity gases.

5.4.1 Water droplet

A water droplet (initial mass 36.1mg) rests on a hydrophobic PTFE substrate and forms a quasi-semispherical body (~2.5mm radius). Air is evacuated from the chamber by imposing a partial vacuum, followed by CH_4 pressurization (P=5.9MPa, T=293K, Fig 5.3-b) and subsequent cooling. Some water evaporates into the methane atmosphere; we predict a ~1.2mg water mass loss from the droplet (based on solubility information in Table 5.3-b). Given a water density of ~1000 kg/m^3 (Table 5.1-c), this agrees with the volume reduction we measured after 5 days (±0.1mg precision). The first hydrate formation event follows transient ice formation. Later, we dissociate this CH_4 hydrate by heating (not shown in Fig. 5.3-b), and we cool the sample back into the CH_4 hydrate stability field. CH_4 hydrate nucleates again in the form of a hydrate film that grows at the water-gas interface and propagates along the interface at a velocity of ~0.02mm/s, forming a complete hydrate shell in less than 5 minutes (data shown in the auxiliary material). For this growth velocity, heat transfer models predict a hydrate film thickness greater than 40μm [*Mochizuki and Mori*, 2006]. We estimate the initial film thickness is equal to ~60 μm based on the droplet volume expansion $V_{final}/V_{initial}$=1.016 and the theoretical volume change from water to hydrate V_{hyd}/V_w=1.234 (Table 5.1). Stable P-T conditions are maintained for ~2 days; during this period, further hydrate growth is controlled by CH_4 diffusion through the hydrate layer (Fig. 5.4-a). The shell remains stable (Note: shell depressions were observed in hydrate-coated droplet experiments by Servio and Englezos [2003]).

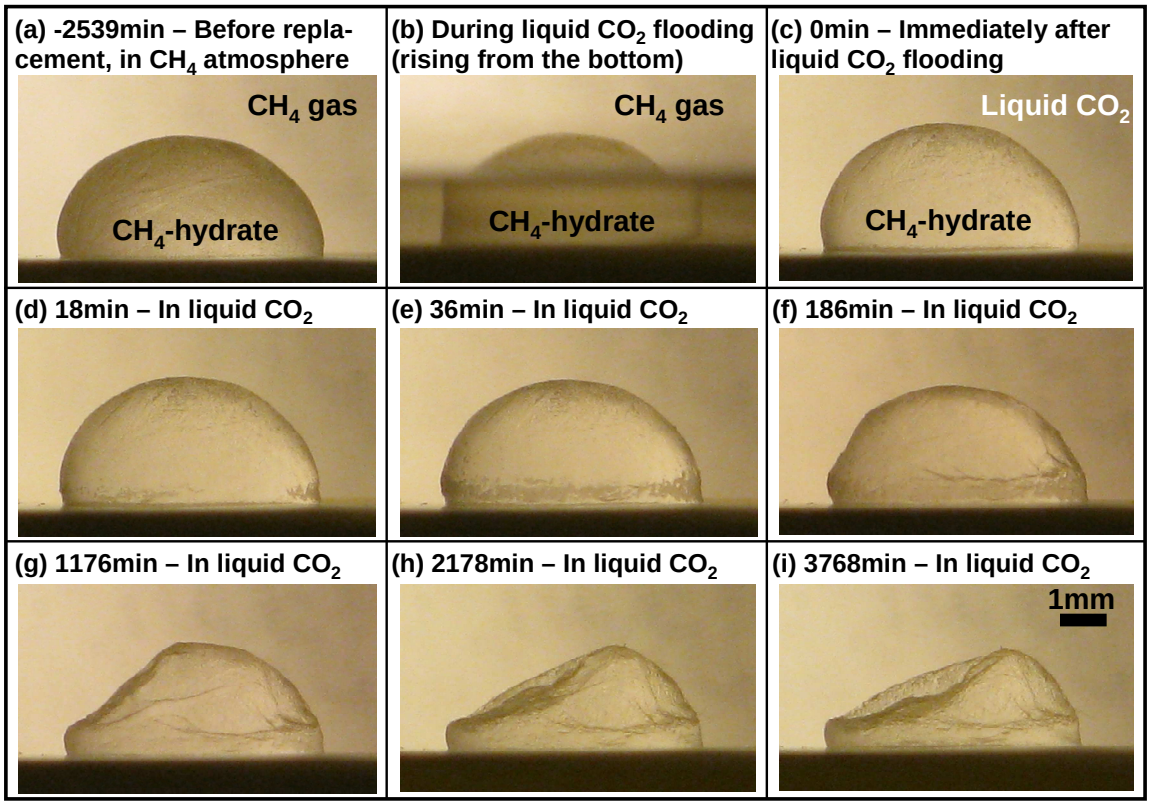

Figure 5.4. Droplet experiment: time evolution of the CH_4 hydrate shell after flooding with liquid CO_2. Pressure is 6MPa and the chamber temperature stays at 274±1K, after point (iv) in Fig. 5.3-b. This sequence of images suggests that liquid CO_2 "dries" the water either in the hydrate shell and/or inside the hydrate droplet.

We flood the chamber with liquid CO_2, displacing CH_4 gas through a vent (Fig. 5.4-b); the pressure and temperature conditions are inside the CH_4 hydrate stability field (P=7±1MPa, T=275±1.5K during the short injection period). The amount of water needed to saturate the liquid CO_2 in the absence of any hydrate in the chamber is ~45mg (based on solubility data in Table 5.3-a). We measure ~15mg of water migration from the droplet to the surrounding liquid CO_2 in a period of 2 days; this is a form of "drying" in a CO_2 atmosphere (Fig. 5.4). Thereafter, the droplet size remains constant for ~4 days under stable P-T conditions (P=6MPa, T=274±1K; Fig. 5.4-i). These measurements

suggest a lower solubility of water in CO_2 in the presence of hydrate than the value reported in the absence of hydrate (similarly to gas solubility in water, Table 5.3-a). While we assume replacement is taking place, no CH_4 gas bubbles form in the liquid CO_2 due to the high solubility of CH_4 in CO_2 (Table 5.3-a). We depressurize the chamber gradually. The hydrate shell remains stable after CO_2 vaporizes and also across the CH_4 hydrate phase boundary. We hold stable P-T conditions above the CO_2 hydrate boundary for ~30min. Finally, we depressurize the chamber further and hydrate dissociates across the CO_2 hydrate phase boundary at ~1.8MPa and 276.5K.

5.4.2 Water meniscus

In this second study, the water droplet rests between two water-wet hydrophilic transparent glass surfaces, creating a cylindrically-shaped body of water similar to a water meniscus between two grains (8.7mm diameter, 1.97mm in height; and 120mg water mass). Fig. 5.3-c shows the P-T trajectory imposed during the test. The evolution of the droplet is observed through the lower plate (Fig. 5.5-a). We trigger nucleation by causing transient ice formation (Fig. 5.5-b). Methane hydrate starts forming at the interface (similar observation in [*Stern et al.*, 1998]). Hydrate does not grow homogeneously but advances in the form of lobes that invade the water meniscus (Fig. 5.5-c,d – Note: needle-type growth is observed in the results reported by [*Subramanian and Sloan*, 2002]. Volume expansion during hydrate growth (V_{hyd}/V_w=1.234 - Table 5.1) causes water to flow out of the meniscus along the hydrophilic glass surfaces, readily forming a thin hydrate layer on the glass plates (Fig. 5.5-c,d,e). The hydrate growth rate inside the meniscus is between 0.05mm/hour and 0.11mm/hour. This fast growth rate

suggests that gas reaches the water through cracks in the hydrate shell rather than by diffusion through the hydrate layer.

The injection of liquid CO_2 is expected to trigger CH_4-CO_2 replacement and water dissolution into the liquid CO_2 (the amount of water needed to saturate the liquid CO_2 in this chamber is 171mg, Table 5.3-a). Hence, the CO_2 hydrate film observed coating the glass plates in Fig. 5.5-f appears to be thinner (i.e., more transparent) than the CH_4 hydrate film in Fig. 5.5-d-e. Once again, CH_4 gas bubbles are not observed. The lobular hydrate structure remains inside the meniscus, that is, the overall geometry of the solid hydrate mass is preserved. Depressurization from liquid CO_2 to gaseous CO_2 causes the water dissolved in liquid CO_2 to precipitate as CO_2 hydrate on the glass plate (Fig. 5.5-g). Depressurization out of the CH_4 phase-boundary has no "observable" effect on the hydrate phase within the meniscus or coating the glass surfaces (Fig. 5.5-h). Finally, hydrate dissociates during depressurization below the CO_2 hydrate phase boundary.

5.4.3 Summary

These two experiments reveal marked differences in CH_4 hydrate formation behavior on hydrophilic and hydrophobic substrates, and show the significance of mutual solubilities during CH_4-CO_2 replacement. There is no visual evidence of CH_4-CO_2 replacement when the CH_4 atmosphere is changed for CO_2 gas or liquid, i.e., there is no bubbling, volume change or alterations in the solid phase. The final depressurization stage confirms the presence of CO_2 hydrate at the CO_2 hydrate dissociation boundary.

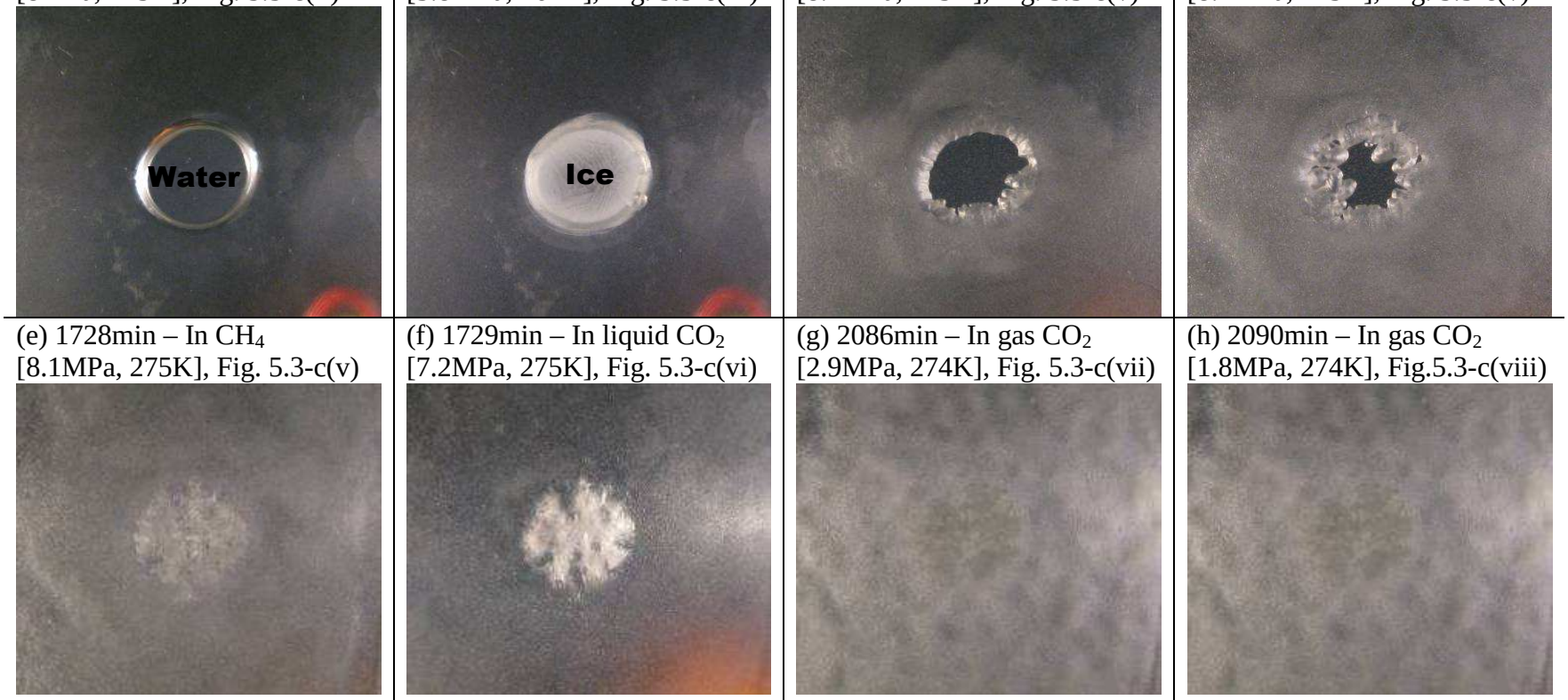

Figure 5.5. Meniscus experiment. (a) Water droplet – Scale: 8.7mm diameter, (b) Ice formation, (c)-(e) CH_4 hydrate formation and growth, (f) Injection of liquid CO_2, (g) Depressurization from liquid CO_2 to gas CO_2, (h) Image for P-T conditions outside the CH_4 hydrate stability field.

5.5 Analysis – Sediment scale implications

Analyses and experimental results presented in previous sections allow us to anticipate potential thermo-hydro-mechanical coupled processes during CH_4-CO_2 replacement in hydrate bearing sediments.

5.5.1 Molecular scale CH_4-CO_2 replacement process

Molecular scale observations (Section 5.2), diffusion rates (Table 5.1 and 5.4), and experimental results (Table 5.5) point to a "local" solid-liquid-solid transition during CH_4-CO_2 replacement. Inside the stability field, CH_4 hydrate in equilibrium is constantly forming and breaking down at the interface, releasing and capturing CH_4 molecules [See molecular dynamics insight in *Baez and Clancy*, 1994; *Baez and Clancy*, 1995; *Walsh et al.*, 2009]. In a CO_2-rich medium, freed CH_4 molecules may be replaced by CO_2 molecules, forming CO_2 hydrate and releasing excess heat [William F. Waite, personal communication]. This released heat causes a positive feedback by locally raising the temperature of neighboring hydrate cages towards the CH_4 hydrate phase boundary to facilitate the atomic-scale solid-liquid-solid CH_4-CO_2 replacement in a form of "chain-reaction".

This hypothetical replacement process allows us to identify two end-member replacement scenarios. First, constant hydrate break down and formation make CH_4-CO_2 replacement possible within the CH_4 hydrate stability field (zone A in Fig. 5.2); in this case, reaction rates will be strongly dependent on the contact area between CO_2 and CH_4 hydrate. Second, excess heat liberated in the CH_4-CO_2 replacement transformation may

sustain a high solid-liquid-solid reaction rate; in this case we anticipate a lower reaction rate as P-T conditions are further inside the CH_4 hydrate stability field.

5.5.2 Bound for excess heat-assisted reaction within the CH_4 stability field

The second end-member is analyzed next, taking into consideration all the phases involved. We assume that local P-T conditions reach the CH_4 hydrate dissociation boundary driven by the excess heat liberated in the total reaction (Section 5.2, Table 5.1). How far inside the stability field can the hydrate bearing sediment be to experience this excess heat-assisted reaction?

Consider CH_4 hydrate at initial pressure P_o, temperature T_o and surrounded by CO_2 (liquid in zones A and C; and gas in zone B, Fig. 5.2), water and the mineral structure of the host sediment. Let's also assume that all hydrate cages undergo gas replacement so that the liberated heat is proportional to the difference between the heat of dissociation of CH_4 hydrate, H^d_{CH4hyd}[kJ/kg], and the heat of formation of CO_2 hydrate, H^f_{CO2hyd} [kJ/kg]. We consider isobaric conditions and 100% replacement to calculate the increase in temperature ΔT from the in situ condition T_0 to the temperature T_b on the CH_4 hydrate stability boundary corresponding to pressure P_0,

$$\begin{aligned}&\left(M_{CO_2}c_{CO_2}+M_{CH_4hyd}c_{CH_4hyd}+M_w c_w+M_m c_m\right)T_o=\\&\left(M_{CH_4}c_{CH_4}+M_{CO_2hyd}c_{CO_2hyd}+M_w c_w+M_m c_m\right)T_b-\left(H^f_{CO_2hyd}M_{CO_2hyd}-H^d_{CH_4hyd}M_{CH_4hyd}\right)\end{aligned} \quad (5.1)$$

where subscripts for specific heat c and mass M, are m for mineral and w for water. In this analysis, we do not consider changes in P-T phase boundary conditions for gas mixtures (refer to Section 5.2e-1). All masses M convert to volume V through the corresponding bulk densities ρ, and partial volumes are related to the total sediment

volume V_T through the sediment porosity ϕ, and the volumetric fractions of hydrate S_{hyd}, water S_w, and gas S_g (CH_4 gas or CO_2 gas/liquid) in the pore space,

$$V_{hyd} = S_{hyd}\phi V_T, \quad V_w = S_w\phi V_T, \quad V_g = S_g\phi V_T, \quad V_m = (1-\phi)V_T \tag{5.2}$$

where $S_{hyd}+S_w+S_g=1$. A simple close-form analytical expression is obtained assuming that the heat stored in CO_2 and CH_4, and hydrates is similar before and after replacement $\rho_{CO2}S_{CO2}\phi c_{CO2} + \rho_{CH4hyd}S_{hyd}\phi c_{CH4hyd} \approx \rho_{CH4}S_{CH4}\phi c_{CH4} + \rho_{CO2hyd}S_{hyd}\phi c_{CO2hyd}$. Then, the CH_4-CO_2 replacement rate within the sediment will be maximized if the initial temperature of the reservoir is equal or greater than,

$$T_o = T_b(P_0) - \frac{\left(H^f_{CO_2hyd}\rho_{CO2hyd} - H^d_{CH_4hyd}\rho_{CH4hyd}\right) S_{hyd}\phi}{\rho_{CO_2}S_{CO_2}\phi\, c_{CO_2} + \rho_w S_w\phi\, c_w + \rho_{CH_4hyd}S_{hyd}\phi\, c_{CH_4hyd} + (1-\phi)\rho_m c_m} \tag{5.3}$$

Numerical results are presented in Fig. 5.6 for a CH_4 hydrate volume fraction S_{hyd}=0.5. This equation is a lower bound for the excess heat-assisted CH_4-CO_2 replacement, since we assume that the liberated heat warms up the whole sediment mixture. The upper bound corresponds to the CH_4-CO_2 replacement for pure hydrate (line on the upper left corner in Fig. 5.6). Local heating during replacement is between these two bounds.

5.5.3 Hydrate dissolution in liquid CO_2

Liquid CO_2 will draw water and methane from the CH_4 hydrate until it reaches the solubility limit of water in CO_2 y_{CO2}^{H2O} (Section 5.2e-2). The change in hydrate saturation in the sediment ΔS_{hyd} due to hydrate dissolution in liquid CO_2 is,

$$\Delta S_{hyd} = (1-S_{hyd})\left(\frac{1}{y_{CO2}^{H2O}}\frac{\rho_{CH4hyd}}{\rho_{CO2}}\frac{n\cdot m_{H2O}}{m_{CH4}+n\cdot m_{H2O}}\frac{m_{CO2}}{m_{H2O}}+1\right)^{-1} \tag{5.4}$$

where the *m* represents molar mass, *n* the stoichiometric ratio, and ρ_{CH4hyd} and ρ_{CO2} are the mass densities of CH_4 hydrate and liquid CO_2 at the prevailing P-T conditions. A change in hydrate saturation of ΔS_{hyd}~0.001 is estimated for reservoir conditions S_{hyd}<0.3, P=5-to-8MPa, and T=273-to-278K. While this is a small number, continuous flow of pure liquid CO_2, can cause significant hydrate dissolution, for instance near the CO_2 injection well.

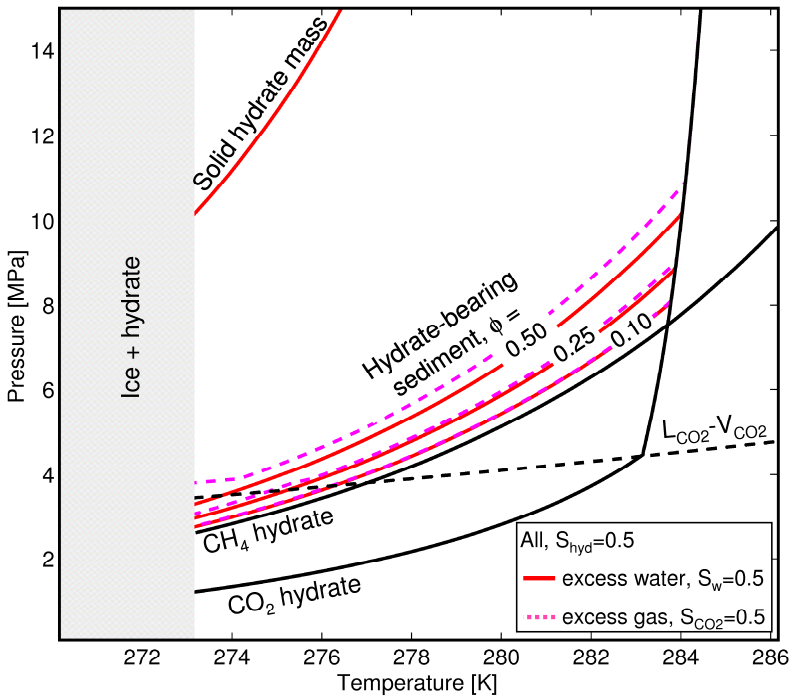

Figure 5.6. Pressure-temperature upper and lower bounds for initiating excess heat CH_4-CO_2 hydrate replacement by raising the local temperature to the CH_4 hydrate dissociation boundary. The temperature increases due to the heat released after CH_4 hydrate dissociation and CO_2 hydrate formation. Upper bound: the reaction can begin far inside the CH_4 hydrate stability zone for a solid hydrate mass (upper bound ~10K from the CH_4 hydrate dissociation boundary). Lower bound: the reaction must begin closer to the CH_4 hydrate phase boundary in hydrate bearing sediments where minerals and water absorb liberated heat. Bounds are computed using Equation 5.3 and parameters from Table 5.1, porosity ϕ=0.5, 0.25, 0.10; c_m=0.83 kJ/(kg·K); H^f_{CO2hyd} =395kJ/kg; H^d_{CH4hyd} =440kJ/kg, ρ_{CO2hyd}=1100 kg/m^3, and ρ_{CH4hyd}=930 kg/m^3. Note: this analysis does not consider intermediate hydrate phase boundaries for hydrate grown from gas mixtures (Section 5.2e-1).

5.5.4 Methane gas bubble formation

CH_4-CO_2 replacement releases CH_4 into the pore space. The critical CH_4 hydrate saturation S^*_{hyd} required to cause CH_4 bubble formation depends on the bubble point molar ratio R_{BP} for the CH_4-CO_2 fluid mixture at the specific P-T conditions. The value of S^*_{hyd} can be estimated as

$$S^*_{hyd} = (1 - S_w)\left(\frac{1}{R_{BP}} \frac{\rho_{CH4hyd}}{\rho_{CO2}} \frac{m_{CH4}}{m_{CH4} + n \cdot m_{H2O}} \frac{m_{CO2}}{m_{CH4}} + \frac{\rho_{CO2hyd}}{\rho_{CO2}} \frac{m_{CO2}}{m_{CO2} + n \cdot m_{H2O}} + 1 \right)^{-1} \quad (5.5)$$

For reservoir conditions P=7.25MPa and T=278.15K, the bubble point is R_{BP}=0.12 [*Donelly and Katz*, 1954], and the critical hydrate saturation for gas bubble formation is S^*_{hyd} ~0.21 (See Fig. 5.7-b).

5.5.5 Fluid volume expansion during CH_4-CO_2 replacement

Above bubbling conditions CH_4-CO_2 replacement involves either volume change at constant fluid pressure, or pressure change under isochoric conditions. Let's compute first the change in volume during hydrate formation as a function of the hydration number n, mass densities ρ, and molar masses m

$$\frac{V_{hyd}}{V_w} = \frac{m_{hyd} / \rho_{hyd}}{m_w / \rho_w} = \frac{m_g + n \cdot m_w}{n \cdot m_w} \cdot \frac{\rho_w}{\rho_{hyd}} \quad (5.6)$$

where the density of water is ρ_w=1000kg/m^3, and molar masses are m_w=18g/mol, m_{CH4}=16g/mol and m_{CO2}=44g/mol. As shown in Fig. 5.7-a, an initial volume of water expands by V_{hyd}/V_w=1.234 to form CH_4 hydrate (n=6, ρ_{CH4hyd}=930kg/m^3), and V_{hyd}/V_w=1.279 to form CO_2 hydrate (n=6, ρ_{CO2hyd}=1110kg/m^3).

The volume change of the hydrate mass during CH_4-CO_2 replacement can be analyzed following a similar formulation and using experimentally measured macroscale quantities n and ρ (Note: ρ is a function of n). Let's assume all CH_4 in hydrate exchanges with the injected liquid CO_2. The change in hydrate volume is:

$$\frac{V_{CO2hyd}}{V_{CH4hyd}} = \frac{44+18\cdot n_{CO2}}{16+18\cdot n_{CH4}} \cdot \frac{\rho_{CH4hyd}}{\rho_{CO2hyd}} \tag{5.7}$$

The volume occupied by the hydrate mass expands about 1-to-6% after CH_4-CO_2 hydrate replacement (n_{CH4}=6, n_{CO2}=6, and pressure-dependent mass densities ρ_{CH4hyd}=910-940kg/m^3, ρ_{CO2hyd}=1090-1110kg/m^3). The change in lattice size ~2.9% is in agreement with this macroscale analysis (refer to values in Table 5.1).

On the other hand, released CH_4 gas after replacement occupies a volume that is strongly dependent on pressure and initial hydrate saturation. The final volume occupied by the released methane V_g^{CH4} which did not dissolve into the liquid CO_2, relative to the volume occupied by the CO_2 that became trapped in hydrate V_l^{CO2} is,

$$\frac{V_g^{CH_4}}{V_l^{CO_2}} = \frac{\left[\frac{\rho_{CH4hyd}}{m_{CH4}}\frac{S_{hyd}\cdot m_{CH4}}{m_{CH4}+n\cdot m_{H2O}} - \frac{R_{BP}}{m_{CO2}}\left(\left(1-S_{hyd}\right)\rho_{CO2} - \frac{\rho_{CO2hyd}\cdot S_{hyd}\cdot m_{CO2}}{m_{CO2}+n\cdot m_{H2O}}\right)\right]\frac{m_{CH4}}{\rho_{CH4}}}{S_{hyd}\frac{\rho_{CO2hyd}}{\rho_{CO2}}\frac{m_{CO2}}{m_{CO2}+n\cdot m_{H2O}}} \tag{5.8}$$

There is a very pronounced increase in pore fluid volume associated with CH_4-CO_2 replacement at constant pressure. The volumetric ratio V_g^{CH4}/V_l^{CO2} is plotted in Fig. 5.7-b as a function of S_{hyd} for reservoir conditions P=7.25MPa, T=278.15K, R_{BP}=0.12 [*Donelly and Katz*, 1954]; for example V_g^{CH4}/V_l^{CO2}~390% for S_{hyd}=50%. Conversely, a marked increase in fluid pressure and decrease in effective stress will take place if constant volume is imposed during CH_4-CO_2 replacement. Field conditions will be between these

two extreme scenarios. If replacement conditions result in a CH_4/CO_2 mixture, the volume of the mixture fluid can be computed using cubic equations of state [*Li and Yan*, 2009].

(a)

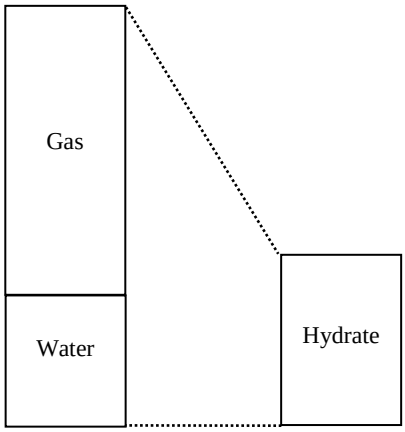

$$\frac{V_{CH_4\ hydrate}}{V_{water}} = 1.234$$

$$\frac{V_{CO_2\ hydrate}}{V_{water}} = 1.279$$

(b)

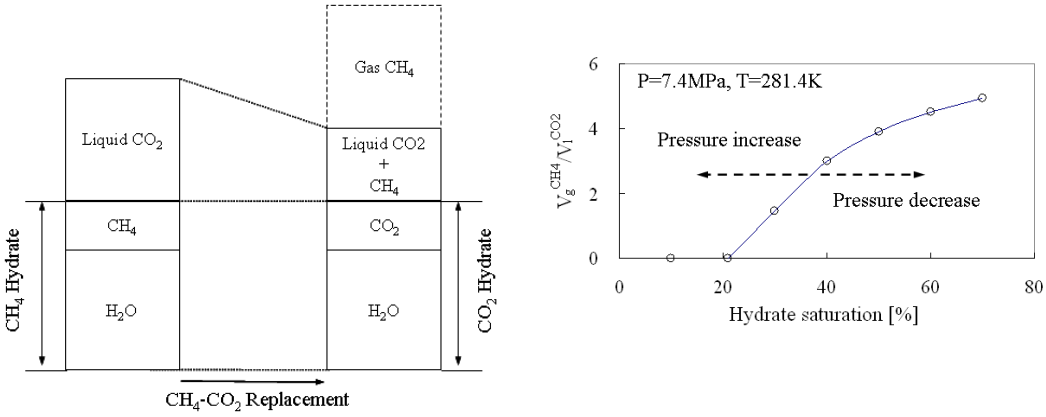

Figure 5.7. Volume change analysis. (a) During hydrate formation/dissociation, i.e. Eq. 5.7 (b) During CH_4-CO_2 replacement, i.e. Eq. 5.8 (P=7.4MPa, T=281.4K, ρ_{CO2}=906kg/m^3, bubble point for CH_4/CO_2 mixture R_{BP}= 12% mol CH_4 / mol CO_2).

5.5.6 Sediment volume change during CH_4-CO_2 replacement

A soil subjected to an increase in effective stress $\Delta\sigma$` from an initial effective stress $\sigma_o$` to a final stress σ_o`+$\Delta\sigma$` experiences a volumetric strain $\varepsilon_{vol}=C_c^*\log[(\sigma_o`+\Delta\sigma`)/\sigma_o`]$ that is proportional to the compression index C_c^*. The presence of hydrates stiffens the soil skeleton so that lower values of the compression index are expected for hydrate bearing sediments than for the same sediment without hydrates [*Lee et al.*, 2010]. The stiffening effect of hydrate depends on the pore habit: pore-filling (smallest effect), load-bearing and cementing (largest effect) [*Waite et al.*, 2009]. While CH_4-CO_2 replacement involves transient "local" dissociation, preliminary experimental evidence we have gathered using cementing CH_4 hydrate-bearing sands with hydrate saturation S_{hyd}=5-to-10% shows no significant change in global stiffness when wave propagation velocity data are gathered during CH_4-CO_2 gas replacement. Thus, low volumetric strains should be expected during CH_4-CO_2 replacement under free-draining flow conditions. Fluid volume change may affect sediment stability if free-draining conditions are lost during replacement. The following sequence of events may take place [*Santamarina and Jang*, 2009]: fluid volume expansion during the CH_4-CO_2 replacement causes an increase in fluid pressure, a decrease in effective stress, and a loss in sediment strength leading to shear failure, gas driven fractures, and/or collapse of the sediment skeleton.

5.5.7. Mixed fluid flow

CO_2 is considerably less viscous than water, and CO_2 will tend to produce viscous fingering in excess-water reservoirs. Some recent numerical simulations show finger-like

patterns when CO_2 invades water-saturated formations [*Kang et al.*, 2005; *Qi et al.*, 2009], while other simulations show minimal CO_2 fingering [*Chang et al.*, 1994]. The analysis of pore scale capillary and viscous forces suggests higher tendency to viscous fingering in the near field of the injection well where flow velocities are high [*Lenormand et al.*, 1988].

5.5.8 Anticipated sediment-scale emergent phenomena

Four different injection scenarios are identified in Table 5.6 in terms of P-T conditions that control either liquid CO_2 or gas CO_2 injection (zones A and B in Fig. 5.2), and either excess-water (gas-limited) or excess-gas (water limited) hydrate-bearing sediments. Phenomena and properties listed above help us identify the following processes that may take place during injection:

- The release of CH_4 above the bubble point leads to gas formation $S_g>0$ and lowers the relative permeability of the liquid phase [van Genutchen's equation as in *Kleinberg et al.*, 2003].
- A low velocity of the invading CO_2 front, compared to the rate of CO_2 hydrate formation, will promote the growth of new CO_2 hydrate in excess-water reservoirs, occlude regions with CH_4 hydrate, prevent the direct contact of CH_4 hydrate with CO_2, and hinder CH_4-CO_2 replacement (see numerical simulation of CO_2 hydrate clogging in [*Kang et al.*, 2005]).
- The replacement rate in both excess-gas and excess-water reservoirs will be controlled by the spatial distribution of CO_2 during injection and the replacement reaction rate.

Clogging by CO_2 hydrate formation can be analyzed by comparing the velocity of the invading CO_2 advective front and the growth velocity of CO_2 hydrate at the water-CO_2 interface. The advection fluid velocity in pores v_A[m/s]= $q/(2\pi r H_r \phi)$ is determined by the injection flow rate q[m^3/s], the distance from the well to the front r, the hydrate-bearing reservoir thickness H_r [m], and the sediment porosity ϕ. The velocity of diffusion-controlled growth of the hydrate plug in pores is approximately $v_D=D/\delta$, where D is the diffusion coefficient [m^2/s] of CO_2 through hydrate and δ[m] the length of the hydrate plug. The ratio of these two velocities $v_D/v_A=2\pi DrH\phi/(\delta q)$ determines whether hydrate clogging ($v_D/v_A >>1.0$) or unconstrained advection ($v_D/v_A << 1.0$) will take place. For example, clogging is not anticipated in sandy sediments and sandstones near the injection well during continuous injection, (assuming $\delta \sim 10^{-4}$m, i.e., the plug length is similar to the pore size). However, a stagnant CO_2 fluid front will promote hydrate formation and a differential pressure p_{CO2}-p_w will be needed to break the CO_2 hydrate seal in order to continue injecting CO_2. Assuming cylindrical pore geometry, the additional CO_2 pressure is p_{CO2}-$p_w=4\beta\delta/d$ where β is the hydrate-mineral bonding strength, d is the pore diameter and δ the plug thickness. For plugs $d \cong \delta$ and a bonding strength $\beta \sim 250$kPa, the differential pressure to re-initiate pumping is p_{CO2}-$p_w \sim 1$MPa.

The complex interaction among coexisting processes may give rise to emergent bifurcation phenomena such as viscous fingering and gas-driven fractures. On the other hand, self-homogenizing effects may also arise; for example, CH_4 gas production during CO_2 injection will reduce the local permeability and hinder CO_2 fingers formation.

Table 5.6. Anticipated sediment scale phenomena during CH_4-CO_2 gas replacement

		Reservoir Type	
		Gas-limited, excess-water	**Water-limited, excess-gas**
Injected fluid	**Gas CO_2**	• Gas buoyancy affects invasion [a] • Slow gas replacement rate due to low gas activity [b] • Expect viscous fingering of CO_2 gas [c,d]	• CH_4 hydrate is found at contacts [e]. • Low hydrate volume expansion (1-to-6%) [*1] • High CO_2 gas permeability • CO_2 and CH_4 mix, and flow together [f]
	Liquid CO_2	• Released CH_4 gas lowers the mixture bulk modulus (if above bubble point concentration) [g] • Large fluid volume expansion if released methane exceeds bubble point concentration [*2] • Expect viscous fingering of liquid CO_2 [c,d]	• Some of the water in CH_4 hydrate will dissolve into the liquid CO_2 and the final hydrate saturation will decrease; in fact, liquid CO_2 might "dry" hydrate near the injection well [*3] • Some CH_4 gas will remain trapped in the sediment
	Either gas or liquid CO_2	• Replacement rate is limited by spatial invasion of gas/liquid CO_2 • At low injection rates or due to flow interruptions, CO_2 will react with the excess water to form hydrate during injection, plugging the formation and shielding CH_4 hydrate at reservoir and pore scales [b,c] • Hydrate saturation increases and hydraulic conductivity decreases [h] • Water acidifies [i]	• The sediment is water limited so it does not clog by forming new hydrate

a - [*Lu et al.*, 2009]; b - [*McGrail et al.*, 2007]; c - [*Kang et al.*, 2005]; d - [*Lenormand et al.*, 1988]; e - [*Waite et al.*, 2009]; f - [*Donelly and Katz*, 1954]; g - [*Span and Wagner*, 1996; *Trusler and Zarari*, 1992]; h - [*Kleinberg et al.*, 2003]; i - [*Kneafsey and Pruess*, 2010]; *1– this study, equation 5.7; *2 – this study, equation 5.8; *3 – this study, section 5.4, Fig. 5.4.

5.6 Conclusions

The replacement of CH_4 by CO_2 in hydrate bearing sediments involves multiple coexisting processes, such as mass and heat transport, heat liberation, dissolution, gas production, and fluid volume change.

The CH_4 hydrate cage must separate to release the CH_4 molecule and trap the CO_2 molecule. This transient and local solid-liquid-solid transition within the stability field is assisted by the excess heat liberated during CH_4-CO_2 replacement and can extend as far as ~10K inside the stability field. The presence of minerals, water, and excess gas can limit this self-sustaining reaction to within ~3K of the CH_4 hydrate boundary. While available data are limited, experimental and theoretical considerations suggest that replacement rates increase near the CH_4 hydrate phase boundary, with increasing pore fluid pressure until the CO_2 liquefies, and, when CH_4 hydrate masses are small so the surface available for CO_2 exchange is high.

New experimental results highlight the high solubility of water and CH_4 in liquid CO_2. Hydrate forming water dissolves into liquid CO_2, so that lower hydrate saturation is expected after CH_4-CO_2 replacement in water-limited reservoirs. The transient in hydrate stiffness that should accompany local solid-liquid-solid CH_4-CO_2 replacement has a very small effect on macro-scale skeleton stiffness and the sediment should experience low volumetric strains during CH_4-CO_2 replacement under drained conditions.

Processes and properties reviewed in this manuscript allow us to anticipate various reservoir scale phenomena during CH_4-CO_2 replacement, including: potential decrease in water saturation, decrease in the liquid relative permeability, pronounced increase in fluid volume when a CH_4 gas phase is formed, CO_2 hydrate clogging when

the velocity of the invading front is low and there is enough water to supersaturate the CO_2, and the possibility of CO_2 fingering leading to CH_4 hydrate occlusion within the reservoir. Excess-gas methane hydrate reservoirs should be more amenable to CH_4-CO_2 replacement because of high permeability to CO_2, large interface between CH_4 hydrate and CO_2, and no early CO_2 hydrate clogging. Volume-pressure changes associated to CH_4-CO_2 replacement in excess-water reservoirs may cause increase in fluid pressure, decrease in effective stress and strength loss, volume expansion, and gas-driven fractures if a CH_4 gas phase develops and the permeability is low enough to prevent pressure dissipation.

CHAPTER 6

P-WAVE MONITORING OF HYDRATE-BEARING SAND DURING CH_4-CO_2 REPLACEMENT

6.1 Introduction

The simultaneous injection and geological entrapment of CO_2, along with enhanced hydrocarbon recovery may increase the efficiency and sustainability of fossil fuels. Examples of these combined processes are CO_2 enhanced oil recovery, and CO_2 enhanced coal bed methane recovery. In this study, we focus on CH_4-CO_2 hydrate replacement whereby methane is recovered from hydrate-bearing sediments with the concurrent entrapment of CO_2.

Published theoretical studies and laboratory-scale experiments have shown the successful release of CH_4 as a result of the replacement reaction caused by CO_2 injection [*Hirohama et al.,* 1996; *Kvamme et al.,* 2007a; *Lee et al.,* 2003; *McGrail et al.,* 2007; *Tegze et al.,* 2007]. Pore scale phenomena include heat release and diffusion controlled reactions, dissolution of fluid phases, gas production, and porefluid volume expansion [Note: a comprehensive review of phenomena relevant to CH4-CO2 replacement can be found in *Jung et al.,* 2010]. The first reservoir-scale trial test has been planned for the Alaska North Slope in 2011 (DOE - project DE-NT0006553).

P-waves provide insight into the stiffness evolution of hydrate-bearing sediments. The stiffness evolution affects the mechanical stability of production wellbores and gas hydrate reservoirs. P-wave methods have been used to monitor CO_2 field injection tests [*Arts et al.,* 2004; *Daley et al.,* 2008; *James et al.,* 1995; *Spyros and Bruce,* 1997; *Spyros*

et al., 1995; *Xue et al.*, 2006] and to assess CO_2 transport and saturation in laboratory experiments [*Angeli et al.*, 2009a; *Lei and Xue*, 2009; *Sarout et al.*, 2009; *Shi et al.*, 2007]. In this study we use P-waves to monitor the evolution of CH_4 hydrate formation, CO_2 flooding, CH_4-CO_2 replacement, and final hydrate dissociation in sands. The properties of CO_2 and CH_4 are reviewed first. This is followed by the experimental study and complimentary analyses.

6.2 Review of CO_2 and CH_4 properties

The physical and chemical properties of CO_2 depend on pressure-temperature PT conditions. The critical point of CO_2 is at P=7.38MPa and T=304.1K. The density of liquid CO_2 is usually lower than that of water, but there may be a density reversal at high pressure, such as in deep-sea settings (at 277.15K, ρ_{CO2}>1035kg/m^3 when pressure is above ~28MPa). The bulk compressibility of liquid CO_2 is an order of magnitude higher than that of water [*Span and Wagner*, 1996]. The most important properties of CO_2 relevant to transport-conduction processes are: (a) very low viscosity, typically 10 times lower than that of water [μCO2=10-4 Pa·s at 10MPa and 280K - *Fenghour et al.*, 1998]; (b) high diffusivity of water into liquid CO_2 [D≈2-to-20×10-8m2/s at 7-20MPa and ~300K - *Espinoza and Santamarina*, 2010c], (c) significant solubility of water in liquid CO_2 [0.05mol/kg at 10MPa and 285K - *Spycher et al.*, 2003], and (f) high solubility of CO_2 in water [0.83mol/kg at 6.6MPa and 274K in the presence of hydrate - *Hashemi et al.*, 2006].

The critical point of CH_4 is at P=4.60MPa and T=190.6K, therefore, CH_4 does not form as a liquid phase in geological reservoir applications. The mass density of gas CH_4

can be approximated with a cubic equation of state [See parameters in Table 1 - *Peng and Robinson,* 1976]. The mass density and viscosity of CH_4 are low at reservoir conditions when compared to water; for example, ρ_{CH4}=232kg/m^3 and μ_{CH4}=2.7×10^{-5}Pa·s at *P*=30MPa and *T*=280K [*NIST*, 2010].

Both, CO_2 and CH_4 can form gas hydrates at high pressure and low temperature. Water molecules form a polyhedral structure, which allows them to host the corresponding gas molecules [*Sloan and Koh*, 2008]. Even though both CO_2 and CH_4 form hydrate structure I, their solubility in water, cage occupancy in the hydrate, and thermodynamic stability inside hydrate cages differ significantly [*Adisasmito et al.*, 1991; *Anderson et al.*, 2003; *Servio and Englezos,* 2001; 2002]. Mixed CH_4-CO_2 gas conditions cause a shift in stability boundaries which depends on the CH_4/CO_2 mass ratio [*Adisasmito et al.*, 1991; *Seo and Lee*, 2001].

Gas hydrates form in the pore space of sediments at the bottom of the ocean and at great depths in permafrost where P-T conditions are within the hydrate stability zone and CH_4 is abundant [*Kvenvolden,* 1988]. The pore habit of hydrates in sediments has a large impact on the physical properties of hydrate-bearing sediments [e.g. pore filling, segregated lenses, and cementing - *Waite et al.*, 2009].

6.3 Design of experiments

We use P-waves to assess the evolution of hydrate in sediments. We purposely localize hydrate growth at contacts by using a partially saturated sand pack, so that all of the water is found at interparticle menisci. Therefore, the granular medium acts as a "sensor" that amplifies the signature of the physical processes taking place at tens of

thousands of grain contacts. In particular, sand grains work as Hertzian stiffness sensors that can reflect minor changes in contact conditions. Thus, compressive and shear wave velocities increase significantly even with small changes in hydrate saturation (Note: hydrate nucleates on grain surfaces and grows into the pore in water saturated sediments; much lower changes in stiffness take place in this case).

Materials. Ottawa Sand #20/30 is the host sediment [round grains, d50=0.72mm and d60/d10=1.2, where dx is the diameter for the x-percentile in the distribution - details in *Cho et al.*, 2006]. Fluids include research purity CO_2 and CH_4 gases, and distilled water.

Apparatus. The tests are conducted within a high-pressure chamber equipped with multiple ports for fluid injection, electronics connections, and pressure measurement devices (transducer Omega PX303-GV). A sapphire window allows for direct observation into the pressure chamber. Inside the chamber, we place a spring-loaded sediment cell (25mm diameter and ~20mm height - Fig. 6.1) designed to apply a 100kPa effective axial stress at zero lateral strain conditions. The cell is equipped with piezoelectric transducers (5mm radius, 0.2mm thickness) to generate and receive P-waves (Fig. 6.1). The piezoelectric transducers are connected to a signal generator BK PRECISION 4012A and an oscilloscope HP54600B. The input signal is a step function that repeats every 20ms. The output signal is passed through a 300kHz low-pass analogue filter and is sampled at 5Mhz. A total of 32 consecutive signals are averaged to increase the signal-to-noise ratio, and stored every 30s (Note: we observe the waveforms on the oscilloscope screen continuously during critical processes). A thermocouple (Copper Constantan, Conax Buffalo) placed inside the sediment cell measures the pore-fluid

temperature within the sand specimen. The sediment cell is perforated (0.5mm diameter holes) to retain the sand grains and but to allow the free flow of CH_4 and CO_2.

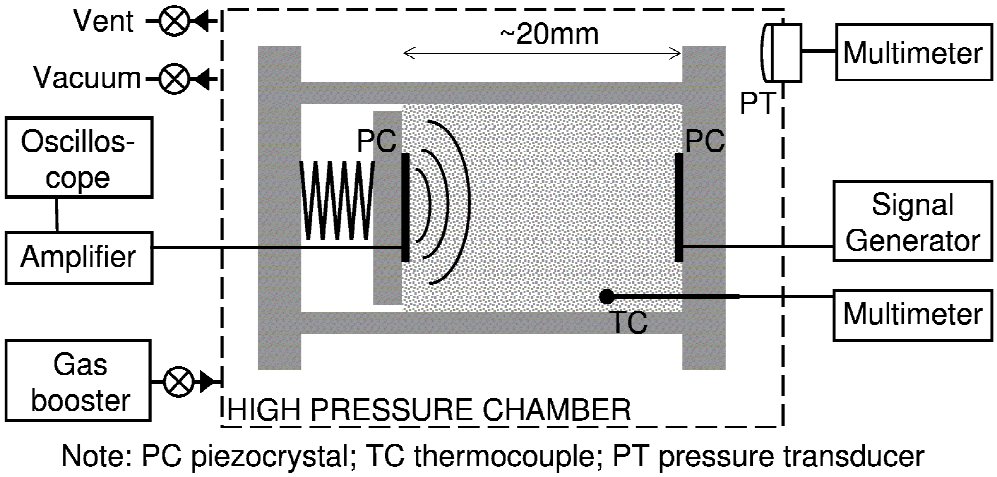

Figure 6.1. Experimental devices. The spring-loaded sediment cell is housed inside the pressure chamber (shown with a dashed line). The spring applies a constant effective axial stress $\sigma' \approx 100$kPa to the sand. The piezoelectric transducers attached to the lower and upper plates of the cell are used to generate and measure the compressive P-waves. A thermocouple (bottom right corner in the cell) measures the sediment temperature.

Experimental procedure. The sand is mixed with distilled water, packed inside the sediment cell, and loaded to a constant effective axial stress. Then, we place the sediment cell inside the pressure chamber, briefly apply a partial vacuum, and flush the system with CH_4 gas at least five times in order to remove the air inside of the chamber and specimen pore space. Immediately after, we start to log pressure, temperature, and P-wave arrivals.

We run a total of seven multi-stage tests using the same sand, at the same effective stress, but with different initial values of water saturation. We subject each specimen to a pre-specified pressure-temperature PT time history to gain detailed information related to hydrate formation, CH_4-CO_2 replacement, and subsequent

dissociation. Ice and hydrate formation PT paths are chosen to facilitate hydrate formation and to gain physical insight. The PT histories during CO_2 flooding represent two plausible scenarios: (a) flooding inside the CH_4 hydrate stability field is expected to be safer but slower, while (b) CO_2 gas injection coupled with depressurization may be quicker but may be accompanied by sediment compaction. PT paths that induce hydrate dissociation allow us to confirm PT conditions at phase transition for either CO_2 or CH_4 hydrate. Finally, successive CO_2 flushing is relevant to anticipate the response of hydrate-bearing sediments subjected to high CO_2 advection. Results are summarized in the following section

6.4 Results

The main stages in the various PT time histories are shown in Fig. 6.2. Fig. 6.3 shows typical waveform cascades measured during the different stages. The dominant frequency of the transducer-sediment coupled system is in the ultrasonic regime and ranges from ~20kHz (sand pack in air) to 150kHz (cemented by ice or hydrate). Specific observations for each PT stage are summarized next.

6.4.1 Ice and hydrate formation

(a) *Specimen cooling and ice formation at grain contacts* (path a_1 in Fig. 6.2). Ice formation lasts from 30-to-350s for water saturation S_w=0.045-to-0.37 (exothermic-heat transport controlled). A pronounced increase in stiffness accompanies ice formation (e.g. Fig. 6.3-a, initial S_w=0.045).

(b) *CH_4 hydrate formation from ice in an excess-CH_4 atmosphere* (paths a_2 and b in Fig. 6.2). The ice-bearing sediment is pressurized with CH_4 (path a_2) and warmed outside of the ice stability field (path b). We observe that CH_4 hydrate nucleates

as ice melts. While hydrate formation at each meniscus is CH_4 diffusion-limited, the volume average P-wave velocity remains higher than in the unfrozen sediment at all times (Fig. 6.3-b is a continuation of Fig. 6.3-a - initial S_w=0.045). Hydrate continues growing for ~12h and the sediment mixture continues to increase in stiffness (only 45min shown in Fig. 6.3-b).

(c) *CH_4 hydrate formation from water in an excess-CH_4 atmosphere* (path c in Fig. 6.2). In this case, the initial sediment temperature is above that of the hydrate phase boundary, and the hydrate is formed by cooling (Fig 6.3-c). This process is much longer than ice formation because the growth is not governed by heat transfer but instead by the CH_4 diffusive transport through the hydrate layer that forms at the interface between the pendular water and the bulk CH_4 gas (for S_w=0.10, ice formation takes place in less than 30 seconds, yet hydrate formation requires about 24h). The duration of hydrate formation increases with the initial water saturation S_w.

6.4.2 CO_2 flooding

(d) *CO_2 flooding and displacement of CH_4* (path d in Fig. 6.2). After CH_4 hydrate forms at grain contacts, we flood the pore space with gaseous, then, liquid CO_2 while the PT conditions remain within the CH_4 hydrate stability field. CH_4 is slowly vented while CO_2 is pumped into the chamber. The liquid phase formation is observed through the sapphire window; the interface rises to eventually fill the chamber as the injection of CO_2 continues. From PT conditions and bubble point data, we estimate that less than 10% of the methane remained in the chamber,

mostly above the sediment cell [see CH4-CO2 phase equilibria in *Donelly and Katz,* 1954]. Fig. 6.3-d shows the results gathered during the liquid CO_2 flooding of a CH_4 hydrate-bearing sand at a hydrate saturation of S_{hyd}~0.045; based on the evolution of P-wave velocity to an asymptotic value and on the time for diffusion-controlled growth (Section 6.5.3), we assume all water has converted to hydrate at this point. P-T conditions remain within the CH_4 hydrate stability field. There is no significant stiffness change.

(e) *Liquid-gas-liquid CO_2 cycle at S_{hyd}* ~0.045 (path e in Fig. 6.2). We renew the CO_2 in the pore space by imposing a liquid-gas-liquid CO_2 cycle, to simulate extensive flushing of the sediment with pure liquid CO_2. Fig. 6.3-e_1 shows the first of ten CO_2 flushing cycles. The wave velocity does not change significantly when the pore-fluid is changed from liquid CO_2 to gaseous CO_2.

Liquid-gas-liquid CO_2 cycle at S_{hyd}<<0.045 (same as path e in Fig. 6.2). When hydrate saturation is very low, the difference in bulk stiffness when pores are filled with liquid CO_2, as opposed to gaseous CO_2, is evident (Fig. 6.3-e_2): as soon as CO_2 vaporizes, the waveform shifts to having long travel time (~20 μs to >40μs) and low frequency.

6.4.3 Hydrate dissociation

(f) *Dissociation of CH_4 hydrate* (path f in Fig. 6.2). Fig. 6.3-f shows CH_4 hydrate-bearing sand in CH_4 gas as it is heated beyond the hydrate stability field. The dissociation of CH_4 hydrate takes ~20min for initial S_{hyd}~0.10 (Fig. 6.3-f). As soon as the specimen crosses the CH_4 hydrate dissociation boundary, the P-wave

velocity starts to decrease. After complete dissociation, the effective stress acting on the granular skeleton dominates the sediment stiffness (Note: Fig. 6.3-c is a continuation of Fig. 6.3-f).

(g) *Dissociation of CH_4 hydrate in the presence of CO_2* (path g in Fig. 6.2). In this experiment, we take a specimen of CH_4 hydrate-bearing sand in CH_4 gas beyond the CH_4 hydrate stability field and simultaneously inject CO_2 in order to reach the region bound by the CH_4 and CO_2 hydrate phase boundaries. Upon continued CO_2 injection, the CO_2 gas becomes liquid CO_2. From PT conditions and dew point data, we estimate that less than 10% methane stayed in the chamber, mostly above the sediment cell [see CH4-CO2 phase equilibria in *Donelly and Katz*, 1954]. The P-wave velocity hardly changes during the process (Fig. 6.3-g, S_{hyd}=0.27, during the time shown and afterwards. We observe this "hydrate preservation behavior" at low hydrate saturation as well (S_{hyd}=0.03 - not shown in Fig. 6.3).

(h) *Hydrate dissociation after CO_2 flooding* (path h in Fig. 6.2). Fig. 6.3-h shows the dissociation of originally pure CH_4 hydrate in sand (S_{hyd}~0.10) ~48h after the injection of liquid CO_2. During depressurization, the specimen goes through the CH_4 hydrate phase boundary first; but the P-wave velocity remains almost constant until the CO_2 hydrate phase boundary is reached. A rapid loss of stiffness occurs once the PT conditions are beyond the CO_2 hydrate stability field, and the sediment stiffness returns to the original water-wet condition. Complete dissociation lasts ~15 minutes.

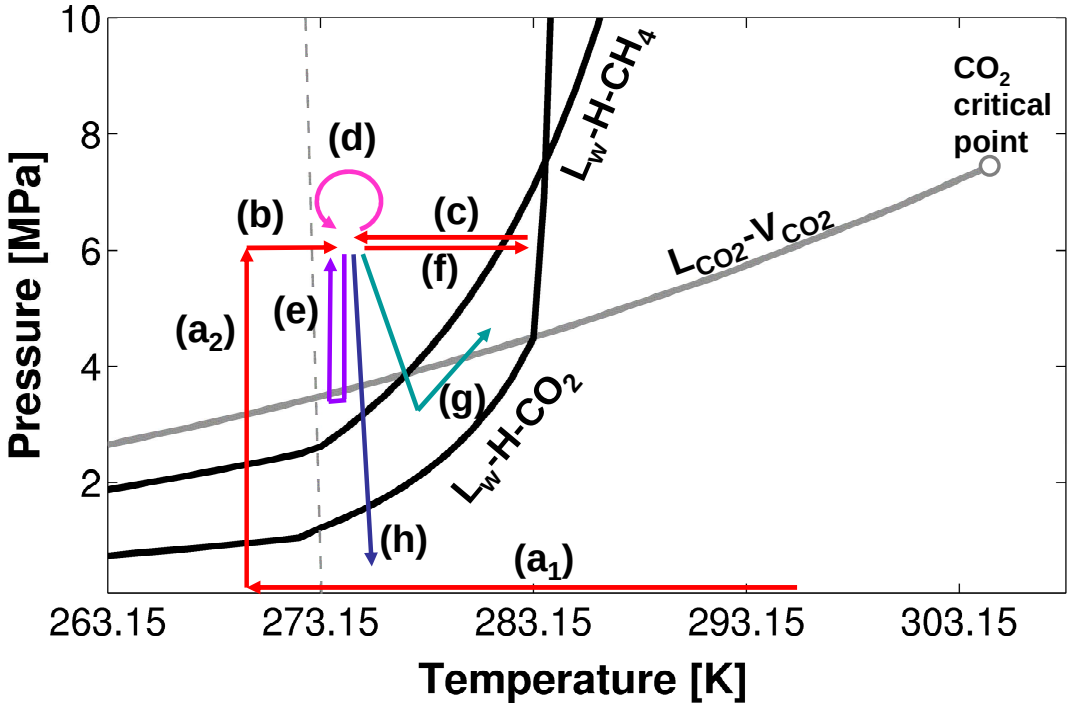

(a) Freezing and pressurization
(b) CH_4 hydrate formation from ice
(c) CH_4 hydrate formation from water
(d) CO_2 flooding inside CH_4 HSZ
(e) CO_2 liquid-gas-liquid cycle
(f) CH_4 hydrate dissociation
(g) CO_2 flooding outside CH_4 HSZ
(h) Depressurization - Dissociation

Figure 6.2. Pressure-temperature time histories. The arrows show the PT conditions followed in various tests, not necessarily in chronological order (letters match datasets in Fig. 6.3). Phase boundaries are shown for CH_4 and CO_2 hydrate, the liquid-vapor boundary for pure CO_2 and the water-ice boundary as a dashed line [equations in *Jung et al.*, 2010]. Initially, we freeze the water in a CH_4 atmosphere (a_1) and then increase pressure by injecting CH_4 gas (a_2). We formed hydrate from ice to hydrate (b) and from liquid water (c). CO_2 injection is shown as loops, first CO_2 flooding (d), followed by liquid-gas-liquid CO_2cycles (e). The CH_4-CO_2 replacement is sought during the first CO_2 flooding inside the CH_4 HSZ (d) or during the excursion outside the CH_4 hydrate stability field (g). We dissociate any hydrate during the final depressurization step (h).

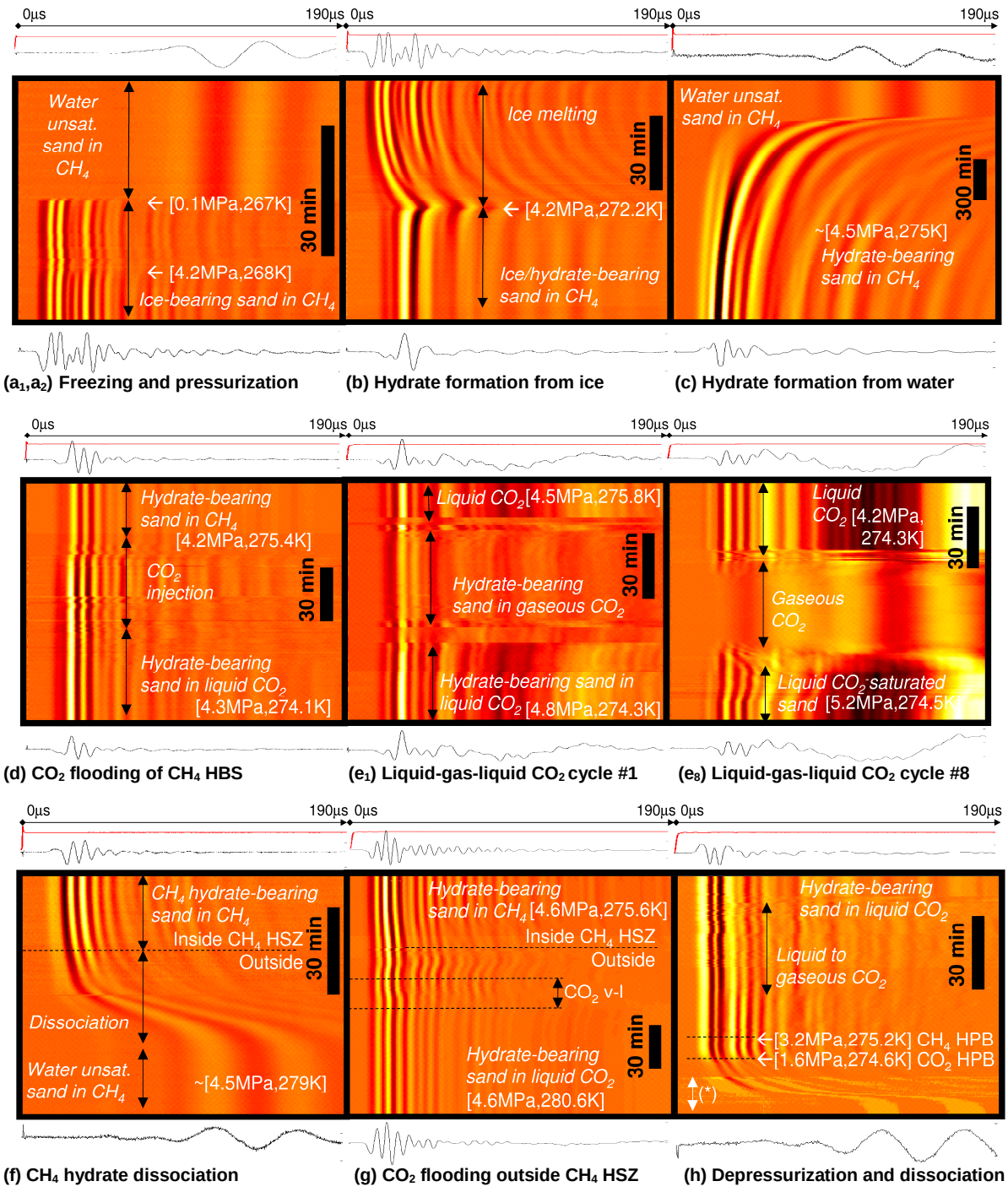

Figure 6.3. P-wave measurements in hydrate-bearing sand (void ratio e~0.7, effective confining stress σ`~100kPa, and mean particle size d_{50}=0.72mm). Waveforms from time-lapse P-wave monitoring: x-axis, oscilloscope time [µs]; y-axis, experimental time from the top to the bottom [min]. Waveform voltage in colors, white denotes the signal peaks and black the signal troughs. Each frame represents a different process (results from various tests – Refer to Fig. 6.2 and Section 6.3). Notice the high contrast

in frequency and amplitude between water unsaturated and either ice or hydrate-bearing sediments. Notes: HPB hydrate phase boundary, * increased contrast to show low amplitude waveforms. Summary of PT histories for experiments shown in this figure: 1) initial S_w=0.045 (a_1, a_2, b, d, e, and h); 2) initial S_w=0.10 (a_1, a_2, b, f, c, d, h); and 3), initial S_w=0.27(a_1, a_2, b, f, c, g, and final depressurization).

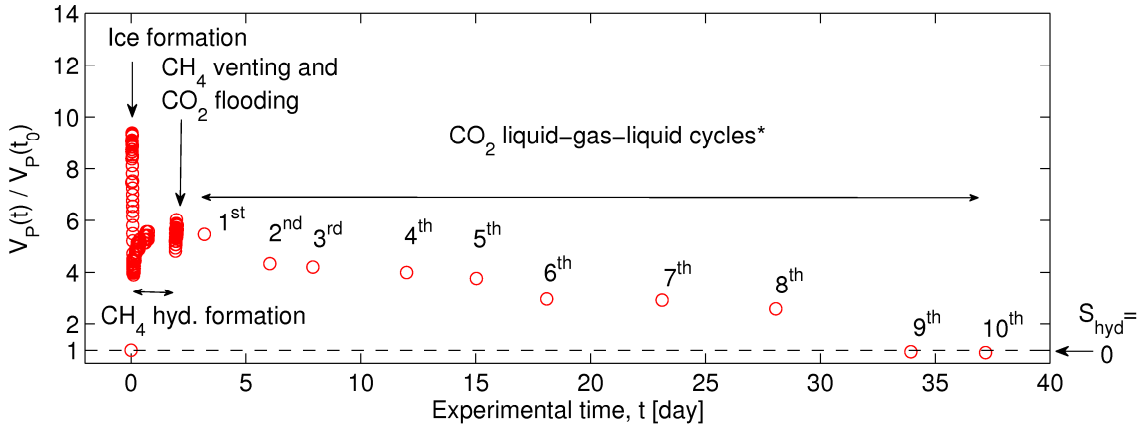

Figure 6.4. Reduction of hydrate-bearing sand stiffness during successive flushes of pure liquid CO_2, as liquid-gaseous-liquid CO_2 cycles inside the CH_4 hydrate stability field. The vertical axis represents the ratio between the P-wave velocity at experimental time t and the initial P-wave velocity at time t_0 before ice and hydrate formation. Each liquid-gas-liquid CO_2 cycle replaces 0.030kg of pure CO_2 every ~3 days, which is equivalent to 8.5 times the pore space of the sand specimen. Note: (*) During the CO_2 liquid-gase-liquid cycles, we show the V_P ratio for the specimen in gas CO_2 to highlight the effect of cementing hydrate on the granular skeleton. The sand does not show any evidence of cementation after the 8th liquid-gas-liquid CO_2 cycle (28th day in the figure).

6.4.4 CO_2 flushing

We flush the CO_2 in the sediment by imposing the CO_2 pressure cycles sketched as path e in Fig. 6.2. Fig. 6.4 shows the complete stiffness evolution for a hydrate-bearing sand (S_{hyd}~0.045) subjected to ten CO_2 flushing cycles (Note: this is a 35 day long experiment; ice formation, hydrate formation from ice, and CH_4 displacement by liquid CO_2 are shown for completeness). The granular skeleton stiffness decreases gradually

with each CO_2 flushing cycle. The P-wave velocity at the eighth flushing cycle is the same as for the water-wet sand pack at 100kPa. We dismantled the chamber and recovered only dry sand from the sediment cell.

6.5 Complimentary analyses and discussion

Earlier physico-chemical arguments at the lattice-scale suggested that a solid-liquid-solid transition is required for CH_4-CO_2 replacement [*Jung et al.*, 2010]. However, macroscale experimental results presented here show almost constant sediment stiffness during CH_4-CO_2 replacement. It is concluded that the solid-liquid-solid transition takes place locally at a scale small enough that the sediment volume average properties remain unchanged. Clearly, hydrate dissolution in liquid CO_2-saturated reservoirs will be accompanied by stiffness loss (e.g. near the injection well), while new hydrate formation in excess-water reservoirs will increase the sediment stiffness (typically in the far field of the injection well).

The following complimentary analyses permit extracting additional information from these experiments and provide an approach to assess changes in the geological formation.

6.5.1. Frequency effects

The piezoelectric transducers used in this study have a high resonant frequency in air. Once buried in the sand, the resonant frequency is strongly dependent on the sand stiffness and the sediment mass within the near field of the transducer. Assuming a parallel stiffness model, we can estimate the effective natural frequency of the coupled

sand-transducer system f_c [underlying expressions in *Bevlins*, 1979; an analogous analysis for buried bender elements can be found in *Lee and Santamarina*, 2005]

$$f_c \approx \frac{1}{2\pi}\sqrt{\frac{\frac{70^2}{3}\left(\frac{t}{r}\right)^3 \frac{E_p}{\left(1-\nu_p^2\right)} + \eta E_s}{\left[\left(\frac{t}{r}\right)\rho_p + \beta\rho_s\right]\pi r^2}} \qquad (6.1)$$

where β=2 (first mode of vibration) and η~1.6 [*Poulos and Davis*, 1974] are geometry related factors, and E_p and ν_p are the Young's modulus and Poisson's ratio of the transducer. The sediment stiffness E_s determines the resonant frequency of these buried, thin transducers (thickness much smaller than the radius, $t/r<<1$). Indeed, experimental results show that at an effective stress of σ'=100kPa, the dominant spectral frequency ranges from 20kHz (sediment without ice or hydrate) to 150kHz (sediment with ice or hydrate). These values are readily corroborated by time series shown in Fig. 6.3. In all cases, the wavelength λ is greater than 20 times the grain size d_{50} and satisfies the equivalent continuum assumption. The wavelength λ remains significantly shorter than the travel distance in all measurements.

The frequency content of P-waves in the sand saturated with liquid CO_2 (refer to Fig. 6.3) often exceeds Biot's characteristic frequency [*Biot*, 1956] for our experimental conditions (ϕ~0.42, $\mu_{liquidCO2}=10^{-4}$Pa·s, $\rho_{liquidCO2}$~0.9kg/m^3, and κ~10^{-12}m^2)

$$f_c = \frac{\phi\mu_{CO2}}{2\pi\rho_{CO2}\kappa} \sim 10kHz \qquad (6.2)$$

The ratio between the high and low frequency P-wave velocity is ~1.07 [equation in *Santamarina et al.*, 2001a] and has a minor effect in these results and analysis. In view

of field applications, we continue the analysis of P-wave velocity for the low frequency regime.

6.5.2. P-wave velocity – changes during liquid CO_2 flooding

In the low-frequency regime, the mixture bulk compressibility B_{mix} can be estimated using the low frequency Biot-Gassman equation [*Bourbie et al.*, 1987; *Mavko et al.*, 2009], while the mixture mass density ρ_{mix} is computed as a volume average. The general expressions for the system under consideration are,

$$B_{mix} = B_{sk} + \left(1 - \frac{B_{sk}}{B_m}\right)^2 \left[\left(\frac{S_w}{B_w} + \frac{S_{CO_2}}{B_{CO_2}} + \frac{S_{CH_4}}{B_{CH_4}} + \frac{S_{hyd}}{B_{hyd}} \right) \phi + \frac{1-\phi}{B_m} - \frac{B_{sk}}{B_m^2} \right]^{-1} \quad (6.3)$$

$$\rho_{mix} = \phi \, (S_w \rho_w + S_{CO_2} \rho_{CO_2} + S_{CH_4} \rho_{CH_4} + S_{hyd} \rho_{hyd}) + (1-\phi) \rho_m \quad (6.4)$$

where ϕ is the sediment porosity and S is the relative saturation with subindeces w for water, CO_2, CH_4, and *hyd* for hydrate. A similar expression can be used for ice by replacing S_{hyd}, B_{hyd} and ρ_{hyd} with S_{ice}, B_{ice} and ρ_{ice}. The physical and mechanical properties of water, CO_2, CH_4 and solids (i.e., quartz, ice, and hydrate) are summarized in Table 6.1; notice that the bulk stiffnesses sort as $B_m > B_{ice} > B_{hyd}$ (m: mineral). A proper equation of state is used for the fluid phase to account for variations in pressure and temperature (see Table 6.1).

Equation 3 disregards the stiffening effect of capillary forces in mixed fluid conditions, such as water-CO_2 mixtures; this approximation is adequate for coarser sediments and/or high effective stress levels. If needed, the value of B_{sk} can be increased as a function of suction and saturation [*Rebata-Landa*, 2007].

Table 6.1. Physical and mechanical properties of hydrate-bearing sediment constituents. The following constants and equations are used to predict P-wave velocity for the multiphase fluid-sediment system using the Biot-Gassman equation (Equations 6.3 and 6.4).

Phase	CO_2	CH_4	Water-brine	Ice	Gas Hydrate	Mineral
			Physical properties			
Mass density, ρ [kg/m^3]	CO_2 EOS [A]	CH_4 Peng-Robinson EOS [B]	Correlation [C]	921 [D]	CH_4 hyd: 930 [E] CO_2 hyd: 1100 [F]	Quartz: 2650
Viscosity, μ [Pa s]	Experimental fitting [G]	$2\pm0.5\times10^{-5}$ [H]	$\sim1.5\times10^{-3}$ [I]	Does not apply	Does not apply	Does not apply
			Mechanical properties			
P-wave velocity, V_P [m/s]	Correlation based on [J]	Polynomial equation [K]	Equation [L]	3870 [D]	3780 [D]	6060 [M]
S-wave velocity, V_S [m/s]	0	0	0	1949 [D]	1963 [D]	4110 [M]
Shear Modulus, G [GPa]	0	0	0	3.45 [D]	3.2 [N] 3.54 [D]	45 †
Bulk Modulus, B [GPa]	f(V_P, ρ) †	f(V_P, ρ) †	f(V_P, ρ) †	9.18 [D]	7.1 [M] 8.51 [D]	37 †
Poisson ratio, ν	~0.5	~0.5	~0.5	0.33 [D]	0.32 [D]	~0.08 [M]

A- [*Duan and Sun*, 2003b]; B- Peng-Robinson parameters: T_c=191.15K, P_c=4.641MPa, ω=0.0115; C- [*Mavko et al.*, 2009]; D- 31MPa effective stress and 273.15K [*Helgerud et al.*, 2009]; E [*Sloan and Koh*, 2008]; F- [*Aya et al.*, 1997] ; G- [*Fenghour et al.*, 1998; *Vesovic et al.*, 1990]; H- At 298K, 10-to-20MPa [*Bicher and Katz*, 1943]; I- Brine at 293K [*Netherton et al.*, 1977]; J- [*Span and Wagner*, 1996]; K- [*Trusler and Zarari*, 1992]; L- [*Belogol'skii et al.*, 2002; *Mavko et al.*, 2009]; M- [*Gueguen and Palciauskas*, 1994]; and † means computed value.

The constrained modulus of the skeleton M_{sk} can be determined from V_P measurements in gas saturated sands $M_{sk}=V_P^2\rho_{sk}$. From the theory of elasticity, the bulk and shear modulus of the skeleton are $B_{sk}=1/3[(1+\nu_{sk})/(1-\nu_{sk})]M_{sk}$ and $G_{sk}=[(1-2\nu_{sk})/(2-2\nu_{sk})]M_{sk}$, where the small strain Poisson's ratio for the granular skeleton is low ν_{sk}=0.1 [*Santamarina et al.*, 2001a]. Knowing B_{mix} (Equation 3), G_{sk} and ρ_{mix} (Equation 4), the compressive wave velocity of the fluid saturated porous medium can be computed as,

$$V_P = \sqrt{\frac{B_{mix} + \frac{4}{3}G_{sk}}{\rho_{mix}}} \tag{6.5}$$

Fig. 6.5 shows the ratio β between the P-wave velocity predictions for the sediment saturated with a water-CO_2 mixture (S_w+S_{CO2}=1), and the same sediment saturated with water only (S_w=1). Values of β are shown as a function of CO_2 saturation for different skeletal stiffnesses V_{Psk}, fluid pressures, and porosities. Parameters used in each pane are selected to match the conditions in our experiments and other published studies; data are superimposed on the graphs. The β-ratio is always less than one because the P-wave velocity of liquid CO_2 ranges between ~300m/s (7MPa, 300K) and 590m/s (10MPa, 280K) as compared to that of water $V_{P\text{-}water}$~1500m/s. The β-ratio is most sensitive to the stiffness of the skeleton B_{sk} and G_{sk}, and it tends to β=1 as the stiffness of the skeleton increases. The β-ratio changes significantly with PT conditions and CO_2 saturation S_{CO2}. Similar trends apply to brine-saturated media (P=10MPa; T=280K; S=10%; B_w= 2.11GPa; B_{brine}= 2.64GPa; ρ_w= 1004kg/m^3 ; ρ_{brine}= 1075 kg/m^3).

An immediate implication of this analysis is that the injection of liquid CO_2 into water-saturated sediment in the field replaces high bulk stiffness water for the more compressible liquid CO_2 and a lower P-wave velocity is anticipated. Also we note that due to the low P-wave velocities of gas CH_4 and both gas and liquid CO_2 compared to the P-wave velocity of the hydrate-bearing sand (V_P ~900m/s at 100kPa vertical effective stress), P-wave velocities measured in this study closely track the evolution of skeletal stiffness.

While the forward prediction of V_P is viable, flat trends in Fig. 6.5 indicate that the estimation of CO_2 saturation from V_P measurements will be inaccurate, especially in

stiff, low porosity sediments where marked changes in CO_2 saturation have almost no impact on V_P.

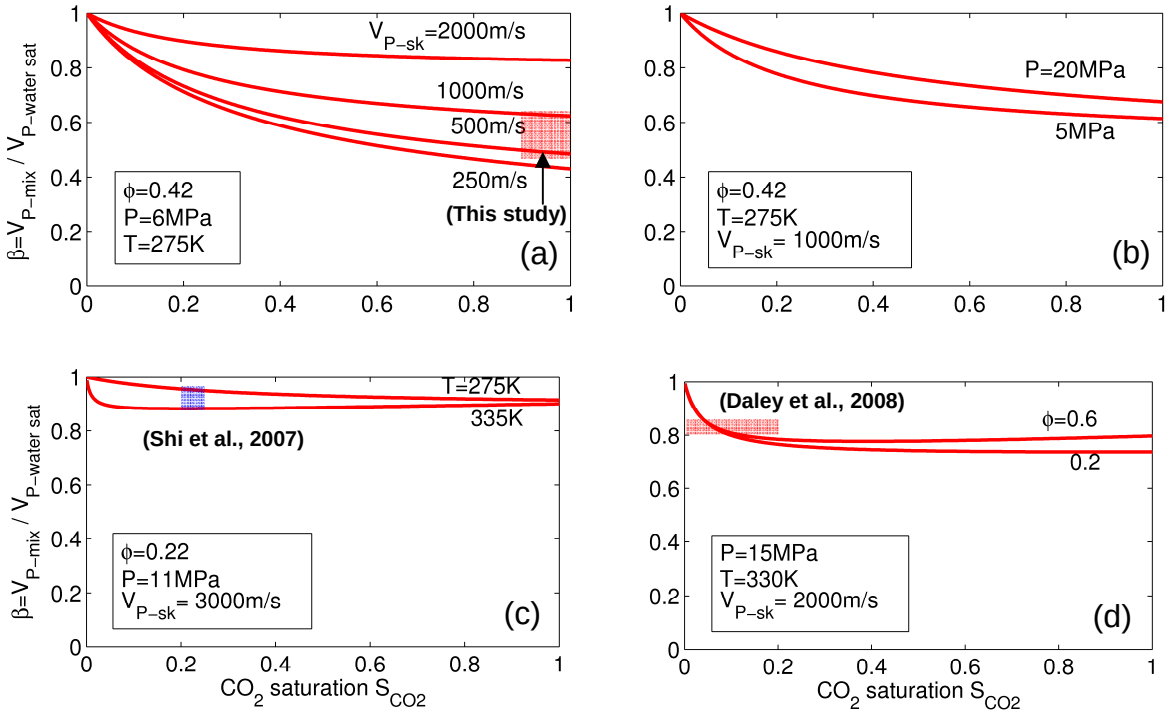

Figure 6.5. Ratio of compressive P-wave velocities for liquid and supercritical CO_2-water saturated sediment and the same sediment saturated with water as a function of CO_2 saturation. The effects of (a) Skeletal stiffness as represented in V_{Psk}; (b) pore-fluid pressure P; (c) temperature T; (d) porosity ϕ. The bulk modulus and density of CO_2, and water are calculated with equations of state as a function of pressure and temperature (Table 6.1). Laboratory and field results are superimposed.

6.5.3 Time evolution: Formation Rate

Diffusion controlled hydrate growth is anticipated at menisci (excess-gas conditions). CH_4 hydrate formation is limited by methane gas transfer through the hydrate layer thickness s that forms around the menisci (excess-gas sediment). At steady state, the flux of gas F_g from the pore space (concentration C_{bulk}) to the water inside the meniscus (concentration C_{aq}) is

$$F_g = D\frac{C_{bulk} - C_{aq}}{s} \tag{6.6}$$

where D is the diffusivity of CH_4 through CH_4 hydrate. The concentrations $C_{bulk}=\rho_{CH4}$[mol/L] and C_{aq} depend on pressure and temperature conditions [*Servio and Englezos*, 2002; *Servio et al.*, 1999]. The gas concentration in hydrate is C_{hyd}=7.3mol/L (full occupancy n=5.75; lattice size 12Å). For a quasi cylindrical geometry, the evolution of the hydrate shell thickens in time becomes,

$$s = \sqrt{2D\frac{C_{bulk} - C_{aq}}{C_{hyd} - C_{aq}}t} \tag{6.7}$$

We estimate the time required for hydrate formation t_{form} in pendular water at interparticle menisci by combining Equations 6.6 and 6.7, and substituting s for r_m,

$$t_{form} = \frac{1}{8D}\frac{C_{hyd} - C_{aq}}{C_{bulk} - C_{aq}} d_{50}^2 \sqrt{S_w^{init} e} \tag{6.8}$$

Experimental diffusion values D=3.4-to-7.6×10^{-13} m^2/s [*Davies et al.*, 2008], combined with Equation 6.8 lead to the conclusion that water in submillimetric menisci converts to hydrate in few days. Similar rates are expected to happen in diffusion controlled CH_4-CO_2 replacement processes.

6.5.4 Water solubility in liquid CO_2 and hydrate dissolution

Both CO_2 and CH_4 hydrates tend to dissolve in liquid CO_2 that is not water saturated, as confirmed by the results shown in Fig. 6.4 [see also *Jung et al.*, 2010]. An estimated ~30mg of water could be dissolved into liquid CO_2 given the void space in our chamber under the experimental conditions in this study. Alternatively, only ~3mg of water can dissolve into the CO_2-filled pore space of the sediment cell. The experiment shown in

Fig. 6.4 starts with 180mg of water in the sediment; i.e., S_w=0.045. Thus, ~180mg/30mg = 6 to ~180mg/3mg = 60 flushing cycles of CO_2 are needed to dissolve all hydrate-forming water into the surrounding liquid CO_2. Nine CO_2 flushing cycles were sufficient in the experiment documented in Fig. 6.4.

6.6 Conclusions

CH_4-CO_2 replacement in hydrate-bearing sediments presents a unique opportunity to address increasing energy demands within the context of climate change. Considerable research efforts are needed to understand the complexity of underlying processes leading to commercial scale technological developments.

We designed an experiment that takes advantage of the contact-dependent sand stiffness to follow CH_4 hydrate formation, CO_2 flooding and gas replacement, and subsequent hydrate dissociation. The test design amplifies the process signatures by simultaneously measuring phase reactions that take place at thousands of interparticle menisci.

Hydrate growth in excess-gas sediments is controlled by CH_4 diffusion through the intermediate hydrate shell that separates bulk gas and free water.

After CO_2 flooding, the hydrate mass dissociates at the CO_2 hydrate dissociation boundary, which confirms the successful CH_4-CO_2 replacement.

The hydrate-bearing sediment retains its stiffness during CO_2 flooding and gas replacement. Therefore, while a lattice-scale solid-liquid-solid transition is required for CH_4-CO_2 replacement, the reaction is local and does not cause an appreciable effect on the macroscale mechanical properties of the hydrate bearing sediment.

The mutual solubility and diffusivity of water, CO_2, and CH_4 components play a crucial role in the process of CH_4-CO_2 replacement. Liquid CO_2 will dry water from the existing hydrate, causing a decrease in both hydrate saturation and sediment stiffness in regions subjected to extensive CO_2 flow, such as near the injection wells. This may lead to volume contraction, trigger borehole instability, and facilitate sand production.

The bulk modulus of CO_2 at reservoir conditions is lower than that of water. Therefore, P-wave velocity decreases as CO_2 displaces water from the pore space. The change in P-wave velocity is small in hard rocks and stiff sediments. This observation limits the use of P-wave monitoring of CO_2 injection.

CHAPTER 7

CLAY INTERACTION WITH LIQUID AND SUPERCRITICAL CO_2: THE RELEVANCE OF ELECTRICAL AND CAPILLARY FORCES

7.1 Introduction

Carbon capture and geological storage have been proposed to reduce greenhouse gas emissions into the atmosphere. CO_2 would be captured at concentrated point sources (typically power plants), and then compressed and injected into nearby geological formations [*IPCC*, 2005]. Most carbon storage target sites, such as deep saline formations, consist of high permeability rocks or loose sands which act as repositories for pressurized and buoyant CO_2, overlaid by a low permeability formation which serves as a sealing cap rock (See Fig. 7.1 [*Dooley et al.*, 2006; *Gale*, 2004]). Two important macro-scale characteristics of good seal layers are continuity and ductility [*Downey*, 1984]: faults, fractures, and existing wellbores are major discontinuities and may result in preferential paths for CO_2 leakage; on the other hand, ductility allows cap rock deformation without fracturing.

Shales and evaporites commonly serve as cap rocks for natural hydrocarbon accumulations; similarly these rocks are considered as potential seal layers for CO_2 storage. Table 7.1 shows a compilation of petrographical properties of shale cap rocks at selected carbon storage sites; clay minerals are a major component of these rocks. Evaporite seal layers serve as CO_2 cap rocks at Weyburn, the K12-B project, and the Salt Creek CO_2 injection site [*Benison and Goldstein*, 2000; *Chiaramonte et al.*, 2008; *Li et al.*, 2005; *Vandeweijer et al.*, 2011].

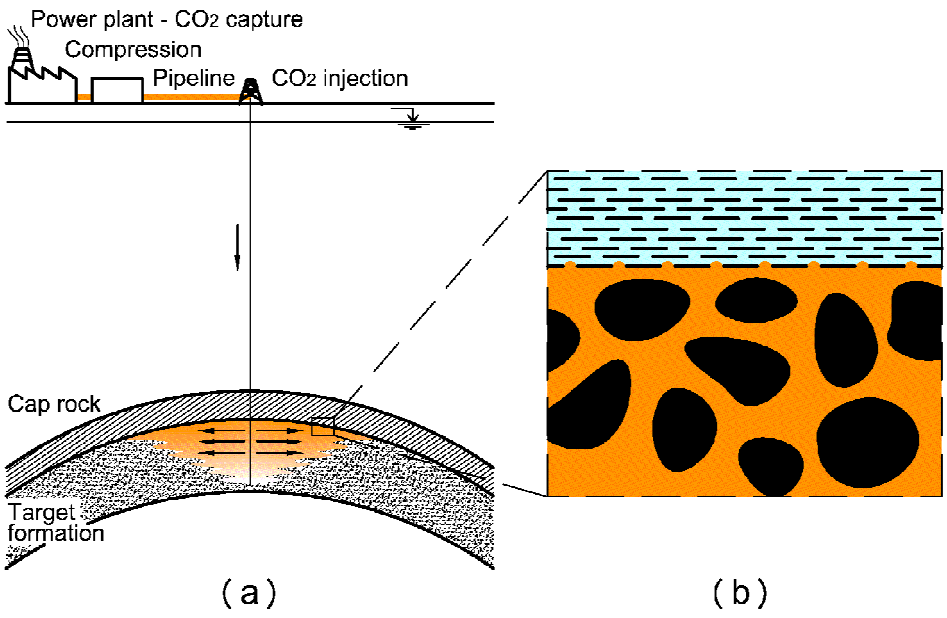

Figure 7.1 Carbon capture and geological storage. (a) A power plant equipped with carbon capture technology delivers CO_2 to the storage site where CO_2 is injected into a porous formation overlaid by a cap rock. (b) Close-up of shale-sandstone interface where pressurized buoyant CO_2 is retained by capillary fringes.

The sealing efficiency of intact shale cap rocks is dominated by high specific surface clays [Chapter 3]. Fine grained clays can resist high capillary entry pressures, but are more susceptible to changes in electrical forces. Capillary forces and changes in electrical interactions will inherently arise as CO_2 invades the cap rock because of the CO_2-water interfacial tension, water acidification, and the nonpolarity of CO_2. Eventually, capillary and electrical phenomena upscale, causing mechanical couplings which will affect porosity, sediment fabric, hydraulic conductivity, compressibility, and the sediment shear strength [e.g. NAPL and clays in *Jo et al.*, 2001; *Kaya and Fang*, 2005; *Montoro and Francisca*, 2010; *Santamarina et al.*, 2001b]. Yet, the interaction between clay minerals and CO_2 is poorly understood. Apart from a few polymer

manufacturing investigations [*Serhatkulu et al.*, 2006; *Urbanczyk et al.*, 2010], there are no experimental studies of clay behavior when invaded or surrounded by CO_2.

Table 7.1 Petrographical properties of cap rocks at selected carbon storage sites

Site	Dominant clay minerals weight %	Carbonates minerals	Evaporites	Approximate overburden depth	Porosity
Frio, USA [*Hovorka*, 2009; *Lynch*, 1997]	Illite-smectite ~45% Illite ~10% Kaolinite 13% Chlorite ~3%	Calcite	-	1450 m	8-10%
Sleipner, Norway [*Bøe and Zweigel*, 2001; *Chadwick et al.*, 2004; *Pilliteri et al.*, 2003]	Mica-Illite ~25% Kaolinite 14-18% Smectite 3-9% Chlorite 1-4%	Calcite 1-3% Siderite 2%	-	750 m	35%
Krechba, Algeria [*Armitage et al.*, 2010; *Mathieson et al.*, 2010]	Muscovite-illite ~25-50% Chlorite ~20-4% Kaolonite ~8-4%	Siderite ~15-0%	-	1850 m	1.8-11.3%
Otway, Australia [*Watson et al.*, 2005]	Kaolinite 44-17% Illite 6-1% Smectite 3-1%	Siderite 35-2%	-	1980 m	2.5-7.5%
SACROC, USA [*Carey et al.*, 2007; *Han et al.*, 2010]	62% Illite-smectite	Calcite 2.5% Dolomite 2%	0.1% Halite	2000 m	1.3%
Rousse, France [*Tonnet et al.*, 2011]	Illite 2.2-14.5% Kaolinite 0.3-4.1% Chlorite 0.1-2%	Calcite 30-65% Dolomite 3-63% Siderite 0.1-6.2%	-	4000 m	0.5-3%
Carnarvon, Australia [*Dewhurst et al.*, 2002]	Illite-smectite 30-25% Illite 15-20% Kaolinite ~15% Chlorite ~5%	Siderite 1-4%	-	1100 m	21%
Ketzin, Germany [*Förster et al.*, 2007]	Iliite 42-74% Chlorite 1-3%	Dolomite 4-35%	Halite (small fraction)	600 m	10%

In this study, we explore the particle-scale interactions between liquid and supercritical CO_2 with clay minerals to discern the role of electrical and capillary forces on potential cap rock performance (Note: CO_2 dissolution and water acidification effects on clay surfaces are not addressed in this manuscript). The research approach seeks to gain insight into complex phenomena relevant to CO_2 storage conditions. The study starts with an assessment of electrical and capillary forces in clay-water-CO_2 systems; then experimental evidence gathered in simple and well constrained experiments is presented. Finally, the study concludes with an analysis of anticipated geomechanical and hydrological implications for CO_2 storage sites that involve clayey cap rocks.

7.2 Review on clay-water-CO_2 systems

7.2.1 Clay minerals and shales

Shales are sedimentary rocks made of clay minerals, fine-grained quartz, feldspar and carbonates, with particles size typically less than 60 μm [*Gueguen and Palciauskas*, 1994]. Burial, chemical diagenesis, and cementation reduce the pore size of these fine-grained deposits. Chemical reactions and even changes in clay mineralogy at the high temperature and pressure conditions can result in further chemical compaction [*Nygard et al.*, 2004].

Clay minerals are phyllosilicates that crystallize, typically in small-size platy grains <10μm [*Mitchell and Soga*, 2005; *Sposito*, 1989]. Clay minerals control the mechanical and transport properties of shales. The mean pore size of shales ranges from 5nm to 100nm, porosity from ~1% to 12%, and permeability from $10^{-22}m^2$ to $10^{-19}m^2$ [*Armitage et al.*, 2010; *Katsube and Williamson*, 1994; *Watson et al.*, 2005].

The forces acting on clay particles can be grouped into [*Santamarina*, 2001; *van Oort*, 2003]: (1) mechanical, including effective stress, seepage-drag, capillarity, and cementation forces; and (2) electrical, including van der Waals attraction, electrostatic Born repulsion, and electrical forces due to surface hydration and osmotic effects. Because of their physico-chemical nature, electrical forces depend on the pore fluid chemistry.

7.2.2 Electrical forces

The surface charge of clay particles is pH dependent: the abundance of H^+ at low pH promotes protonation leading to positively charged surfaces ([*Lyklema*, 1995; *Santamarina et al.*, 2001a; *Stumm*, 1992]. Note: implications of acidification, such as in CO_2 storage, on clay fabric are discussed in [*Palomino and Santamarina*, 2005]).

Hydrated ions are attracted to the charged clay surfaces and form the diffuse counter-ion cloud; the ensuing interparticle repulsion increases with the pore fluid relative permittivity κ' and it is inversely proportional to the pore fluid ionic strength c_0. When water-saturated clay dries, counter ions bind to the particle surface and excess salts precipitate. The discrete nature of molecules, short-range Born repulsion and periodically varying hydration forces must be considered at interparticle distances smaller than ~2nm [*Israelachvili*, 1991; *van Oort*, 2003]. Finally, van der Waals interactions give rise to attraction forces between clay minerals; this force is proportional to the Hamaker constant which is a function of the permittivity of the fluid and minerals involved.

Changes in pore fluid chemistry (ionic concentration c_0, pH, relative permittivity κ') and their impact on electrical interactions have complex consequences on the sediment hydraulic and mechanical properties. Clearly, the role of these surface phenomena is proportional to the specific surface of the clay sediment.

7.2.3 Capillary forces: interfacial tension and contact angle

The water-CO_2 interfacial tension is pressure-temperature dependent. It decreases from T_s~72 to 25 mN/m as the pressure increases from 0.1MPa to 6.4MPa at ~298K. Eventually T_s reaches a plateau at T_s =25±5 mN/m in the supercritical CO_2 state; high salinity can increase the interfacial tension by up to 10 mN/m [*Chalbaud et al.,* 2009; *Espinoza and Santamarina,* 2010a]. The contact angle formed by the CO_2-water interface on the mineral surfaces also varies with fluid pressure in response to changes in CO_2-water interfacial tension: as the fluid pressure increases to reservoir conditions, the contact angle increases on oil-wet amorphous silica (θ~85° to 95°), coal (θ~50° to 120°) and mica (θ~40° to 60°) and slightly decreases in water-wet amorphous silica and calcite surfaces (θ~40°) [*Chalbaud et al.,* 2009; *Chi et al.,* 1988; *Chiquet et al.,* 2007; *Dickson et al.,* 2006; *Espinoza and Santamarina,* 2010a]. Together, interfacial tension T_s and contact angle θ determine the magnitude of capillary phenomena ($T_s \cdot \cos\theta$). The interaction between capillary phenomena and mechanical stress is critical to evaluate hydro-mechanical couplings [*Alonso et al.,* 1990].

7.2.4 Particle forces and strains

Let's estimate the effect of water displacement by CO_2 on interparticle interactions. The capillary force computed for a water meniscus between two platy particles thickness t, slenderness $\beta=l/t$ and specific surface $S_s=2(1+2/\beta)/t\rho$ in a shale with porosity n is (assume contact angle $\theta\sim0°$),

$$F_{cap} = S_s \rho T_s \frac{1-n}{n} l^2 = S_s \rho T_s \frac{1-n}{n} \beta^2 \left[\frac{2(1+2/\beta)}{S_s \rho} \right]^2 \tag{7.1}$$

The average force carried by a particle with slenderness β being part of the granular skeleton subjected to an effective stress σ' is

$$F_{sk} = \sigma' \left(\frac{\beta^2}{1-n} \right)^{2/3} \left[\frac{2(1+2/\beta)}{S_s \rho} \right]^2 \tag{7.2}$$

Therefore, the ratio between these forces is

$$\frac{F_{cap}}{F_{sk}} = \rho T_s \frac{S_s}{\sigma'} \frac{(1-n)^{5/3}}{n} \frac{\beta^{2/3}}{(1+2/\beta)} \tag{7.3}$$

On the other hand, the colinearity of electrical forces and skeletal forces hinders a force-based comparison. Instead, let's estimate the impact of a reduction δ in interparticle separation s as a result of the decrease in electrical repulsion forces and increase in van der Waals attraction. The corresponding strain is

$$\varepsilon = \frac{\delta \, S_s \rho}{2} (1-n) \tag{7.4}$$

Fig. 7.2 shows a plot of the force ratio F_{cap}/F_{sk} and of the shrinkage strain ε versus specific surface in the context of carbon geological storage. We identify two zones:

- Reservoir domain: grains are large ($d>10^{-6}$m), rotund, and the specific surface is low. Contact forces F_{sk} due to effective stress prevail (Note: capillarity and mixed

fluid flow conditions do affect fluid flow in this regime). Electrical forces effects are negligible.

- Cap rock domain: Capillary forces and physico-chemical interactions gain relevance when small particles are involved as in the cap rocks ($d<10^{-6}$m). Specific surface $S_s=2/(d\cdot\rho_m)$ [m^2/g] is an adequate physical quantity for characterizing platy fine grained sediments and it is intimately linked to the clay composition in the cap rock (e.g., S_s~400-700 m^2/g for montmorillonite, 50-100 m^2/g for illite and 5-10m^2/g for kaolinite [*Mitchell and Soga*, 2005; *Santamarina et al.*, 2002; *Van Olphen*, 1977]).

Cap rock conditions at CO_2 storage sites currently being considered are superimposed on the figure. It can be concluded that physico-chemical effects must be taken into consideration when high specific surface clayey rocks are selected as cap rocks for CO_2 storage.

7.3 Study of electrical forces - Sedimentation tests

Observations in the previous section showed the importance of physico-chemical effects in clayey cap rocks. The purpose of this section is to further explore differences in clay behavior in non-polar CO_2 versus polar water. Sedimentation tests are used to magnify the effects of electrical interactions between fine grained clay particles.

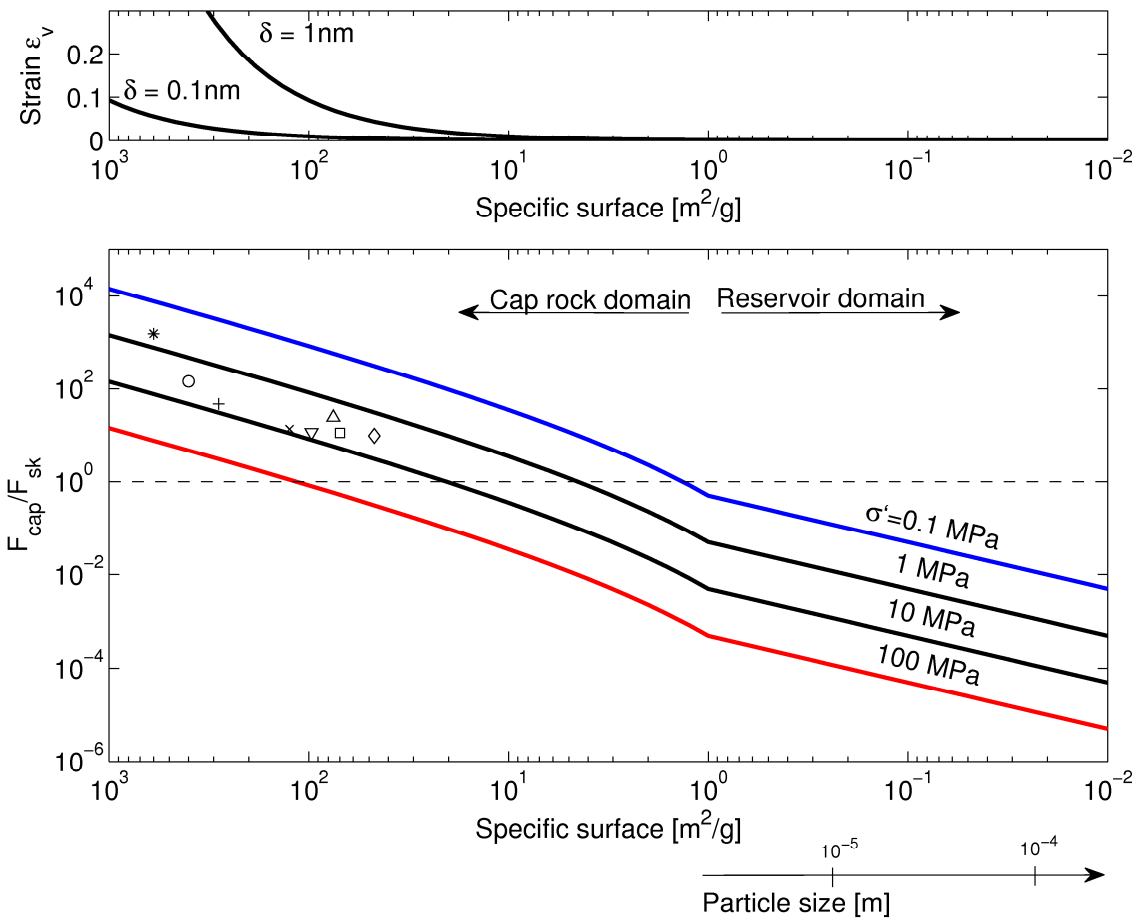

Figure 7.2 Particle scale analysis of CO_2 storage formations: ratio of capillary to skeletal forces (Eq. 3) and strain due to reduction in interparticle distance with changes in electrical forces (Eq. 4 – initial porosity 0.3) versus specific surface. The response of high specific surface clay particles that form the cap rocks is governed by capillary and electrical forces. The interaction between the coarser particles that form the reservoir is governed by interparticle contact forces that result from effective stress. The symbols represent conditions of cap rocks at Frio (○), Sleipner (×), Krechba (□) and Otway (◊), SACROC (*), Rousse (△), Carnarvon (+), Ketzin (▽). In each case, the specific surface is estimated from reported clay composition, and the effective stress is estimated from the overburden depth (details and references in Table 7.1). The particle slenderness is assumed to be β for S_s<1m^2/g and β =(log(S_s/(0.1m^2/g))$^{2.5}$ for S_s>1m^2/g.

7.3.1 Device, materials, and experimental procedure

Sedimentation tests were conducted in a polycarbonate tube (effective height 95mm, ID = 6.35mm and OD = 19.0mm) held between aluminum caps, and sealed with buna-N o-rings (Fig. 7.3-a). Pressure transducers and thermocouples track pressure-temperature conditions. Time-lapse photography is used to monitor and record all experiments.

Two clays were selected for this study: kaolinite SA1 (1:1 clay provided by Wilkinson; details in [*Palomino*, 2003]) and calcium montmorillonite (2:1 clay, montmorillonite-rich bentonite provided by the American Colloid Company). Sedimentation tests were conducted with different polar and non-polar fluids including deionized/deaerated water, brine consisting of 2M NaCl aqueous solution, heptane (Fisher Scientific), and research grade CO_2 (Airgas). Table 7.2 and 7.3 summarize the physical properties of the clays and fluids used in these experiments. Depending on the selected fluids, we performed experiments at atmospheric pressure and at 7-12MPa (see Table 7.3).

The experimental procedure consists of five sequential steps: (1) fill the tube with clay (~0.060g, i.e., the solids volume fraction is less than 0.01), (2) remove adsorbed water on the clay with vacuum and heat, (3) fill the tube with the selected fluid (2-3 ml), (4) shake the cell to thoroughly mix the fluid and clay into a colloidal suspension, and (5) place the tubes vertically, allowing the clay to settle at the bottom of the tubes. This procedure is repeated several times for each clay-fluid combination (2 clays and 5 fluids, see Table 7.4). We measure the settling rate, sedimentation height, and observe particle

agglomeration and flocculation following the test procedure outlined in [*Palomino*, 2003].

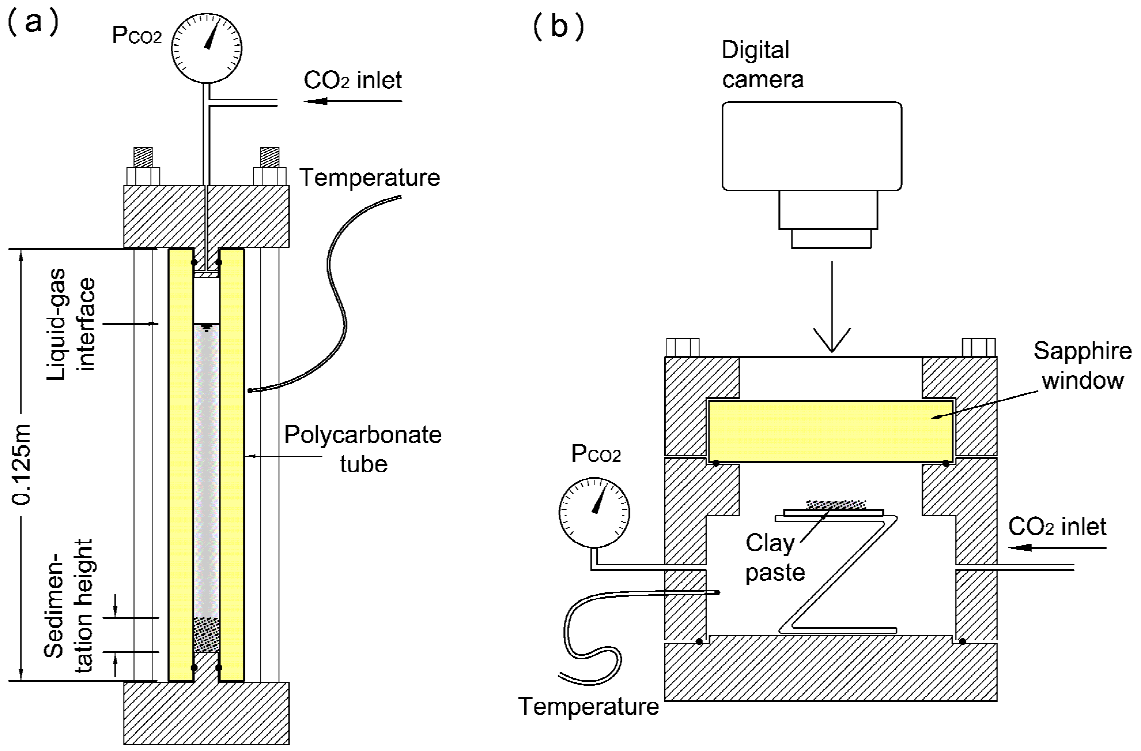

Figure 7.3 Schematic views of experimental devices. (a) Sedimentation tube (ID=6.35mm): the transparent polycarbonate tube is held between by two aluminum caps with buna-N o-rings; external transducers measure pressure and temperature. (b) High pressure chamber equipped with a see-through sapphire window: the clay slurry is placed on a glass slide; the large volume of the chamber compared to the volume of the slurry allows a significant water mass to dissolve into the $scCO_2$ that fills the chamber.

Table 7.2 Physical properties of the clays used in these experiments.

Physical property	Kaolinite	Montmorillonite
Mineralogy	1:1	2:1
Specific surface* S_s[m^2/g]	50-55	610-670
Particle thickness** t [m]	15×10^{-9}	1×10^{-9}
Specific gravity G_s [ ]	2.6	2.7
Liquid limit*** LL [%]	45	250
Relative permittivity κ' (a)	5.1	5.5
Refractive index n (b)	1.56	1.5

Notes: (*) measured with methylene blue spot technique [*Santamarina et al.*, 2002]
(**) estimated from $t\sim2/(S_s\rho_w G_s)$
(***) fall cone test
Refs.: a- [*Robinson*, 2004]
b- [*Leach et al.*, 2005; *Weidler and Friedrich*, 2007]

Table 7.3 Physical properties of the fluids used for sedimentation experiments.

Physical property (Test condition)	**Water** (0.1MPa, 298K)	**Brine, 2M NaCl** (0.1MPa, 298K)	**Heptane** (0.1MPa, 298K)	**Supercritical CO_2** (12MPa, 313K)	**Liquid CO_2** (7 MPa, 298K)
Density ρ [kg/m^3]	997	1072 (a)	680 (g)(b)	719 (c)	745 (c)
Viscosity η [Pa·s]	0.90×10^{-3}(a)	1.08×10^{-3} (a)	0.386×10^{-3} (b)	0.059×10^{-3} (d)	0.0620×10^{-3} (d)
Polarity	Polar	Polar	Non-polar	Non-polar	Non-polar
Relative permittivity κ' at 1-10 GHz [ ]	78.5 (e)	56 (f)	1.92 (g)	1.43 (h)	~1.4 (m)
Refractive index n	1.333 (e)	~1.36 (n)	1.385	1.167 (h)	1.167 *
Solubility of water [mol H_2O / mol fluid]	NA	NA	$0.5\text{-}0.6\times10^{-3}$ (k)	4.5×10^{-3} (j)	2.9×10^{-3} (j)
Interfacial tension with water T_s [N m]	NA	NA	0.051 (o)	0.028 (p)	0.030 (q)

Note.: (*) Assumed
Refs.: a - [*Zhang and Han*, 1996];
b - [*Aucejo et al.*, 1995];
c - [*Span and Wagner*, 1996];
d - [*Fenghour et al.*, 1998];
e - [*Israelachvili*, 1991];
f - [*Buchner et al.*, 1999; *Santamarina et al.*, 2001b];
g - [*Friiso and Tjomsland*, 1997];
h - [*Obriot et al.*, 1993; *Sun et al.*, 2003];
j - [*Spycher et al.*, 2003];
k - [*Polak and Lu*, 1973; *Susilo et al.*, 2005]
m - [*May et al.*, 2005];

n - [*Maykut and Light*, 1995].
o - [*Zeppieri et al*., 2001]
p – [*Kvamme et al.*, 2007b]
q – [*Espinoza and Santamarina*, 2010a]

7.3.2 Results

Sedimentation patterns, such as final sediment height, floc size and sedimentation mode, change noticeably with different pore fluids; these characteristics are summarized in Table 7.4. For example, montmorillonite remains in suspension for days in distilled water, but it aggregates and settles in a matter of seconds in supercritical CO_2 (Fig. 7.4). Details follow.

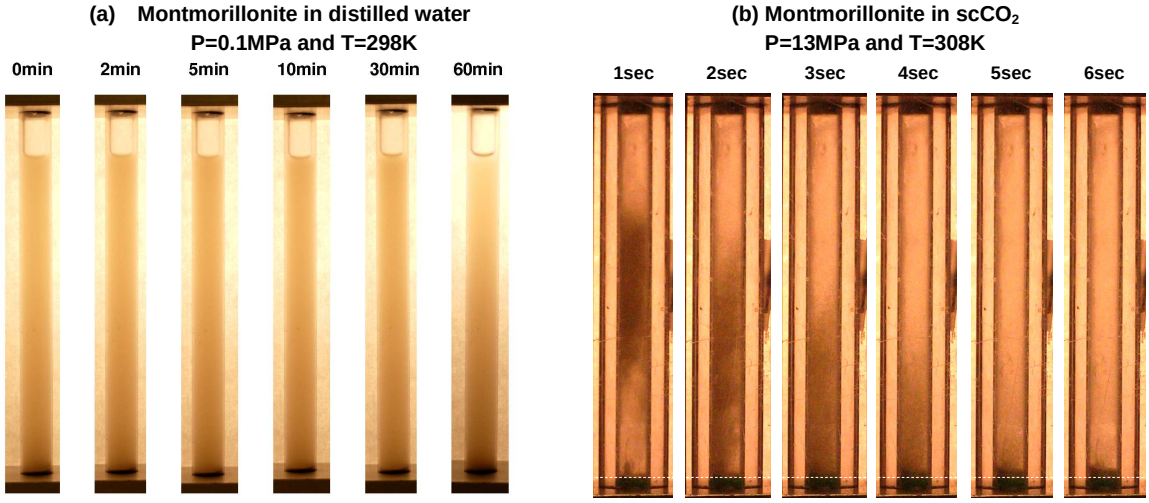

Figure 7.4 Pictures of montmorilonite settling (a) in distilled water and (b) in supercritical CO_2. Notice the pronounced difference in time scales. Montmorillonite particles remain dispersed in suspension for days when the pore fluid is deionized water, however, they readily form 50-150µm size observable flocs in $scCO_2$ and settle in few seconds. This pronounced difference reflects the role of governing electrical interparticle forces.

Flocculation/Aggregation. Clay particles remain dispersed in distilled water, but flocculate in brine. The diameter of kaolinite and bentonite aggregations in brine is

inferred from Stokes' law (laminar regime expected at low sedimentation velocity), $d_{eq}=[18v_s\mu g^{-1}(\rho_{floc}-\rho_{fluid})^{-1}]^{1/2}$ = 50-to-140 µm, and it is two orders of magnitude larger than the actual particle size. In this estimations, the assumed floc density is $\rho_{floc}=\rho_f n+\rho(1-n)$, where ρ_f is the fluid mass density, ρ is the mineral mass density and n is the final sedimentation porosity).

Both kaolinite and montmorillonite show extensive particle aggregation when suspended in low permittivity fluids (heptane, liquid CO_2 and supercritical CO_2 - see Table 7.4 and Fig. 7.4 and 7.5). Due to fast sedimentation, floc sizes are determined from image analysis and range from ~90-to-600µm for kaolinite and up to 160µm for montmorillonite.

Sediment final porosity. The final sediment height is used to compute the sediment final porosity from the total volume V_T corresponding to the final sedimentation height h and the volume of solids V_S (values in Table 7.4):

$$n=\frac{V_T-V_S}{V_T}=1-\frac{M_{clay}/\rho}{1/4\cdot\pi D^2 h} \tag{7.5}$$

where M_{clay} is the clay mass, ρ is the mass density of the clay mineral, and D is the tube inside diameter. Results are plotted in Figure 7.5. Salient remarks follow:

(a) *Kaolinite.* The final porosity n~0.9 does not show a consistent trend with changes in fluid permittivity κ' or ionic concentration c_0. Flocculation in heptane or CO_2 creates large void spaces. (Note: porosity results for $scCO_2$ are biased because increased attraction forces produce particle attachment to the walls of the polycarbonate tube).

(b) *Montmorillonite*. The sediment porosity is maximum n~0.99 for clays submerged in deionized water. Porosity decreases for low fluid permittivity k' or high ionic concentration c_0.

Table 7.4 Summary of sedimentation results.

Fluid	Water	Brine	Heptane	Liquid CO_2	Supercritical CO_2
Kaolinite M_{clay} =0.060g					
Number of experiments	12	6	4	5	2
Final height h [mm]	6.3 (5.3-7.9)	6.7 (6.2-7.5)	8.9 (8.0-9.5)	7.1 (6.7-7.5)	3.3** (3.0-3.6)
Floc size [µm]	3-30	15-20	370-610	280-550	88-220
Sedimentation mode*	Dispersed sedimentation	Flocculated	Flocculated free	Flocculated free (flocs attach to polycarbonate)	Flocculated free (flocs attach to polycarbonate)
Montmorillonite M_{clay}=0.056g					
Number of experiments	5	3	3	4	4
Final height h [mm]	NA cloudy	6.0 (5.5-6.2)	2.0 (1.9-2.1)	2.7 (2.4-2.9)	2.4 (2.0-2.7)
Floc size [µm]	<0.7	15-40	41-165	47-94	47-142
Sedimentation mode*	Dispersed Sedimentation	Flocculated	Flocculated	Flocculated free	Flocculated free

Note: * see sedimentation mode details in [*Palomino*, 2003]
** result biased by clay attachment to the tube walls.

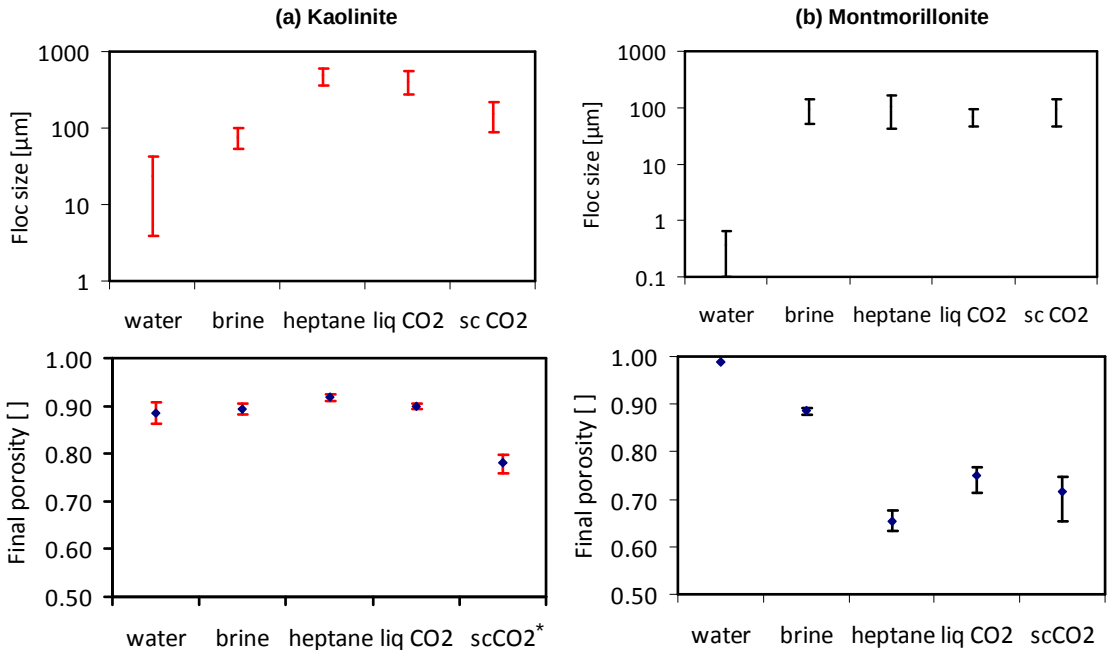

Fluid permittivity	78.5	56	1.385	1.167	1.167
A_h [10^{-20} J]	1.57	1.24	0.84	4.20	4.20
Double layer	large low c_0	short high c_0	none	none	none
Aggregation	disper -sed	face to face	edge to edge		

78.5	56	1.385	1.167	1.167
0.98	0.73	0.42	3.14	3.14
large low c_0	short high c_0	none	none	none
disper -sed	face to face			

Figure 7.5 Sedimentation test results: floc size and final porosity. The floc size in water and brine is computed using Stokes' law and it is evaluated by direct visual measurement in heptane and CO_2. The Hamaker constants for mineral-fluid-mineral systems are calculated using Lifschitz theory (permittivity and refractive index values in Table 7.1). Notice the low sedimentation porosity of montmorillonite in supercritical CO_2. Significant particle flocculation is observed in both kaolinite and montmorillonite in liquid and supercritical CO_2.

7.3.3 Analysis

Forces between suspended clay particles are governed by electrical interactions. The double layer repulsion force can be estimated as

$$F_{rep} = 16\pi RTc_0 d^2 e^{-\frac{t}{\zeta}} \qquad \text{for large } t > 2 \text{ nm} \qquad (7.6)$$

Where d is the diameter of the disk-shaped particles [m], t is the distance between discs [m], R=8.314 J/(mol·K) is the ideal gas constant, T is absolute temperature [K], c_0 is the bulk fluid ionic concentration [mol/L], and ζ is the Debye-Hückel length for a 1/e decay of the Stern potential [*Mitchell and Soga*, 2005; *Santamarina et al.*, 2001b]. This length can be estimated as

$$\zeta = \sqrt{\frac{1}{2}\frac{\varepsilon_0 \kappa' RT}{c_0 z^2 F^2}} \tag{7.7}$$

where ε_0=8.854·10^{-12} C^{2}J^{-1}m^{-1} is the real permittivity of the vacuum, κ' is the relative permittivity of the solution, z is the valence of the ion, and F=96485.3 C/mol is the Faraday constant.

On the other hand, the van der Waals electrostatic attraction force F_{Att} between two disc-shaped clay particles with diameter d suspended in a fluid with Hamaker constant A_h is [*Israelachvili*, 1991; *Santamarina et al.*, 2001b],

$$F_{att} = \frac{1}{24} A_h \frac{d^2}{t^3} \tag{7.8}$$

where t is the separation between the two particles. The Hamaker constant A_h depends on the dielectric permittivity of the medium which can be estimated from Lifschitz theory in terms of the relative permittivity κ' and the refractive index $n_{m,f}$ of the mineral m and the fluid f [*Israelachvili*, 1991],

$$A_h = \frac{3}{4} k_B T \left(\frac{\kappa'_m - \kappa'_f}{\kappa'_m + \kappa'_f} \right)^2 + \frac{3h\nu_e}{16\sqrt{2}} \frac{\left(n_m^2 - n_f^2\right)^2}{\left(n_m^2 + n_f^2\right)^{3/2}} \tag{7.9}$$

where k_B=1.38×10^{-23} J/K is Boltzmann's constant, T[K] temperature, h=6.626×10^{-34} J·s is Planck's constant, and ν_e~3×10^{15} Hz is the assumed relaxation frequency. The calculated

values for the various clay-fluid systems under consideration including montmorillonite and kaolinite in water, brine, heptane, and CO_2 are shown in Fig. 7.5.

The two electrical forces F_{rep} and F_{att} control the tendency for clay particles to agglomerate. Repulsion F_{rep} vanishes in non polar fluids (i.e., salts do not dissolve and ions do not hydrate). On the other hand, the Hamaker constant and F_{att} are higher in CO_2 than in water (mainly due to differences in the refractive index n). While a higher Hamaker constant explains the flocculation of kaolinite and montmorillonite in CO_2, significant kaolinite and montmorillonite flocculation is observed in heptane regardless of the computed low Hamaker constant due to the absence of repulsive double layer effects. Indeed, the combined F_{rep} and F_{att} forces predict a decrease in repulsion with increasing c_0 and decreasing κ'. In particular, flocculation in non-polar fluids stems from high attractive forces in the absence of repulsive double layer forces.

The mean interparticle distance t can be approximated from the sediment porosity n or void ratio e and the platelet thickness w, assuming a parallel platelets fabric,

$$t = \frac{n}{1-n} w = ew \tag{7.10}$$

In the case of montmorillonite, the mean interparticle distance is t~100 nm for the high porosity sediment in deionized water (n=0.99) and t=2 nm for the low final porosity measured in heptane and CO_2 (n~0.7) assuming w_{mont}~1nm. In the case of kaolinite, the mean interparticle distance is t~135nm for the high porosity sediment in deionized water (n~0.88) and t=35nm for the low porosity measured in heptane and CO_2 (n~0.7) assuming w_{kaol}~15nm. Therefore, volumetric contraction is expected as CO_2 displaces water from the clay pore space.

7.4 Study of capillary forces - Desiccation tests

The particle level analysis presented earlier suggested the emergence of relevant capillary phenomena in clayey cap rocks in the presence of water and CO_2. A special test is designed to corroborate the emergence of capillary phenomena within the sediment as the water-CO_2 interface invades the sediment pore space. In these tests, "water drying" results from the solubility of water in supercritical CO_2, as ~5×10^{-3} mol of water can dissolve per mol of CO_2 at 16MPa and 313K, this is ~1.5g of water per liter of CO_2.

7.4.1 Device, materials, and experimental procedure

Three independent experiments were carried out in a stainless steel chamber equipped with a see-through sapphire window at temperatures ranging from 308-to-313K and pressures ~16MPa. The internal volume of the cylindrical chamber is 210 cm^3 – Fig. 7.3-b. A pressure transducer and a thermocouple are used to monitor pressure and temperature conditions inside the chamber and time-lapse photography is used to observe the evolution of the clay paste.

The test procedure follows: (1) place a 1.5cm^3 montmorillonite paste mixed with a 0.1M NaCl, at an initial water content =1000%, on a glass slide inside the chamber (initial volume ~1.5 cm^3), (2) remove air and inject "dry" CO_2 (research grade - Airgas), and pressurize to the target pressure-temperature conditions (supercritical), (3) monitor changes in the clay paste at steady temperature and pressure. Periodically, we replaced the "wet" CO_2 with dry CO_2 under pressure.

7.4.2 Results

The clay paste contracted and cracked in the three experiments. Snapshots in Fig. 7.6 show images gathered at various stages in one test. During the first 48 hours, water dissolves into CO_2 and causes a significant volume contraction without cracking (not shown in the figure); later on, as more water dissolves into the supercritical CO_2, desiccation cracks gradually emerge (Fig. 7.6).

For the specific case shown in Fig. 7.6, the initial height of the clay slurry patch is ~4mm, with an initial void ratio $e_0 = \omega G_s/S = 10\times2.7/1 = 27$. After desiccation, the thickness of the thin clay crust is ~0.4mm and shows a horizontal contraction of ~20%. Thus, the volume has contracted almost 12 times. The final void ratio of the clay crust pieces is about e=1.2 (porosity n~0.55) and the mean interparticle distance is $t = ew$ ~1nm.

7.4.3 Analysis

The initiation mechanism for desiccation cracks can be explained within an effective stress framework [*Shin and Santamarina,* 2010]. The initial sediment compaction during desiccation follows 1D consolidation: suction causes the water-CO_2 interface to squeeze the clay paste. Thus, the void ratio decreases as suction P_{CO2}-P_w increases,

$$e = e_{1\text{kPa}} - C_c \log\left(\frac{P_{CO2} - P_w}{1\text{kPa}}\right) \qquad (7.11)$$

where the consolidation parameters for this montmorillonite clay are C_c = 0.46 and $e_{1\text{kPa}}$ = 3 (blue line in Fig. 7.6-b). Eventually, as the differential pressure between water and CO_2 increases, the increasing clay stiffness prevents further consolidation; instead, the water-

CO_2 interface invades the water saturated clay. The capillary entry value for parallel clay platelets, is computed using Laplace's equation and the separation between platelets $t=2e/(S_s\rho)$ as a function of the clay specific surface S_s and its mineral mass density ρ,

$$P_{CO2} - P_w\big|_{\max} = \frac{\rho\, T_s \cos\theta\, S_s}{10^{\alpha} e} \tag{7.12}$$

where the coefficient 10^{α} accounts for the pore size distribution within the clay mass $\alpha=\log(d^*)/\log(d_{mean})$. Clay particles remain water-wet in the presence of CO_2 (hydrophilic with θ~40 to 60° in silica surfaces – section 7.1.3). Capillary forces are primarily normal to the water-CO_2 interface in the funicular regime. Then, CO_2 invasion alters the distribution of particle forces from vertical-dominant during consolidation, to transverse-dominant at invasion points leading to crack formation.

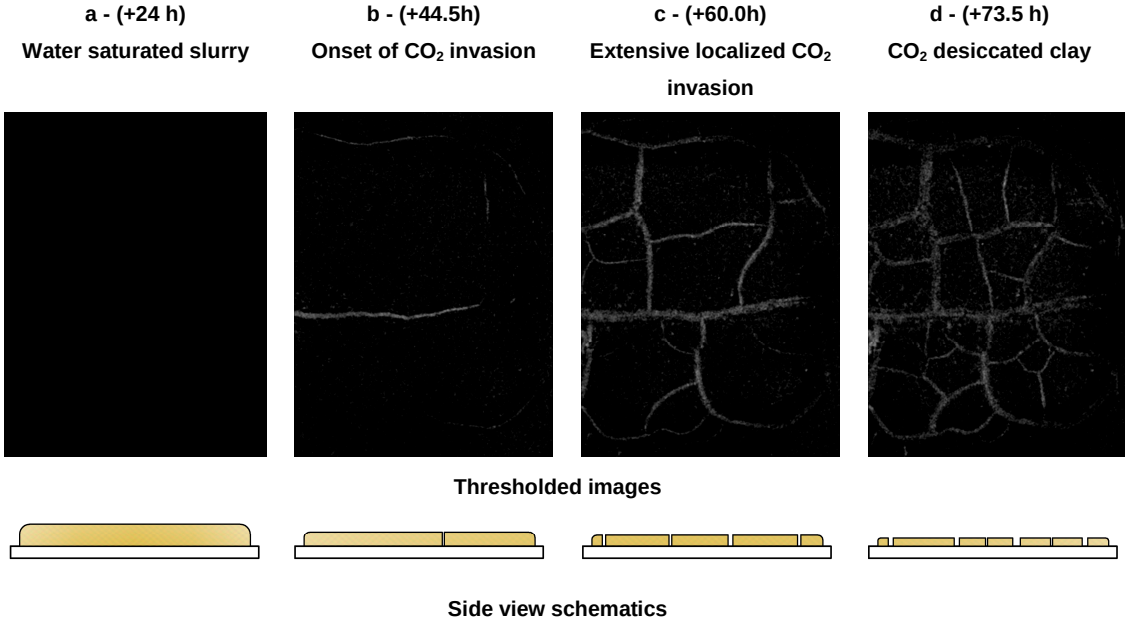

Figure 7.6 Montmorillonite-water slurry subjected to a supercritical CO_2 atmosphere (15MPa, 311K). Time lapse photography and associated sketches show the evolution of desiccation and the formation of capillary-driven fractures. The water-CO_2 interface initially "compresses" the sediment until supercritical CO_2 invades the sediment locally and triggers desiccation cracks.

Fig. 7.7 shows in red a set of capillary entry value curves for different values of α>0 (capillary entry always starts at the largest voids). We can conclude that: (1) capillary entry and crack initiation cannot be explained considering a uniform pore size distribution (α=0) in these experiments as P_{CO2}-P_w should exceed 40MPa; (2) CO_2 capillary entry starts at the largest voids, such as surface imperfections; (3) non-cracked clay patches remain water saturated; and (4) CO_2 capillary drying reduces the clay porosity to levels equivalent to thousands of meters of overburden.

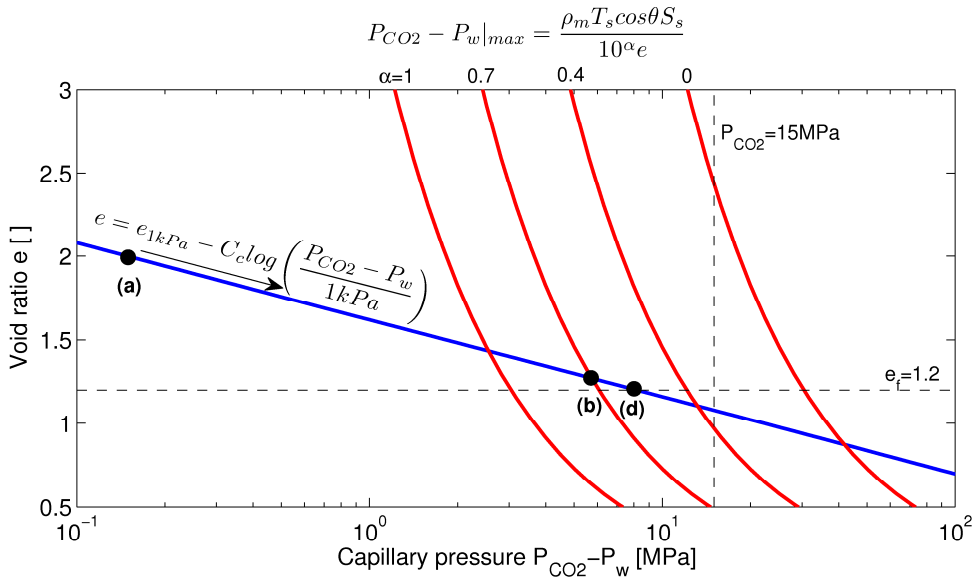

Figure 7.7 Effective stress analysis of desiccation crack initiation. The clay slurry starts at a high void ratio (point a which corresponds to Fig 7.6-a) and follows the clay normal consolidation line (blue line) as it is compressed by the CO_2-water interface. The water-CO_2 interface invades the sediment when it reaches conditions that satisfy the capillary entry curve (red lines for different α values where 10^{α} takes into account a log normal pore size distribution). Eventually, higher water suction forces the water-CO_2 interface to invade the sediment pore space (say point b for α=0.7). Interface invasion occurs at larger pores first, hence, these are nucleation sites for fracture initiation. The process ends when the mutual CO_2- water solubility is reached (point d which corresponds to Fig. 7.6-d). Capillary-driven fractures will not form if the original effective stress is higher than the effective stress where the capillary entry curve and the normal consolidation line meet.

7.5 Discussion and implications

7.5.1 Implications for geological carbon storage sites

The buoyancy of $scCO_2$ in water creates a static overpressure of 0.27MPa to 0.4MPa for a 100m column of CO_2 where ρ_{CO2} depends on in-situ pressure-temperature conditions (ρ_{CO2}~720kg/m^3 at P=16MPa and T=324 K; ρ_{CO2}~590kg/m^3 at P=16MPa and T=339K). The CO_2 column height depends the reservoir thickness, geometry, and injectability (capillary and viscous effects). The additional injection overpressure may gradually dissipate in time, in part due to CO_2 dissolution in water, reservoir hydrogeology and convective effects. The pressure discontinuity at the seal layer must be resisted by the seal layer.

Fractures, faults, and existing wellbores are major discontinuities that favor CO_2 leakage. In addition, the cap rock sealing capacity might be compromised by: (1) hydraulic fracture, (2) fault reactivation by reservoir overpressure [*Chiaramonte et al.*, 2008; *Rutqvist and Tsang*, 2002], (3) aqueous CO_2 diffusion into water at the cap rock (without bulk CO_2 invasion) and consequent water acidification and mineral dissolution [*Berne et al.*, 2010; *Gaus et al.*, 2005; *Gherardi et al.*, 2007; *Shin et al.*, 2008]; and (4) CO_2 invasion into the cap rock, capillary breakthrough, and CO_2 advection [*Angeli et al.*, 2009b; *Hildenbrand et al.*, 2004; *Li et al.*, 2005; *Wollenweber et al.*, 2010]. The assumptions of seal structural integrity lead to an "upper bound seal capacity" estimate.

The experimental study presented above highlight that additional electrical and capillary effects that may be involved in CO_2 invasion of the cap rock and offer insight related to changes in electrical forces and the emergence of capillary suction.

Summary of electrical effects in the cap rock. Published studies and new results presented in this manuscript are combined to anticipate potential effects of CO_2 on cap rocks:

- The double layer thickness tends to be thin on cap rock minerals surrounded by high salinity water ~1 to 2M [pore fluid characteristics from *Gaus et al.*, 2005; *Gherardi et al.*, 2007].
- Water will be displaced from the large pores by the invasion of CO_2 and locally reduce the osmotic repulsion effects.
- Free ions will migrate with the displaced water, yet counterions will remain to satisfy electroneutrality in addition to brine in the form of residual saturation in smaller pores [see molecular simulations in *Cole et al.*, 2010].
- The residual interparticle water dissolve in CO_2, the ionic concentration will increase, osmotic repulsion decrease, and excess salts will precipitate. CO_2 and precipitated salts will fill the interparticle space and dominate the interaction between clay platelets.
- There will be a four-fold increase in the Hamaker constant for clay-CO_2-clay as compared to clay-water-clay systems.
- Water will acidify due to CO_2 dissolution in water, and changes in pH will modify the surface charge of clay particles. Changes in pH, ionic concentration, and Hamaker constant combine to cause fabric changes that can be analyzed in a pH-c_0 fabric map [*Santamarina et al.*, 2001b].

While these effects are magnified in high specific surface clays like montmorillonite, the same effects will take place in other clays but moderated by particle size, and possible differences in surface charge (silica and gibbsite faces).

Summary of capillary effects in the cap rock. Desiccation tests show the effects of mutual water-CO_2 solubility, interfacial tension, the emergence of suction, and the ensuing capillary-driven contraction and possible open-mode fracture development. Capillary driven fractures will not develop in high effective stress and low porosity cap rocks (to the right of the capillary entry curve – Fig. 7.7). Given typical values of clay consolidation parameters (e_{1kPa}, C_c) and specific surface S_s [*Burland*, 1990a; *Santamarina et al.*, 2001a] and disregarding diagenetic cementation, we anticipate that capillary-driven fractures will not happen in kaolinite-, chlorite- or illite-rich shales at a burial depth greater than 1km. However, smectite-rich shales may be prone to capillary-driven fracture at depths less than ~4km. The sequence of possible events is captured in Fig. 7.8.

- The water-CO_2 interface reaches the cap rock and the sediment compresses,
- capillary pressure overcomes the entry pressure for CO_2 p_{CO2}(entry) at surface imperfections and invades the largest pores;
- desiccation fracture nuclei may develop depending on effective stress conditions;
- a percolating CO_2 path forms and CO_2 breaks through the medium, this path typically connects pores bigger than the mean [Chapter 3],
- Further CO_2 flow into the pore space will occur through CO_2 advection, water dissolves into $scCO_2$ (cap rock dehydration), suction increases further, accompanied by additional sediment contraction, and interparticle water eventually vanishes causing salt precipitation.

Related effects relevant to reservoir rocks. A relatively small fraction of clay minerals can affect the performance of reservoir rocks in CO_2 storage projects. Fines control

hydraulic properties if they exceed a critical clay mass fraction where clay particles fill all the voids between the coarse-grained sediment skeleton; this critical clay mass fraction m_{clay}/m_{total} can be estimated from the void ratio of the coarse e_{coare} and fines e_{clay} as:

$$\frac{m_{clay}}{m_{total}} = \frac{e_{coarse}}{1 + e_{coarse} + e_{clay}} \tag{7.13}$$

Critical clay mass fractions can be as low as m_{clay}/m_{total} = 10% for montmorillonite and up to 20% for kaolinite.

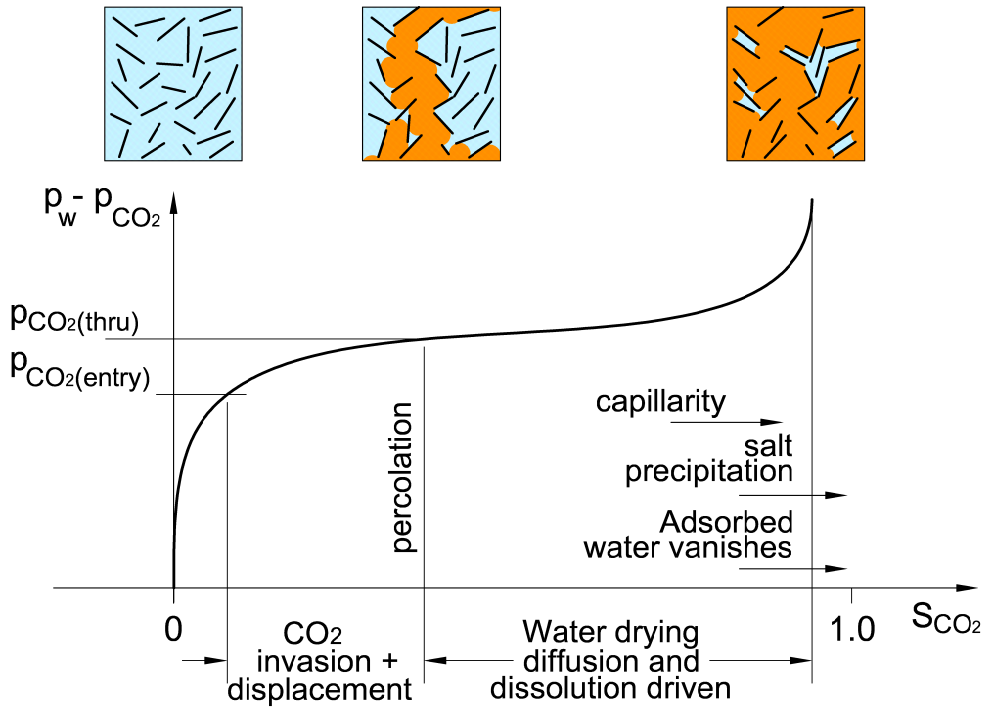

Figure 7.8 CO_2 invasion into water saturated cap rocks: capillary pressure and relative CO_2 saturation. As suction increases: (1) the sediment compresses, (2) capillary pressure overcomes the entry pressure; (3) desiccation fracture nuclei may develop, (4) a percolating path forms and CO_2 breaks through the medium, (5) water dissolves into $scCO_2$, suction increases further and interparticle water eventually vanishes causing salt precipitation.

The injection of CO_2 into reservoirs may favor clay detachment from mineral surfaces (acidification and change in surface charge) or attachment (increased Hamaker constant). CO_2 may also open clay-filled pores by capillary driven contraction. Overall, we expect an increase in permeability in clayey sandstones during CO_2 invasion. In fact, experimental evidence shows that the permeability of clay rich sandstones increases almost six fold when flushed with CO_2 instead of water [*Rimmele et al.*, 2010]. The permeability of clay-filled fractures and faults will also be adversely affected by clay sensitivity to CO_2 and this situation should be assessed carefully to estimate leakage potential.

7.6 Conclusions

CO_2 geological storage is one alternative for reducing greenhouse gas emissions. Evaporites and shales will act as seal layers and retain pressurized and buoyant CO_2. The assumptions of seal structural integrity and homogeneity lead to upper bound estimates of the sealing capacity from intact non-fractured rock properties. Clay minerals play a fundamental role in shale seal layers. Because of the charged surfaces of clay, the pore fluid between clay platelets can readily affect the hydraulic and mechanical properties of shale, e.g. permeability and osmotic repulsion.

Sedimentation experiments and analyses show that: (1) clay flocculates when submerged in CO_2, (2) montmorillonite sedimented in CO_2 has a lower porosity than montmorillonite sedimented in brine as a result of decreased osmotic repulsion, and (3) there is a four-fold increase in the Hamaker constant from clay-water-clay to clay-CO_2-clay systems which indicates higher attraction forces when CO_2 invades clay rich rocks.

Desiccation experiments and analyses show that: (1) the capillary forces that develop upon fluid invasion can trigger open-mode fractures if the effective stress is lower than the effective stress at which the capillary entry value curve and normal consolidation line meet, (2) pore size distribution plays a critical role in the initiation of fractures, and (3) cap rock may be moderately dehydrated upon the injection of dry CO_2.

Despite the apparent high sealing capacity of shales, CO_2 might breakthrough the cap rock at elevated pressure gradients, facilitated by the low CO_2-water interfacial tension at high pressure. Once it breaks through, continuous flow will be determined by the cap rock permeability and low CO_2 viscosity. We anticipate that CO_2 invasion, breakthrough, and continuous flow will likely be accompanied by (1) volumetric contraction, because of increased suction and reduced osmotic repulsion, (2) increased permeability because of clay platelet tighter aggregation, (3) cap rock dehydration, and (4) capillary-driven fractures under low effective stress conditions. These consequences may hinder the sealing capacity of cap rocks.

Phenomena discussed in this manuscript have been individually confirmed/observed using either experimental or theoretical methods. Yet, the complex interplay between chemo-hydro-mechanical processes may lead to positive feedback mechanisms that can either degrade (e.g., platelet collapse → increase in pore size → further fluid conduction) or self-stabilize (e.g., water dissolution in CO_2 → salt precipitation from brine → porosity reduction) the cap rock seal capacity.

We can conclude that good shale seals have a high specific surface, are subjected to a high effective confining stress, have low porosity and uniform pore size distribution,

are saturated with a high ionic concentration brine, and form a thick and continuous seal layer.

CHAPTER 8

CO_2 BREAKTHROUGH IN CLAY BARRIERS - IMPLICATIONS FOR CAP ROCK SEALING CAPACITY AND INTEGRITY IN CARBON GEOLOGICAL REPOSITORIES

8.1 Introduction

Carbon geological storage is one alternative to help mitigate the emission of greenhouse-gas carbon dioxide CO_2 into the atmosphere [*IPCC*, 2005]. Carbon capture and geological storage involves CO_2 capture at large point sources, transportation, and injection into a suitable geological formation. Most carbon storage target sites considered to date involve high permeability rocks and unconsolidated sands, as CO_2 repositories, overlaid by a low permeability formation that serves as a sealing layer. Although the gas and oil industries currently possess the technology to inject CO_2 underground, significant improvements in the understanding of trapping mechanisms, chemo-hydro-mechanical coupled effects, and leak estimations are needed before carbon geological storage can be decisively adopted.

CO_2 is lighter than water at the pressure and temperature conditions in most target formations. The uppermost part of the formation closest to the CO_2 injection well will have high CO_2 saturation while the lower and lateral boundaries will contain mostly CO_2 acidified water [*Kneafsey and Pruess*, 2010]. CO_2 buoyancy creates a differential pressure proportional to the CO_2 plume thickness and mass density difference, e.g. 0.27MPa (if ρ_{CO2}~720kg/m^3) to 0.4MPa (if ρ_{CO2}~590kg/m^3) for a 100m column of CO_2, where ρ_{CO2} depends on in-situ pressure-temperature conditions (Fig. 8.1-a). The shape of

the CO_2 pool depends on the reservoir physical and geometric properties (e.g., entry value, permeability, layering, homogeneity, and dipping), and injection conditions (e.g. fingering). An additional excess pressure remains in the CO_2 after injection unless water-extraction wells are operated concurrently with CO_2 injection [*Bergmo et al.*, 2011; *Ehlig-Economides and Economides*, 2010]. Buoyancy and injection-related excess-pressure must be resisted by the overlying sealing formation or cap rock.

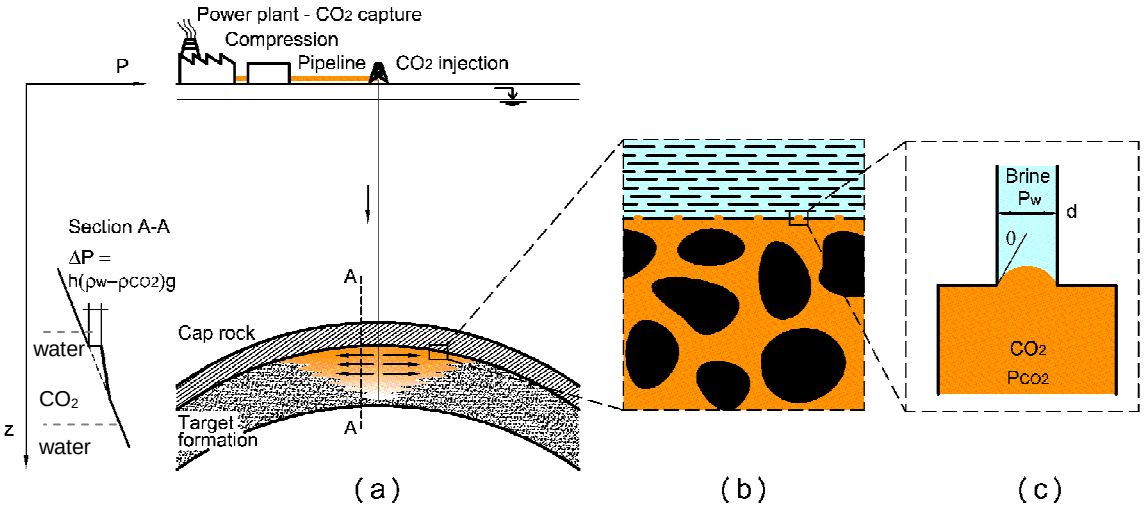

Figure 8.1 Carbon geological storage. (a) Schematic of a fossil fuel plant equipped with CO_2 capture technology and CO_2 delivery to the injection point: deep geological formation overlaid by a cap rock. (b) CO_2-water capillary menisci form the repository meets the cap rock; these menisci at small pore throats hold the buoyant CO_2. (c) Capillary tube analogy in water-wet minerals.

Cap rocks are the critical component for long-term CO_2 sequestration underground. For example, a leak of 3 kg/m^2 per year is enough to saturate in a time frame of ~100 years the pore water in a shallow 100m column of soil with porosity ~0.4; this will drive the pH to ~3.5 and trigger mineral dissolution. However, the thickness of the CO_2 pool would decrease in only ~2cm. Two of the main macro-characteristics of a

good seal layer are continuity and ductility [*Downey*, 1984]. Faults, fractures, and existing wellbores are major discontinuities and may result in preferential paths for CO_2 leakage. Ductility allows cap rock deformation without fracturing.

Flow through the "intact" cap rock is hindered by capillary and viscous forces (Fig. 8.1). However, the cap rock sealing capacity may degrade in time due to: (1) hydraulic fracture and fault reactivation by reservoir overpressure [*Chiaramonte et al.*, 2008; *Rutqvist and Tsang*, 2002], (2) aqueous CO_2 diffusion into cap rock water (without bulk CO_2 invasion) and consequent water acidification and mineral dissolution [*Berne et al.*, 2010; *Gaus et al.*, 2005; *Gherardi et al.*, 2007; *Shin et al.*, 2008]; and (3) CO_2 invasion into the cap rock, capillary breakthrough, and CO_2 advection [*Angeli et al.*, 2009b; *Hildenbrand et al.*, 2004; *Li et al.*, 2005; *Wollenweber et al.*, 2010]. For example, extensive mineral dissolution and precipitation has been reported at natural CO_2 reservoirs [*Allis et al.*, 2001; *Watson et al.*, 2004], and evidence of remineralization has been observed in the time frame of decades at enhanced oil recovery sites [*Emberley et al.*, 2004; *Gunter et al.*, 2000; *Kaszuba et al.*, 2005]. Other less known couplings include: (1) reactivity of water dissolved in CO_2 [*McGrail et al.*, 2009], (2) changes in electrical balance between clay particles due to water acidification and water displacement by CO_2, (3) emergence of capillary forces, and (4) cap rock dehydration and volumetric contraction [in this thesis - Chapter 7].

CO_2 may be transported by advection or diffusion through the intact cap rock. Furthermore, the development of a percolating CO_2 phase, and cap rock permeability and thickness are critical factors for assessing post-breakthrough CO_2 transport [*Fleury et al.*, 2010; *Gherardi et al.*, 2007]. The low viscosity of CO_2 and the low interfacial tension of

water-CO_2 interfaces inherently enhance the risk of leaks. Clay and shale cap rocks, commonly assumed as perfect seals, may present non-negligible CO_2 conductivity.

The purpose of this study is to analyze the transport of CO_2 through well-characterized consolidated sediments, estimate potential leaks in cap rocks, and explore geotechnical implications. To reach these objectives, we run a parametric CO_2 pressure breakthrough experimental study involving various sediments saturated with water and brine, and developed analytical models. Finally, we use the new findings to anticipate reservoir scale implications. In this study we assume that the seal is structurally sound and homogeneous; these simplifications allow us to estimate an "upper bound seal capacity". Degradation of the cap rock sealing properties may lead to CO_2 leaks. Such failure would facilitate the escape of CO_2 to overlaying layers and destabilize other trapping mechanisms (CO_2 dissolution and mineral trapping).

8.2 Fundamental concepts, physical properties, and previous studies

8.2.1 CO_2-water properties

The physical properties of CO_2 depend on pressure and temperature conditions. CO_2 mass density ρ_{CO2} varies widely and can be calculated with a proper equation of state [*Span and Wagner*, 1996]; values at reservoir depths greater than 1000m range from ~500 kg/m^3 to 800kg/m^3. Other important pressure-temperature dependent properties of CO_2 include high bulk compressibility typically an order of magnitude higher than that of water, and very low viscosity, typically 10 times lower than that of water, $\mu_{CO2}=10^{-4}$ Pa·s at 10MPa and 280K [*Fenghour et al*., 1998]. CO_2 is electrically non-conductive [*Tanaka et al.*, 2008].

The water-CO_2 interfacial tension is pressure-temperature dependent. It decreases from T_s~72 to 25 mN/m as the pressure increases from 0.1MPa to 6.4MPa at ~298K, and eventually plateaus at T_s =25±5 mN/m when CO_2 is in the supercritical state [*Kvamme et al.*, 2007b]. High salinity levels can increase the interfacial tension by 10 mN/m [*Espinoza and Santamarina*, 2010a]. The contact angle formed by the CO_2-water interface on mineral surfaces also varies with fluid pressure in response to changes in CO_2-water interfacial tension: as the fluid pressure increases to reservoir conditions, the contact angle increases on oil-wet amorphous silica (θ~85° to 95°), coal (θ~50° to 120°) and mica (θ~40° to 60°) and decreases slightly in water-wet amorphous silica and calcite surfaces (θ~40°) [*Chalbaud et al.*, 2009; *Chi et al.*, 1988; *Chiquet et al.*, 2007; *Espinoza and Santamarina*, 2010a].

CO_2 dissolves in water to form aqueous carbon dioxide. The solubility of CO_2 in water x_{CO2} [mol/L] can be estimated using Henry's law $x_{CO2} = k_H \varphi P_{CO2}$, where the Henry's coefficient is approximately k_H≈0.035 and the fugacity coefficient φ≤1 can be estimated with an equation of state [*Stumm and Morgan*, 1996]. Water at room temperature and 0.1MPa may contain up to x_{CO2}≈0.03-to-0.04 mol of CO_2 per liter of water. Solubility increases by two orders of magnitude x_{CO2}≈1-to-2 mol/L as pressure and temperature increase to reservoir conditions.

8.2.2 Cap rocks and clay minerals

Shales and evaporites commonly serve as cap rocks for hydrocarbon accumulations. The trapping ability of cap rocks depends on physical and geometrical properties: high capillary pressure, ductility, homogeneity, lateral continuity, and

thickness [*Downey*, 1984]. Different types of trapping configurations include: anticlines, fault traps, stratigraphic traps, and other diagenetic traps, such as tar and gas hydrate seals [*Dikkers*, 1985; *Downey*, 1984]. Table 8.1 shows a compilation of petrographical properties of shale and evaporite cap rocks at selected carbon storage sites. Shales are sedimentary rocks made of clay minerals, fine-grained quartz, feldspar and carbonates, with particle size less than 60 μm [*Gueguen and Palciauskas*, 1994].

Table 8.1 Petrographical properties of cap rocks at selected carbon storage sites. Most seal layers are shales, evaporites or a layered sequence of the two.

Site	Depth (over-burden)	Cap rock thickness	Reservoir thickness	Dominant minerals	Porosity	Pore size distribution	Permeability	CO_2 breakthrough pressure
Frio, USA [*Hovorka*, 2009; *Lynch*, 1997; *Sakurai et al.*, 2006]	1450 m	75 m	12 m	Illite-smectite ~45% Illite ~10% Kaolinite 13% Chlorite ~3% --- Calcite	8-10%	-		1.7 MPa*
SACROC, USA [*Carey et al.*, 2007; *Han et al.*, 2010]	2000 m	150 m	150 m	62% Illite-smectite --- Calcite 2.5% Dolomite 2% --- 0.1% Halite	1.3%	-	<50nD perpendicular to bedding	-
Mississippi, USA (Esposito et al 2008)	3480 m 1800 m	-	-	Oil reservoirs capped by anhydrite Upper saline aquifers capped by shales	-	-	-	-
Salt creek, USA [*Benison and Goldstein*, 2000; *Chiaramonte et al.*, 2008].	1650 m	-	-	Mix of evaporites and shales	-	-	-	-
Weyburn, Canada [*Li et al.*, 2005]	3800 m	-	-	Mostly anhydrite --- Dolomite traces	0.2-0.5%	-	6-25 nD	5-11.2 MPa
Sleipner, Norway [*Bøe and Zweigel*, 2001; *Chadwick et al.*, 2004; *Pilliteri et al.*, 2003]	750 m	100 m	250 m	Mica-Illite ~25% Kaolinite 14-18% Smectite 3-9% Chlorite 1-4% --- Calcite 1-3%	35%	45-55% particles < 2μm	-	-

				Siderite 2%				
Rousse, France [*Tonnet et al.*, 2011]	4000 m	2000 m	400 m	Illite 2.2-14.5% Kaolinite 0.3-4.1% Chlorite 0.1-2% --- Calcite 30-65% Dolomite 3-63% Siderite 0.1-6.2%	0.5-3%	Primary porosity: d=1-100µm and secondary porosity d~10nm	<1nD at σ'>10MPa	2.25-3MPa† and >7.6 MPa
Ketzin, Germany [*Förster et al.*, 2007]	600 m	85 m	20 m	Iliite 42-74% Chlorite 1-3% --- Dolomite 4-35% --- Halite (small fraction)	10%	Pore bodies <500nm and pore throats 10-36nm	<10nD	-
K12-B, Netherlands [*Vandeweijer et al.*, 2011]	3750 m	-	-	Anhydrite and halite	-	-	-	-
Otway, Australia [*Watson et al.*, 2005]	1980 m	-	-	Kaolinite 44-17% Illite 6-1% Smectite 3-1% --- Siderite 35-2%	~ 2.5-7.5%	-	-	1-2MPa*
Carnarvon, Australia [*Dewhurst et al.*, 2002]	1100 m	-	-	Illite-smectite 30-25% Illite 15-20% Kaolinite ~15% Chlorite ~5% --- Siderite 1-4%	21%	µ~17nm* (fit curve from Dewhurst Henning) 40% particles less than 2µm	-	3-4 MPa*
Krechba, Algeria [*Armitage et al.*, 2010; *Mathieson et al.*, 2010]	1850 m	950 m	20 m	Muscovite-illite ~25-50% Chlorite ~20-4% Kaolonite ~8-4% --- Siderite ~15-0%	1.8-11.3%	µ ~5-236 nm (low porosity layers)	-	-

Notes: * capillary threshold pressure converted from mercury ($T_{s\ Hg\text{-}air}$=0.485 N/m) to CO_2 ($T_{s\ CO2\text{-}water}$=0.025 N/m)
† converted from nitrogen ($T_{s\ N2\text{-}brine}$=0.057 N/m)) to CO_2 ($T_{s\ CO2\text{-}water}$=0.025 N/m)

Clay minerals are phyllosilicates that crystallize in small-size platy grains (<10µm) [*Mitchell and Soga*, 2005; *Sposito*, 1989]. The surface charge of clay particles is pH dependent: low pH promotes protonation, leading to positively charged surfaces

[*Lyklema*, 1995; *Santamarina et al.*, 2001a; *Stumm*, 1992]. Hydrated ions are attracted to charged clay surfaces, form a diffuse counter-ion cloud, and promote interparticle osmotic repulsion. One dimensional consolidation parameters (e_{1kPa}, C_c), and the specific surface S_s of clays allow us to estimate porosity and pore-size at a given effective stress [*Burland*, 1990b; *Santamarina et al.*, 2001a]. A cursory analysis readily shows that clay minerals control the mechanical and transport properties of shales because of their high specific surface.

Burial (mechanical compaction), chemical diagenesis, and cementation reduce the pore size and throats of these fine-grained deposits. Chemical reactions are favored at the high temperature and pressure conditions found at great depth, and result in further chemical compaction; for example, smectite changes to illite at temperatures higher than ~60°C and kaolinite may transform to illite or chlorite at 135°C under the right pore fluid conditions [*Nygard et al.*, 2004]. The porosity of shales ranges from ~1% to 12%, the mean pore size ranges from 5nm to 100 nm, and permeability ranges from $10^{-22}m^2$ to $10^{-19}m^2$ [*Armitage et al.*, 2010; *Katsube and Williamson*, 1994; *Watson et al.*, 2005].

8.2.3 CO_2-water in natural porous media – Chemo-hydro-mechanical phenomena

*Breakthrough pressure.*The capillary entry pressure (P_{CO2}-P_w) for a water-CO_2 interface in an ideal porous medium comprised of a bundle of cylindrical pores with diameter d is,

$$P_{CO2} - P_w = \frac{4T_s \cos\theta}{d} \tag{8.1}$$

where T_s is the interfacial tension between water and CO_2 and θ is the contact angle formed by the water-CO_2 interface on the mineral surface. The CO_2 displaces the water and breaks through the medium when (P_{CO2}-P_w) is exceeded. Real sediments and rocks

have a non-uniform pore size distribution. Most sediment pore structures follow a log-normal distribution. Some fine grained sediments exhibit a dual porosity made of micro and nanopores [*Lloret et al.*, 2003]. Thus, the critical pressure for breakthrough depends on the pore size distribution and connectivity. Table 8.2 shows a compilation of breakthrough studies and results.

Table 8.2 Previous gas breakthrough experimental studies.

Medium	**Fluid**	**CO_2 breakthrough pressure[MPa]**	**Permeability [10^{-21} m^2]**	**Reference**
Bentonite blocks	He	2.6-6.25 †	5-30	[*Horseman et al.*, 1999]
Claystone and mudstone	N_2	0.03-2.9 †	3-550	[*Hildenbrand et al.*, 2002]
Shale, marl, limestone, and sandrock	CO_2, CH_4 and N_2	0.1-4.9	~0-89	[*Hildenbrand et al.*, 2004]
Limestone and clay rich marl	CO_2 and He	0.74 (limestone) ~0.5 (marl)	~0.5 (limestone) ~3 (marl)	[*Wollenweber et al.*, 2010]
Evaporite	CO_2, CH_4 and N_2	21-5	6-70	[*Li et al.*, 2005]
Marl	CO_2 and N_2	>7.6	20 to <1	[*Tonnet et al.*, 2010; *Tonnet et al.*, 2011]
Shale	CO_2	3.5 to 4	60	[*Angeli et al.*, 2009b]

† Converted from nitrogen ($T_{s\ N2\text{-}water}$=0.057 N/m) or Helium ($T_{s\ He\text{-}water}$=0.068 N/m), to CO_2 ($T_{s\ CO2\text{-}water}$=0.025 N/m)

The CO_2 breakthrough pressures are less than ~7MPa in clayey rocks and less than ~21MPa in evaporite rocks. Higher capillary pressures could be anticipated in these tight sediments, assuming mean pore size in Eq. 8.1, however, these breakthrough experimental data gathered for various types of rocks point to the fact that breakthrough percolating paths connect pores larger than ~5nm. Further analysis of these results shows

that the percolating path that breakthroughs clays typically connects pores with diameters greater than the mean pore size [*Espinoza and Santamarina*, 2010a]

Mineral dissolution. Quartz presents the lowest reactivity to acidified water. Carbonates are among the minerals with highest reaction rate when exposed to low pH and may experience significant dissolution. Minerals such as anorthite, phlogopite, and kaolinite show intermediate chemical reactivity with CO_2-acidified water when compared to calcite and quartz [*Li et al.*, 2006; *Shao et al.*, 2010]. Silicates yield more dissolved cations than carbonates do, but their reaction rates are slower [*Gunter et al.*, 2000]. The reactivity of evaporites and CO_2 is negligible - see [*Dusseault et al.*, 2004]).

Electrical forces. Cap rocks are water saturated. Clay-forming cap rocks react to changes in the surrounding pore fluid. As opposed to water, CO_2 is a non-polar, low permittivity fluid. Hence, a change in the electrical equilibrium of the forces acting on clay particles is expected as CO_2 fills the pore space, including: a reduction in osmotic repulsion, residual water dissolution in CO_2 and salt precipitation, and a four-fold increase in the Hamaker constant for clay-CO_2-clay as compared to clay-water-clay [this thesis – Chapter 7]. These effects take place in all clays and are magnified in high specific surface clays like montmorillonite.

Suction and volumetric changes. The mechanical properties of clay sediments are sensitive to water saturation, dependent suction, leading to phenomena such as swelling during wetting [*Alonso et al.*, 1990; *Sánchez et al.*, 2005] and volumetric contraction and

even desiccation cracks during drying [*Espinoza et al.*, 2011; *Shin and Santamarina*, 2010]. A change in suction *ds* produces a change in the void ratio *de* that it is proportional to the suction compressibility coefficient κ_s (generally κ_s<0.01 for clays) and inversely proportional to the current suction [*Alonso et al.*, 1990],

$$de = -\kappa_s \frac{ds}{(s + p_{at})} \tag{8.2}$$

Where p_{at}=0.1MPa is the atmospheric pressure.

Relative permeability and residual saturation. The sediment permeability, water saturation, and viscosity control the advective transport of CO_2 after breakthrough. The residual water saturation is a critical parameter [*Pentland et al.*, 2011]. The relative permeability of CO_2 in cap rocks is commonly assumed because there is a lack of experimental data.

8.3 Device, materials, and experimental procedure

8.3.1 Device

We designed a multi-cell high-pressure oedometer system to apply a constant vertical effective stress σ'_v [MPa] up to 3MPa, and withstand pore-fluid pressures up to 20MPa (Fig. 8.2). The oedometers are machined out of stainless steel rods and sealed with buna-N o-rings. Effective stress is provided by a steel spring. These cells are designed to impose a radial fluid pressure gradient, from the periphery towards the drainage tube at the center of the specimen. This design seeks to minimize leaks between the specimen and chamber walls in standard 1D permeameters. The chamber accommodates sediment specimens with diameter d_c~40mm and height h~35mm. We

measure: (1) the input CO_2 pressure P_{in}[MPa] = P_{CO2} at the periphery at the reservoir side, (2) the exit pressure P_{out}[MPa] = $P_{w,}$ i.e., the water side (before breakthrough), (3) the amount of water displaced during CO_2 invasion m_w [m^3], (4) the flow of CO_2 through the sediment q_{CO2} [m^3/s], and (5) the vertical deformation of the sediment specimen Δz to cumpute volumetric strain $\varepsilon_v=\Delta z/h$. An auxiliary water-filled transparent pressure cell connected to the exit port is used to observe CO_2 leaks in the form of bubbles exiting the discharge pipe.

8.3.2 Materials

We prepared homogeneus specimens made of: fine sand F110 (U.S. Silica), precipitated calcium carbonate PCC (Imerys), crushed calcium carbonate CCC (Hubercarb), kaolinite SA1 and RP2 (Wilkinson), and bentonite (GEL - PureGold). Some specimens were mixed with deionized water and others with brine (2 mol of NaCl per kg of water). CO_2 research grade purity (Airgas) was used in all tests. Table 8.3 summarizes the parametric study and materials involved in all tests.

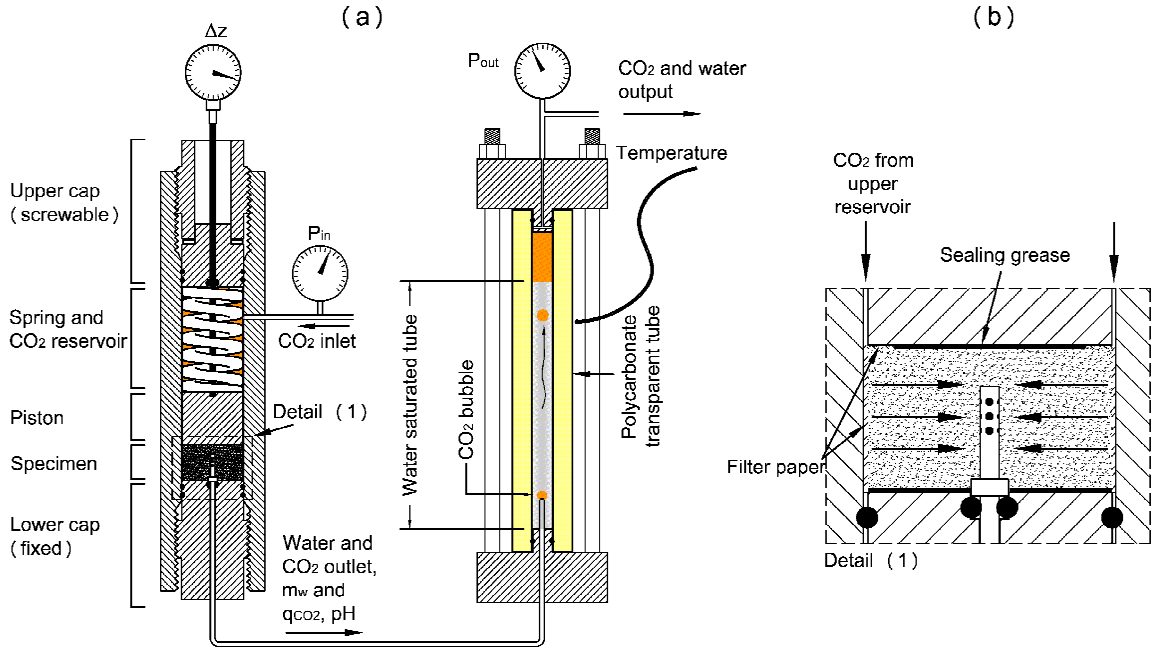

Figure 8.2 Experimental device. (a) Specimens are compacted within a high pressure oedometer to impose a zero lateral strain bound condition. The space above the piston hosts a heavy-load spring which applies constant vertical effective stress to the sediment, serves as a CO_2 "reservoir". The complimentary observation chamber on the right allows for CO_2 flow rate estimations. Pressure tranducers, dial gauges, and pipettes are used to measure pressure P_{in}, P_{out}, settlement Δz, water displacement m_w, and CO_2 flow rate q_{CO2}. (b) Close up of the sediment plug boundary conditions.

8.3.3 Procedure

The water/brine and soil mixture is first consolidated in stages to an effective stress $\sigma`_v$~0.4MPa. Sediment pieces are cut to fit the pressure cell. Filter paper is placed in between the oedometer walls and the specimen to create homogeneus peripheral boundary flow condition. A sealing grease that is non-reactive with CO_2 (Goop, Swagelok) is placed on the lower and upper pistons to prevent transport through these interfaces. Once in the cell, the specimen is consolidated to an effective stress $\sigma`_v$~2MPa. Then, we increase the inlet pressure P_{in} to cause CO_2 radial invasion into the sediment.

After each injection-pressurization cycle, the inlet valve is closed and the inlet pressure P_{in} is monitored in time. Each pressure stage finishes when the settlement Δz and the volume of displaced water m_w approach an asymptotic trend. Eventually, CO_2 breakthroughs, and CO_2 flow rate q_{CO2} are monitored thereafter. Most experiments were carried out with an atmospheric backpressure at the outlet port P_{out}=0.1MPa.

After breakthrough, CO_2 is circulated through the sediment to measure the evolution of CO_2 permeability k_{CO2}. Finally, selected specimens are subjected to high resolution local electrical resistivity profiling (more details in [*Cho et al.*, 2004]) and magnetic resonance imaging MRI 3D (Bruker Pharmascan 7T – bme.gatech.edu/mri) to analyze the spatial distribution of CO_2 within the pore structure. The electrical resistance at the tip is computed from external voltage measurements [*Cho et al.*, 2004],

$$R_{tip} = \frac{V_{meas}}{V_{in} - V_{meas}} R_{known} \tag{8.3}$$

where the imposed input voltage is V_{in}=1Vpp (100kHz sinusoidal wave), and the known resistance used is R_{known}=2.2kΩ. The needle is driven at 2mm/min and data are collected at rate of 12 samples/min. Thus, the spatial resolution is ~150μm.

Table 8.3 Sediments used in this study – properties.

Sediment	Specific surface S_s [m^2/g]	Mineral density ρ_m [kg/m^3]	Mean grain size d_{50}	Saturating pore fluid	Number of independent experiments	Void ratio at breakthrough e
Sand F110	0.02	2650	110 μm	Deionized water	5	0.85
CCC	0.25	2700	8μm	Deionized water	3	0.60
PCC	10	2710	1 μm	Deionized water	1	1.2
Kaolinite clay SA1	13	2600	1.1 μm	Deionized water	5	0.6-0.7
Kaolinite clay RP2	21.9	2600	0.36 μm	Brine 2M	1	0.73
Montmorillonite clay	320	2500	-	Brine 2M	4	0.69

8.4 Results and analyses

A total of 12 experiments were completed as part of this study. A typical time-response is presented first, followed by a compilation of results to identify common trends and behavior. Fig. 8.3 shows typical system signatures, which are explained in the next sections.

8.4.1 Typical response - breakthrough pressure

Let's define the breakthrough pressure P^* as the minimum pressure that causes CO_2 to percolate through the sample. In order to identify this threshold value, the pressure gradient is gradually increased in stages. Following each differential pressure increase, the CO_2-water interface compresses the sediment and squeezes water $dm_w/dt > 0$. If the differential pressure ΔP is below the breakthrough pressure ΔP, $\Delta P < P^*$, volume contraction and water displacement decay gradually towards $dm_w/dt \sim 0$ and $dz/dt \sim 0$. When the differential pressure exceeds the breakthrough pressure $\Delta P > P^*$, CO_2 breaks

through, there is a rapid decrease in ΔP and CO_2 starts leaking through the exit pipe $q_{CO2}>0$.

Fig. 8.3 shows the response of a kaolinite specimen. The CO_2 pressure is gradually increased in stages (Fig. 8.3a). At low pressures; the clay plug contracts but does not allow for CO2 flow so that it performs as a perfect seal (Fig. 8.3b). The pressure finally reaches $\Delta P>P^*$after day ~70, there is a sudden rise in CO_2 flow (Fig. 8.3c) and water flow vanishes (Fig. 8.3b). The CO_2 flow rate reaches a peak and then decays due to the decrease in the pressure gradient (no additional CO_2 is injected into the reservoir tank).

Fig. 8.3d shows the evolution of the volume average void ratio with time, which is computed from the sediment strain $\varepsilon_z= \Delta z/h$ and initial void ratio e_0, $e=e_0 - \varepsilon_z(1+e_0)$. The change in void ratio depends on the sediment compressibility (parameters C_c and e_{1kPa}).

8.4.2 CO_2 advective flow after breakthrough

We estimate water permeability k_w from the time rate of consolidation during initial loading and early CO_2 pressurization stages before breakthrough. The sediment permeability to CO_2 after pressure breakthrough k_{CO2} is estimated using the measured CO_2 flow rate q_{CO2}[kg/s] and assuming axisymmetric flow towards the central collecting pipe,

$$k_{CO2} = \frac{q_{CO2}}{2\pi\, h} \frac{\mu_{CO2}}{\rho_{CO2}\left(P_{in} - P_{out}\right)} \ln \frac{d_c}{d_p} \qquad (8.4)$$

where μ_{CO2}[Pa s] is the average CO_2 viscosity (typically 1.6×10^{-5}Pa·s to 1.7×10^{-5}Pa·s at laboratory temperature and P<5MPa), ρ_{CO2}[kg/m^3] is the CO_2 average mass density

across the specimen, h is the specimen height, P_{in} and P_{out} are the upstream and downstream pressures, d_c~40mm is the specimen diameter, and d_p=3.17mm is the collecting pipe diameter.

Fig. 8.3c shows the measured CO_2 flow rate q_{CO2} and Fig. 8.3e the estimated CO_2 permeability k_{CO2} for a kaolinite specimen. Notice that permeability increases after breakthrough because CO_2 flushing gradually decreases the specimen water saturation.

8.4.3 Post-test forensic analysis

We carefully inspected all specimens after dismantling the oedometers. All but bentonite specimens exhibited visual and mechanical integrity. One bentonite specimen showed a visually observable crack at the base. Electrical resistivity profiles and magnetic resonance data follow.

Electrical resistivity profiles. A 1D electrical needle probe (diameter 1.27mm; electrode separation ~0.3mm), is used to gather high resolution electrical resistivity profiles of the sediment plugs after breakthrough. The sediment electrical resistivity Ω_{sed} increases with decreasing sediment porosity n and increasing CO_2 saturation S_{CO2},

$$\Omega_{sed} = \Omega_w \frac{1}{n(1 - S_{CO2})} \tag{8.5}$$

Where Ω_w is the resistivity of the aqueous solution.

Results for a kaolinite plug are shown in Fig. 8.5. Higher resistivity values are measured towards the center of the specimen where the CO_2 flow rate is higher (radial flow conditions). These electrical resistivity profiles in this and most other tested specimens point to consistent desiccation near the exit pipe.

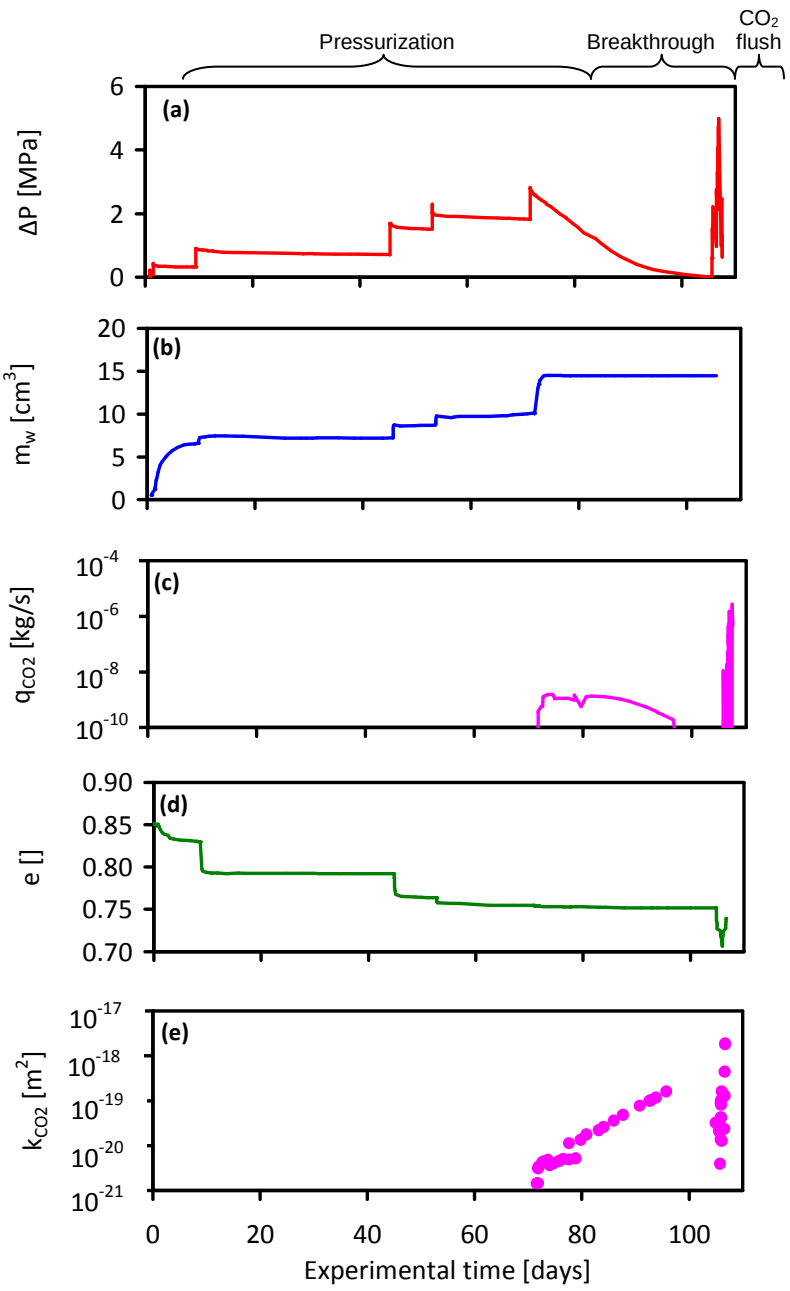

Figure 8.3 Typical experimental signals. From top to bottom: differential pressure $\Delta P=P_{in}-P_{out}$ (P_{out} is the back pressure); displaced water mass m_w; CO_2 flow rate q_{CO2}, specimen void ratio $\Delta e=f(\Delta z)$, and CO_2 permeability k_{CO2}. As CO_2 pressures increases, it invades the porous medium and displaces water $m_w>0$; eventually CO_2 percolates and flows freely through the specimen $q_{CO2}>0$. Capillary suction promotes volumetric contraction $de/dt<0$. Specimen: kaolinite RP2.

MRI. Fig. 8.4 shows MRI images obtained for a kaolinite plug specimen that underwent CO_2 breakthrough and extensive CO_2 fluid flow after breakthrough. These images have a 350μm pixel size; The spatial resolution is coarser due to regularization strategies used for tomographic inversion. We observe a lower signal intensity at the top of the specimen, which is a result of local higher CO_2 saturation or lower porosity, or both. The water moisture gradient is symmetric and smooth. No localization of CO_2 flow is apparent from these images.

8.4.4 Parametric study

Breakthrough data. Breakthrough pressure results from all 12 experiments with different sediments are plotted as a function of the estimated average pore diameter μ (Fig. 8.5). Data are shown as intervals to capture the uncertainty in pressure gradient at the time of breakthrough. The breakthrough pressure increases as the mean pore size decreases. Capillary breakthrough values computed using Laplace's equation are superimposed on the figure,

$$P^* = \psi \frac{T_s \cos\theta}{\mu} \tag{8.5}$$

where the estimated average mean pore throat diameter is $\mu=2e/(S_s \cdot \rho)$ for fine grained sediments and $\mu=0.15 \cdot d_{50}$ for coarse grained sediments (cubic tetrahedral packing). The interfacial tension is calculated as function of pressure for the 298K isotherm and contact angle is assumed constant $\theta=40°$ [*Espinoza and Santamarina*, 2010a]. The parameter Ψ captures particle shape and fabric, and pore size distribution. Fig. 8.6 shows that a good match is obtained with Laplace's equation for $\Psi=4$ (rotund grains – tube model) and $\Psi=2$ (platy particles - parallel plates model) as an upper bound for breakthrough pressure. a)

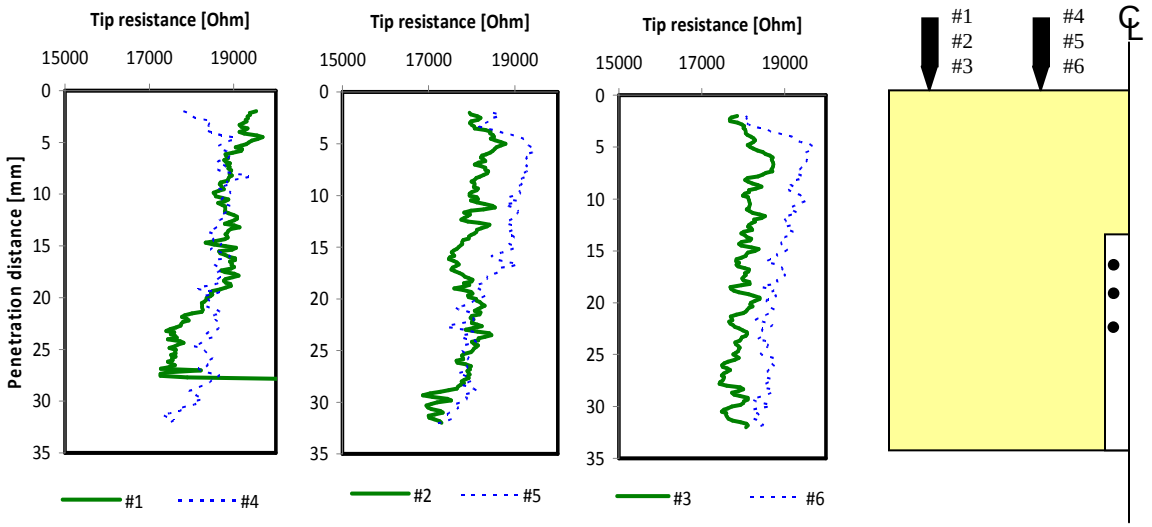

b)

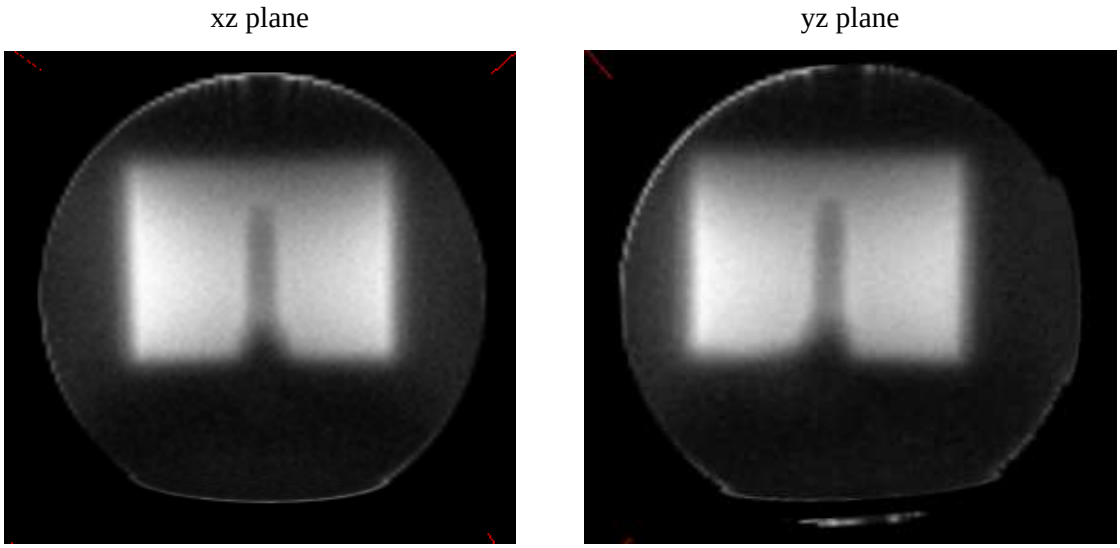

Figure 8.4 Post test completion forensic analysis of two kaolinite specimen. (a) Electrical needle probe characterization (Each signal pair 1-4, 2-5, and 3-6 are in the same plane with the center of the specimen and distributed every 120°). Desiccation near the central discharge pipe is evident from the higher electrical resistivity. (b) Tomographic reconstruction using magnetic resonance imaging; brighter colors correspond to higher water content. Water desiccation is higher in the upper part of the specimen which experiences higher CO_2 advective rates (radial flow).

Lower Ψ values matching experimental values means that either breakthrough happens in pores larger than the mean or ensuing fractures facilitate CO_2 breakthrough. In fact, the

low breakthrough values observed in bentonite are consistent with the presence of fractures observed during the forensic study. We also plot the minimum pore size ~5nm which satisfies the highest breakthrough pressures (as much as ~21MPa) measured in various rocks in the literature. We emphasize that Eq. 8.5 may predict high values of capillary breakthrough pressure P* for high specific surface and low void ratio sediments, but experimental data show that P* is much lower.

Permeability data. Fig. 8.6 shows all the water and CO_2 experimentally determined permeability data gathered in this study. The overall trend is a decrease in permeability as the mean pore size decreases. The CO_2 permeability of the clayey sediments tested in this study ranges from 10^{-21} m^2 to $10^{-18}m^2$ after CO_2 flushing. Note that the measured CO_2 permeabilities depend on water saturation. The final water saturation after breakthrough and CO_2 flushing in kaolinite ranged from S_w=0.48 to 0.92 depending on the magnitude of the applied CO_2 pressure (higher CO_2 pressure correlates with lower water saturation). The final saturation of montmorillonite specimens ranged from S_w=0.82 to 0.89.

Theoretical as well as empirical predict a change of permeability with the square of pore size. Let's consider Kozeny-Carman equation and the Hazen equation for fine- and coarse-grained sediment respecively,

$$k = \theta \frac{e}{1+e}\left(\frac{e}{S_s \rho}\right)^2 \quad \text{Kozeny-Carman} \tag{8.6}$$

$$k = C_h d_{10}^2 \qquad \text{Hazen} \tag{8.7}$$

A straight line with slope 2:1 in the log-log space superimposes to the experimentally measured permeability. We observe that the experimental values of permeability for

bentonite lie outside the theoretical trend and point to the presence of higher conductivity channels, such as fractures.

Most measured CO_2 permeabilities fall below the measured water permeabilities, implying relative CO_2 permeabilities after breakthrough and during a CO_2 flush are 10 to 100 times lower. This is not the case for bentonite specimens in which fluid-driven fractures may have developed during CO_2 pressurization.

8.4.5 Analyses of state of stresses

Low breakthrough pressure, high kCO2, and observed fractures in the montmorillonitic specimens raise concerns about the potential effects of test geometry and boundary conditions on the evolution of uneven strain fields that may facilitate flow localization.

A numerical simulation of the state of stresses of the sediment plugs is performed using CODE_BRIGHT, to capture the effect of vertical loading during consolidation and the radial loading due to capillary pressure at the CO_2-water interface on the sediment periphery before CO_2 invasion. We use the non-linear, plastic cam-clay model with parameters C_r=0.0384, C_c=1.67, e_{1kPa}=5.68 , M=1.2.

Fig. 8.7 shows that there is an increase in porosity at the edge of the collection pipe and high local shear stress; conversely, lower porosity is observed on top of the collection pipe. High local porosity and shear stress level subsist upon radial CO_2 pressurization. However, these porosity and stress fields provide no clear justification for the possible emergence of CO_2-driven fractures.

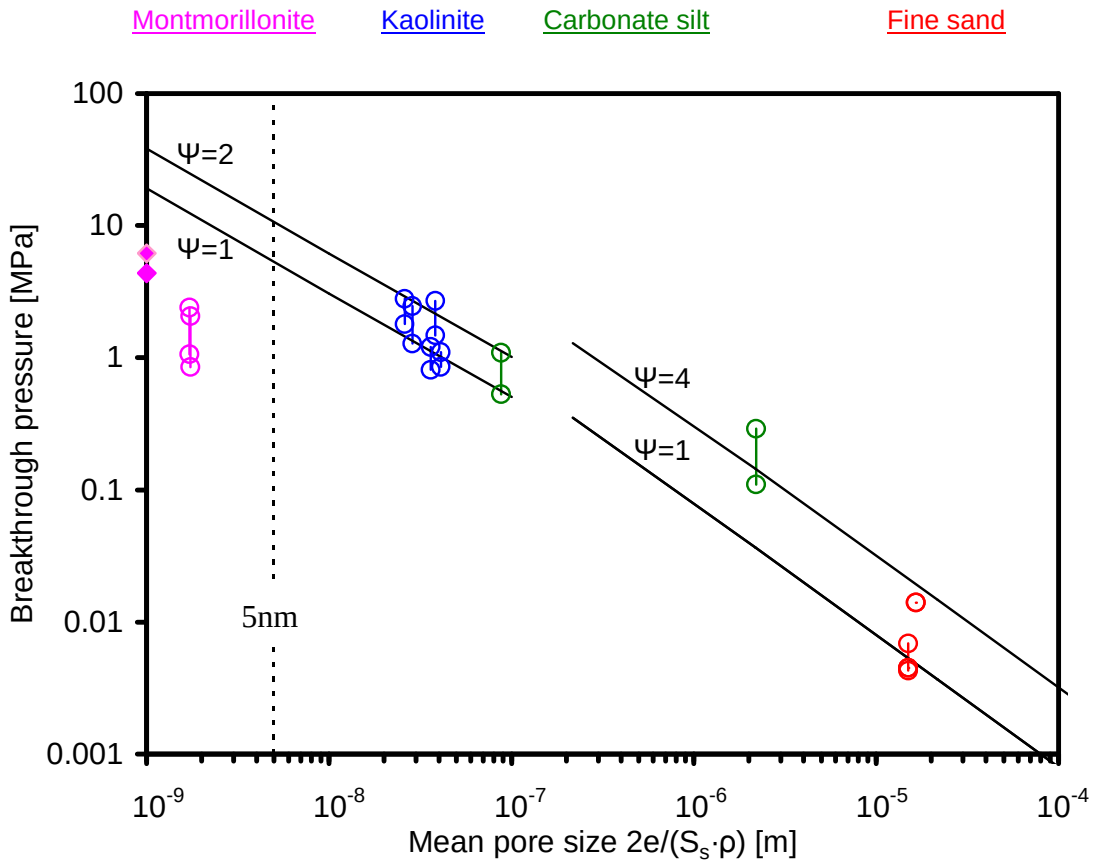

Figure 8.5 Experimental breakthrough pressures (valued bounded by empty circles) for different sediments (bounded by empty circles) as a function of mean pore size. Laplace's formula is superimposed for different values of the geometric fabric factor Ψ (Eq. 5). Notice that much higher breakthrough pressure is expected from Laplace's equation for high specific montmorillonite sediments than the ones measured experimentally. The theoretical prediction bends at high breakthrough pressure because of lower interfacial tension (T_s: 298K isotherm). We added two experimental values for similar test conditions with filled circles [*Horseman et al.*, 1999].

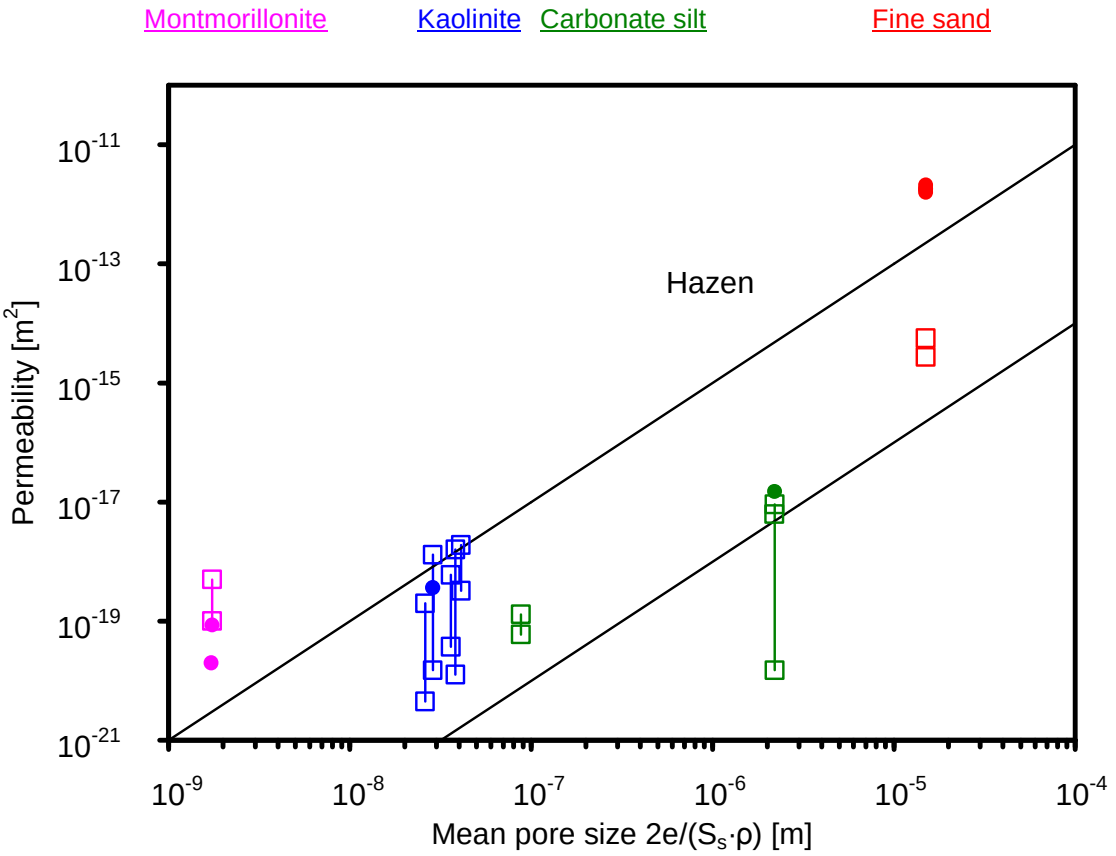

Figure 8.6 Water permeability (filled circles) and CO_2 permeability after breakthrough and after CO_2 flushing (empty squares connected by solid line) for different consolidated sediments. 2:1 slope curves in the log-log space predicted by Kozeny-Carman and Hazen models are superimposed. Note: CO_2 permeability increases after breakthrough mainly due to a decrease in water saturation.

(a) Vertical displacements and porosity after consolidation (vertical load)

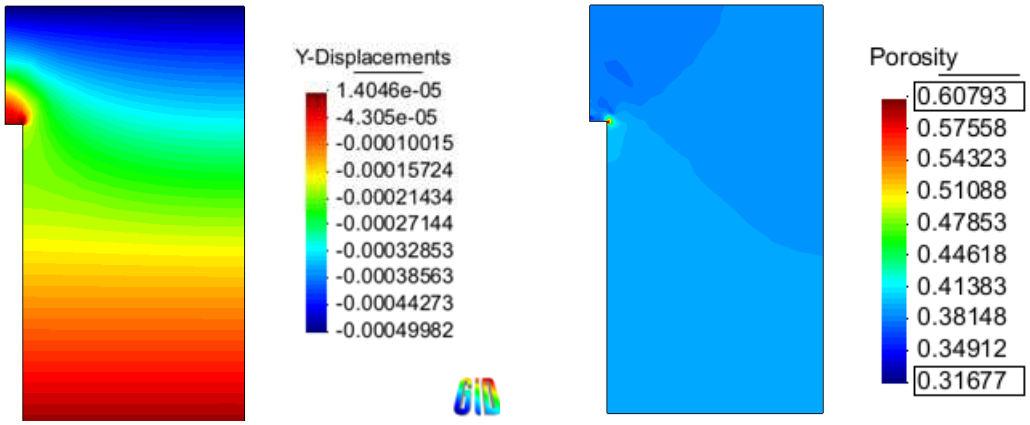

(b) Mean stress and porosity after capillary compression (lateral loading)

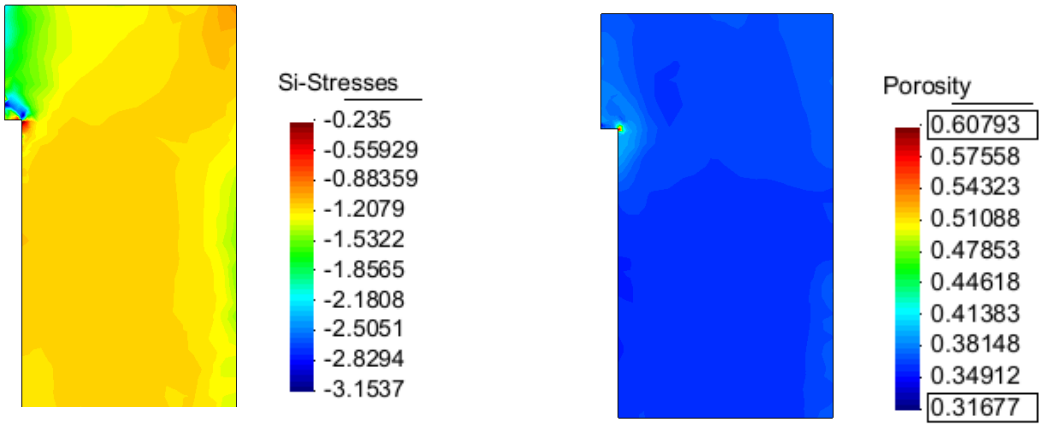

Figure 8.7 FEM analysis of the porosity and stress field in the clay specimen using a modified cam-clay model (parameters C_r=0.0384, C_c=1.67, e_{1kPa}=5.68, M=1.2). The simulation has two stages: (a) vertical loading – consolidation, and (b) lateral capillary loading. Results show the localization of stresses and plastic deformations around the collection pipe.

8.5 Implications - Cap rock integrity and CO_2 leaks

8.5.1 Order-of-magnitude estimation of leaks

Consider a formation overlaid by a cap rock of thickness t_h, diffusion coefficient D^*, and intrinsic permeability k. Let's estimate CO_2 transport through the cap rock, both by diffusion without breakthrough and then by advection after breakthrough.

The time to achieve steady state diffusive flux is proportional to $T_{diff}^*=t^2/D^*$, e.g., ~32 years for a 1m cap rock and ~3200yr for a 10m cap rock, assuming $D^*=10^{-9}m^2/s$. Once steady-state is reached, the steady-state diffusive flux is calculated using Fick's law,

$$q_{CO2}^{diff} = -nD^* \frac{\Delta x_{CO2}}{t_h} \tag{8.8}$$

Where x_{CO2} is the concentration of CO_2 in water and φ the cap rock porosity (the tortuosity coefficient is neglected in this approximation). Fig. 8.8 shows the diffusive flux for various cap rock thicknesses, assuming Δx_{CO2}=1mol(CO_2)/kg(water), $D^*=10^{-9}m^2/s$, n=0.1. The diffusive flux is $q^{diff}_{CO2}\sim10^{-1}kg/m^2/yr$ or lower. High temperature conditions increase the diffusion coefficient and high pressure increases the solubility of CO_2 in water (effects not accounted in Fig. 8.8).

The advective flow after breakthrough is computed using Darcy's equation,

$$q_{CO2}^{adv} = \frac{k\ k_{CO2}^r \rho}{\mu} \frac{\Delta P}{t_h} \tag{8.9}$$

While these flow rates correspond to constant pressure gradient conditions, the pressure at the CO_2 repository will drop as CO_2 escapes (and CO_2 dissolves/convects in the reservoir). Fig 8.7 shows the results for a cap rock with a relatively high permeability $k\sim10^{-19}m^2$ as compared to values in Tables 8.1 and 8.2 and Fig. 8.6. The advective flow

rate can be as high as 10 kg/m^2/yr considering a thin cap rock (t_h=1m) subjected to a high pressure gradient (ΔP=10MPa). For more realistic field conditions, advective flow rates remain smaller than 1kg/m^2/yr.

(a)

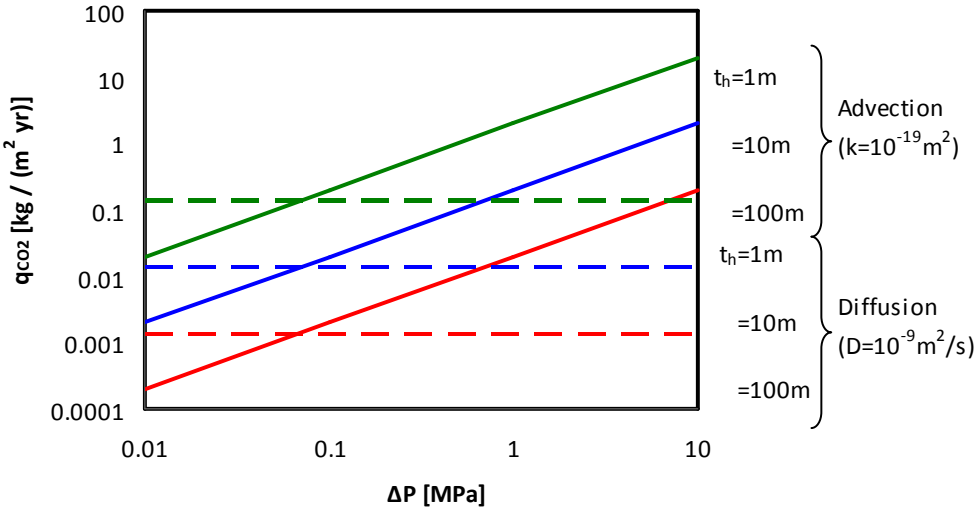

(b)

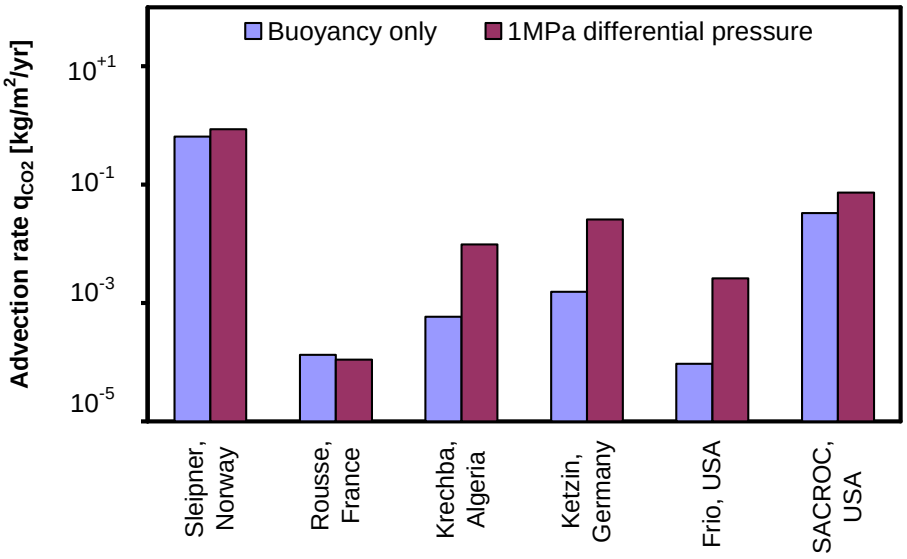

Figure 8.8 Order of magnitude analysis of CO_2 leaks for a cap rock thickness t_h. (a) Diffusion before and advection after breakthrough (Eq. 8 and 9; n=0.1, D^*=10^{-9}m^2/s, S^r_{CO2}=0.3, k^r_{CO2}=$(S^r_{CO2})^2$, μ_{CO2}=10^{-4}Pa·s). Notice that the time to achieve steady state diffusive flux is proportional to t_h^2/D^*; (b) upper bound advective flow rate estimate for different CO_2 stotage sites due to buoyancy and a 1MPa pressure gradient. (Note: Kozeny-Carman equation is used to evaluate permeability when permeability data is not available from Table 8.1)

Let's estimate the rate of advection after CO_2 breakthrough due to CO_2 buoyancy $\Delta P=h(\rho_w- \rho_{CO2})g$ for several existent and planned CO_2 storage sites. Cap rock permeabilities are based on reported values or reported rock descriptions (Table 8.1), assuming a CO_2 pool thickness equal to the reservoir thickness, and a mass density difference $\rho_w-\rho_{CO2}$=300kg/m^3. Fig. 8.7 shows the calculated advection rates. While values vary linearly with order-of-magnitude ranges in permeability, a post-breakthrough leak rate lower than 0.1kg/m^2/yr appears as an adequate upper bound in the absence of flow localization features.

This leak rate 0.1 kg/m^2/yr would release 100 kg/m^2 in a thousand years. This amount of CO_2 is equivalent to a ~0.5m reduction in the CO_2 pool thickness in a reservoir rock with porosity 0.2. For comparison, ~315kg/m^2 of CO_2 is needed to saturate and decrease pH to ~3.5 in a 100m water column in a potential shallow water aquifer with porosity 0.4 (disregarding the buffering effects of minerals).

Contrary to advective flow, diffusion is not affected by buoyancy, pressure difference (except pressure-dependent solubility), or small pore size in the cap rocks. In long term, the pressure-difference will vanish, and CO_2 diffusive transport will remain. Advective and diffusive fluxes are in the same order of magnitude when the pressure difference is small, i.e., thin CO_2 pools $\Delta P=h(\rho_w- \rho_{CO2})g$; from equations 8.8 and 8.9, $\Delta P<(n/k^r_{CO2}/\rho)(\mu D*\Delta x_{CO2}/k)$.

8.5.2 Storativity rating – dimensionless parameters

Let's compare values to define the sealing capacity of carbon geological storage systems as a function of pool and cap rock characteristics.

The capillary entry pressure C is an intrinsic cap rock property parameter $C \sim T_s \cos\theta / [e/(S_s \rho_m) \cdot 10^{\alpha}]$ (from Eq. 8.5 – fine-grained sediments), where α takes pore size distribution into consideration ; if α>1, breakthrough happens along pores larger than the computed mean $2e/(S_s \rho_m)$.

The buoyancy pressure ΔP depends on the thickness of the CO_2 pool h, $\Delta P = h(\rho_w - \rho_{CO2})g$. (Note: the CO_2 pool thickness h may be thinner than the reservoir thickness due to lateral spreading, or thicker such as in the case of an anticline system).

Let's define the "sealing ratio" as the π-ratio between capillary breakthrough pressure and buoyancy pressure,

$$\text{Sealing ratio} = \pi_1 = \frac{C}{\Delta P} = \frac{S_s T_s \cos\theta \ \rho_m}{ehg(\rho_w - \rho_{CO2})} \tag{8.10}$$

Sealing ratios $\pi_1 >> 1$ are sought for safe storage. Fig. 8.9 shows π_1 for different carbon storage sites and the range of uncertainty in these value. Upper and lower bounds are calculated considering maximum and minimum capillary and buoyancy pressures. The maximum capillary pressure is computed with the estimated mean pore diameter, adopting a minimum pore diameter of ~5nm in view of experimentally measured breakthrough pressures reported in Table 8.2. The minimum capillary pressure is computed assuming that CO_2 breakthrough connects pores ~30 times larger than the estimated mean [*Espinoza and Santamarina*, 2010a]. The maximum buoyancy pressure is calculated assuming that the CO_2 pool height could be higher than the reservoir thickness in thin reservoirs (complex geo-plumbing), and significantly lower in thick reservoirs.

Extreme scenarios plotted in Fig. 8.9 consider the CO_2 pool height 0.1h for thick reservoirs, h>50, and 3h for thin reservoirs h<50. Results in the previous section show that most clayey cap rocks exhibit breakthrough pressures between 1 to 5MPa while a 100m column of CO_2 develops a buoyancy pressure ΔP~0.2MPa to 0.4MPa). Additional injection pressure may change this pressure balance during the early life of the storage system.

The second evaluation of a CO_2 geological storage system addresses its mechanical stability. Changes in effective stress can trigger fault reactivation, and fluid-driven open-mode fracturing. Let's compare the initial in-situ vertical effective stress at the reservoir depth z to the buoyancy pressure created by a CO_2 column height h,

$$\text{Stability ratio} = \pi_2 = \frac{\sigma'}{\Delta \text{P}} = \frac{z\left(\rho_{sed} - \rho_w\right)}{h\left(\rho_w - \rho_{CO2}\right)} \tag{8.11}$$

Where subindices correspond to sediment 'sed', water 'w', and CO_2.

Small changes in effective stress, π_2>>1, are preferred to avoid mechanical instabilities. The stability ratio is computed for some field cases listed in Table 8.1; uncertainty in the CO_2 pool height (see π_1-analysis) and overburden depth (z±0.2·z) are included in the ranges shown in Figure 8.9. Once again,additional injection pressure would reduce this ratio during the early life of the project.

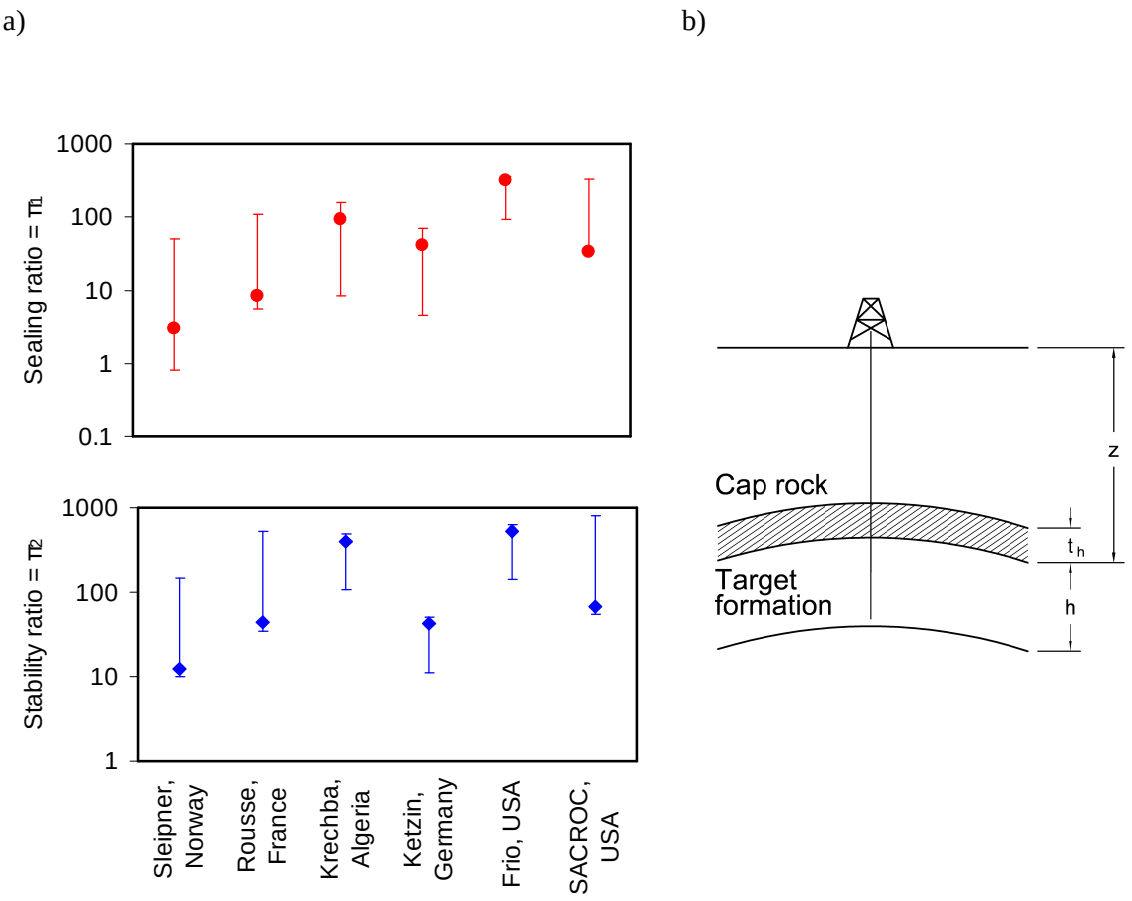

Figure 8.9 Analysis of sealing capacity at existent and target CO_2 storage sites in dimensionless ratios: π_1 ratio of capillary pressure over buoyancy pressure. Eq. 8.10, and π_2 ratio of effective stress over buoyancy pressure, Eq. 8.11. The error bars represent uncertainty in capillary pressure, buoyancy and effective stress (refer to text). Overburden, cap rock thickness, and CO_2 storage capacity are key parameters for evaluating the safety of storage sites.

8.6 Conclusions

- The cap rock is the fundamental component of carbon geological storage systems. Most target storage sites are capped by shales, evaporites, or a combination of both. Clay minerals play a fundamental role in the performance of shales as cap rocks. Small pores in clayey cap rocks create high capillary pressure and generate high viscous drag to hinder the migration of buoyant CO_2.
- Low CO_2 mass density, CO_2 viscosity, and CO_2-water interfacial tension facilitate CO_2 leaks.
- Breakthrough pressure, ensuing CO_2 permeability, and specimen volumetric deformation were measured on sediment plugs using specially designed high pressure oedometers. Results show that the breakthrough pressure increases as the pore size decreases (1:1 slope in log-log space), and it is 1MPa<P*<3MPa for kaolinite and bentonite plugs consolidated to $\sigma`_v$~2MPa.
- CO_2 permeability arises after breakthrough and increases by orders of magnitude with continued CO_2 advection. Most specimens showed a final water saturation of 0.7-0.9.
- Bentonite plugs developed fluid-driven open-mode fractures that limited the capillary entry and breakthrough pressur. Higher CO_2 permeability than anticipated followed.
- Flow-localization may be favored by reservoir geometric conditions. For example, the numerical model of plugs tested in this study showed an increase in porosity and shear at the edge of the drainage pipe.

- The sediment dries during CO_2 transport. Electrical resistivity and magnetic resonance data show higher drying close to the drainage pipe (radial flow).
- Order of magnitude analyses show that leaks in most storage sites will be advection-controlled once percolation takes place (in the absence of high conductivity geological features). Diffusive and advective CO_2 leaks through non-fractured cap rocks will be minor and will not compromise the storage capacity of CO_2 injection sites.
- A rating system is proposed to evaluate potential storage sites. The rating system is based on a comparison of the buoyancy pressure caused by the CO_2 pool, the capillary breakthrough pressure of the cap rock, and the effective stress at the reservoir depth. These parameters are combined to define the sealing ratio and stability ratio.

CHAPTER 9

CONCLUSIONS

This research investigated phenomena related to carbon geological storage, including the possibility of CH_4-CO_2 replacement in hydrate-bearing sediments. The scope of the work included data compilation from published studies, and new experimental results related to interfacial properties in CO_2- and CH_4-water-mineral systems, mechanisms involved in CH_4-CO_2 replacement in hydrate-bearing sediments, and the sealing capacity of clayey sediments to retain CO_2 underground. Complimentary numerical and analytical analyses extend the applicability of the results to reservoir conditions and anticipate geotechnical implications. The main conclusions are presented separately for each study.

CO_2 Geological Storage - Geotechnical Implications.

- The physical properties of CO_2 such as density, viscosity, interfacial tension and bulk compressibility are pressure-temperature dependent
- Geometric boundaries, spatial variability, flow conditions and the emergence of viscous fingering affect the volume of the geological formation injected with CO_2.
- Water acidification in the presence of CO_2 enhances mineral dissolution.
- Complex hydro-chemo-mechanical interactions, which lead to emergent phenomena, may hinder the storativity of injected carbon dioxide.
- The contrasting physical properties of CO_2 and water support the application of geophysical monitoring methods based on elastic and electromagnetic waves.

*Water-CO_2-mineral systems: interfacial tension, contact angle and diffusion – Implications to CO_2 geological storage***.**

- CO_2-water interfacial tension decreases significantly from 72mN/m to ~25mN/m as pressure increases to reservoir pressure-temperature conditions.
- Contact angle varies with CO_2 pressure in response to changes in CO_2-water interfacial tension.
- Water solubility and diffusivity in liquid CO_2 govern the evolution of interparticle pendular water.
- Pressure-dependent interfacial tension and contact angle affect injection patterns and breakthrough mechanisms.

Water-CH_4-mineral systems: interfacial tension and contact angle – Implications to natural gas geological systems.

- CH_4-water interfacial tension decreases up to 20mN/m from atmospheric pressure to high pressure relevant to reservoir conditions.
- Minor changes in contact angle are measured upon CH_4 pressurization. Amorphous silica, calcite, coal, and PTFE substrates show receding contact angles $\theta<90°$ (water-wet); calcite, coal and PTFE show advancing contact angles $\theta>90°$ (gas-wet).
- While stable displacement is expected during gas recovery from natural gas conventional reservoirs, gas fingering and high residual water saturation are expected from the depressurization of coal beds and hydrate-bearing sediments.

Properties and phenomena relevant to CH_4-CO_2 replacement in hydrate bearing sediments.

- The CH_4 hydrate cage must separate to release the CH_4 molecule and trap the CO_2 molecule. This transient and local solid-liquid-solid transition is assisted by the excess heat liberated during CH_4-CO_2 replacement.
- Hydrate forming water dissolves into liquid CO_2, so that lower hydrate saturation is expected after CH_4-CO_2 replacement in water-limited reservoirs.
- Volume expansion, CO_2 hydrate clogging, and CO_2 fingering leading to CH_4 hydrate occlusion within the reservoir are expected during CH_4-CO_2 replacement.

P-wave monitoring of hydrate-bearing sand during CH_4-CO_2 replacement.

- CH_4-CO_2 replacement within the stability field occurs without loss of stiffness in the granular medium.
- CO_2-flooded sandy reservoirs can remain mechanically stable during and after CH_4 gas production.
- Continued sediment flushing with dry CO_2 dissolves the hydrate, opens the pore throats, and weakens the granular skeleton.

Clay interaction with liquid and supercritical CO_2: the relevance of electrical and capillary forces.

- Clay minerals determine the properties of shales as seal layers.

- Clay flocculates when sedimented in CO_2, and may attain lower porosity than when it is sedimented in brine. A four-fold increase in the Hamaker constant predicts higher attraction forces.
- The cap rock may become dehydrated upon the injection of dry CO_2. Capillary forces that develop upon CO_2 invasion can cause contraction and may eventually lead to the formation of desiccation cracks.

CO_2 breakthrough in clay barriers - Implications for cap rock sealing efficiency and integrity in carbon geological repositories.

- The breakthrough pressure is less than ~2MPa for sediments consolidated to σ_v`=2MPa, except for smectite rich sediments.
- Relative permeability increases suddenly after CO_2 breakthrough and advection.
- The advective and diffusive transport through intact cap rocks is not negligible, yet it does not significantly affect the storativity of CO_2 over millennia.
- The geometric properties of target formations and cap rock physical properties are needed to evaluate the potential sealing capacity of candidate CO_2 storage sites.

REFERENCES

Adisasmito, S., R. J. Frank, and E. D. Sloan (1991), Hydrates of carbon-dioxide and methane mixtures, *Journal of Chemical and Engineering Data*, *36*(1), 68-71.

Algive, L., S. Bekri, and O. Vizika-kavvadias (2009), Reactive Pore Network Modeling Dedicated to the Determination of the Petrophysical Property Changes While Injecting CO2, paper presented at SPE Annual Technical Conference and Exhibition, 4-7 October 2009, New Orleans, Louisiana, 2009. Society of Petroleum Engineers.

Allis, R. G., T. Chidsey, W. Gwynn, C. Morgan, S. P. White, M. Adams, and J. Moore (2001), Natural CO2 reservoirs on the Colorado Plateau and Southern Rocky Mountains: candidates for CO2 sequestration., paper presented at 1st National Conference on Carbon Sequestration, May 14-17, 2001, DOE-NETL, Washington DC.

Alnes, H., O. Eiken, and T. Stenvold (2008), Monitoring gas production and CO2 injection at the Sleipner field using time-lapse gravimetry, *Geophysics*, *73*(6), WA155-WA161.

Alonso, E. E., A. Gens, and A. Josa (1990), A constitutive model for partially saturated soils, *Geotechnique*, *40*(3), 405-430.

Anderson, G. K. (2003), Enthalpy of dissociation and hydration number of carbon dioxide hydrate from the Clapeyron equation, *Journal of Chemical Thermodynamics*, *35*(7), 1171-1183.

Anderson, G. K. (2004), Enthalpy of dissociation and hydration number of methane hydrate from the Clapeyron equation, *Journal of Chemical Thermodynamics*, *36*(12), 1119-1127.

Anderson, R., M. Llamedo, B. Tohidi, and R. W. Burgass (2003), Experimental measurement of methane and carbon dioxide clathrate hydrate equilibria in mesoporous silica, *Journal of Physical Chemistry B*, *107*(15), 3507-3514.

Angeli, M., M. Soldal, E. Skurtveit, and E. Aker (2009a), Experimental percolation of supercritical CO2 through a caprock, *Energy Procedia*, *1*(1), 3351-3358.

Angeli, M., M. Soldal, E. Skurtveit, and E. Aker (2009b), Experimental percolation of supercritical CO2 through a caprock, in *Greenhouse Gas Control Technologies 9*, edited by J. Gale, H. Herzog and J. Braitsch, pp. 3351-3358.

Armitage, P. J., R. H. Worden, D. R. Faulkner, A. C. Aplin, A. R. Butcher, and J. Iliffe (2010), Diagenetic and sedimentary controls on porosity in Lower Carboniferous fine-grained lithologies, Krechba field, Algeria: A petrological study of a caprock to a carbon capture site, *Marine and Petroleum Geology*, *27*(7), 1395-1410.

Arts, R., O. Eiken, A. Chadwick, P. Zweigel, L. van der Meer, and B. Zinszner (2004), Monitoring of CO2 injected at Sleipner using time-lapse seismic data, *Energy*, *29*(9-10), 1383-1392.

Aucejo, A., M. C. Burguet, R. Munoz, and J. L. Marques (1995), Densities, viscosities, and refractive-indexes of some n-alkane binary-liquid systems at 298.15-K, *J. Chem. Eng. Data*, *40*(1), 141-147.

Augustin, L., C. Barbante, P. Barnes, J. Barnola, M. Bigler, E. Castellano, O. Cattani, J. Chappellaz, D. Dahl-Jensen, and B. Delmonte (2004), Eight glacial cycles from an Antarctic ice core, *Nature*, *429*(6992), 623-628.

Austegard, A., E. Solbraa, G. De Koeijer, and M. J. Mølnvik (2006), Thermodynamic models for calculating mutual solubilities in H2O-CO2-CH4 mixtures, *Chemical Engineering Research and Design*, *84*(9), 781-794.

Aya, I., K. Yamane, and H. Nariai (1997), Solubility of CO2 and density of CO2 hydrate at 30 MPa, *Energy*, *22*(2-3), 263-271.

Baez, L. A., and P. Clancy (1994), Computer-simulation of the crystal-growth and dissolution of natural-gas hydrates, in *International Conference on Natural Gas Hydrates*, edited by E. D. Sloan, J. Happel and M. A. Hnatow, pp. 177-186.

Baez, L. A., and P. Clancy (1995), The kinetics of crystal-growth and dissolution from the melt in Lennard-Jones systems, *Journal of Chemical Physics*, *102*(20), 8138-8148.

Belogol'skii, V. A., S. S. Sekoyan, L. M. Samorukova, V. I. Levtsov, and S. R. Stefanov (2002), Temperature and pressure dependence of the speed of sound in seawater, *Measurement Techniques*, *45*(8), 879-886.

Benison, K. C., and R. H. Goldstein (2000), Sedimentology of ancient saline pans: an example from the Permian Opeche Shale, Williston Basin, North Dakota, U.S.A, *Journal of Sedimentary Research*, *70*(1), 159-169.

Bergmo, P. E. S., A.-A. Grimstad, and E. Lindeberg (2011), Simultaneous CO2 injection and water production to optimise aquifer storage capacity, *International Journal of Greenhouse Gas Control*, *5*(3), 555-564.

Berne, P., P. Bachaud, and M. Fleury (2010), Diffusion Properties of Carbonated Caprocks from the Paris Basin, *Oil & Gas Science and Technology-Revue De L Institut Francais Du Petrole*, *65*(3), 473-484.

Bevlins, R. D. (1979), *Formulas for natural frequency and mode shape*, Krieger Publishing Company, Malabar, Florida.

Bhatt, D., J. Newman, and C. J. Radke (2004), Molecular dynamics simulations of surface tensions of aqueous electrolytic solutions, *Journal of Physical Chemistry B*, *108*(26), 9077-9084.

Bicher, L. B., and D. L. Katz (1943), Viscosities of the methane-propane system, *Industrial & Engineering Chemistry*, *35*(7), 754-761.

Bielinski, A., A. Kopp, H. Schutt, and H. Class (2008), Monitoring of CO2 plumes during storage in geological formations using temperature signals: Numerical investigation, *International Journal of Greenhouse Gas Control*, *2*(3), 319-328.

Biot, M. A. (1956), Theory of propagation of elastic waves in a fluid-saturated porous solid: 2. Higher frequency range, *Journal of the Acoustical Society of America*, *28*(2), 179-191.

Bjerrum, L., R. M. Kennard, R. E. Gibson, and J. Nash (1972), Hydraulic fracturing in field permeability testing., *Geotechnique*, *22*(2), 319-332.

Blokhuis, E. M. (2004), Liquid drops at surfaces, in *Surface and interfacial tension : measurement, theory, and applications*, edited by S. Hartland, p. 619, Marcel Dekker, New York.

Blunt, M., F. J. Fayers, and F. M. Orr (1993), Carbon-dioxide in enhanced oil-recovery, *Energy Conversion and Management*, *34*(9-11), 1197-1204.

Bøe, R., and P. Zweigel (2001), Characterisation of the Nordland Shale in the Sleipner area by XRD analysis - A contribution to the Saline Aquifer CO2 Storage (SACS) project.*Rep.*

Bohnhoff, M., M. D. Zoback, L. Chiaramonte, J. L. Gerst, and N. Gupta (2010), Seismic detection of CO2 leakage along monitoring wellbores, *International Journal of Greenhouse Gas Control*, *4*(4), 687-697.

Bourbie, T., O. Coussy, and B. Zinszner (1987), *Acoustics of porous media*, Editions Technip, Paris.

Bradshaw, A., and K. E. Schleicher (1970), Direct measurement of thermal expansion of sea water under pressure, *Deep Sea Research*, *17*(4), 691-698.

Brown, M. A., and F. Southworth (2008), Mitigating climate change through green buildings and smart growth, *Environment and Planning A*, *40*(3), 653-675.

Bryar, T. R., and R. J. Knight (2003), Laboratory studies of the effect of sorbed oil on proton nuclear magnetic resonance, *Geophysics*, *68*(3), 942-948.

Buchner, R., G. T. Hefter, and P. M. May (1999), Dielectric relaxation of aqueous NaCl solutions, *Journal of Physical Chemistry A*, *103*(1), 1-9.

Burland, J. B. (1990a), On the Compressibility and Shear Strength of Natural Clays, *Geotechnique*, *40*(3), 329-378.

Burland, J. B. (1990b), On the compressibility and shear strength of natural clays, *Geotechnique*, *40*(329-378).

Butt, H.-J., K. Graf, and M. Kappl (2006), *Physics and chemistry of interfaces. Second, revised and enlarged edition.*, Wiley- VCH Verlag GmbH & Co. KGaA, Weinheim.

Canny, J. (1986), A computational approach to edge-detection, *Ieee Transactions on Pattern Analysis and Machine Intelligence*, *8*(6), 679-698. DOI: 610.1109/TPAMI.1986.4767851.

Carey, J. W., M. Wigand, S. J. Chipera, G. WoldeGabriel, R. Pawar, P. C. Lichtner, S. C. Wehner, M. A. Raines, and J. G. D. Guthrie (2007), Analysis and performance of oil well cement with 30 years of CO2 exposure from the SACROC Unit, West Texas, USA, *International Journal of Greenhouse Gas Control, 1*(1), 75-85.

CDIAC (2009), National CO2 Emissions from Fossil-Fuel Burning, Cement Manufacture, and Gas Flaring: 1751-2007 edited, ORNL, http://cdiac.ornl.gov/ftp/ndp030/nation1751_2007.ems.

Ceglarska-Stefanska, G., and K. Zarebska (2002a), The competitive sorption of CO2 and CH4 with regard to the release of methane from coal, *Fuel Processing Technology*, *77-78*, 423-429.

Ceglarska-Stefanska, G., and K. Zarebska (2002b), Expansion and Contraction of Variable Rank Coals During the Exchange Sorption of CO2 and CH4, *Adsorption Science and Technology*, *20*(1), 49-62.

Chadwick, R. A., P. Zweigel, U. Gregersen, G. A. Kirby, S. Holloway, and P. N. Johannessen (2004), Geological reservoir characterization of a CO2 storage site: The Utsira Sand, Sleipner, Northern North Sea, *Energy*, *29*(9-10), 1371-1381.

Chalbaud, C., M. Robin, J. M. Lombard, F. Martin, P. Egermann, and H. Bertin (2009), Interfacial tension measurements and wettability evaluation for geological CO2 storage, *Advances in Water Resources*, *32*(1), 98-109.

Chang, Y. B., M. T. Lim, G. A. Pope, and K. Sepehrnoori (1994), CO2 flow patterns under multiphase flow - heterogeneous field-scale conditions, *SPE Reservoir Engineering*, *9*(3), 208-216.

Charpentier, F., B. Bureau, J. Troles, C. Boussard-Pledel, K. Michel-Le Pierres, F. Smektala, and J. L. Adam (2009), Infrared monitoring of underground CO2 storage using chalcogenide glass fibers, *Optical Materials*, *31*(3), 496-500.

Chi, S. M., B. I. Morsi, G. E. Klinzing, and S. H. Chiang (1988), Study of interfacial properties in the liquid CO2 water coal system, *Energy & Fuels*, *2*(2), 141-145.

Chiaramonte, L., M. Zoback, J. Friedmann, and V. Stamp (2008), Seal integrity and feasibility of CO 2 sequestration in the Teapot Dome EOR pilot: geomechanical site characterization, *Environmental Geology*, *54*(8), 1667-1675.

Chiquet, P., D. Broseta, and S. Thibeau (2007), Wettability alteration of caprock minerals by carbon dioxide, *Geofluids*, *7*(2), 112-122.

Cho, G.-C., J. Dodds, and J. C. Santamarina (2006), Particle shape effects on packing density, stiffness, and strength: natural and crushed sands, *Journal of Geotechnical & Geoenvironmental Engineering*, *132*(5), 591-602.

Cho, G. C., J. S. Lee, and J. C. Santamarina (2004), Spatial Variability: High-resolution Assessment with Electrical Needle Probe, *ASCE Journal of Geotechnical and Geoenvironmental Engineering*, *130*(8), 843-850.

Chrastil, J. (1982), Solubility of solids and liquids in supercritical gases, *Journal of Physical Chemistry*, *86*(15), 3016-3021.

Chun, B.-S., and G. T. Wilkinson (1995), Interfacial tension in high-pressure carbon dioxide mixtures, *Ind. Eng. Chem. Res.*, *34*(12), 4371-4377.

Circone, S., S. H. Kirby, and L. A. Stern (2005), Direct measurement of methane hydrate composition along the hydrate equilibrium boundary, *Journal of Physical Chemistry B*, *109*(19), 9468-9475.

Cole, D. R., A. A. Chialvo, G. Rother, L. Vlcek, and P. T. Cummings (2010), Supercritical fluid behavior at nanoscale interfaces: Implications for CO2 sequestration in geologic formations, *Philosophical Magazine*, *90*(17-18), 2339-2363.

Collett, T. S. (2002), Energy resource potential of natural gas hydrates, *AAPG Bulletin*, *86*(11), 1971-1992.

Cowan, J. C., and D. J. Weintritt (1976), *Water-formed scale deposits*, Gulf Publishing Co., Houston, Texas.

da Rocha, S. R. P., K. P. Johnston, R. E. Westacott, and P. J. Rossky (2001), Molecular Structure of the Water-Supercritical CO2 Interface, *J. Phys. Chem. B*, *105*(48), 12092-12104.

Daley, T. M., R. D. Solbau, J. B. Ajo-Franklin, and S. M. Benson (2007), Continuous active-source seismic monitoring of CO2 injection in a brine aquifer, *Geophysics*, *72*(5), A57-A61.

Daley, T. M., L. R. Myer, J. E. Peterson, E. L. Majer, and G. M. Hoversten (2008), Time-lapse crosswell seismic and VSP monitoring of injected CO2 in a brine aquifer, *Environmental Geology*, *54*(8), 1657-1665.

Danten, Y., T. Tassaing, and A. Besnard (2005), Dynamic of solitary water in hydrophobic solvents, *Journal of Molecular Liquids*, *117*(1-3), 49-61.

Davies, S. R., J. W. Lachance, E. D. Sloan, and C. A. Koh (2008), A novel approach to measuring methane diffusivity through a hydrate film using differential scanning calorimetry, paper presented at 6th International conference on gas hydrates, Vancouver, British Columbia, Canada.

Decker, E. L., B. Frank, Y. Suo, and S. Garoff (1999), Physics of contact angle measurement, *Colloids and Surfaces. A: Physicochemical and Engineering Aspects*, *156*(1-3), 177-189.

Defay, R., and I. Prigogine (1966), *Surface tension and adsorption*, 432 pp., Wiley New York.

Delage, P., Y. J. Cui, and C. Schroeder (1996), Subsidence and capillary effects in chalks, paper presented at Dans EUROCK '96, Prediction and performance in rock mechanics and rock engineering - ISRM International symposium, Torino : France.

Demurov, A., Radhakrishnan, and B. L. Trout (2002), Computations of diffusivities in ice and CO_2 clathrate hydrate via molecular dynamics and Monte Carlo simulations, *Journal of Chemical Physics*, *116*(2), 702-709.

Dewhurst, D. N., R. M. Jones, and M. D. Raven (2002), Microstructural and petrophysical characterization of Muderong Shale: application to top seal risking, *Petroleum Geoscience*, *8*(4), 371-383, doi: 310.1144/petgeo.1148.1144.1371.

Dickson, J. L., G. Gupta, T. S. Horozov, B. P. Binks, and K. P. Johnston (2006), Wetting Phenomena at the CO2/Water/Glass Interface, *Langmuir*, *22*(5), 2161-2170.

Dikkers, A. J. (1985), *Geology in petroleoum production*, Elsevier, Amsterdam.

DOE-NETL (2008), Carbon sequestration atlas of the United States of America and Canada - Second Edition. *Rep.*

DOE (2010a), Fossil fuels, http://www.fossil.energy.gov/programs/sequestration/index.html, edited.

DOE (2010b), Fossil Fuels, http://www.energy.gov/energysources/fossilfuels.htm, accessed on 11/14/2010, edited.

Donelly, H., and D. Katz (1954), Phase equilibria in the carbon dioxide–methane system, *Industrial and Engineering Chemistry*, *46*(3), 511-517.

Dooley, J. J., R. Dahowski, C. Davidson, M. A. Wise, N. Gupta, S. H. Kim, and E. L. Malone (2006), Carbon Dioxide Capture and Geologic Storage: A core element of a Global Energy Technology Strategy to address climate change.*Rep.*, PNNL, Richland, WA.

Downey, M. W. (1984), Evaluating seals for hydrocarbon accumulations, *AAPG Bulletin*, *68*(11), 1752-1763.

Drever, J. I. (1997), *The Geochemistry of Natural Waters: Surface and Groundwater Environments. Third Edition*, 437 pp., Prentice-Hall, New Jersey.

Duan, Z., and R. Sun (2003a), An improved model calculating CO2 solubility in pure water and aqueous NaCl solutions from 273 to 533 K and from 0 to 2000 bar, *Chemical Geology*, *193*(3-4), 257-271.

Duan, Z. H., and R. Sun (2003b), An improved model calculating CO2 solubility in pure water and aqueous NaCl solutions from 273 to 533 K and from 0 to 2000 bar, *Chemical Geology*, *193*(3-4), 257-271.

Dullien, F. A. L. (1979), *Porous media. Fluid transport and pore structure*, 396 pp., Academic Press, New York.

Dunk, R. M., P. G. Brewer, E. T. Peltzer, P. M. Walz, K. C. Hester, and E. D. Sloan (2006), The exchange reaction between methane hydrate and carbon dioxide: an oceanic feasibility test, paper presented at American Geophysical Union, Fall Meeting, Abstract #MR43A-1070.

Dusseault, M., S. Bachu, and L. Rothenburg (2004), Sequestration of CO2 in salt caverns, *JCPT*, *43*(11).

Ehlig-Economides, C., and M. J. Economides (2010), Sequestering carbon dioxide in a closed underground volume, *Journal of Petroleum Science and Engineering*, *70*(1-2), 118-125.

EIA (2011), Natural Gas Annual 2009 <eia.doe.gov>, edited.

Emberley, S., I. Hutcheon, M. Shevalier, K. Durocher, W. D. Gunter, and E. H. Perkins (2004), Geochemical monitoring of fluid-rock interaction and CO2 storage at the Weyburn CO2-injection enhanced oil recovery site, Saskatchewan, Canada, *Energy*, *29*(9-10), 1393-1401.

Espinoza, D. N., and J. C. Santamarina (2010a), Water-CO2-mineral systems: interfacial tension, contact angle and diffusion–Implications to CO2 geological storage, *Water Resources Research*, *46*(W07537), doi:10.1029/2009WR008634.

Espinoza, D. N., and J. C. Santamarina (2010b), Water-CO2-mineral systems: interfacial tension, contact angle and diffusion – Implications to CO2 geological storage, *Water Resources Research - In Press*, doi:10.1029/2009WR008634.

Espinoza, D. N., and J. C. Santamarina (2010c), Water-CO2-mineral systems: interfacial tension, contact angle and diffusion – Implications to CO2 geological storage, *Water Resources Research*, *46*(W07537), doi:10.1029/2009WR008634.

Espinoza, D. N., K. Olson, and J. C. Santamarina (2011), Clay interaction with liquid and supercritical CO2: the relevance of electrical and capillary forces, *Submitted*.

Fenghour, A., W. A. Wakeham, and V. Vesovic (1998), The viscosity of carbon dioxide, *Journal of Physical and Chemical Reference Data*, *27*(1), 31-44.

Fleury, M., et al. (2010), Evaluating Sealing Efficiency of Caprocks for CO2 Storage: an Overview of the Geocarbone-Integrity Program and Results, *Oil & Gas Science and Technology-Revue De L Institut Francais Du Petrole*, *65*(3), 435-444.

Folas, G. K., E. W. Froyna, J. Lovland, G. M. Kontogeorgis, and E. Solbraa (2007), Data and prediction of water content of high pressure nitrogen, methane and natural gas, *Fluid Phase Equilibria*, *252*(1-2), 162-174.

Förster, A., N. Springer, G. Beutler, J. Luckert, B. Norden, and H. Lindgren (2007), The mudstone-dominated caprock system of the CO2-storage site at Ketzin, Germany, paper presented at AAPG Annual Convention, Long Beach, California.

Fredd, C., and H. Fogler (1998), Influence of transport and reaction on wormhole formation in porous media, *AIChE Journal*, *44*(9), 1933-1949.

Friiso, T., and T. Tjomsland (1997), Monitoring of density changes in low-permittivity liquids by microwave-permittivity measurements with an open-ended probe, *Measurement Science & Technology*, *8*(11), 1295-1305.

Funazukuri, T., Y. Ishiwata, and N. Wakao (1992), Predictive correlation for binary diffusion-coefficients in dense carbon-dioxide, *Aiche Journal*, *38*(11), 1761-1768.

Galashev, A. E., V. N. Chukanov, A. N. Novruzov, and O. A. Novruzova (2006), Molecular-dynamic calculation of spectral characteristics of absorption of infrared radiation by (H2O)(j) and (CH4)(i)(H2O)(n) clusters, *High Temperature*, *44*(3), 364-372.

Gale, J. (2004), Geological storage of CO2: What do we know, where are the gaps and what more needs to be done?, *Energy*, *29*(9-10), 1329-1338.

Garcia, J. E. (2001), Density of aqueous solutions of CO2*Rep.*, Lawrence Berkeley National Laboratory, http://escholarship.org/uc/item/6dn022hb.

Gasperikova, E., and G. M. Hoversten (2006), A feasibility study of nonseismic geophysical methods for monitoring geologic CO2 sequestration, *The Leading Edge*(October), 1282-1288.

Gaus, I., M. Azaroual, and I. Czernichowski-Lauriol (2005), Reactive transport modelling of the impact of CO2 injection on the clayey cap rock at Sleipner (North Sea), *Chemical Geology*, *217*(3-4), 319-337.

Gherardi, F., T. F. Xu, and K. Pruess (2007), Numerical modeling of self-limiting and self-enhancing caprock alteration induced by CO2 storage in a depleted gas reservoir, *Chemical Geology*, *244*(1-2), 103-129.

Global-Carbon-Project (2010), The carbon budget 2009*Rep.*

Goldfarb, D. L., D. P. Fernandez, and H. R. Corti (1999), Dielectric and volumetric properties of supercritical carbon dioxide(1) plus methanol(2) mixtures at 323.15 K, *Fluid Phase Equilibria, 158*, 1011-1019.

Golfier, F., C. Zarcone, B. Bazin, R. Lenormand, D. Lasseux, and M. Quintard (2002), On the ability of a Darcy-scale model to capture wormhole formation during the dissolution of a porous medium, *Journal of fluid Mechanics, 457*, 213-254.

Golomb, D. (1993), Ocean disposal of CO2 - feasibility, economics and effects, *Energy Conversion and Management, 34*(9-11), 967-976.

Gueguen, Y., and V. Palciauskas (1994), *Introduction to the physics of rocks*, Princeton University Press.

Gunter, W. D., E. H. Perkins, and I. Hutcheon (2000), Aquifer disposal of acid gases: modelling of water-rock reactions for trapping of acid wastes, *Applied Geochemistry, 15*(8), 1085-1095.

Han, W. S., B. J. McPherson, P. C. Lichtner, and F. P. Wang (2010), Evaluation of trapping mechanisms in geologic CO2 sequestration: case study of SACROC northern platform, a 35-year CO2 injection site, *American Journal of Science, 310*(4), 282-324.

Handa, Y. P. (1986), Compositions, enthalpies of dissociation, and heat-capacities in the range 85-K to 270-K for clathrate hydrates of methane, ethane, and propane, and enthalpy of dissociation of isobutane hydrate, as determined by a heat-flow calorimeter, *Journal of Chemical Thermodynamics, 18*(10), 915-921.

Hashemi, S., A. Macchi, S. Bergeron, and P. Servio (2006), Prediction of methane and carbon dioxide solubility in water, *Fluid Phase Equilibria, 246*(1-2), 131-136.

Heddle, G., H. Herzog, and M. Klett (2003), The Economics of CO2 storage*Rep.*, MIT LFEE, 2003-003 RP.

Helgerud, M. B., W. F. Waite, S. H. Kirby, and A. Nur (2009), Elastic wave speeds and moduli in polycrystalline ice Ih, sI methane hydrate, and sII methane-ethane hydrate, *Journal of Geophysical Research-Solid Earth, 114*.

Hildenbrand, A., S. Schlomer, and B. M. Krooss (2002), Gas breakthrough experiments on fine-grained sedimentary rocks, *Geofluids*, *2*(1), 3-23.

Hildenbrand, A., S. Schlomer, B. M. Krooss, and R. Littke (2004), Gas breakthrough experiments on pelitic rocks: comparative study with N-2, CO2 and CH4, *Geofluids*, *4*(1), 61-80.

Hirohama, S., Y. Shimoyama, A. Wakabayashi, S. Tatsuta, and N. Nishida (1996), Conversion of CH4-hydrate to CO2-hydrate in liquid CO2, *Journal of Chemical Engineering of Japan*, *29*(6), 1014-1020.

Horseman, S. T., J. F. Harrington, and P. Sellin (1999), Gas migration in clay barriers, *Engineering Geology*, *54*(1-2), 139-149.

Hough, E. W., B. B. Wood, and M. J. Rzasa (1952), Adsorption at water-helium water-methane and water-nitrogen interfaces at pressures to 15,000 psia, *Journal of Physical Chemistry*, *56*(8), 996-999.

Hough, W., M. J. Rzasa, and B. B. Wood (1951), nterfacial tensions at reservoir pressures and temperatures; apparatus and the water-methane system, *Published in Petroleum Transactions*, *192*, 57-60.

House, K. Z., D. P. Schrag, C. F. Harvey, and K. S. Lackner (2006), Permanent carbon dioxide storage in deep-sea sediments, *Proceedings of the National Academy of Sciences of the United States of America*, *103*(33), 12291-12295.

Hovorka, S. D. (2009), Frio brine pilot: the first U.S. sequestration test, *Southwest Hydrology*, *September/October*.

Husebo, J., A. Graue, B. Kvamme, J. Stevens, J. J. Howard, and B. A. Baldwin (2008), Experimental investigation of methane release from hydrate formation in sandstone through both hydrate dissociation and CO_2 sequestration, *Proceedings of the 6th International Conference on Gas Hydratess, Vancouver, British Columbia, CANADA*.

IEA (2009), CO2 emissions from fuel combustion highlights*Rep.*, 115p pp.

Ikeda-Fukazawa, T., K. Kawamura, and T. Hondoh (2004), Mechanism of Molecular Diffusion in Ice Crystals, *Molecular Simulation, Vol. 30*(13-15), 973-979.

IPCC (Ed.) (2001), *Climate Change 2001: The Scientific Basis. Contribution of Working Group I to the Third Assessment Report of the Intergovernmental Panel on Climate Change. [Houghton, J.T.,Y. Ding, D.J. Griggs, M. Noguer, P.J. van der Linden, X. Dai, K. Maskell, and C.A. Johnson (eds.)]*, 881 pp., Cambridge University Press, United Kingdom and New York.

IPCC (2005), *IPCC Special Report on Carbon Dioxide Capture and Storage. Prepared by Working Group III of the Intergovernmental Panel on Climate Change [Metz, B., O. Davidson, H. C. de Coninck, M. Loos, and L. A. Meyer (eds.)]*. 442 pp., Cambridge University Press, Cambridge, United Kingdom and New York, NY, USA.

Israelachvili, J. (1991), *Intermolecular and surface forces, 2nd ed.*, Academic Press, London.

Jaccard, M. (2005), *Sustainable Fossil Fuels*, 381 pp., Cambridge University Press, New York, USA.

Jackson, K., L. E. Bowman, and J. L. Fulton (1995), Water solubility measurements in supercritical fluids and high-pressure liquids using near-infrared spectroscopy, *Analytical Chemistry*, *67*(14), 2368-2372.

Jaeger, P., and A. Pietsch (2009), Characterization of reservoir systems at elevated pressure, *Journal of Petroleum Science and Engineering*, *64*, 20-24.

Jaky, J. (1944), The coefficient of earth pressure at rest. In Hungarian

(A nyugalmi nyomas tenyezoje). *J. Soc. Hung. Eng. Arch. (Magyar Mernok es Epitesz-Egylet Kozlonye)*, 355-358.

James, W. R., III, K. L. Spyros, M. H. Jerry, and S. Mark Van (1995), High-resolution crosswell imaging of a west Texas carbonate reservoir: Part 3---Wavefield separation of reflections, *Geophysics*, *60*(3), 692-701.

Jaworski, G. W., J. M. Duncan, and H. B. Seed (1981), Laboratory study of hydraulic fracturing., *J. Geotech. Eng. Div.*, *107*(6), 713-732.

Jennings, H. Y., and G. H. Newman (1971), Effect of temperature and pressure on interfacial tension of water against methane-normal decane mixtures, *Society of Petroleum Engineers Journal*, *11*(2), 171-&.

Jo, H. Y., T. Katsumi, C. H. Benson, and T. B. Edil (2001), Hydraulic Conductivity and Swelling of Nonprehydrated GCLs Permeated with Single-Species Salt Solutions, *Journal of Geotechnical and Geoenvironmental Engineering*, *127*(7), 557-567.

Johnson, J. W., E. H. Oelkers, and H. C. Helgeson (1992), SUPCRT92: A software package for calculating the standard molal thermodynamic properties of minerals, gases, aqueous species, and reactions from 1 to 5000 bar and 0 to 1000[degree sign]C, *Computers & Geosciences*, *18*(7), 899-947.

Juang, C. H., and R. D. Holtz (1986), A probabilistic permeability model and the pore size density function, *International Journal for Numerical and Analytical Methods in Geomechanics*, *10*(5), 543-553. DOI: 510.1002/nag.1610100506.

Jung, J., D. N. Espinoza, and J. C. Santamarina (2010), Properties and phenomena relevant to CH4-CO2 replacement in hydrate-bearing sediments, *Journal of Geophysical Research-Solid Earth - In press*, *115*(B10102), doi:10.1029/2009JB000812.

Kang, Q. J., I. N. Tsimpanogiannis, D. X. Zhang, and P. C. Lichtner (2005), Numerical modeling of pore-scale phenomena during CO2 sequestration in oceanic sediments, *Fuel Processing Technology*, *86*(14-15), 1647-1665.

Kaszuba, J. P., D. R. Janecky, and M. G. Snow (2005), Experimental evaluation of mixed fluid reactions between supercritical carbon dioxide and NaCl brine: Relevance to the integrity of a geologic carbon repository, *Chemical Geology*, *217*(3-4), 277-293.

Katsube, T. J., and M. A. Williamson (1994), Effects of diagenesis on shale nano-pore structure and implications for sealing capacity, *Clay Minerals*, *29*(4), 451-461.

Kaya, A., and H. Y. Fang (2005), Experimental evidence of reduction in attractive and repulsive forces between clay particles permeated with organic liquids, *Canadian Geotechnical Journal*, *42*(2), 632-640.

Kempka, T., M. Waschbusch, R. Azzam, and T. M. Fernandez-Steeger (2008), Reducing ground subsidence involving geological CO2 storage during longwall mining

operations, *Quarterly Journal of Engineering Geology and Hydrogeology*, *41*, 439-448.

Kiefte, H., M. J. Clouter, and R. E. Gagnon (1985), Determination of acoustic velocities of clathrate hydrates by brillouin spectroscopy, *Journal of Physical Chemistry*, *89*(14), 3103-3108.

Kiessling, D., C. Schmidt-Hattenberger, H. Schuett, F. Schilling, K. Krueger, B. Schoebel, E. Danckwardt, and J. Kummerow (2010), Geoelectrical methods for monitoring geological CO2 storage: First results from cross-hole and surface-downhole measurements from the CO2SINK test site at Ketzin (Germany), *International Journal of Greenhouse Gas Control*, *4*(5), 816-826.

Kim, H. C., P. R. Bishnoi, R. A. Heidemann, and S. S. H. Rizvi (1987), Kinetics of methane hydrate decomposition, *Chemical Engineering Science*, *42*(7), 1645-1653.

Klapproth, A., E. Goreshnik, D. Staykova, H. Klein, and W. F. Kuhs (2003), Structural studies of gas hydrates, *Canadian Journal of Physics*, *81*(1-2), 503-518.

Kleinberg, R. L., C. Flaum, D. D. Griffin, P. G. Brewer, G. E. Malby, E. T. Peltzer, and J. P. Yesinowski (2003), Deep sea NMR: Methane hydrate growth habit in porous media and its relationship to hydraulic permeability, deposit accumulation, and submarine slope stability, *Journal of Geophysical Research-Solid Earth*, *108*(B10).

Kneafsey, T. J., and K. Pruess (2010), Laboratory Flow Experiments for Visualizing Carbon Dioxide-Induced, Density-Driven Brine Convection, *Transport in Porous Media*, *82*(1), 123-139.

Komai, T., Y. Yamamo, and K. Ohga (2000), Dynamics of reformation and replacement of CO2 and CH4 gas hydrates, paper presented at Gas Hydrate: Challenge for the future, Annals of the New York Academy of Sciences.

Krynicki, K., C. D. Green, and D. W. Sawyer (1978), Pressure and temperature-dependence of self-diffusion in water, *Faraday Discussions*, *66*, 199-208, DOI: 110.1039/DC9786600199.

Kuznetsova, T., and B. Kvamme (2002), Thermodynamic properties and interfacial tension of a model water-carbon dioxide system, *Physical Chemistry Chemical Physics*, *4*(6), 937-941.

Kvamme, B., A. Graue, T. Buanes, T. Kumetsoua, and G. Ersland (2007a), Storage of CO2 in natural gas hydrate reservoirs and the effect of hydrate as an extra sealing in cold aquifers, paper presented at International Journal of Greenhouse Gas Control.

Kvamme, B., T. Kuznetsova, A. Hebach, A. Oberhof, and E. Lunde (2007b), Measurements and modelling of interfacial tension for water plus carbon dioxide systems at elevated pressures, *Computational Materials Science*, *38*(3), 506-513.

Kvenvolden, K. A. (1988), Methane hydrate -- A major reservoir of carbon in the shallow geosphere?, *Chemical Geology*, *71*(1-3), 41-51.

Larsen, J. W. (2004), The effects of dissolved CO2 on coal structure and properties, *International Journal of Coal Geology*, *57*(1), 63-70.

Leach, E. S. H., A. Hopkinson, K. Franklin, and J. S. van Duijneveldt (2005), Nonaqueous suspensions of laponite and montmorillonite, *Langmuir, 21*(9), 3821-3830.

Lee, H., Y. Seo, Y. T. Seo, I. L. Moudrakovski, and J. A. Ripmeester (2003), Recovering methane from solid methane hydrate with carbon dioxide, *Angewandte Chemie-International Edition*, *42*(41), 5048-5051.

Lee, J. S., and J. C. Santamarina (2005), Bender elements: Performance and signal interpretation, *Journal of Geotechnical and Geoenvironmental Engineering*, *131*(9), 1063-1070.

Lee, J. Y., J. C. Santamarina, and C. Ruppel (2010), Volume change associated with formation and dissociation of hydrate in sediment, *Geochem. Geophys. Geosyst.*, *11*(Q03007), doi:10.1029/2009GC002667.

Lei, X. L., and Z. Q. Xue (2009), Ultrasonic velocity and attenuation during CO2 injection into water-saturated porous sandstone: Measurements using difference seismic tomography, *Physics of the Earth and Planetary Interiors*, *176*(3-4), 224-234.

Lenormand, R., E. Touboul, and C. Zarcone (1988), Numerical-models and experiments on immiscible displacements in porous-media, *Journal of Fluid Mechanics*, *189*, 165-187. doi:110.1017/S0022112088000953.

Leuning, R., D. Etheridge, A. Luhar, and B. Dunse (2008), Atmospheric monitoring and verification technologies for CO2 geosequestration, *International Journal of Greenhouse Gas Control*, *2*(3), 401-414.

Li, H., and J. Yan (2009), Evaluating cubic equations of state for calculation of vapor-liquid equilibrium of CO2 and CO2-mixtures for CO2 capture and storage processes, *Applied Energy*, *86*(6), 826-836.

Li, L., C. Peters, and M. Celia (2006), Upscaling geochemical reaction rates using pore-scale network modeling, *Advances in Water Resources*, *29*(9), 1351-1370.

Li, S., M. Dong, Z. Li, S. Huang, H. Qing, and E. Nickel (2005), Gas breakthrough pressure for hydrocarbon reservoir seal rocks: implications for the security of long-term CO2 storage in the Weyburn field, *Geofluids*, *5*(4), 326-334.

Liong, K. K., P. A. Wells, and N. R. Foster (1992), DIFFUSION OF FATTY-ACID ESTERS IN SUPERCRITICAL CARBON-DIOXIDE, *Industrial & Engineering Chemistry Research*, *31*(1), 390-399.

Lloret, A., M. V. Villar, M. Sanchez, A. Gens, X. Pintado, and E. E. Alonso (2003), Mechanical behaviour of heavily compacted bentonite under high suction changes, *Geotechnique*, *53*(1), 27-40.

Lu, C., W. S. Han, S. Y. Lee, B. J. McPherson, and P. C. Lichtner (2009), Effects of density and mutual solubility of a CO2-brine system on CO2 storage in geological formations: "Warm" vs. "cold" formations, *Advances in Water Resources*, *32*(12), 1685-1702.

Lyklema, J. (1995), *Fundamentals of interface and colloid science. Volume II: solid-liquid interfaces.*, Academic Press, New York.

Lynch, F. L. (1997), Frio shale mineralogy and the stoichiometry of the smectite-to-illite reaction: The most important reaction in clastic sedimentary diagenesis, *Clays and Clay Minerals*, *45*(5), 618-631.

Makogon, Y. (1997), *Hydrates of hydrocarbons*, 482 pp., PennWell Books, Tulsa, Okla.

Massoudi, R., and A. D. King (1974a), Effect of pressure on interfacial-tension of aqueous-solutions in equilibrium with compressed gases, *Abstracts of Papers of the American Chemical Society*, 179-179.

Massoudi, R., and A. D. King (1974b), Effect of pressure on surface-tension of water - adsorption of low-molecular weight gases on water at 25 degrees, *Journal of Physical Chemistry*, *78*(22), 2262-2266.

Mathieson, A., J. Midgley, K. Dodds, I. Wright, P. Ringrose, and N. Saoul (2010), CO2 sequestration monitoring and verification technologies applied at Krechba, Algeria, *The Leading Edge*, *29*(2), 216-222.

Mavko, G., T. Mukerji, and J. Dvorkin (2009), *The rock physics handbook, second edition. Tools for seismic analysis of porous media.*, 511 pp., Cambridge University Press, New York.

Max, M. D. (2000), Hydrate as a future energy resource for Japan, in *Natural gas hydrate in oceanic and permafrost environments*, edited by M. D. Max, pp. 225-238

Kluwer Academic Publishers, Netherlands.

May, E. F., M. R. Moldover, and J. W. Schmidt (2005), The dielectric permittivity of saturated liquid carbon dioxide and propane measured using cross capacitors, *International Journal of Thermophysics*, *26*(3), 563-576.

Maykut, G. A., and B. Light (1995), Refractive-index measurements in freezing sea-ice and sodium-chloride brines, *Applied Optics*, *34*(6), 950-961.

Mayne, P. W., and F. H. Kulhawy (1982), Ko-OCR Relationships in soil, *Journal of the Geotechnical Engineering Division-ASCE*, *108*(6), 851-872.

Mazumder, S., A. Karnik, and K. H. Wolf (2006), Swelling of coal in response to CO{sub 2} sequestration for ECBM and its effect on fracture permeability, *Journal: SPE Journal; Journal Volume: 11; Journal Issue: 3*, Size: page(s) 390-398.

Mazumder, S., K. Wolf, P. van Hemert, and A. Busch (2008), Laboratory experiments on environmental friendly means to improve coalbed methane production by carbon dioxide/flue gas injection, *Transport in Porous Media*, *75*(1), 63-92.

McCutcheon, S. C., J. L. Martin, and T. O. J. Barnwell (1993), Water Quality, in *Handbood of Hydrology (Editor: D.R. Maidment)*, edited by D. R. Maidment, McGraw-Hill, New York.

McGrail, B. P., H. T. Schaef, V. A. Glezakou, L. X. Dang, and A. T. Owen (2009), Water reactivity in the liquid and supercritical CO2 phase: Has half the story been neglected?, *Energy Procedia*, *1*(1), 3415-3419.

McGrail, B. P., H. T. Schaef, M. D. White, T. Zhu, A. S. Kulkami, R. B. Hunter, S. L. Patil, A. T. Owen, and P. F. Martin (2007), Using carbon dioxide to enhance recovery of methane from gas hydrate reservoirs: final summary report. PNNL-17035.*Rep.*, Pacific Northwest National Laboratory operated by Battelle Memorial Institute for the U.S. Department of Energy, Oak Ridge, TN.

Milkov, A. V. (2004), Global estimates of hydrate-bound gas in marine sediments: how much is really out there?, *Earth-Science Reviews*, *66*(3-4), 183-197.

Millero, F. J., and A. Poisson (1981), International one-atmosphere equation of state of seawater *Deep-Sea Reserach*, *28*(6A), 625-629.

Mitchell, J. K., and K. Soga (2005), *Fundamentals of soil behavior (3rd ed.)*, Wiley.

Mochizuki, T., and Y. H. Mori (2006), Clathrate-hydrate film growth along water/hydrate-former phase boundaries - numerical heat-transfer study, *Journal of Crystal Growth*, *290*(2), 642-652.

Montes-Hernandez, G., F. Renard, N. Geoffroy, L. Charlet, and J. Pironon (2007), Calcite precipitation from CO2-H2O-Ca(OH)(2) slurry under high pressure of CO2, *Journal of Crystal Growth*, *308*(1), 228-236.

Montoro, M., and F. Francisca (2010), Soil Permeability Controlled by Particle–Fluid Interaction, *Geotechnical and Geological Engineering*, *28*(6), 851-864.

Mori, Y. H., and T. Mochizuki (2000), Modeling of simultaneous heat and mass transfer to/from and across a hydrate film, in *Gas Hydrates: Challenges for the Future*, edited by G. D. Holder and P. R. Bishnoi, pp. 633-641.

Moridis, G. J., T. S. Collett, R. Boswell, M. Kurihara, M. T. Reagan, C. Koh, and E. D. Sloan (2009), Toward Production From Gas Hydrates: Current Status, Assessment of Resources, and Simulation-Based Evaluation of Technology and Potential, *Spe Reservoir Evaluation & Engineering*, *12*(5), 745-771.

Mraw, S. C., S. C. Hwang, and R. Kobayashi (1978), Vapor-liquid-equilibrium of CH4-CO2 system at low-temperatures, *Journal of Chemical and Engineering Data*, *23*(2), 135-139.

Nagakubo, S., N. Arata, I. Yabe, H. Kobayashi, and K. Yamamoto (2011), Environmental impact assessment study on Japan's methane hydrate program, *Fire in the ice, January 2011*, 4-11.

Nakatsuka, Y., Z. Q. Xue, H. Garcia, and T. Matsuoka (2010), Experimental study on CO2 monitoring and quantification of stored CO2 in saline formations using resistivity measurements, *International Journal of Greenhouse Gas Control*, *4*(2), 209-216.

Netherton, R., A. J. Piwinskii, and M. Chan (1977), Viscosity of brine from Salton sea geothermal field, California, from 25-degrees-C to 90-degrees-C at 100 kPa, *Transactions-American Geophysical Union*, *58*(12), 1248-1248.

Newell, D. L., J. P. Kaszuba, H. S. Viswanathan, R. J. Pawar, and T. Carpenter (2008), Significance of carbonate buffers in natural waters reacting with supercritical CO2: Implications for monitoring, measuring and verification (MMV) of geologic carbon sequestration, *Geophysical Research Letters*, *35*(23).

NIST (2010), Scientific and technical databases - thermophysical and thermochemical, edited.

Nygard, R., M. Gutierrez, K. Hoeg, and K. Bjorlykke (2004), Influence of burial history on microstructure and compaction behaviour of Kimmeridge clay, *Petroleum Geoscience*, *10*(3), 259-270.

Obriot, J., J. Ge, T. K. Bose, and J. M. Starnaud (1993), Determination of the density from simultaneous measurements of the refractive-index and the dielectric-constant of gaseous CH4, SF6 and CO2, *Fluid Phase Equilibria*, *86*, 315-350.

Oldenburg, C., J. Lewicki, and R. Hepple (2003), Near-surface monitoring strategies for geologic carbon dioxide storage verification.

Onishi, K., T. Ueyama, T. Matsuoka, D. Nobuoka, H. Saito, H. Azuma, and Z. Q. Xue (2009), Application of crosswell seismic tomography using difference analysis with data normalization to monitor CO2 flooding in an aquifer, *International Journal of Greenhouse Gas Control*, *3*(3), 311-321.

Ota, M., Y. Abe, M. Watanabe, R. L. Smith, and H. Inomata (2005a), Methane recovery from methane hydrate using pressurized CO2, *Fluid Phase Equilibria*, *228*(Sp. Iss, SI), 553-559.

Ota, M., K. Morohashi, Y. Abe, M. Watanabe, R. L. Smith, and H. Inomata (2005b), Replacement of CH4 in the hydrate by use of liquid CO2, *Energy Conversion and Management*, *46*(11-12), 1680-1691.

Ota, M., T. Saito, T. Aida, M. Watanabe, Y. Sato, R. L. Smith, and H. Inomata (2007), Macro and microscopic CH4-CO2 replacement in CH4 hydrate under pressurized CO2, *Aiche Journal*, *53*(10), 2715-2721.

Pacala, S., and R. Socolow (2004), Stabilization wedges: Solving the climate problem for the next 50 years with current technologies, *Science*, *305*(5686), 968-972.

Palomino, A. M. (2003), Fabric formation and control in fine-grained materials, Georgia Institute of Technology, Atlanta.

Palomino, A. M., and J. C. Santamarina (2005), Fabric map for kaolinite: Effects of pH and ionic concentration on behavior, *Clays and Clay Minerals*, *53*(3), 211-223.

Park, Y., D. Y. Kim, J. W. Lee, D. G. Huh, K. P. Park, J. Lee, and H. Lee (2006), Sequestering carbon dioxide into complex structures of naturally occurring gas hydrates, *Proceedings of the National Academy of Sciences of the United States of America*, *103*(34), 12690-12694.

Pegram, L. M., and M. T. Record (2007), Hofmeister salt effects on surface tension arise from partitioning of anions and cations between bulk water and the air-water interface, *Journal of Physical Chemistry B*, *111*(19), 5411-5417.

Pekot, J. L., and S. R. Reeves (2002), Modeling coal matrix shrinkage and differential swelling with CO2 injection for enhanced coalbed methane recovery and carbon sequestration applications*Rep.*, Advanced Resources International - U.S. Department of Energy, Houston, Texas.

Peng, D., and D. B. Robinson (1976), New 2-constant equation of state, *Industrial & Engineering Chemistry Fundamentals*, *15*(1), 59-64.

Pennell, K. D., G. A. Pope, and L. M. Abriola (1996), Influence of viscous and buoyancy forces on the mobilization of residual tetrachloroethylene during surfactant flushing, *Environmental Science & Technology*, *30*(4), 1328-1335.

Pentland, C. H., R. El-Maghraby, A. Georgiadis, S. Iglauer, and M. J. Blunt (2011), Immiscible Displacements and Capillary Trapping in CO2 Storage, *Energy Procedia*, *4*, 4969-4976.

Perry, R., and D. Green (1997), *Perry's chemical engineering handbook 7th ed*, McGraw-Hill, New York.

Phillips, O. M. (1991), *Flow and Reactions in Permeable Rocks*, Cambridge University Press.

Pilliteri, A., P. Cerasi, J. Stavrum, P. Zweigel, and R. Bøe (2003), Rock mechanical tests of shale samples from the cap rock of the Utsira Sand in well 15/9-A11*Rep.*, SINTEF Petroleum Research.

Pitzer, K. S., J. C. Pelper, and R. H. Busey (1984), Thermodynamic properties of aqueous sodium chlorine solutions, *J. Phys. Chem. Ref. Data*, *13*(1), 1-101.

Plug, W. J., and J. Bruining (2007), Capillary pressure for the sand-CO2-water system under various pressure conditions. Application to CO2 sequestration, *Advances in Water Resources*, *30*, 2339-2353.

Pokrovsky, O., S. Golubev, and J. Schott (2005), Dissolution kinetics of calcite, dolomite and magnesite at 25 C and 0 to 50 atm pCO2, *Chemical Geology*, *217*(3-4), 239-255.

Polak, J., and B. C. Y. Lu (1973), Mutual solubilities of hydrocarbons and water at 0 and 25 degrees C, *Canadian Journal of Chemistry-Revue Canadienne De Chimie*, *51*(24), 4018-4023.

Pope, G. A., and M. Baviere (1991), Reduction of capillary forces by surfactants, in *Basic concepts in enhanced oil recovery processes*, edited by M. Baviere, Elsevier Applied Science, London.

Poulos, H. G., and E. H. Davis (1974), *Elastic solutions for soil and rock mechanics*, Wiley.

Pusch, G., G. F. Ionescu, F. May, G. Voigtlander, L. Stecken, and H. D. Vosteen (2010), Common Features of Carbon Dioxide and Underground Gas Storage (1), *Oil Gas-European Magazine*, *36*(3), 131-137.

Qi, R., T. C. LaForce, and M. J. Blunt (2009), A three-phase four-component streamline-based simulator to study carbon dioxide storage, *Computational Geosciences*, *13*(4), 493-509.

Qin, J. F., R. J. Rosenbauer, and Z. Duan (2008), Experimental measurements of vapor-liquid equilibria of the H2O+CO2+CH4 ternary system, *Journal of Chemical and Engineering Data*, *53*(6), 1246-1249.

Rebata-Landa, V. (2007), Microbial activity in sediments: effects on soil behavior, Georgia Institute of Technology, Atlanta.

Ren, Q. Y., G. J. Chen, W. Yan, and T. M. Guo (2000), Interfacial Tension of (CO2+CH4) plus water from 298 K to 373 K and pressures up to 30 MPa, *J. Chem. Eng. Data*, *45*(4), 610-612.

Renard, F., E. Gundersen, R. Hellmann, M. Collombet, and Y. Le-Guen (2005), Numerical Modeling of the Effect of Carbon Dioxide Sequestration on the Rate of Pressure Solution Creep in Limestone: Preliminary Results, *Oil & Gas Science and Technology – Rev. IFP*, *60*(2), 381-399.

Riaz, A., M. Hesse, H. A. Tchelepi, and F. M. Orr (2006), Onset of convection in a gravitationally unstable diffusive boundary layer in porous media, *Journal of Fluid Mechanics*, *548*, 87-111.

Rimmele, G., V. Barlet-Gouedard, and F. Renard (2010), Evolution of the Petrophysical and Mineralogical Properties of Two Reservoir Rocks Under Thermodynamic Conditions Relevant for CO2 Geological Storage at 3 km Depth, *Oil & Gas Science and Technology-Revue De L Institut Francais Du Petrole*, *65*(4), 565-580.

Robinson, D. A. (2004), Measurement of the solid dielectric permittivity of clay minerals and granular samples using a time domain reflectometry immersion method, *Vadose Zone Journal*, *3*(2), 705-713.

Rosborg, B., and J. Pan (2008), An electrochemical impedance spectroscopy study of copper in a bentonite/saline groundwater environment, *Electrochimica Acta*, *53*(25), 7556-7564.

Rosen, M. J., H. Z. Wang, P. P. Shen, and Y. Y. Zhu (2005), Ultralow interfacial tension for enhanced oil recovery at very low surfactant concentrations, *Langmuir*, *21*(9), 3749-3756.

Rotenberg, Y., L. Boruvka, and A. W. Neumann (1983), Determination of surface tension and contact angle from the shapes of axisymmetric fluid interfaces, *J. Colloid Interface Sci. ; Vol/Issue: 93:1*, Pages: 169-183.

Ruppel, C., and J. W. Pohlman (2008), Climate change and the global carbon cycle: perspectives and opportunities, in *Fire in the Ice*, edited, p. 5.

Rutqvist, J., and C. Tsang (2002), A study of caprock hydromechanical changes associated with CO 2-injection into a brine formation, *Environmental Geology*, *42*(2), 296-305.

Sabirzyanov, A. N., A. P. Il'in, A. R. Akhunov, and F. M. Gumerov (2002), Solubility of water in Supercritical carbon dioxide, *High Temperature*, *40*(2), 203-206.

Sachs, W., and V. Meyn (1995), Pressure and temperature-dependence of the surface-tension in the system natural-gas water - principles of investigation and the first precise experimental-data for pure methane water at 25-degrees-c up to 46.8-MPa,

Colloids and Surfaces a-Physicochemical and Engineering Aspects, *94*(2-3), 291-301.

Sakurai, S., T. S. Ramakrishnan, A. Boyd, N. Mueller, and S. D. Hovorka (2006), Monitoring saturation changes for CO2 sequestration: petrophysical support for the Frio brine pilot experiment, *Petrophysics*, *47*(6), 483-496.

Sánchez, M., A. Gens, L. d. N. Guimarães, and S. Olivella (2005), A double structure generalized plasticity model for expansive materials, *International Journal for Numerical and Analytical Methods in Geomechanics*, *29*(8), 751-787.

Santamarina, J. C. (2001), Soil behavior at the microscale: particle forces, in *Symp. Soil Behavior and Soft Ground Construction, in honor of Charles C. Ladd*, edited, MIT.

Santamarina, J. C., and J. Jang (2009), Gas production from hydrate bearing sediments: geomechanical implications, *NETL methane hydrate newsletter: Fire in the Ice*, *9*(4), http://www.netl.doe.gov/technologies/oil-Gas/FutureSupply/MethaneHydrates/newsletter/newsletter.htm.

Santamarina, J. C., K. A. Klein, and M. A. Fam (2001a), *Soils and waves*, Wiley.

Santamarina, J. C., K. A. Klein, A. Palomino, and M. S. Guimaraes (2001b), Micro-scale aspects of chemical-mechanical coupling: interparticle forces and fabric, paper presented at Chemo-mechanical coupling in clays - from nano-scale to engineering applications, C. Di Maio, T. Hueckel, B. Loret (eds).

Santamarina, J. C., K. A. Klein, Y. H. Wang, and E. Prencke (2002), Specific surface: determination and relevance, *Canadian Geotechnical Journal*, *39*(1), 233-241.

Sarout, J., C. D. Piane, and D. Dewhurst (2009), Elastic properties of a mixed shale/sandstone specimen simulating reservoir/cap-rock interface, paper presented at 8th Euro-conference of rock physics and geomechanics, Ascona, Switzerland.

Sassiat, P. R., P. Mourier, M. H. Caude, and R. H. Rosset (1987), Measurement of diffusion-coefficients in supercritical carbon-dioxide and correlation with the equation of Wilke and Chang, *Analytical Chemistry*, *59*(8), 1164-1170.

Schmidt, K. A. G., G. K. Folas, and B. Kvamme (2007), Calculation of the interfacial tension of the methane-water system with the linear gradient theory, *Fluid Phase Equilibria*, *261*(1-2), 230-237.

Seo, Y., H. Lee, and T. Uchida (2002), Methane and carbon dioxide hydrate phase behavior in small porous silica gels: Three-phase equilibrium determination and thermodynamic modeling, *Langmuir*, *18*(24), 9164-9170.

Seo, Y. T., and H. Lee (2001), Multiple-phase hydrate equilibria of the ternary carbon dioxide, methane, and water mixtures, *Journal of Physical Chemistry B*, *105*(41), 10084-10090.

Seol, Y., and T. J. Kneafsey (2009), X-ray computed-tomography observations of water flow through anisotropic methane hydrate-bearing sand, *Journal of Petroleum Science and Engineering*, *66*(3-4), 121-132.

Serhatkulu, G. K., C. Dilek, and E. Gulari (2006), Supercritical CO2 intercalation of layered silicates, *Journal of Supercritical Fluids*, *39*(2), 264-270.

Servio, P., and P. Englezos (2001), Effect of temperature and pressure on the solubility of carbon dioxide in water in the presence of gas hydrate, *Fluid Phase Equilibria*, *190*(1-2), 127-134.

Servio, P., and P. Englezos (2002), Measurement of dissolved methane in water in equilibrium with its hydrate, *Journal of Chemical and Engineering Data*, *47*(1), 87-90.

Servio, P., and P. Englezos (2003), Morphology of methane and carbon dioxide hydrates formed from water droplets, *Aiche Journal*, *49*(1), 269-276.

Servio, P., F. Lagers, C. Peters, and P. Englezos (1999), Gas hydrate phase equilibrium in the system methane-carbon dioxide-neohexane and water, *Fluid Phase Equilibria*, *158*, 795-800.

Seto, C. J., K. Jessen, and F. M. Orr (2009), A multicomponent, two-phase-flow model for CO2 storage and enhanced coalbed-methane recovery, *SPE Journal*, *14*(1), 30-40.

Shao, H. B., J. R. Ray, and Y. S. Jun (2010), Dissolution and Precipitation of Clay Minerals under Geologic CO2 Sequestration Conditions: CO2-Brine-Phlogopite Interactions, *Environmental Science & Technology, 44*(15), 5999-6005.

Sharma, H. D., and K. R. Reddy (2001), *Geoenvironmental engineering: site remediation, waste containment, and emerging waste management technologies.*, John Wiley & Sons, Inc. , Hoboken, New Jersey.

Shi, J. Q., Z. Q. Xue, and S. Durucan (2007), Seismic monitoring and modelling of supercritical CO2 injection into a water-saturated sandstone: Interpretation of P-wave velocity data, *International Journal of Greenhouse Gas Control, 1*(4), 473-480.

Shin, H., and J. Santamarina (2009), Mineral dissolution and the evolution of k0, *Journal of Geotechnical and Geoenvironmental Engineering, 135*, 1141.

Shin, H., and J. C. Santamarina (2010), Fluid-driven fractures in uncemented sediments: Underlying particle-level processes, *Earth and Planetary Science Letters, 299*(1-2), 180-189.

Shin, H., J. C. Santamarina, and J. A. Cartwright (2008), Contraction-driven shear failure in compacting uncemented sediments, *Geology, 36*(12), 931-934.

Siemons, N., H. Bruining, H. Castelijns, and K. H. Wolf (2006), Pressure dependence of the contact angle in a CO2-H2O-coal system, *Journal of Colloid and Interface Science, 297*(2), 755-761.

Sloan, E. D., and C. A. Koh (2008), *Clathrate hydrates of natural gases - Third edition*, 701 pp., CRC Press, Boca Raton, FL.

Solomon, S. (2007), *Climate Change 2007: the physical science basis: contribution of Working Group I to the Fourth Assessment Report of the Intergovernmental Panel on Climate Change*, Cambridge University Press.

Somerton, W. H., I. M. Soylemezolu, and R. C. Dudley (1975), Effect of stress on permeability of coal, *International Journal of Rock Mechanics and Mining Science & Geomechanics Abstracts, 12*(5-6), 129-145.

Span, R., and W. Wagner (1996), A new equation of state for carbon dioxide covering the fluid region from the triple-point temperature to 1100 K at pressures up to 800 MPa, *Journal of Physical and Chemical Reference Data*, *25*(6), 1509-1596.

Sposito, G. (1989), *The chemistry of soils*, Oxford University Press, New York.

Spycher, N., K. Pruess, and J. Ennis-King (2003), CO2-H2O mixtures in the geological sequestration of CO2. I. Assessment and calculation of mutual solubilities from 12 to 100 degrees C and up to 600 bar, *Geochimica Et Cosmochimica Acta*, *67*(16), 3015-3031.

Spyros, K. L., and P. M. Bruce (1997), Crosswell seismic imaging of reservoir changes caused by CO2 injection, *The Leading Edge*, *16*(9), 1300-1308.

Spyros, K. L., M. H. Jerry, W. R. James, III, and S. Mark Van (1995), High-resolution crosswell imaging of a west Texas carbonate reservoir: Part 4---Reflection imaging, *Geophysics*, *60*(3), 702-711.

Stern, L. A., S. H. Kirby, and W. B. Durham (1998), Polycrystalline Methane Hydrate: Synthesis from Superheated Ice, and Low-Temperature Mechanical Properties, *Energy & Fuels*, *12*(2), 201-211.

Stevens, C. J., J. J. Howard, B. A. Baldwin, G. Ersland, J. Husebo, and A. Graue (2008), Experimental hydrate formation and gas production scenarios based on CO2 sequestration, paper presented at Proceedings of the 6th International Conference on Gas Hydratess, Vancouver, British Columbia, Canada.

Strazisar, B. R., A. W. Wells, J. R. Diehl, R. W. Hammack, and G. A. Veloski (2009), Near-surface monitoring for the ZERT shallow CO2 injection project, *International Journal of Greenhouse Gas Control*, *3*(6), 736-744.

Streit, E. E., and R. R. Hillis (2004), Estimating fault stability and sustainable fluid pressures for underground storage of CO2 in porous rock, *Energy*, *29*(9-10), 1445-1456.

Stumm, W. (1992), *Chemistry of the solid-water interface*, Wiley, New York.

Stumm, W., and J. J. Morgan (1996), *Aquatic chemistry: chemical equilibria and rates in natural waters, 3rd ed*, JohnWiley & Sons, Inc, New York.

Suarez-Iglesias, O., I. Medina, C. Pizarro, and J. L. Bueno (2008), Limiting diffusion coefficients of ethyl benzoate, benzylacetone, and eugenol in carbon dioxide at supercritical conditions, *J. Chem. Eng. Data*, *53*(3), 779-784.

Subramanian, S., and E. D. Sloan (2002), Solubility effects on growth and dissolution of methane hydrate needles, paper presented at Fourth International Conference on Gas Hydrates, Yokohama.

Suekane, T., N. Furukawa, S. Tsushima, S. Hirai, and M. Kiyota (2009), Application of MRI in the Measurement of Two-Phase Flow of Supercritical CO2 and Water in Porous Rocks, *Journal of Porous Media*, *12*(2), 143-154.

Sun, C. Y., G. J. Hen, and L. Y. Yang (2004), Interfacial tension of methane plus water with surfactant near the hydrate formation conditions, *J. Chem. Eng. Data*, *49*(4), 1023-1025.

Sun, R., and Z. H. Duan (2005), Prediction of CH4 and CO2 hydrate phase equilibrium and cage occupancy from ab initio intermolecular potentials, *Geochimica Et Cosmochimica Acta*, *69*(18), 4411-4424.

Sun, R., and Z. H. Duan (2007), An accurate model to predict the thermodynamic stability of methane hydrate and methane solubility in marine environments, *Chemical Geology*, *244*(1-2), 248-262.

Sun, Y. D., B. Y. Shekunov, and P. York (2003), Refractive index of supercritical CO2-ethanol solvents, *Chemical Engineering Communications*, *190*(1), 1-14.

Susilo, R., J. D. Lee, and P. Englezos (2005), Liquid-liquid equilibrium data of water with neohexane, methylcyclohexane, tert-butyl methyl ether, n-heptane and vapor-liquid-liquid equilibrium with methane, *Fluid Phase Equilibria*, *231*(1), 20-26.

Sutjiadi-Sia, Y., P. Jaeger, and R. Eggers (2008), Interfacial tension of solid materials against dense carbon dioxide, *Journal of Colloid and Interface Science*, *320*(1), 268-274.

Sutjiadi-Sia, Y., H. Marckmann, R. Eggers, C. Holzknecht, and S. Kabelac (2007), The effect of in liquids dissolved dense gases on interfacial and wetting characteristics, *Forschung Im Ingenieurwesen-Engineering Research*, *71*(1), 29-45.

Svandal, A., B. Kvamme, L. Granasy, T. Pusztai, T. Buanes, and J. Hove (2006), The phase-field theory applied to CO2 and CH4 hydrate, *Journal of Crystal Growth*, *287*(2), 486-490.

Takenouchi, S., and G. Kennedy (1965), Dissociation pressures of the phase CO2· 5.75 H2O, *J. Geol*, *73*, 383–390.

Tanaka, Y., N. Yamachi, S. Matsumoto, S. Kaneko, S. Okabe, and M. Shibuya (2008), Thermodynamic and transport properties of CO2, CO2-O-2, and CO2-H-2 mixtures at temperatures of 300 to 30,000 K and pressures of 0.1 to 10 MPa, *Electrical Engineering in Japan*, *163*(4), 18-29.

Tegze, G., L. Granasy, and B. Kvamme (2007), Phase field modeling of CH4 hydrate conversion into CO2 hydrate in the presence of liquid CO2, *Physical Chemistry Chemical Physics*, *9*(24), 3104-3111.

Terzaghi, K., R. B. Peck, and G. Mesri (1996), *Soil Mechanics in Engineering Practice, Third Edition*, 549 pp., John Wiley & Sons, New York.

Thomas, W. J., and M. J. Adams (1965a), Measurement of diffusion coefficients of carbon dioxide and nitrous oxide in water and aqueous solutions of glycerol, *Transactions of the Faraday Society*, *61*(508P), 668.

Thomas, W. J., and M. J. Adams (1965b), Measurement of diffusion coefficients of carbon dioxide and nitrous oxide in water and aqueous solutions of glycerol, *Transactions of the Faraday Society*, *61*(508P), 668-&.

Tonnet, N., D. Broseta, and G. Mouronval (2010), Evualation of the petrophysical properties of a carbonate-rich caprock for CO2 geological storage purposes, in *SPE EUROPEC/EAGE Annual Conference and exhibition*, edited, Barcelona, Spain 14-17 June 2010.

Tonnet, N., G. Mouronval, P. Chiquet, and D. Broseta (2011), Petrophysical assessment of a carbonate-rich caprock for CO2 geological storage purposes, *Energy Procedia*, *4*, 5422-5429.

Trusler, J. P. M., and M. Zarari (1992), The speed of sound and derived thermodynamic properties of methane at temperatures between 275-K and 375-K and pressures up to 10-MPa, *Journal of Chemical Thermodynamics*, *24*(9), 973-991.

Tuckermann, R. (2007), Surface tension of aqueous solutions of water-soluble organic and inorganic compounds, *Atmospheric Environment*, *41*(29), 6265-6275.

Uchida, T., T. Ebinuma, J. Kawabata, and H. Narita (1999), Microscopic observations of formation processes of clathrate-hydrate films at an interface between water and carbon dioxide, *Journal of Crystal Growth*, *204*(3), 348-356.

Urbanczyk, L., C. Calberg, C. Detrembleur, C. Jerome, and M. Alexandre (2010), Batch foaming of SAN/clay nanocomposites with scCO(2): A very tunable way of controlling the cellular morphology, *Polymer*, *51*(15), 3520-3531.

Van Olphen, H. (1977), *An Introduction to Clay Colloid Chemistry: For Clay Technologists, Geologists, and Soil Scientists (2nd edition)*, Wiley, New York.

van Oort, E. (2003), On the physical and chemical stability of shales, *Journal of Petroleum Science and Engineering*, *38*(3-4), 213-235.

Vandeweijer, V., B. van der Meer, C. Hofstee, F. Mulders, D. D'Hoore, and H. Graven (2011), Monitoring the CO2 injection site: K12-B, *Energy Procedia*, *4*, 5471-5478.

Verdon, J., and A. Woods (2007), Gravity-driven reacting flows in a confined porous aquifer, *Journal of fluid Mechanics*, *588*, 29-41.

Vesovic, V., W. A. Wakeham, G. A. Olchowy, J. V. Sengers, J. T. R. Watson, and J. Millat (1990), The transport-properties of carbon-dioxide, *Journal of Physical and Chemical Reference Data*, *19*(3), 763-808.

Waite, W. F., L. A. Stern, S. H. Kirby, W. J. Winters, and D. H. Mason (2007), Simultaneous determination of thermal conductivity, thermal diffusivity and specific heat in sI methane hydrate, *Geophysical Journal International*, *169*(2), 767-774.

Waite, W. F., et al. (2009), Physical properties of hydrate-bearing sediments, *Reviews of Geophysics*, *47*, *RG4003*, doi:10.1029/2008RG000279.

Walsh, M. R., C. A. Koh, E. D. Sloan, A. K. Sum, and D. T. Wu (2009), Microsecond Simulations of Spontaneous Methane Hydrate Nucleation and Growth, *Science*, *326*(5956), 1095-1098.

Watanabe, K., S. Imai, and Y. H. Mori (2005), Surfactant effects on hydrate formation in an unstirred gas/liquid system: An experimental study using HFC-32 and sodium dodecyl sulfate, *Chemical Engineering Science*, *60*(17), 4846-4857.

Watson, M. N., N. Zwingmann, and N. M. Lemon (2004), The Ladbroke Grove-Katnook carbon dioxide natural laboratory: A recent CO2 accumulation in a lithic sandstone reservoir, *Energy*, *29*(9-10), 1457-1466.

Watson, M. N., R. F. Daniel, P. R. Tingate, and C. M. Gibson-Poole (2005), CO2 related seal capacity enhancement in mudstones: evidence from the pine lodge natural CO2 accumulation, Otway Basin, Australia, paper presented at International Conference on Greenhouse Gas Control Technologies (7th : 2004 : Vancouver, Canada).

Weidler, P. G., and F. Friedrich (2007), Determination of the refractive index of particles in the clay and sub-micrometer size range, *American Mineralogist*, *92*(7), 1130-1132.

Wiebe, R. (1941), The binary system carbon dioxide-water under pressure, *Chemical Reviews*, *29*(3), 475-481.

Wiegand, G., and E. U. Franck (1998), Interfacial tension between water and non-polar fluids up to 473K and 2800bar, *Bunsenges. Phys. Chem.*, *98*(6), 809-817.

Wielopolski, L., and S. Mitra (2010), Near-surface soil carbon detection for monitoring CO2 seepage from a geological reservoir, *Environmental Earth Sciences*, *60*(2), 307-312.

Witherspoon, P. A. a. B., L (1969), Correlation of diffusion coefficients for Aaraffin, Aromatic, and Cycloparaffin Hydrocarbons in Water, *Industrial&Engineering Chemistry Fundamentals*, *8*(3), 589-591.

Wollenweber, J., S. Alles, A. Busch, B. M. Krooss, H. Stanjek, and R. Littke (2010), Experimental investigation of the CO2 sealing efficiency of caprocks, *International Journal of Greenhouse Gas Control*, *4*(2), 231-241.

World-Resources-Institute (2010a), Earth Trends (Energy and resources-country profiles) http://earthtrends.wri.org, edited.

World-Resources-Institute (2010b), Climate Analysis Indicator Tool (CAIT) version 7.0, edited.

Xu, B., K. Nagashima, J. M. DeSimone, and C. S. Johnson (2003), Diffusion of water in liquid and supercritical carbon dioxide: An NMR study, *Journal of Physical Chemistry A*, *107*(1), 1-3.

Xue, Z., D. Tanase, and J. Watanabe (2006), Estimation of CO2 saturation from time-lapse CO2 well logging in an onshore aquifer, Nagaoka, Japan, *Exploration Geophysics*, *37*(1), 19-29, doi:10.1071/EG06019.

Xue, Z. Q., T. Ohsumi, and H. Koide (2005), An experimental study on seismic monitoring of a CO2 flooding in two sandstones, *Energy*, *30*(11-12), 2352-2359.

Yoon, J. H., T. Kawamura, Y. Yamamoto, and T. Komai (2004), Transformation of methane hydrate to carbon dioxide hydrate: In situ Raman spectroscopic observations, *Journal of Physical Chemistry A*, *108*(23), 5057-5059.

Yoon, J. H., Y. Yamamoto, T. Komai, H. Haneda, and T. Kawamura (2003), Rigorous approach to the prediction of the heat of dissociation of gas hydrates, *Industrial & Engineering Chemistry Research*, *42*(5), 1111-1114.

Zeppieri, S., J. Rodriguez, and A. L. L. de Ramos (2001), Interfacial tension of alkane plus water systems, *J. Chem. Eng. Data*, *46*(5), 1086-1088.

Zhai, Z., and M. M. Sharma (2005), A New Approach to Modeling Hydraulic Fractures in Unconsolidated Sands, *SPE Annual Technical Conference and Exhibition*.

Zhang, H. L., and S. J. Han (1996), Viscosity and density of water plus sodium chloride plus potassium chloride solutions at 298.15 K, *J. Chem. Eng. Data*, *41*(3), 516-520.

Zhou, X. T., S. S. Fan, D. Q. Liang, and J. W. Du (2008a), Replacement of methane from quartz sand-bearing hydrate with carbon dioxide-in-water emulsion, *Energy & Fuels*, *22*(3), 1759-1764.

Zhou, X. T., S. S. Fan, D. Q. Liang, and J. W. Du (2008b), Determination of appropriate condition on replacing methane from hydrate with carbon dioxide, *Energy Conversion and Management*, *49*(8), 2124-2129.

VITA

DAVID NICOLAS ESPINOZA

Nicolas was born in San Salvador de Jujuy, Argentina. His passion for mathematics and physics was triggered by the Mathematics Olympics during primary school, and inspiring teachers at Colegio del Salvador. He obtained his diploma of "Ingeniero Civil" in 2006 from Universidad Nacional de Córdoba, the oldest academic institution in South America. He was accepted at the Georgia Institute of Technology in 2006 and received the degrees of Master Science in Civil Engineering in 2009 and Philosophy Doctor in 2011. Nicolas will pursue an academic carrier. He has accepted a post doctoral position at École des Ponts, Paris Tech.